Diese Dissertation haben begutachtet:

_____   _____
Prof. Dr. K. Held   Prof. Dr.

DISSERTATION

From DFT to DMFT:
correlation effects in transition metal oxides

ausgeführt zum Zwecke der Erlangung des akademischen Grades eines
Doktors der Naturwissenschaften unter der Leitung von

Univ. Prof. Dr. Karsten Held

und unter Co-Betreuung

von

Prof. Dr. Zhicheng Zhong & Dr. Oleg Janson

E 138 - Institut für Festkörperphysik
eingereicht an der Technischen Universität Wien
Fakultät für Physik

von

M.Sc. Liang SI

Matrikelnummer: 1328817

Wagramer Straβe 147, A-1220 Wien, Österreich

Wien, am 31. Januar 2017

_____
M.Sc. Liang SI

From DFT to DMFT:
correlation effects in transition metal oxides

Liang SI

January 2017, Vienna

For my wife and daughter

Xiang Fiona LI & Nian Charlotte SI

Contents

Technische Universität Wien

Abstract

Fakultät für Physik

Doctor of Physics

From DFT to DMFT: correlation effects in transition metal oxides

by Liang SI

The physics of transition metal oxides (TMOs) is shaped by the interplay between strong electronic correlations, spin-orbit interaction, directional anisotropy and doping, leading to a playground for exotic physical phenomenons. The fast development of *ab-initio* computational methods contributes to our fundamental understanding of TMOs and boosts the research aiming at functional materials design. However, more advanced computational themes, which are beyond the current density-functional theory (DFT), are needed to describe electrons in strongly correlated materials where the one-electron description breaks down. This thesis firstly reviews the state-of-the-art *ab-initio* computational methods: from DFT to tight-binding (TB) to dynamical mean field theory (DMFT). To demonstrate the importance of correlation effects in the prototypical correlated metal $SrRuO_3$, we study its electronic, magnetic and topological properties in the bulk, thin films and heterostructures using DFT+DMFT method. The advantages of DMFT are illustrated for $SrRuO_3$ thin films where correlation effects play a dominant role: the interplay between correlations and the confinement of the electrons in a heterostructures dramatically modifies the electronic structure. Further more, we apply DFT($+U$) and DMFT methods to a large variety of other strongly correlated materials, including $BaXO_3$:$BaTiO_3$ superlattices (X=Os, Ru, Ir), V_2O_3 surfaces, double pervoskite Sr_2CrMoO_6 and ferromagnetic $La_{(1-x)}Sr_xMnO_3$ surface and thin films. Our theoretical results are compared with experimental observations.

Chapter 1

Introduction

The fast development of computational materials science can be attributed to the success of density-functional theory (DFT) (Hohenberg and Kohn, 1964). In the past decades years, the number of applications and articles reporting *ab-initio* (or *first-principles*) material calculations have been increasing astonishingly. Numerous successful cases indicate that physicists have created a framework capable of calculating/predicting/explaining the electronic structure of materials. The first notable milestone in the process is the DFT developed by P. Hohenberg, W. Kohn and L. J. Sham (Hohenberg and Kohn, 1964; Kohn and Sham, 1965) between 1964 and 1965. The ideas behind DFT are: (i) calculating the one-to-one correspondence between the ground-state electron density $\rho_{GS}(\mathbf{r})$ of an interacting system and the external potential $v_{ext}(\mathbf{r})$ acting on it; (ii) dividing total energy into four parts: kinetic energy $T_0(\rho)$ of a non-interacting system, the classical Hartree electrostatic energy $E_H(\rho)$, the energy of the external potential acting on electrons $E_{ext}(\rho)$, and the exchange-correlation correction energy $E_{xc}(\rho)$, which accounts for the differences between interacting system and the auxiliary non-interacting system; (iii) solving the Kohn-Sham equations self-consistently, the ground-state density $\rho_{GS}(\mathbf{r})$ and the eigenvalues ϵ_{nk} are obtained.

Although DFT is an exact theory, the exchange-correlation energy $E_{xc}(\rho)$ is not known. This term includes the information of Coulomb interaction strengths, including Hund's exchange J and intra-orbital U and inter-orbital U' Coulomb repulsion, therefore it largely determines electronic structure and physical properties of materials. Two major approximations designed to accounts for this process are: the local (spin) density approximation (LDA/LSDA) (Kohn and Sham, 1965) and the generalized gradient approximation (GGA) (Perdew, 1985). The former one (LDA) is a very successful approximation for many systems of interest, especially for those materials in which the electronic density is quite uniform such as alkali metals and alkaline earth metals, also for less uniform systems such as semiconductors and ionic crystals. The later one (GGA) retains the correct features of L(S)DA and combines them with the first order in the inhomogeneity which is supposed to be the most energetically important.

With GGA and LDA approximations, DFT works for materials with weakly correlated electrons, due to that for those systems in LSDA/GGA both the correlation and exchange energy parts are satisfactory because of the classical Hartree electrostatic term and Pauli exclusion principle. But in practical LDA/GGA fails for both strongly correlated systems and semiconductors because both correlation and exchange energy are seriously underestimated. Thus here we come to the second milestone of computational materials science: the U corrections.

To simply describe correlated systems, usually one (also DFT) treats them as *uncorrelated* systems, i.e. the average of expectation value of a product of quantities is the same as the product of the averages of the individual quantities: $\langle AB \rangle = \langle A \rangle \langle B \rangle$.

However in real systems they are obviously different: $\langle AB \rangle \neq \langle A \rangle \langle B \rangle$. This difference is attributed to *correlations*. One typical example in *first-principles* calculations is the electronic density in interacting electron systems. In such systems, the electrons, which locate at position $\boldsymbol{r}$, influence the electronic distribution at position $\boldsymbol{r}'$. Thus the density-density correlation functions of this interacting system is:

$$\langle \rho(\boldsymbol{r})\rho(\boldsymbol{r}') \rangle \neq \langle \rho(\boldsymbol{r}) \rangle \langle \rho(\boldsymbol{r}') \rangle = \rho^2. \tag{1.1}$$

That is, it is not given by the square of the average density ρ. In short, this is why electronic correlations are seriously underestimated in standard DFT.

DFT simulations have failed for strongly correlated materials due to this underestimation. So which materials can be classified as strongly correlated materials? Generally these materials contain a wide class of heavy fermion compounds that host partially filled f-orbitals. Also transition metal oxides such as V_2O_3, $SrVO_3$ or $SrRuO_3$ based on partially filled d-orbitals, fall into this category. Their unusual electronic and magnetic properties are of fundamental interest and range from Mott-insulator transitions, half-metallic states, spin-charge separations to excitonic peaks. Correlation effects in these materials are far beyond the classical static Coulomb repulsion [the Hartree term $E_H(\rho)$] and factorization approximations such as Hartree-Fock (Fock, 1930; Slater, 1930). This calls for more advanced *ab-initio* calculation methods that treat electronic correlations appropriately.

Localized *d*-orbitals

$\boldsymbol{d_{xy}}$ $\boldsymbol{d_{yz}}$ $\boldsymbol{d_{xz}}$ $\boldsymbol{d_{x^2\text{-}y^2}}$ $\boldsymbol{d_{z^2\text{-}r^2}}$
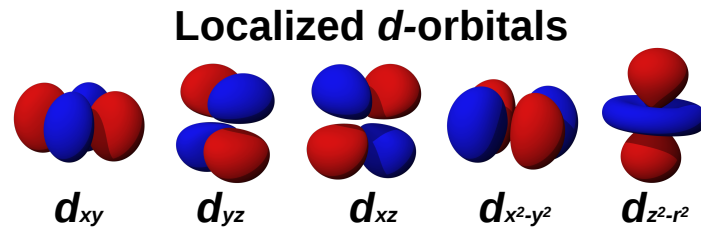
Regrading electronic correlations, three articles (Hubbard, 1963; Hubbard, 1964(a); Hubbard, 1964(b)) of J. Hubbard were published between 1963 to 1964 which introduce the Hubbard Hamiltonian for describing d- or f-orbital correlated materials at the model level. In this Hubbard model the correlations between electrons with opposite spin are attributed to a local U term: $U \sum_i n_{i\uparrow} n_{i\downarrow}$. Here i indicates orbital, and n is electron occupation, U is the Coulomb interaction. Double occupation in orbital i will be suppressed because it increases the total energy by U, thus penalizing fractional occupations in correlated d- or f-orbitals.

The first merger of DFT with the Hubbard Hamiltonian is the DFT+U method (also referred to as LDA+U) (Anisimov, Zaanen, and Andersen, 1991), which includes a Coulomb interaction U between opposite-spin electrons (usually for d- or f-orbitals) and treats it on the Hartree level. This static mean field theory works well for magnetically- or orbitally-ordered insulators but cannot account for dynamically correlation effects, e.g. that underlies the behavior of moderately correlated systems.

This is possible using a more advanced method: DFT+dynamic mean field theory (DFT+DMFT) (Metzner and Vollhardt, 1989; Georges and Kotliar, 1992; Georges et al., 1996; Kotliar and Vollhardt, 2004; Held et al., 2008; Held, 2007), in which the lattice Hubbard model is mapped onto a self-consistent quantum impurity model. DMFT accounts for the Mott-Hubbard metal-insulator transitions and incoherent peaks in the one-electron spectra appear as the result of the transfer of spectral weight from the quasiparticle peak to the Hubbard bands.

This thesis is aiming to (i) review the framwork of the state-of-the-art *ab-initio* computational theme DFT+DMFT, (ii) list my doctoral research focusing on electronic structure of strongly correlated electron systems. This thesis is includable following chapters.

In **Chapter 1** (this part) we are aiming to give a brief outline of this thesis.

Chapter 2

Ab-initio **calculations**
Density-functional theory
Tight-binding method
Spin-orbit coupling
Dynamical mean field theory
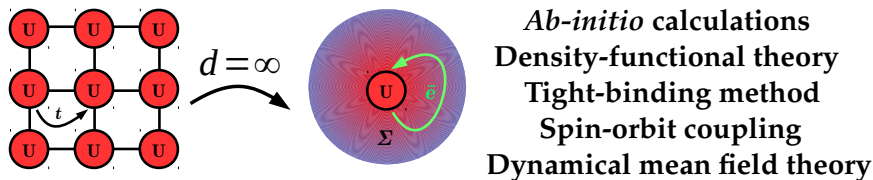
In **Chapter 2** we briefly review the development of *ab-initio* calculation methods: from very basic and early many-electrons methods such as *Hartree* and *Hartree-Fock* approximations to the framework of present-day computational method DFT. Later, we discuss the physics behind the first successful implementation of Hubbard model into the framwork of DFT: DFT+U. Next, we wil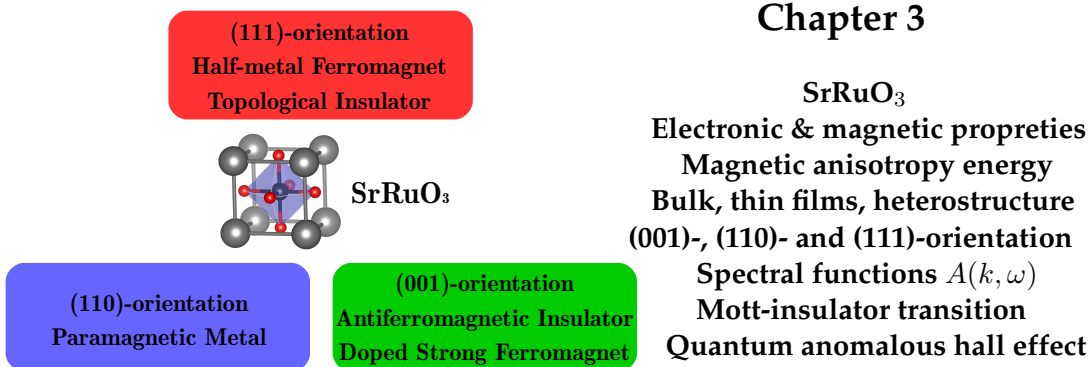l derive and explain the DMFT equations in a schematic way. Then we will discuss the combination of DFT and dynamical correlations by the state-of-the-art *ab-initio* computational scheme, DFT+DMFT, and how the corresponding equations are solved by continuous-time quantum monte-carlo (CT-QMC) method. In the last section of this chapter, we give a brief summary about derivation of tight-binding Hamiltonians of ABO_3 materials by means of maximum localized Wannier functions (Marzari et al., 2012).

Chapter 3

(111)-orientation
Half-metal Ferromagnet
Topological Insulator

SrRuO₃

(110)-orientation
Paramagnetic Metal

(001)-orientation
Antiferromagnetic Insulator
Doped Strong Ferromagnet

$SrRuO_3$
Electronic & magnetic propreties
Magnetic anisotropy energy
Bulk, thin films, heterostructure
(001)-, (110)- and (111)-orientation
Spectral functions $A(k, \omega)$
Mott-insulator transition
Quantum anomalous hall effect

Chapter 3 is devoted to the research of $SrRuO_3$ in its bulk, thin films and heterostructures. $SrRuO_3$ belongs to a handful stoichiometric $4d$ oxides with a ferromagnetic metallic ground state. Driven by the interplay between spin, orbital, charge degrees of freedom, in films and heterostructures states new physical phenomenons can emerge, such as exotic ferromagnetic states, metal-to-insulator and ferroelectric-to-nonferromagnetic transitions. Our work indicates that the properties of $SrRuO_3$ thin films and heterostructures are dramatically different from those of ordinary bulk states. DFT fails at simulating such states while the DMFT approach turns out to be effective and suited to capture the physics of such states.

Specifically, we start from the DFT($+U$) and DMFT research for the bulk properties and demonstrate how to calculate magnetic anisotropy energy in $SrRuO_3$ by tight-binding method. Then we discuss the electronic properties of $SrRuO_3$ (001)-, (110)-, (111)-oriented thin films. Different orientations are realized by growing $SrRuO_3$ thin films on various oriented $SrTiO_3$ substrates, or capping by $SrTiO_3$ atomic slabs. Our main findings are:

(1) $SrRuO_3$ (001)-oriented thin films are experimentally determined to be non-magnetic insulators. However a detailed theoretical explanation is lacking. In agreement with experiment, we find an intrinsic thickness limitation for metallic ferromagnetism in $SrRuO_3$ (001) thin films. Proposing charge carrier doping as a new route to manipulate thin films, we predict room temperature ferromagnetism in electron-doped $SrRuO_3$ ultra thin films.

(2) $SrRuO_3$ (110) thin films exhibit paramagnetic metallic states from monolayer to trilayer. The expected strong ferromagnetism due to the "flat bands" is absent. However the metallic state survives even down to a monolayer. This is different with (001)- and (111)-oriented $SrRuO_3$ thin films.

(3) $SrRuO_3$ (111) trilayer is a ferromagnetic half-metal even at room temperature. The half-metallic ferromagnetic state with an ordered magnetic moment of $2\,\mu_B/Ru$ survives the ultimate dimensional confinement down to bilayer even at elevated temperatures of $500\,K$. In the minority channel, the spin-orbit coupling opens a gap at the linear band crossing corresponding to $\frac{3}{4}$ filling of the t_{2g} shell. We demonstrate that the respective state is Haldane's quantum anomalous Hall state with Chern number C=1 that can be realized, without an external magnetic field or magnetic impurities.

Finally, to solve the experimental puzzle about the existence of the high-spin states in $SrRuO_3$, we carry out DFT$+U$ calculations for bulk $SrRuO_3$ in the presence of oxygen vacancies. By creating a single oxygen vacancy in a $SrRuO_3$ supercell, we show that the two Ru atoms next to the vacancy host high-spin states.

Chapter 4

At bulk   **At interface/surface**

Spin degeneracy   **Separation of spin**
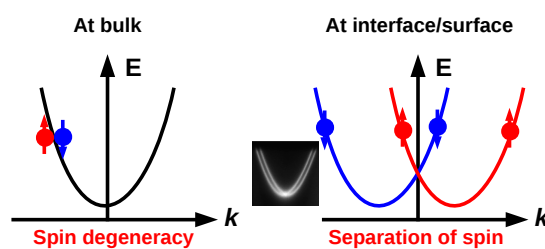
$BaOsO_3$:$BaTiO_3$ superlattice
Rashba splitting
V_2O_3 surfaces
Mott-insulator transition
Sr_2CrMoO_6
Double perovskite
$La_{1-x}Sr_xMnO_3$
d-p hybridization

The focus of **Chapter 4** is to extend DFT$+U$ and DFT+DMFT methods to other transition metal oxides: $BaXO_3$:$BaTiO_3$ superlattice (X=Ru, Os, Ir), differently terminated V_2O_3 surfaces, the double perovskite Sr_2CrMoO_6 and the $3d$ ferromagnetic $La_{(1-x)}Sr_xMnO_3$ thin films. The research of $BaXO_3$:$BaTiO_3$ superlattice and $La_{(1-x)}Sr_xMnO_3$ thin films are carried out by tight-binding and DFT($+U$) methods. Firstly, DMFT calculations in the presence of spin-orbit interaction is still a challenging issue. However the spin-orbit interaction is essential for certain physics

such as Rashba splitting (in $BaXO_3$:$BaTiO_3$ superlattices), magnetic anisotropy energy (in bulk $SrRuO_3$), topological insulating states [in $SrRuO_3$ (111) bilayer]. Secondly, for large system DMFT is usually time consuming, e.g. for cubic $SrRuO_3$ (one Ru site) a standard self-consistent spin-polarized DFT/DFT+U calculation normally costs minutes at most, however a spin-polarized DMFT can cost up to 3072 ($128 \, \text{cores} \times 24 \, \text{hours}$) CPU hours. Our main findings are:

(1) By heterostructuring the ferroelectric material $BaTiO_3$ and the paramagnetic metal $BaOsO_3$, we obtain a giant switchable Rashba effect system. The spin-splitting of the Rashba effect emerges when the crystal inversion symmetry breaking couples with strong spin-orbit coupling effect. This conclusion can be generally extended to $4d$ and $5d$ transition metal elements such as Ru, Ir. Another advantage of our conclusion is that in such heterostructures the Rashba splitting can be easily tuned through thickness and external electric field.

(2) In a joint experimental and theoretical study, we explore surface effects that affect the metal-insulator transition in the model Mott-Hubbard compound: Cr-doped V_2O_3. We find a microscopic domain formation that is clearly affected by the crystallographic orientation of the surface. DFT+DMFT study of different surface terminations shows that the surface reconstruction with excess vanadyl cations leads to doped, and hence more metallic, surface states, which explains the experimental observations.

(3) We study the electronic structure of the double perovskite compound Sr_2CrMoO_6. Its ferrimagnetic half-metallic nature is successfully captured after considering both dynamic and static local correlations. We reveal that the change in charge transfer energy is due to a shift of Cr-d states in Sr_2CrMoO_6 compared to Fe-d in Sr_2FeMoO_6 that suppresses the hybridization between Cr-t_{2g} and Mo-t_{2g}. This strongly weakens the hybridization-driven mechanism of magnetism discussed for Sr_2FeMoO_6. Nonetheless, the magnetic transition temperature of Sr_2CrMoO_6 remains high since an additional superexchange contribution to magnetism arises with a finite intrinsic moment at the Mo site.

(4) Sr-doped $LaMnO_3$ ($3d^4$) is a strong ferromagnetic correlated metal with high-T_C of 378 K and a moment of $3.7 \, \mu_B/$Mn. Experiments confirm that the rotation and tilting of MnO_6 octahedra in $La_{(1-x)}Sr_xMnO_3$ thin films depend on the sample thickness, thus one would expect that the electronic structure of $La_{(1-x)}Sr_xMnO_3$ systems is sensitive to the thickness and the degree of octahedron rotation and tilting. We artificially change the degree of octahedron rotation and tilting and find that the Mn-d bandwidth is affected by two factors: (i) the Mn-O bond length, and (ii) rotation and tilting of the octahedra. We also discuss the magnetic properties of $La_{(1-x)}Sr_xMnO_3$ thin films.

In **Chapter 5** we summary the results discussed in **Chapter 2-4** and outline directions for further research in a short outlook.

Throughout this thesis the reader will find some "*Calculation Details*" blocks. These discussions contain technical information and computational parameters and are not necessary for understanding the content of this thesis.

Chapter 2

Review on the DFT+DMFT Merhod for Strongly Correlated Electrons

2.1 Many-Body Hamiltonian

In the field of *classical physics*, the position and motion of a object can be described by the velocity formula: $\vec{v} = \frac{\Delta \vec{r}}{\Delta t}$, and the Newton's second law of motion: $\vec{F} = m\frac{\partial \vec{v}}{\partial t}$. By the help of these motion equations, with knowing the initial position of the object, the positions and velocity at any time t can be obtained. In principle, the complex objects systems can contain a large number of single constituents (atoms, electrons etc), and also they can be extended from a single electron to the whole universe. The *explaining/predicting* solutions are what theoretical physicists are aiming at, in order to describe the motion of everything. In the field of *classical physics* this looks not impossible, from using law of universal gravitation to explain why apples fall down onto earth, to using Maxwell's equations to unify electricity and magnetism. However even a three-body problem is very complicated, as it allows for the chaotic solutions. Despite the success that *classical physics* has achieved, this theory fails when describing black-body radiation and the movement of microscopic particles.

The development of *quantum physics* paved a new way to understand the movement of microscopic particles. For any many-body systems if we use wave functions to describe their ground states and include certain boundary conditions, *quantization* eigenvalues would be obtained if we use the Schrödinger equation to describe the evolution of particle wave:

$$H|\Psi\rangle = E|\Psi\rangle \tag{2.1}$$

where E is the energy and Ψ is the respective wave function, H is the Hamiltonian operator of a many-body system. The largest problem we face is actually: the solution of Eq. 2.1 is a difficult computational task on its own because of the many particles contained in $|\Psi\rangle$. Anyway, despite the difficulties of solving a many-body Schrödinger equation, even containing all physics in a mathematical formula sometimes is a hard task. The related elementary particles when describing realistic condensed matter system at the energy scale in daily life are the atomic nuclei, which are usually considered as point-charges, and the electrons that gives rise to the electronic structure. If we are aiming at the daily life physics from meV to KeV, we can restrict ourselves to nuclei and electrons. In this case, to describe any realistic multi-atoms/particles systems, a specific Hamiltonian can be given (in atomic units):

$$H = -\frac{1}{2}\sum_i \nabla_i^2 - \frac{1}{2}\sum_\alpha \frac{1}{M_\alpha}\nabla_\alpha^2 - \sum_{\alpha,i}\frac{Z_\alpha}{|r_i - R_\alpha|} + \frac{1}{2}\sum_{i,i'}\frac{1}{|r_i - r_{i'}|} + \frac{1}{2}\sum_{\alpha,\alpha'}\frac{Z_\alpha Z_{\alpha'}}{|R_\alpha - R_{\alpha'}|}$$

(2.2)

where the atoms are labeled by atomic nuclei $\{\alpha\}$; $\{Z_\alpha\}$ and $\{M_\alpha\}$ indicate nuclear charges and masses, respectively; electrons are labeled by subscript $\{i\}$. This Hamiltonian includes the information of kinetic energy of electrons and nuclei, the electronic interaction energy, and the spin which does not appear explicitly in Eq. 2.2 because to the lowest order in the relativistic correction, the energy is spin independent. Nevertheless, the Hamiltonian Eq. 2.2 can give rise to magnetism, it constructs the *many-body theory*.

If this equation (Eq. 2.2) can be exactly solved for all macroscopic systems (even tiny microscopic systems!), it will terminate further development in theoretical physics and chemistry, calculating molecules and solids would be an exercise in applied mathematics, merely a technical problem. However, because of the quantum many-body nature of the problem in Eq. 2.2, finding the solution, though possible in principle, is impossible in practice. To understand why, we consider a canonical example, a single atom of oxygen, which has 8 electrons, its ground state wave-function $\Psi(\mathbf{r}_1, \mathbf{r}_2, ..., \mathbf{r}_8)$ is a function of 24 coordinates. What does it take to store such a wave function? If we compute Ψ at only 10 values for each coordinate [i.e., to measure 10 values for each directions (x, y, z), thus for each electron we measure 1000 values], we would have to record 10^{24} values. And this is only a O atom on a crude mesh! For any crystals with more than several atoms, storing such an amount of data is hardly possible, let alone to self-consistently calculate their wave functions. However, such wave functions are the essential quantity to describe the ground state of condensed matter systems. Simplifications/approximations have to be taken.

For a realistic condensed matter system the first simplification we can introduce is reducing the number of the degrees of freedom. Experimental observation indicates that the timescale associated to the motion of nuclei is usually much slower than that of electrons. In fact, the mass ratio of the electrons to that of the protons is about 1 in 1836, so that their velocity is larger than that of protons. At 1927, M. Born and R. Oppenheimer proposed that the motion of atomic nuclei and electrons in a molecule can be separated, i.e., the Born–Oppenheimer approximation (Born and Oppenheimer, 1927). By this theory, it was generally believed that when the distribution of nuclei changes sightly, electrons are able to change their motion states to adapt the motion of nuclei, staying always in the same stationary state of the many-body Hamiltonian Eq. 2.2. The wave functions Ψ will vary in time but if the electrons were, for example, in the ground state, they will remain there forever. This means that as the nuclei follow their dynamical motions, the electrons instantaneously adjust their wave functions according to the nuclear wave functions.

When we fix the positions of nuclei, such an approximation ignores the possibility of transitions between different electronic eigenstates. Transitions can only arise through coupling with an external electromagnetic field and involve the solution of the time-dependent Schrödinger equation, and, of course, with changing the positions of the nuclei. This has been achieved, especially in the linear response regime, but also in a non-perturbative framework. One has to note that the standard DFT can not deal with electronic excited states because it is a static theory. In this thesis the excited states will be discussed through DFT+DMFT method. Under the above conditions, the full wave function factorizes in the following way:

$$\Psi(\mathbf{R}, \mathbf{r}, t) = \Theta(\mathbf{R}, t)\Phi(\mathbf{r}, t) \tag{2.3}$$

where $\Theta(\mathbf{R}, t)$ and $\Phi(\mathbf{r}, t)$ are the wave functions of nuclei and electrons, respectively. Then under the condition of frozen nuclei the problem reduces to solving the time-independent (static) wave functions of all electrons. This reduces the number of values to store, the difficulties of solving and recording realistic systems reduced to only the electrons remain however unfeasible.

The first attempt to simplify the wave function was proposed by D. R. Hartree in 1928 (Hartree, 1928). His main idea was to approximate the many-electron wave function as a product of one-electron wave functions:

$$\Phi(\mathbf{r}) = \prod_i \varphi_i(\mathbf{r}_i) \tag{2.4}$$

and the Schrödinger equation is expressed as:

$$(-\frac{1}{2}\nabla^2 + V_{eff}^i(\mathbf{R}, \mathbf{r}))\varphi_i(\mathbf{r}) = \epsilon_i \varphi_i(\mathbf{r}) \tag{2.5}$$

where

$$V_{eff}^i(\mathbf{R}, \mathbf{r}) = V(\mathbf{R}, \mathbf{r}) + \int \frac{\sum_{j \neq i}^N \psi_j(\mathbf{r}')\psi_j^*(\mathbf{r}')}{|\mathbf{r} - \mathbf{r}'|} d\mathbf{r}' \tag{2.6}$$

and $V(\mathbf{R}, \mathbf{r})$ means external potential. The second term in the right side of equation Eq. 2.6 is the classical electrostatic potential generated by the charge distribution $\sum_{j \neq i}^N \psi_j(\mathbf{r}')\psi_j^*(\mathbf{r}')$, N is the number of total electrons.

This is a set of i one-particle Schrödinger equations in an effective potential that takes into account the interaction with the other electrons in a mean-field way (i labels electrons). This so-called self-consistent *Hartree* approximation is a very rough treatment, because it considers all electrons as distinguishable particles, even the (anti-symmetry) fermionic nature of wave functions is not taken into account. To eliminate this short-coming, V. Fock and J. C. Slater (Fock, 1930; Slater, 1930) restored the anti-symmetry of fermions wave functions by using Slater determinants:

$$\Phi(\mathbf{r}) = \frac{1}{\sqrt{N!}} \begin{vmatrix} \varphi_1(\mathbf{r}_1) & \varphi_1(\mathbf{r}_2) & \dots & \varphi_1(\mathbf{r}_n) \\ \varphi_2(\mathbf{r}_1) & \varphi_2(\mathbf{r}_2) & \dots & \varphi_2(\mathbf{r}_n) \\ \vdots & \vdots & \ddots & \vdots \\ \varphi_n(\mathbf{r}_1) & \varphi_n(\mathbf{r}_2) & \dots & \varphi_n(\mathbf{r}_n) \end{vmatrix}, \tag{2.7}$$

introducing particle exchange in an exact manner. This approximation is called *Hartree-Fock* (HF) or self-consistent field (SCF) approximation and has been for a long time the method of choice to calculate the electronic structure of molecules in real space. Even though the two-body level Coulomb interactions are considered by the Coulomb term [$E_H(\rho)$ in Eq. 2.8], genuine many-body correlations are however absent. In fact, the total wave function cannot simply be written as an anti-symmetric product of single-particle wave functions. Nevertheless, it provides a very reasonable picture for atomic systems, it also provides a reasonably good description of inter-atomic bonding. HF equation is more advanced than Hartree equation because it considers about particle exchange effect. The ground state wave functions and eigenenergies can be consistently obtained, these wave functions can be used for solving Eq. 2.5.

2.2 Density-Functional Theory and Its Approximations

Parallel to the development of real space methods, L. Thomas and E. Fermi proposed (Thomas, 1927; Fermi, 1928; Lang, Lundqvist, and March, 1983) a theory for the ground state which was based on electronic density $|\Psi|^2$ instead of the wave function Ψ, at about the same time (1927-1928) as D. R. Hartree. The main idea is that the full electronic density is the fundamental variable of the many-body problems and a differential equation for the density can be derived without resorting to one-electron orbitals. However the Thomas-Fermi (TF) approximation is too crude: it does not account for electron exchange and correlation effects and it is also unable to sustain bound states. From this point of view, the HF approximation is more elaborate than the TF approximation. However, the TF approximation puts a foundation for the later development of density functional theory (DFT).

DFT is based on two pillars: the first one is the Hohenberg-Kohn (HK) theorem, which was proved by P. Hohenberg and W. Kohn in 1964 (Hohenberg and Kohn, 1964). The HK theorem established the foundation of DFT. It contains two lemmas: (1) if two systems of electrons, one trapped in a potential $v_1(\boldsymbol{r})$ and the other in $v_2(\boldsymbol{r})$, have the same ground-state density $\rho(\boldsymbol{r})$ then necessarily $v_1(\boldsymbol{r}) - v_2(\boldsymbol{r})$ = constant; (2) for any positive integer N and the potential $v(\boldsymbol{r})$, a density functional $F[\rho]$ exists such that $E_{(v,N)}[\rho] = F[\rho] + \int v(\boldsymbol{r})\rho(\boldsymbol{r})d^3\boldsymbol{r}$ obtains its minimal value at the ground-state density of N electrons in the potential $v(\boldsymbol{r})$. The minimal value of $E_{(v,N)}[\rho]$ is then the ground state energy of this system.

The first HK theorem demonstrates that $\rho(\boldsymbol{r})$, which is product of one-particle wave functions $\psi_n(\boldsymbol{r})$, uniquely determines $v(\boldsymbol{r})$. Thus all the ground state properties of this many-electrons system, including the ground state energy, are uniquely determined by the electron density $\rho(\boldsymbol{r})$ that depends on only 3 spatial variables (x, y, z). In this way a many-body problem of N electrons with $3N$ spatial coordinates and an exponentially large Hilbert space is reduced to a problem of 3 spatial coordinates, through a functional of the electron density. The second HK theorem defines an energy functional for the system and proves that the correct ground state electron density minimizes this energy functional.

Up to this step the total energy of many-body system can be separated into kinetic, electrostatic (classical Coulomb energy, in which the two-body Coulomb interaction can be included), external potential energy, exchange and (many-body) correlation contributions. The biggest difficulty is to deal with exchange-correlation effects. It seems that excluding many-body correlation-exchange effects does matter but in fact for most materials e.g. insulators it is quite under control. For semiconductors some corrections regrading the exchange part e.g. modified Becke-Johnson potential (MBJ) (Tran and Blaha, 2009) or some methods like *GW* approximation (GWA) (Hedin, 1965) are needed. On the contrary, there is a problem with the Hamiltonian expression in terms of the kinetic energy $\langle \Psi | T | \Psi \rangle$ electronic density. The only kinetic energy expression that have obtained up to now was the one proposed by Thomas-Fermi model, which is a functional of electronic density. However this is quite a big approximation because the TF model does not support bound states. This problem comes from the fact that the kinetic energy operator is inherently non-local, though short-ranged. In 1965, W. Kohn and L. J. Sham proposed the idea of replacing the kinetic energy of the interacting electrons with that of an equivalent non-interacting system (the second pillars of DFT), in which the single-particle wave functions and kinetic energy can be easily obtained. Then the total energy becomes a function of the electron density distribution and can be divided into four parts:

$$E(\rho) = T_0(\rho) + E_H(\rho) + E_V(\rho) + E_{xc}(\rho)$$
$$= T_0(\rho) + \frac{1}{2}\int d\boldsymbol{r}\int d\boldsymbol{r}'\frac{\rho(\boldsymbol{r})\rho(\boldsymbol{r}')}{\boldsymbol{r}-\boldsymbol{r}'} + \int v_{ext}d\boldsymbol{r}(\boldsymbol{r})\rho(\boldsymbol{r}) + E_{xc}(\rho) \tag{2.8}$$

where the $T_0(\rho)$ is the non-interacting kinetic energy, $E_H(\rho)$ is the classical (*Hartree*) interaction energy, $E_V(\rho)$ is the external potential from the contribution of nuclei, and $E_{xc}(\rho)$ is the so-called *exchange-correlation* energy that describes the Coulomb interactions between electrons. The meaning of $E_{xc}(\rho)$ can be understood as below:

$$E_{xc}(\rho) = E_{ee}(\rho) - E_H(\rho) + T_e(\rho) - T_0(\rho) \tag{2.9}$$

where the $E_{ee}(\rho)$ is the *full* electron-electron interaction energy, $T_e(\rho)$ and $T_0(\rho)$ are the kinetic energies of the real interacting system and a non-interacting auxiliary system.

Because the kinetic energy T_0 and external potential term $E_V(\rho)$ account for a single electron moving in a non-interacting environment, and the *Hartree* Coulomb energy E_H only includes classical electrostatic energy, the last term E_{xc} should accounts for all interaction effects beyond that. All the information about *exchange-correlation* beyond classical Coulomb interaction can be attributed to the E_{xc} term. The major contribution to exchange energy E_x originates from the *Pauli exclusion principle*, hence even a local approximation (GGA/LDA) is well justified. However, the correlation effects are always underestimated due to that the realistic electronic correlation effects are far beyond the static density-density interaction $E_H(\rho)$.

By minimizing the total energy (Eq. 2.8) of systems with respect to $\{\psi_{n,\mathbf{k}}\}$, with the constraint $\langle\psi_{n,\mathbf{k}}|\psi_{n',\mathbf{k}}\rangle = \delta_{n,n'}$, one arrives at the *single-particle Kohn-Sham* equation reads:

$$\hat{h}_e(\boldsymbol{r})\psi_{n,\mathbf{k},\sigma}(\boldsymbol{r}) = \{-\frac{\nabla^2}{2} + v_{eff}(\boldsymbol{r})\}\psi_{n,\mathbf{k},\sigma}(\boldsymbol{r}) = \epsilon_{n,\mathbf{k},\sigma}\psi_{n,\mathbf{k},\sigma}(\boldsymbol{r}) \tag{2.10}$$

where σ is the spin index, n labels all states, $\boldsymbol{r}$ is the real space vector and $\boldsymbol{k}$ is the reciprocal wave vector. Summarily, v_{eff} is the effective potential acting on single-electron, and it is the sum of external field (ion-electrons), classic Coulomb interaction and exchange-correlation energy:

$$v_{eff}(\boldsymbol{r}) = -\sum_{\alpha}\frac{Z_\alpha}{\boldsymbol{r}-\boldsymbol{R}_\alpha} + \int d\boldsymbol{r}'\frac{\rho(\boldsymbol{r}')}{|\boldsymbol{r}-\boldsymbol{r}'|} + \frac{\delta E_{xc}(\rho)}{\delta\rho}. \tag{2.11}$$

The total electron density distribution $\rho(\boldsymbol{r})$ is obtained by summing all the occupied state electrons (N is the number of states of the system):

$$\rho(\mathbf{r}) = \sum_{\sigma}\sum_{\mathbf{k}}^{\Omega}\sum_{n=1}^{N}|\psi_{n,\mathbf{k},\sigma}(\boldsymbol{r})|^2 \tag{2.12}$$

Provided the $E_{xc}(\rho)$ term is known, the Kohn-Sham equations Eq. 2.10 can be exactly solved by following steps, as shown in Fig. 2.1:

(1) Guess an initial density distribution $\rho(\boldsymbol{r})$, e.g. usually one constructs this by summing atomic electron densities up.

(2) Construct the single particle potential $V_{eff}(\boldsymbol{r})$ using this initial electron density distribution and Eq. 2.11.

(3) Solve the single particle Kohn-Sham equation Eq. 2.10, obtaining the single particle wave functions $\psi_{n,\mathbf{k},\sigma}$ and eigen energy $\epsilon_{n,\mathbf{k},\sigma}$.

(4) Calculate the new electron density using Eq. 2.12.

(5) Calculate the difference between the old iteration $\rho_{old}(\mathbf{r})$ and the new iteration electron density $\rho_{new}(\mathbf{r})$. If convergence is reached, then this self-consistent loop is terminated. If not, go back to (2) and use the $\rho_{new}(\mathbf{r})$ to construct a new $V_{eff}(\mathbf{r})$, continuing the calculation.
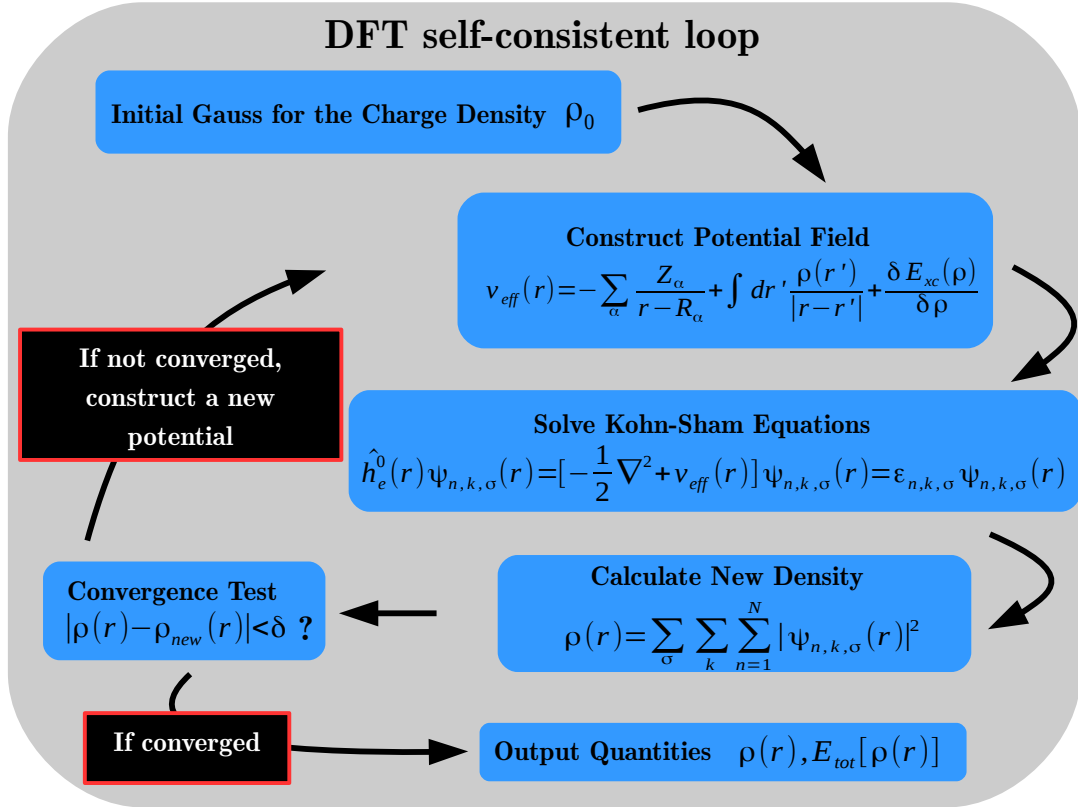

FIGURE 2.1: Self-consistency in density functional theory.

The main difficulty of DFT is finding an appropriate approximation for $E_{xc}(\rho)$. Two commonly used approximations are the local-density approximation (LDA) (Kohn and Sham, 1965) and the generalized gradient approximation (GGA) (Perdew, 1985; Perdew, Burke, and Ernzerhof, 1996). In the LDA, E_{xc} is approximated using a homogeneous interacting electron gas with the density $\rho(\mathbf{r})$ as a reference system:

$$E_{xc}^{LDA}[\rho] = \int \rho(\mathbf{r})\epsilon_{xc}(\mathbf{r})d\mathbf{r} \qquad (2.13)$$

where $\rho(\mathbf{r})$ is electronic density and ϵ_{xc} is the exchange-correlation energy per particle of a homogeneous electron gas of charge density ρ. The exchange-correlation energy is decomposed into exchange and correlation terms: $E_{xc}^{LDA} = E_x + E_c$. For the homogeneous electron gas the exchange term E_x takes a simple analytic form:

$$E_x^{LDA}[\rho] = -\frac{3}{4}\left(\frac{3}{\pi}\right)^{1/3}\int \rho(\mathbf{r})^{4/3}d\mathbf{r}. \qquad (2.14)$$

For the correlation, one of the most used version is the parametrization from Perdew and Zunger (Perdew and Zunger, 1981), who reproduced the exact quantum Monte Carlo results for homogeneous electron gas from D. M. Ceperley and B. J. Alder (Ceperley and Alder, 1980):

$$E_c^{LDA}[\rho] = \int \rho(\boldsymbol{r})\epsilon_c(\boldsymbol{r})d\boldsymbol{r} = \begin{cases} \int \rho(\boldsymbol{r})[A\ln\boldsymbol{r}_s + B + C\boldsymbol{r}_s\ln\boldsymbol{r}_s + D\boldsymbol{r}_s]d\boldsymbol{r} & (\boldsymbol{r}_s \leq 1) \\ \gamma/(1 + \beta_1\sqrt{\boldsymbol{r}_s} + \beta_2\boldsymbol{r}_s) & (\boldsymbol{r}_s > 1) \end{cases}$$
(2.15)

where $\boldsymbol{r}_s$ is the radius of the sphere that, on average, contains one electron, and $\boldsymbol{r}_s = (\frac{3}{4\pi\rho})^{\frac{1}{3}}$. A, B, C, D, β and γ are empirical constants.

The extension of density functionals to spin-polarized systems is straightforward for the exchange, where the exact spin-scaling is known, but for correlations further approximations must be employed. A spin polarized system in DFT employs two spin-densities, $\rho_\uparrow$ and $\rho_\downarrow$ with $\rho = \rho_\uparrow + \rho_\downarrow$, and the form of the local-spin-density approximation (LSDA) is:

$$E_{xc}^{LSDA}[\rho] = \int \rho(\boldsymbol{r})\epsilon_{xc}(\boldsymbol{r}, \sigma)d\boldsymbol{r}.$$
(2.16)

LDA is basis for the construction of more sophisticated approximations to the exchange-correlation energy, such as GGA or hybrid functionals (Heyd, Scuseria, and Ernzerhof, 2003), as a desirable property of any approximate E_{xc} is that it should reproduce the exact results for homogeneous electron gas with non-varying densities. As such, the LDA contribution is often an explicit component of different exchange-correlation functionals. Above all, the LDA is particularly justified in systems with slowly varying spatial electron density $\rho(\boldsymbol{r})$, such as alkali metals and alkaline earth metals. For such materials, we could approximate most parts of the crystal space as a region in which the electron density ρ is basically constant and other small regions as perturbation therefore the whole system can indeed be studied as a homogeneous electron gas. Because LDA approximates the exchange-correlation energy of the true system's electron density by replacing it with an energy of a local constant density, it fails in situations where the electron density undergoes rapid changes such as in molecules in vacuum or surface states, or, as we will discuss in **Chapter 3-4**, TMOs that contain correlated orbitals e.g. d- or f-orbitals.

LDA can be improved by considering the gradient of the electron density, leading to the so-called generalized-gradient approximation (GGA) (Perdew, 1985). The basic idea of GGA is to express the exchange-correlation energy in the following form:

$$E_{xc}^{GGA}[\rho] = \int \rho(\boldsymbol{r})\epsilon_{xc}(\boldsymbol{r})d\boldsymbol{r} + \int F_{xc}[\rho(\boldsymbol{r}), \nabla\rho(\boldsymbol{r})]d\boldsymbol{r}$$
(2.17)

where the function F_{xc} is chosen to satisfy a number of formal conditions for the exchange-correlation hole, such as the sum rules, the long-range decay and so on. For the detailed discussion of F_{xc} please see Ref. (Perdew, Burke, and Ernzerhof, 1996). A thorough comparison of different GGAs can be found in Ref. (Filippi, Umrigar, and Taut, 1994). The most widely used GGA is the PBE of Perdew, Burke and Ernzerhof (Perdew, Burke, and Ernzerhof, 1996). This is very satisfactory from the theoretical point of view, because it verifies many of the exact conditions for the *exchange-correlation* holes and it does not contain any fitting parameters.

GGAs are typically based either on theoretical developments that reproduce a number of exact results in some known limits, for example, zero and infinite electron density, or the correlation potential in He atom, or are generated by fitting a number of parameters using database of molecular structures. Using the GGA, very good results for molecular geometries, predictions of crystal lattice constants, and ground-state energies have been achieved. Normally, these improvements overcome some

drawbacks of LDAs. Even through some achievements have been made by GGA, it is still inadequate in considering the many-body correlation effects.

The great success of DFT is that, via the Kohn-Sham equation Eq. 2.10, the problem of finding the electron density of the original many-electron system is reduced to that of an auxiliary single particle problem, whose Hamiltonian Eq. 2.10 has to be determined self-consistently. All the electrons in the auxiliary problem feel a one-electron potential whose strength and shape are determined not only by the fixed nuclei but also by all the other electrons, hence self-consistency is needed. However, because of the single-electron nature the Kohn-Sham equations Eq. 2.10 to 2.12, practical DFT calculations work well for materials with an electronic structure that can be understood in terms of the energy levels of individual electrons. In these cases DFT calculations not only provide accurate results, but also contribute to our understanding, e.g., of bonding in materials in terms of molecular orbitals, and Wannier functions in solids. The approach has proven so successful that its main creator, W. Kohn, was recognized with the 1998 Nobel Prize in Chemistry. The successes of the DFT with GGA/LDA make it easy to forget the the crude approximation of E_{xc}. The simple LDA and GGA work surprisingly well for some materials, even when describing their magnetic properties by spin-polarized electron densities. In this case, expressing the functional in terms of spin-polarized electron densities greatly simplifies the task of writing down a universal functional, only treating the spin-densities as separate variables gives a simple way, e.g. the local-spin-density approximation (LSDA), of ensuring that states with large spin tend to have lower energy.

We need to identify which properties and which systems DFT is able to describe. If DFT manages to identify the relevant physics, finding a good approximation is significantly simplified. If DFT fails to identify them, finding a good approximation is virtually impossible. By the nature of the Kohn-Sham equation Eq. 2.10, DFT calculations are largely confined to materials, where the picture of single particle physics is adequate, and Fermi-liquid (FL) theory (Baym and Pethick, 2008), which models weakly interacting quasi-particles applies. There is, however, a remarkable variety of strongly correlated materials for which this standard model of electronic structure theory breaks down. The hallmark of these materials is that some of their electrons are neither perfectly localized, nor fully itinerant. In such systems, Coulomb interactions between certain electrons are so strong that the single-electron approximation of DFT breaks down. These electrons can no longer be considered as individual, but correlated.

At this point, the functionality of DFT does not fit the need of an approximation for describing correlated electrons. Interest in strongly correlated materials is increasing as the developments of their technological applications and crystal growth techniques. Prominent examples are TMOs, e.g., high-temperature superconductors (Pickett, 1989) and molecular crystals (Silins and Capek, 1994). All of these lead to the most remarkable failure of the DFT: failing at describing the Mott metal-insulator transition (MIT): within DFT calculations, TMOs, which are of partially filled (usually d or f) bands, always yield a metallic solution. However experimentally many of them exhibit an insulating behavior with a band gap. This discrepancy between theory and experiment is due to the localization of d- or f-orbitals: localized spin-up (down) electrons would forbid spin-down (up) electrons to occupy the same orbital, due to the on-site Coulomb repulsion U. These correlation effects are not well treated in the DFT framework. Anyway, both LDA and GGA exchange-correlation functionals tend to be suitable to describe *over-delocalized* electrons, i.e. s or p orbitals.

2.3 Towards Correlations (1): Hubbard Model and DFT+U

The main shortcoming of DFT is its inability to reproduce the experimental ground state of strongly correlated materials with partially filled d or f bands. Hence alternative, more advanced theoretical models have to be employed. Such methods however pose a serious computational challenge. Initially, the only available strategy was to use minimal models designed to describe a specific phenomenon.

Towards describing electronic correlations, a milestone is the Hubbard model, which was invented by J. Hubbard (Hubbard, 1963; Hubbard, 1964(a); Hubbard, 1964(b)). The single-band Hubbard model is the simplest model of interacting particles in a lattice, with only two terms in the Hamiltonian:

$$H = H_0 + H_{int} = -\sum_{ij,\sigma} t_{ij} c_{i\sigma}^\dagger c_{j\sigma} + U \sum_i n_{i\sigma} n_{i\sigma'}. \qquad (2.18)$$

Where $c_{i\sigma}^\dagger$ ($c_{i\sigma}$) are creation (annihilation) operators with spin σ at the lattice site i, the amplitudes t_{ij} describes the electron hopping energy between orbitals i and j, and U is the added Coulomb interaction between opposite-spin electrons in one orbital. In short, the H_0 term includes the information which is well accounted for by the standard DFT: a kinetic term allowing for tunneling (or defined as hopping) of particles between sites of the lattice, H_{int} introduces the correlations in localized d- or f-orbitals by means of a potential term consisting of an on-site interaction U. The Hubbard model is indeed based on the tight-binding approximation, in which electrons are viewed as hopping between orbitals and atoms. For the multi-orbitals case, this hopping process is represented by the hopping integral $t_{im,i'm'}$ (i and m label sites and orbitals) which depends on the distance and angles between the overlapping orbitals. The bandwidth in turn depends on the magnitude of the overlap.

The DFT band theory does not consider interactions between electrons explicitly. It considers the interaction of a single electron with the potential of nuclei and other electrons in an average way only. In contrast the Hubbard model includes the on-site repulsion U explicitly, which stems from the Coulomb repulsion between electrons. This sets up a competition between the hopping integral and the on-site Coulomb interaction. The Hubbard model can therefore explain the transition from metal to insulator in certain metal oxides as an increase in nearest neighbor spacing, which reduces the hopping integral to the point where the on-site potential is dominant. Thus the Hubbard model can add additional Coulomb interactions to the correlated d- and f-orbitals on the top of DFT and tight-binding methods.

The 1-dimensional Hubbard model was solved by Lieb and Wu using the Bethe ansatz (Lieb and Wu, 2003). However solving the Hubbard model in 2- and 3-dimension is still a hard task and cannot be achieved analytically. Some approximations have to be taken to solve it, e.g. the limit of infinite dimensions (Metzner and Vollhardt, 1989), the limit of unconstrained hopping (Patterson, 1972; van Dongen, P. G. J. and Vollhardt, D., 1989), and the static limit (Kennedy and Lieb, 1986), which is more often referred to as the Falicov-Kimball model (Falicov and Kimball, 1969), or directly as the modified (simplified) version of Hubbard model (Lieb, 2004; van Dongen, P. G. J. and Vollhardt, D., 1990). Among these approximations, the infinite dimensions approximation is the basis of the DMFT method and will be detailed discussed later.

The difficulties of solving the 3-dimensional Hubbard model motivated independent developments at the DFT level, such as the LDA+U method (Anisimov, Zaanen, and Andersen, 1991; Anisimov, Aryasetiawan, and Lichtenstein, 1997; Liechtenstein,

Anisimov, and Zaanen, 1995) (this "+U" correction is usually applied to a generic approximate DFT functionals, not necessarily LDA). In LDA+U correlation effects are added into DFT calculations in terms of the orbital dependence. It should be kept in mind that such correlations correspond to the Hartree-Fock mean field level treatment and true many-body effects are still absent. The general energy functional of DFT+U method reads:

$$E_{DFT+U}[\rho(\boldsymbol{r})] = E_{DFT}[\rho(\boldsymbol{r})] + E_{Hubbard}[n_{mm',i,\sigma}] - E_{dc}[n_{i,\sigma}] \qquad (2.19)$$

where the $n_{mm',i,\sigma}$ is the density matrix comprises projections of occupied Kohn-Sham orbitals $\psi_{kn\sigma}$ (k and n are the k-space vector and band indexes) on the states of a localized atomic-like m orbital and site i, $\varphi_{m,i}$:

$$n_{mm',i,\sigma} = \sum_{k,n} f_{kn\sigma} \langle \psi_{kn\sigma} | \varphi_{m,i} \rangle \langle \varphi_{m',i} | \psi_{kn\sigma} \rangle \qquad (2.20)$$

where $f_{kn\sigma}$ are the Fermi-Dirac occupations of the Kohn-Sham states. In Eq. 2.19 the $H_{Hubbard}$ is the term that describes on-site electron-electron interactions as in the Hubbard model. Because of the additive nature of this correction it is necessary to eliminate from H_{DFT} the part of the interaction energy that is already contained in $H_{Hubbard}$. This task is accomplished by the subtraction of the so-called "double-counting" (dc) term H_{dc} that measures the contribution to the DFT energy from correlated electrons in a Hartree-Fock mean-field approximation. Due to the lack of a precise diagrammatic expansion of the DFT total energy, the H_{dc} term is not uniquely defined, and different formulations and implementations are possible. It is important to stress that the Hubbard correction is usually only applied to the localized states of the system for which the correlation effects are strongest. Here we only discuss the most common implementations of this corrective approach starting from the simplest and most general one:

$$H_{DFT+U} = H_{DFT} + \frac{U}{2} \sum_{i} \sum_{m\sigma \neq m'\sigma} \hat{n}_{im\sigma} \hat{n}_{im'\sigma'} - \frac{U}{2} \sum_{i} \hat{n}_i(\hat{n}_i - 1) \qquad (2.21)$$

where $\hat{n}_{im\sigma} = \sum_{mm'\sigma} \hat{n}_{imm'\sigma} \delta_{mm'}$, and $\hat{n}_i = \sum_{m,\sigma} \hat{n}_{im\sigma}$. The competition between electron hopping t and orbital potential U underlies the classifications of half-filling correlated systems: (1) $t \gg U$, the total energy is minimized by making the kinetic term as small as possible through delocalization of the wave functions (Bloch states). At this point electrons trend to be delocalized and form more extended state, leading to double-occupancy. Thus it is possible to define a Fermi energy which divide occupied and unoccupied states. (2) $t \ll U$, the total energy is minimized by making the Coulomb term as small as possible by avoiding double occupancy of each site. Localized state are preferable as in any case a local occupation $n_{im\sigma}$ needs to be calculated. This might be the Wannier functions, which are made by a linear combination of all k-states [for review about Wannier functions see Ref. (Marzari et al., 2012)]. At this point the system becomes insulator (even for partially filled d- or f-orbitals, when DFT predicts metallic solutions) when electrons fail at hopping around due to that the kinetic energy is too small to overcome the repulsion from other electrons on neighbor sites. The region dominated by weak correlations ($t \gg U$) is well described by DFT, the strongly correlated region ($t \ll U$) is more difficult. After the establish of DFT+U method huge success has been achieved in predicting/explaining the insulating ground states, e.g. the charge-transfer type insulating states in late-transition

metal monoxides (Anisimov, Zaanen, and Andersen, 1991) and the antiferromagnetic insulating states in parents compounds of high-T_C superconductors (Pickett, 1989) (e.g. copper-based compounds).

Comparing with standard DFT, DFT+U improves the quality of theoretical prediction regrading physical properties of TMOs such as the band gap and magnetic moments. For TMOs such as NiO, its DFT resulted band gap and magnetic moment is seriously underestimated. NiO is an antiferromagnetic insulator with a sizable gap of 4.0-4.3 eV (Hüfner et al., 1984; Sawatzky and Allen, 1984) and the experimental magnetic moment is 1.64 to 1.90 μ_B/Ni (Alperin, 1962; Cheetham and Hope, 1983). DFT yields 0.2 eV and 1.0 μ_B/Ni (Anisimov, Zaanen, and Andersen, 1991), respectively, these values are remarkable smaller than the experimental observations and this divergence indicates the importance of including correlations effect. By adding a orbital potential U, the calculated band gap and magnetic moments become 3.1 eV and 1.59 μ_B/Ni, being quite close to the experimental measurements.

The second achievement of the DFT+U method is that it can accurately predict structural parameters for some TMOs, leading to an accurate prediction of electronic structures of ground states. This is due to the fact that for some materials' band gaps appear only when possible degeneracies of orbitals around the Fermi level are lifted. To achieve this it is sometimes necessary to impose realistic crystal symmetry breaking. One textbook example is LaMnO$_3$, an A-type antiferromagnetic insulator of the ABO$_3$ family of strongly correlated TMO with perovskites structure, generally exhibits complex phase diagrams, as a result of the coupling between charge, orbital and spin degrees of freedom (Mitchell et al., 1996; Maezono, Ishihara, and Nagaosa, 1998; Franchini et al., 2012). The ground state electronic structure of LaMnO$_3$ is characterized by the structure-driven breaking of the degeneracy of Mn^{3+} $3d^4$ manifold in the high-spin configuration $t_{2g}^3 \uparrow\uparrow\uparrow e_g^1 \uparrow$, with the t_{2g} orbitals lying lower in energy than the twofold-degenerate e_g ones. Due to the strong Hund's rule coupling, the spins of the fully occupied majority t_{2g} orbitals are aligned parallel with the spin of the singly occupied majority e_g states on the same site. The orbital degeneracy in the e_g orbitals is further lifted via cooperative Jahn-Teller distortions (Qiu et al., 2005; Sánchez et al., 2003). Standard DFT calculations (Sawada et al., 1997; Trimarchi and Binggeli, 2005) showed that when the internal atomic coordinations are fully relaxed, both LDA and GGA incorrectly predict the *Pnma* phase to be metallic, and significantly underestimate the Jahn-Teller distortion. Theoretically calculations (Sawada et al., 1997) based on DFT+U have addressed the electronic structure of bulk LaMnO$_3$ using the experimental equilibrium structural parameters. Such calculations were able to reproduce the insulating band structure of LaMnO$_3$ at ambient (experimental) conditions. In short, DFT+U was found to correct structural details and orbital-splitting and provides a good general description of the complex structural changes observed in the LaMnO$_3$ *Pnma* phase under pressure. Manganites have also been studies intensively by DFT+DMFT, which we introduce in the next sections. For the research about manganites (LaMnO$_3$) with both static and dynamical correlations, see Ref. (Yamasaki et al., 2006; Yang and Held, 2007; Held et al., 2008).

The third advancement of DFT+U method is that it remedies the DFT (especially within LDA) failure in predicting the ground state of magnetic correlated insulators (Pickett, 1989), such as the parent compounds of high-T superconductors La$_2$CuO$_4$ and YBa$_2$Cu$_3$O$_6$. Both materials were concluded as metallic by DFT-LDA calculations, however experiments predicted that they are antiferromagnetic insulators. In contrast to LDA, the LDA+U method successfully reproduces the antiferromagnetic insulating ground states of both materials (Wei and Qing Qi, 1994). The energy gap

for these compounds is of a charge-transfer character, and the values of the energy gap and Cu magnetic moment is in good agreement with experiments (Tranquada, 1988; Thio et al., 1990; Tranquada et al., 1988; Heyen, Kircher, and Cardona, 1992). This situation is quite similar to that of Mott insulating $3d$ monoxides MnO, FeO, CoO, and NiO, for which there is an experimental evidence that they are wide-gap insulators (Eastman and Freeouf, 1975; Roth, 1958) but L(S)DA yields a metal (FeO, CoO) or semiconductor (MnO, NiO) (Andersen et al., 1980; Anisimov, Korotin, and Kurmaev, 1990). However LDA+U gives accurate results about band gap and magnetic moments (Anisimov, Zaanen, and Andersen, 1991).

However, the static nature of DFT+U impedes the simulation of dynamical correlations that give rise to e.g. three peak structure in the photoemission, and the weight transfer between quasi-particle peaks and Hubbard bands. One has to note that a fully spin-splitting induced by U may results in a similar three peak structure in spectra at Hartree-level, however this fails at explaining the non-ferromagnetic Mott-Hubbard insulators, e.g. V_2O_3 (Held et al., 2001). This shortcoming of DFT+U called for the more advanced computational method regrading dynamical correlations.

2.4 Towards Correlations (2): DFT+DMFT

2.4.1 Anderson Impurity Model and $d = \infty$ Limit

In recent years, a significant progress has been achieved on the field of dynamical mean-field theory (DMFT) (Georges et al., 1996; Kotliar and Vollhardt, 2004; Metzner and Vollhardt, 1989; Georges and Kotliar, 1992; Held et al., 2008; Held, 2007), in which the Hubbard model (Eq. 2.18) is dynamically solved. The key observation was that in the limit of infinite dimensions the self energy $\Sigma(k, \omega)$ becomes local: $\Sigma(\omega)$. Even for finite dimensions, the restricting to a local $\Sigma(\omega)$ is a good approximation. In this way, an infinite lattice is mapped approximately onto an impurity problem, which has to be solved self-consistently. From the computational point of view, the techniques developed for impurity models can hence be used for the Hubbard model. From the materials' point of view, the success of DFT+U hinted at the possibility of soling many-body models with parameters calculated *ab-initio*. These two lines of research culminated in the development of the DFT+DMFT, the present day state-of-the-art approach for strongly correlated electron systems. In DFT+DMFT, a more general multi-band Hubbard model is constructed from DFT:

$$H = H_0 + H_{int} = \sum_{ii',mm',\sigma} t_{im,i'm'} c^\dagger_{im\sigma} c_{i'm'\sigma} + \sum_{i,mm'll',\sigma\sigma'} U_{mm'll'} c^\dagger_{im\sigma} c^\dagger_{im'\sigma'} c_{il\sigma'} c_{il'\sigma} \tag{2.22}$$

where $c^\dagger_{im\sigma}$ ($c_{im\sigma}$) are creation (annihilation) operators with spin σ at the lattice site i and the orbital m, the $t_{im,i'm'}$ describe the electron hopping energy between lattice sites i and i' and the orbitals m and m'. The U term is Coulomb interaction between opposite-spin electrons. One of the most used Hamiltonian is the Kanamori interaction, in which intra-orbital interaction U, inter-orbital interaction U' and Hund's exchange J ($U' = U - 2J$) are included:

$$H_{int} = U \sum_m n_{m\sigma} n_{m\sigma'} + \sum_{m>m',\sigma\sigma'} [U' n_{m,\sigma} n_{m',\sigma'} + (U' - J) n_{m,\sigma} n_{m',\sigma'}]$$
$$- \sum_{m\neq m',\sigma\sigma'} J(d^\dagger_{m,\sigma} d^\dagger_{m',\sigma'} d_{m',\sigma} d_{m,\sigma'} + d^\dagger_{m,\sigma} d^\dagger_{m,\sigma'} d_{m',\sigma} d_{m',\sigma'}). \tag{2.23}$$

Here, the third term in the right side represents a spin-flip and paring hopping between orbital m and m'. If the third term at right side was ignored, the above formula reduces to a simpler version, a density-density interaction Hamiltonian. The difference between Kanamori and density-density interactions can be examplified by varying the J parameter from a finite value to 0, when the third term of Eq. 2.23 disappears. The third term of Eq. 2.23 also plays a big role in some materials that are referred to as Hund's metal (Georges, Medici, and Mravlje, 2012). In Eq. 2.22-2.23, the metal-insulator transition at half-filling is a consequence of the large U/t ratio, i.e., an on-site Coulomb repulsion which is large compared to the band-width W, determined by the hopping integral t. The DMFT solution of the Hubbard model shows that with increasing U/t the quasi-particle mass increases and eventually diverges; the Mott transition is associated with the corresponding divergence of the real part of the self energy $Re\Sigma(\omega)$. Following this idea, for some materials, the enhancement of local Coulomb interaction U could induce a metal-insulator transition, if the bandwidth W (i.e. hopping t) is kept unchanged. Although the mechanism behind the paramagnetic insulating phase had been proposed about 60 years ago by

N. Mott (Mott and Friedman, 1974), DMFT is the first computational technique that can indeed describe this physics quantitatively [e.g. see the Mott-insulating states in Cr-doped V_2O_3 by DMFT (Held et al., 2001)]. DMFT yields an approximate solution of the Hubbard model in which spatial correlations are neglected and only dynamical effects are taken into account. Basically for all current techniques the local Anderson impurity problem (Anderson, 1961) in DMFT is solved using Green's functions, and the solutions are frequency dependence (dynamical nature). It is remarkable that a model as simple as the DFT-derived multi-orbital Hubbard model can account for complex real systems such as V_2O_3 (Held et al., 2001) and $SrVO_3$ (Nekrasov et al., 2006) and so on.

Generally, DFT+DMFT could be considered as a natural extension of the DFT+U method by obtaining the ω-dependent self-energy $\Sigma(\omega)$. With this way dynamic correlation effects are included.
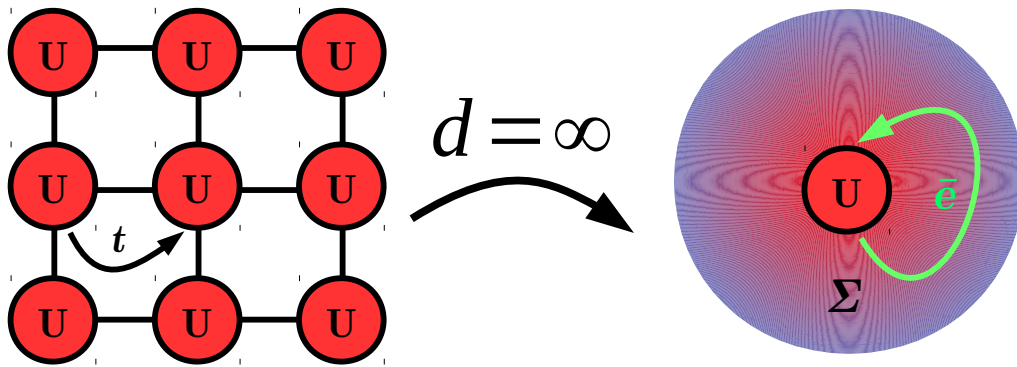
FIGURE 2.2: In the limit of $d = \infty$, the self-energy $\Sigma(k, \omega)$ is reduced to a local one without k-dependence: $\Sigma(\omega)$.

Historically there have been two important steps for arriving at the DMFT method. The first one was proposed by W. Metzner and D. Vollhardt in 1989 (Metzner and Vollhardt, 1989). They considered the limit of an infinite lattice coordination: each lattice site has infinitely many neighbors. This approach retained the competition between kinetic energy t and Coulomb interaction U between electrons. With increasing the number of neighbors, the hopping amplitude is scales as $\frac{t_{ij}}{\sqrt{d}}$ therefore the self-energy becomes totally local: $\Sigma(\mathbf{k}, \omega) \to \Sigma(\omega)$. When frequencies ω are far away from the Fermi level, Σ follows the Hartree-Fock behavior. Also the non-local Coulomb interaction is reduced to the non-ω-dependence Hartree-Fock level in DMFT. The physical picture of infinite dimensions limit is briefly shown in Fig. 2.2.

The second step was done by A. Georges and G. Kotliar, they mapped the Hubbard model (a lattice model) onto a single impurity Anderson model (SIAM) in the limit of $d=\infty$, leading to a set of local quantum mechanical degrees of freedom that interacts with a *bath* or continuum of non-interacting sites (Georges and Kotliar, 1992). That construction provides the basis of the DMFT for correlated electrons. It allowed many-body theorists to formulate and solve a variety of model Hamiltonians on the lattice using numerical techniques such as continues-time quantum Monte Carlo (Gull et al., 2011) (CT-QMC) and exact diagonalization (Caffarel and Krauth, 1994) methods (see **Chapter 2.4.3**). The physical picture of this conclusion is shown in Fig. 2.3.

The problem we are facing now is how to solve this effective Anderson impurity model (AIM), the Hamiltonian reads as below:
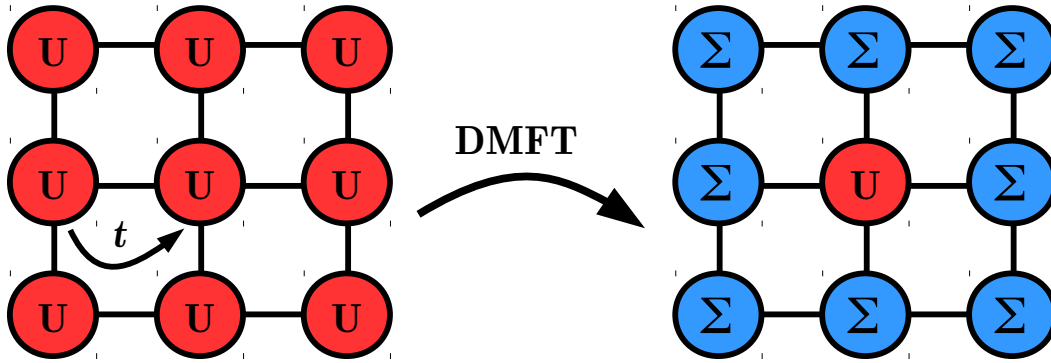
FIGURE 2.3: DMFT maps the lattice many-body problem with interactions U on every site (left side) onto a single site problem where the interaction has been replaced by the self energy Σ except for a single site (right side). The DMFT mapping becomes exact for $d = \infty$ and is an approximation in finite dimensions. The self-energy (in figure labeled as Σ) is defined as the difference between the inverse non-interacting bath Green function $\mathcal{G}$, and the inverse local Green function G at the U site.

$$
\begin{aligned}
H_{AIM} = \sum_{m,\mathbf{k},\sigma} \epsilon_{m,\mathbf{k}} \hat{n}_{m,\mathbf{k},\sigma} + \sum_{m,\mathbf{k},\sigma} [V_{mm'}(\mathbf{k}) \hat{a}_{m,\mathbf{k}\sigma}^\dagger \hat{c}_{m',\sigma} + h.c.] \\
+ \sum_{i,mm'll',\sigma\sigma'} U_{mm'll'} \hat{c}_{i,m\sigma}^\dagger \hat{c}_{i,m'\sigma'}^\dagger \hat{c}_{i,l\sigma'} \hat{c}_{i,l'\sigma}
\end{aligned}
\tag{2.24}
$$

where the number operators are $n_{m,\mathbf{k},\sigma} = \hat{a}_{m,\mathbf{k},\sigma}^\dagger \hat{a}_{m,\mathbf{k},\sigma}$, the index i labels all the interacting sites and m, m', l and l' label all orbitals, $\mathbf{k}$ is the k-space vector, $h.c.$ is the Hermitian conjugate; $V_{mm'}(\mathbf{k})$ is the hybridization function between itinerant and localized electrons.

The advanced version of SIAM is the periodic Anderson model (PAM) (Hewson, 1997). The PAM is a two-band model with the two orbitals per lattice site coupled by a local one-electron hybridization. One band is localized but correlated with interaction U, the other one is uncorrelated but itinerant. With this setting the PAM is able to examine what happens when two species of electrons, one delocalized "conduction" band (often d), and another localized band (often f) are present. For the developments and applications of PAM see Ref. (Rice and Ueda, 1985; Jarrell, 1995; Jarrell, Akhlaghpour, and Pruschke, 1993; Tahvildar-Zadeh, A. N. and Jarrell, M. and Freericks, J. K., 1997; Tahvildar-Zadeh, A. N. and Jarrell, M. and Freericks, J. K., 1998; Ueda, Tsunetsugu, and Sigrist, 1992; Blankenbecler et al., 1987; Robaszkiewicz, Micnas, and Ranninger, 1987).

2.4.2 DMFT Equations

DMFT calculations are carried out in the language of Green's functions hence it is possible to measure the equilibrium properties of a correlated electron system (Fetter and Walecka, 2003). Expectation value of operators A and B taken at different (real or imaginary) times in a thermal state can define the Green's function G_{AB}. The thermal state can be stated by a density matrix $\propto \exp[-\beta(H - \mu B)]$ corresponding to temperature $T = 1/\beta$. Hence it measures the probability amplitude for a particle

propagator or hole excitation in an many-electrons system if we make $A = c_\alpha$ (annihilation operator), and $B = c_\beta^\dagger$ (creation operator), leading to a imaginary-time (τ) fermionic single particle Green's function $G_{\alpha\beta}(\tau)$ reads as:

$$G_{\alpha\beta}(\tau) = -\langle T c_\alpha(\tau) c_\beta^\dagger(0) \rangle = - \begin{cases} -\langle c_\alpha(\tau) c_\beta^\dagger(0) \rangle & \tau > 0 \\ +\langle c_\beta^\dagger(0) c_\alpha(\tau) \rangle & \tau \leq 0 \end{cases}$$
$$= -G_{\alpha\beta}(\tau + \beta) \; for \; -\beta < \tau < 0, \tag{2.25}$$

with imaginary-time Heisenberg operators $A(\tau) = e^{H\tau} A e^{-H\tau}$. A Fourier transformation yields the Matsubara Green's function $G_{\alpha\beta}(i\omega_n)$:

$$G_{\alpha\beta}(i\omega_n) = \int_0^\beta d\tau G_{\alpha\beta}(\tau) e^{i\omega_n \tau}$$
$$G_{\alpha\beta}(\tau) = T \sum_{n=-\infty}^{+\infty} G_{\alpha\beta}(i\omega_n) e^{-i\omega_n \tau}, \tag{2.26}$$

with fermionic Matsubara frequencies $i\omega_n = 2\pi T(n + \frac{1}{2})$. These Fourier transformations are essential for numerical solutions of DMFT. In our discussion, the bath Green's function (Weiss field) (for multi-orbitals case it corresponds to a matrix) is defined as $\mathcal{G}_{im\sigma,i'm'\sigma'}(\omega)$, i labels the interacting sites and m labels orbital; the impurity Green's function are defined as $G_{im\sigma,i'm'\sigma'}(\omega)$. With these definition, the local impurity Green's function matrix $G_{im\sigma,i'm'\sigma'}$ is a k-summation of the lattice Green's function matrix $G_{k,im\sigma,i'm'\sigma'}$:

$$G_{im\sigma,i'm'\sigma'} = \frac{1}{N_k} \sum_k G_{k,im\sigma,i'm'\sigma'}(\omega) = \frac{1}{N_k} \sum_k [\omega + \mu I - H_{mm'}^{DFT}(k) - \Sigma_{im\sigma,im'\sigma'}(\omega)]^{-1} \tag{2.27}$$

where μI is the chemical potential times unit matrix, then the non-interacting bath Green's function can be obtained by Dyson equation:

$$\mathcal{G}_{im\sigma,i'm'\sigma'}^{-1}(\omega) = G_{im\sigma,i'm'\sigma'}^{-1}(\omega) + \Sigma_{im\sigma,i'm'\sigma'}(\omega). \tag{2.28}$$

Since $H_{mm'}^{DFT}(k)$ can be non-diagonal, the matrix element $G_{im\sigma,i'm'\sigma'}$ also can be non-zero. However the impurity Green's function $G_{im\sigma,i'm'\sigma}(\omega)$ can be often approximated as a local Green's function: $G_{\delta_{ii'},mm',\sigma}(\omega) = G_{im\sigma}(\omega)$, at this point the bath Green's function (*Weiss field*) and self-energy also can be approximated as local ones: $\mathcal{G}_{im\sigma}(\omega)$ and $\Sigma_{im\sigma}(\omega)$.

The next step is obtaining the new-iteration local Green's function matrix $G_{i,m,\sigma}$, with the help of the AIM. The thermal average of propagator (interacting Green's functions) can be defined as a functional integral over Grassmann variables ψ, $\psi^\dagger$ (with differentials denoted as D), this provides us with a way to obtain interacting local Green's function from non-interacting bath functions (Weiss field). The local Green's function $G_{mm',\sigma}(i\omega_n)$ (m, m', l and l' are orbital indexes, n decides Matsubara frequency $i\omega_n = \pi(2n + 1)/\beta$) is obtained by a functional integral as:

$$G_{mm',\sigma}(i\omega_n) = -\frac{1}{Z} \int D\psi D\psi^\dagger (\psi_{m,l,\sigma} \psi_{m',l',\sigma}^\dagger e^{A[\psi,\psi^\dagger,\mathcal{G}]}) \tag{2.29}$$

with the partition function:

$$Z = \int D\psi D\psi^\dagger e^{A[\psi,\psi^\dagger,\mathcal{G}]} \tag{2.30}$$

and on-site action:

$$
\begin{aligned}
A[\psi,\psi^\dagger,(\mathcal{G})^{-1}] = & \sum_{n,ml,\sigma} \psi^\dagger_{n,m}[\mathcal{G}^0_{ml,\sigma}(i\omega_n)]^{-1}\psi_{n,l,\sigma} \\
& - \sum_{mm'll',\sigma\sigma'} U_{mm'll'} \int_0^\beta d\tau \psi^\dagger_{m,\sigma}(\tau)\psi_{m',\sigma'}(\tau)\psi^\dagger_{l,\sigma'}(\tau)\psi_{l',\sigma}(\tau)
\end{aligned}
\tag{2.31}
$$

where the new variables, Matsubara frequency $i\omega_n$ and imaginary time τ are needed. The Matsubara frequency is defined as $i\omega_n = \pi(2n+1)/\beta$, where the β is inverse temperature $\beta = 1/k_B T$ (k_B is Boltzmann constant). In the process of solving DMFT equations two Fourier transformations have to be carried out by Eq. 2.26.

2.4.3 Methods of Solutions

As we discussed above, the Hubbard model (Eq. 2.22) is solvable by mapping lattice model onto a a multi-orbital AIM with the same Coulomb interaction U at the impurity site, as shown in Fig. 2.3. With the help of Eq. 2.27 to 2.31 a complete self-consistent DMFT loop can be constructed. That is, a convergent self-energy $\Sigma(i\omega_n)$ and Green's function $G(\tau)$ can be obtained by self-iterations, see Fig. 2.4. In fact, all current DMFT solution methods deal with this self-consistent loop, but with various techniques to solve the AIM model (Eq. 2.24). This is also the most difficulty step of the DMFT self-consistency: the solution of impurity model (Eq. 2.29-2.31) in each iteration step for a new dynamical Weiss field $\mathcal{G}(i\omega_n)$. Technically, various methods of solutions are classified as analytical and numerical ones. Analytical solvers are the iterated perturbation scheme (IPT) (Georges and Kotliar, 1992) and the non-crossing approximation method (Jarrell and Pruschke, 1994; Pruschke, Cox, and Jarrell, 1993). Numerical techniques include numerical renormalization group (NRG) (Wilson, 1975), exact diagonalisation (ED) (Caffarel and Krauth, 1994; Moeller et al., 1995), quantum Monte Carlo (QMC), functional renormalization group (FRG) (Taranto et al., 2014), fluctuation-exchange (FLEX) (Bickers, Scalapino, and White, 1989; Gukelberger, Huang, and Werner, 2015) and density matrix renormalization group (DMRG) (Schollwöck, 2005) methods. Here we briefly introduce the ED and QMC methods which has been employed in this thesis.

In ED, the interacting impurity site in AIM model is mapped onto an effective bath that is approximated by a few orbitals only. One degree of freedom in the *parameterization* is how to *parameterize* the effective bath. The parameters include the information about the site energies and hopping amplitudes of fictitious electrons and an appropriate choice of the geometry of their connections. For a particle calculations many different geometries of electronic baths are possible. However, more orbitals are parameterize, the Hilbert basis grows exponentially, leading to a severe limitation of the size of bath. The ED method proved to be a very successful solver of the AIM, for the applications of ED see Ref. (Ishida and Liebsch, 2010).

The QMC methods include two algorithms: Hirsch-Fye Monte Carlo method (HF-QMC) (Hirsch and Fye, 1986) and continuous-time Monte Carlo method (CT-QMC) (Gull et al., 2011; Rubtsov, Savkin, and Lichtenstein, 2005). The HF-QMC algorithm considers the single-impurity problem in *discretized imaginary time*. The effective bath only enters through bath Green's function $\mathcal{G}$, and there is no need

to discretize the conduction band. The first numerical solutions of the local impurity equations using HF-QMC method were obtained independently by M. Jarrell (Jarrell, 1992), M. J. Rozenberg *et al.* (Rozenberg, Zhang, and Kotliar, 1992), and A. Georges *et al.* (Georges and Krauth, 1992).

The CT-QMC algorithm includes two recently developed complementary methods: (1) the weak-coupling approach, which scales favorably with system size and allows the efficient simulation of large impurity clusters. The weak-coupling approach is based on an expansion of partition function Z in powers of the interaction U, and on the interaction representation in which the time evolution is determined by the *quadratic* part $H_0+H_{bath}+H_{mix}$ of the Hamiltonian; (2) the strong-coupling approach, which can handle impurity models with strong interactions. This is based on expansion of Z in powers of the impurity-bath hybridization V, and an interaction representation in which the time evolution is determined by the local part $H_0+H_U+H_{bath}$ of the Hamiltonian.

2.4.4 DMFT Self-Consistent Loop.

In this thesis, we carried out DFT+DMFT calculations by using strong-coupling CT-QMC code **W2Dynamic** (Parragh et al., 2012). With the DMFT equations Eq. 2.27-2.31, the DFT+DMFT self-consistent procedure works as follows (see Fig. 2.4):

(1) Calculate the lattice Green's function matrix $G_{\mathbf{k},im\sigma,i'm'\sigma'}$ for a initial self-energy $\Sigma^0(i\omega_n)$ by the lattice Dyson equation Eq. 2.27.

(2) Carry out a k-summation to obtain local Green's functions $G_{im\sigma,i'm'\sigma'}(i\omega_n)$ (Eq. 2.27).

(3) Calculate the bath Green's function (Weiss field) matrix $\mathcal{G}_{im\sigma,i'm'\sigma'}(i\omega_n)$ by AIM Dyson equation Eq. 2.28.

(4) Fourier transform $\mathcal{G}_{im\sigma,i'm'\sigma'}(i\omega_n)$ to $\mathcal{G}_{im\sigma,i'm'\sigma'}(\tau)$, by Eq. 2.26.

(5) Obtain the impurity Green's function matrix $G_{im\sigma,i'm'\sigma'}(\tau)$ by solving the quantum-impurity AIM problem given by $\mathcal{G}_{im\sigma,i'm'\sigma'}(\tau)$, the intra-orbital Coulomb interaction U, the Hund's exchange J and the inter-orbital Coulomb interaction $U'=U-2J$, by Eq. 2.29-2.31.

(6) Fourier transform $G_{im\sigma,i'm'\sigma'}(\tau)$ to $G_{im\sigma,i'm'\sigma'}(i\omega_n)$, by Eq. 2.26.

(7) Calculate the new self-energy matrix $\Sigma(i\omega_n)=\mathcal{G}^{-1}(i\omega_n)-G^{-1}(i\omega_n)$, by Eq. 2.28.

(8) Check if the self-consistency is reached. If not, recalculate $G_{im\sigma,i'm'\sigma'}(i\omega_n)$ and start over again with skip (1).

2.4.5 Self-Energy $\Sigma(\omega)$ Modified DFT Results

The CT-QMC method provides local Green's functions $G_{i,m,\sigma}(\tau)$ (i, m and σ are site, orbital and spin index) at imaginary time $\tau = it$ (i in τ is imaginary unit), and self-energies at Matsubara frequency $\Sigma_{i,m,\sigma}(i\omega_n)$. However experiments, e.g. spectral functions $A_{i,m,\sigma}(\omega)$ or the optical conductivity $\sigma(\omega)$, are always given at real frequency ω. Thus a necessary post-processing has to be done to extract real frequency/time results.

The first quantity we can obtain from the imaginary-time Green's function $G(\tau)$ is the real-frequency spectral functions $A_{i,m,\sigma}(\omega)$. The relation between $G(\tau)$ and $A_{i,m,\sigma} = -\frac{1}{\pi}(G_{i,m,\sigma}(\omega))$ is given by Eq. 2.32, and this equation is invented to get $A(\omega)$ from $G(\tau)$ by the maximum entropy method (Gubernatis et al., 1991):

$$G_{i,m,\sigma}(\tau) = \int d\omega \frac{e^{-\tau\omega}}{1+e^{-\beta\omega}} A_{i,m,\sigma}(\omega). \tag{2.32}$$
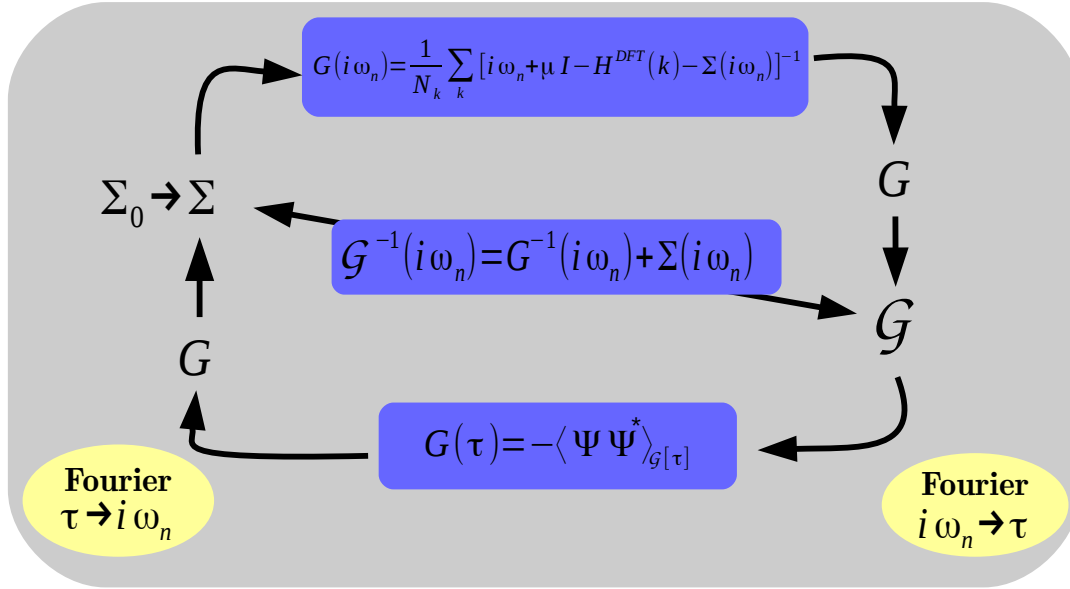
FIGURE 2.4: DMFT self-consistent loop.

From this the real-frequency Green's functions are obtained by:

$$G_{i,m,\sigma}(\omega) = \int_{-\infty}^{\infty} d\omega' \frac{A_{i,m,\sigma}(\omega)}{\omega - \omega'}. \tag{2.33}$$

This local Green's function is obtained on the other hand from integrating the lattice Dyson equation:

$$G_{i,m,\sigma}(\omega) = \frac{1}{N_\mathbf{k}} \sum_\mathbf{k} G_\mathbf{k}(\omega) = \frac{1}{N_\mathbf{k}} \sum_\mathbf{k} [\omega + \mu - H_\mathbf{k} - \Sigma_{i,m,\sigma}(\omega)]^{-1}. \tag{2.34}$$

This way the real-frequency self-energy $\Sigma_{i,m,\sigma}(\omega)$ is obtained from the local Green's function $G(\omega)$ and the DFT Hamiltonian $H_\mathbf{k}$. Finally, the spectral functions $A_{i,m,\sigma}(\omega)$ and k-dependence spectral functions $A_{i,m,\sigma}(\mathbf{k},\omega)$ are obtained from local Green's functions and lattice Green's functions, respectively:

$$A_{i,m,\sigma}(\omega) = -\frac{1}{\pi} Im \frac{1}{N_\mathbf{k}} \sum_\mathbf{k} \frac{1}{\omega - \mu - H_\mathbf{k} - \Sigma_{i,m,\sigma}(\omega)}, \tag{2.35}$$

$$A_{i,m,\sigma}(\mathbf{k},\omega) = -\frac{1}{\pi} Im \frac{1}{\omega - \mu - H_\mathbf{k} - \Sigma_{i,m,\sigma}(\omega)}. \tag{2.36}$$

2.4.6 Beyond Local Correlations: Extension of DMFT

The huge success of DMFT regrading the understanding of dynamical correlations and the Mott-Hubbard metal-to-insulator transitions in simple model systems shows that the main correlation effects in fermionic systems have a local character. However many interesting physical phenomenons indicate the importance of non-local correlations, e.g. d-wave superconductors and antiferromagnetic spin-fluctuation. Going beyond local correlations in DMFT is a challenging topic. There are not only difficulties regrading the development of algorithms, but also the computational effort is large. Here we briefly introduce two ways to go beyond DMFT approximation

and include non-local correlations: cluster DMFT and DΓA approximation, without deducing detailed formulas.
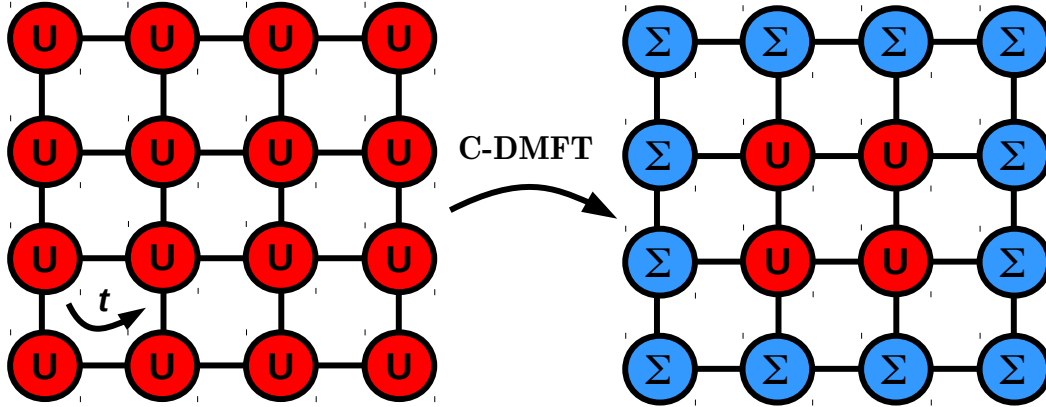

FIGURE 2.5: In cluster DMFT the lattice many-body problem (left side) is mapped onto a DMFT cluster (right hand side) which consists of several (e.g. four) interacting sites. Non-local correlations between the cluster sites are taken into account by including non-zero off-diagonal matrix elements in the self-energy $\Sigma_{i,j}(\omega)$ $(i{\neq}j)$.

Cluster DMFT includes two devisions of algorithms: the first one is extended in real space, named cellular DMFT (C-DMFT); the second one is formulated in reciprocal space and called dynamical cluster approximation (DCA). The idea beyond C-DMFT extensions is to treat a whole cluster that contains several interacting sites, instead of a single site in DMFT, as shown in Fig. 2.5. The multi-sites systems are usually taken out from real space crystal systems, e.g. all the sites contain d- or f-orbitals. Non-local correlations between these interacting sites are considered while the interactions between each multi-sites systems are neglected. Compare with single site DMFT, it brings larger DMFT basis, additionally, off-diagonal matrix elements $\Sigma_{i,j}(\omega)$ $(i{\neq}j)$ are there in the self-energy matrix. With increasing number of sites, the computational task grows considerably. For calculations of real materials, the degrees of freedom from multi-orbitals environment also contribute to the computational efforts. For the applications of C-DMFT see Ref. (Lichtenstein and Katsnelson, 2000; Maier et al., 2000; Poteryaev, Lichtenstein, and Kotliar, 2004; Biermann et al., 2005).

The reciprocal space cluster approximation of DMFT: dynamical cluster approximation (DCA), was proposed by M. H. Hettler *et al.* (Hettler et al., 1998). The idea beyond DCA is to relate k-independent self-energy $\Sigma(\omega)$ by a finite number of basis functions $\psi(\mathbf{k})$: $\Sigma(\mathbf{k}, \omega) \approx \sum_{i=1}^{N} \psi_i(\mathbf{k})\Sigma_i(\omega)$. The first Brillouin zone is divided into N_C patches. In each patch, DCA self-energy is similar to DMFT self-energy: they are both k-independent. However from patch to patch, the DCA self-energy is k-dependent and varying: $\Sigma(\mathbf{K}_n, \omega)$, as shown in Fig. 2.6. Because of this k-dependence, the DCA method obeys periodic boundary conditions while C-DMFT has open boundary conditions (similar to DMFT). If the cluster's size is increased infinitely (i.e. $N_C \rightarrow \infty$), both approximations become exact. Compared with C-DMFT, the DCA method is more suitable for describing long-range correlations than
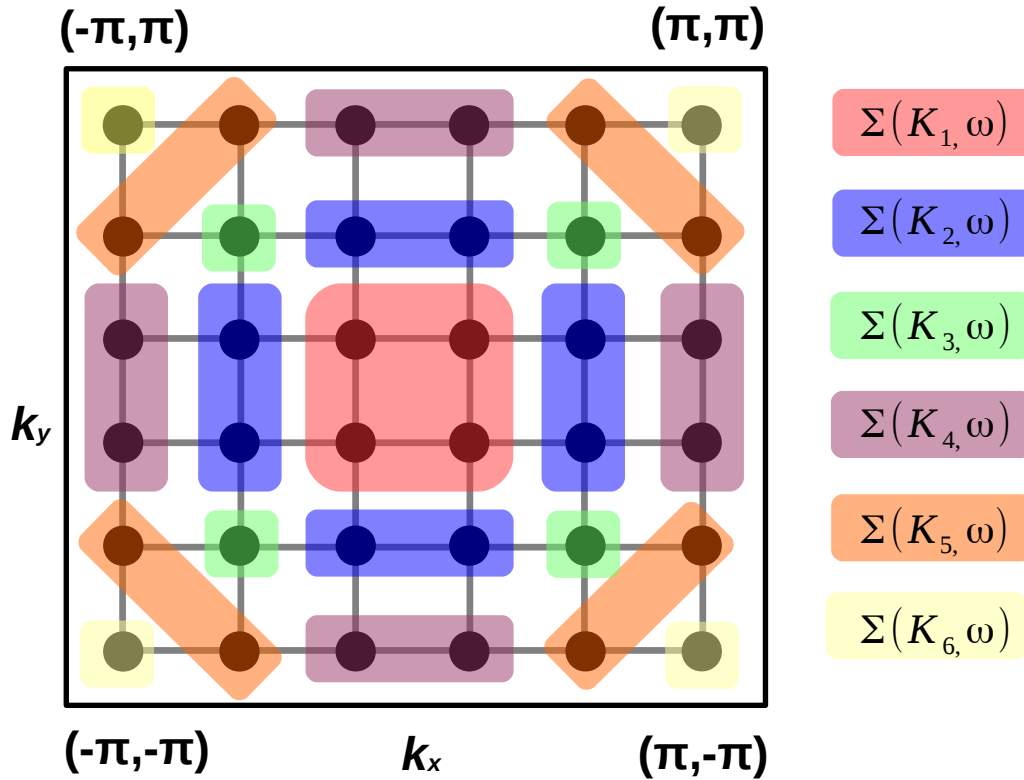
FIGURE 2.6: In Dynamical Cluster Approximation (DCA), the first BZ is divided into several patches, in each patches $\Sigma(k,\omega)$ is k-independent, whereas from patch to patch $\Sigma(k,\omega)$ varies. Here is a example of 6×6 interacting sites, first BZ is split into 6 regions, the k-dependence of $\Sigma(k,\omega)$ is appropriated as $\Sigma(K_1,\omega)$ to $\Sigma(K_6,\omega)$.

C-DMFT, and DCA is more suitable for preserving translational symmetry. For the applications of the DCA method see Ref. (Maier, Pruschke, and Jarrell, 2002).

In the above extensions of DMFT, both in C-DMFT and DCA, correlations are only taken into account in the region of the clusters, the long-range correlations are hence neglected. However the research of e.g. magnons demonstrated the importance of long-range correlations. To include/describe such long-range correlations, more advanced extensions of DMFT are necessary. The dynamical vertex approximation (DΓA), proposed by K. Held *et al.* (Toschi, Katanin, and Held, 2007; Held, 2014), is able to include both short- and long-range non-local correlations. The basic idea is to extend DMFT diagrammatically: one takes the local, fully irreducible two-particle vertex as a starting point and constructs from this vertex all possible (local and non-local) self energy diagrams. For non-local correlations in $SrVO_3$ obtained by DΓA see Ref. (Galler et al., 2016).

2.5 Merging DFT and DMFT: Wannier Functions and Tight-Binding Method

A prerequisite for a DMFT calculation is the $H_{\mathbf{k}}$ Hamiltonian. Taking the full H_k^{DFT} is impractical: strong correlation effects are usually present only for d- and f-states spanning a narrow energy window around the Fermi-level E_f. To carry out DFT+DMFT calculations usually for correlated systems the energy region for $H^{DFT}(\mathbf{k})$ is chosen as the d states around E_f because DMDT treats the local interactions we also need to define locality.

In the framework of DFT, the electronic state of a solid is determined by a set of one-particle orbitals $\psi_n(r)$ and their occupations. The periodicity of crystals leads to the k-dependence wave functions $\psi_{n,\mathbf{k}}(\mathbf{r}) = e^{i\mathbf{k}\cdot\mathbf{r}}u_{n\mathbf{k}}(\mathbf{r})$, satisfying the Bloch theorem. These one-particle wave functions are indexed by three dimensional momentum vector $\vec{\mathbf{k}}$ (k_x, k_y, k_z) which lives in the first Brillouin zone (BZ) and the band index n.

One of the most mature ways to identify local orbitals is the Wannier representation (Wannier, 1937), which is implemented by carrying out Fourier transformation from the Bloch functions $\psi_{n,\mathbf{k}}(\mathbf{r})$ to a set of localized "Wannier functions" $W_n(\mathbf{R}, \mathbf{r})$ labeled by a cell index $\mathbf{R}$ and a band-like index n. In a crystal the Wannier functions at different $\mathbf{R}$ are translational images of one another. Unlike Bloch functions, Wannier functions $W_n(\mathbf{R}, \mathbf{r})$ are not eigenstates of Hamiltonian: the real space localization is obtained at the expenses of energy localization.

The Wannier functions $W_n(\mathbf{R}, \mathbf{r})$ are constructed as:

$$|W_n(\mathbf{R})\rangle = \frac{V}{(2\pi)^3}\int_{BZ} d\mathbf{k}\, e^{-i\mathbf{k}\cdot\mathbf{R}}|\psi_{n,\mathbf{k}}\rangle. \qquad (2.37)$$

A more complex case is the multi-band case, where a "gauge transformation" J dimension unitary matrix $U_{mn}^{(\mathbf{k})}$ is needed:

$$|W_n(\mathbf{R})\rangle = \frac{V}{(2\pi)^3}\int_{BZ} d\mathbf{k}\, e^{-i\mathbf{k}\cdot\mathbf{R}} \sum_{m=1}^{J} U_{mn}^{(\mathbf{k})}|\psi_{n,\mathbf{k}}\rangle. \qquad (2.38)$$

In Eq. 2.37-2.38, V is the real-space primitive cell volume and the integral is carried over the BZ. Eq. 2.37 takes the form of a Fourier transform, and its inverse transform is:

$$|\psi_{n,\mathbf{k}}\rangle = \sum_{\mathbf{R}} e^{i\mathbf{k}\cdot\mathbf{R}}|W_n(\mathbf{R})\rangle. \qquad (2.39)$$

The transformation form Bloch functions $\psi_{n,\mathbf{k}}(\mathbf{r})$ into Wannier functions $W_n(\mathbf{R}, \mathbf{r})$ is illustrated in Fig. 2.7.

The above theory of Wannier functions is made more complex by the presence of a "gauge freedom" that exists in the definition of the $\Psi_{n\mathbf{k}}$. Because we can replace Bloch functions $|\tilde{\psi}_{n\mathbf{k}}\rangle = e^{i\varphi_n(\mathbf{k})}|\psi_{n\mathbf{k}}\rangle$ or, equivalently, $|\tilde{u}_{n\mathbf{k}}\rangle = e^{i\varphi_n(\mathbf{k})}|u_{n\mathbf{k}}\rangle$, without changing the physical description of the system, with $\varphi_n(\mathbf{k})$ being any real function that is periodic in reciprocal space. This replacement can lead to ambiguous defined Wannier functions $|W_n(\mathbf{R})\rangle$, one solution is to introduce a localization criterion: $\Omega = \sum_n[\langle 0n|\mathbf{r}^2|0n\rangle - \langle|\mathbf{r}|\rangle^2] = \sum_n[\langle\mathbf{r}^2\rangle_n - \bar{\mathbf{r}}_n^2]$. Minimizing this local function leads to unique definition of Maximum Localized Wannier Functions (Marzari et al., 2012).

Wannier functions allow us to plot quantities like $|W_n(\mathbf{R}, \mathbf{r})|^2$ in real space. Here we plot the Wannier functions of Ru d-orbitals of SrRuO$_3$, as shown in Fig. 2.8.
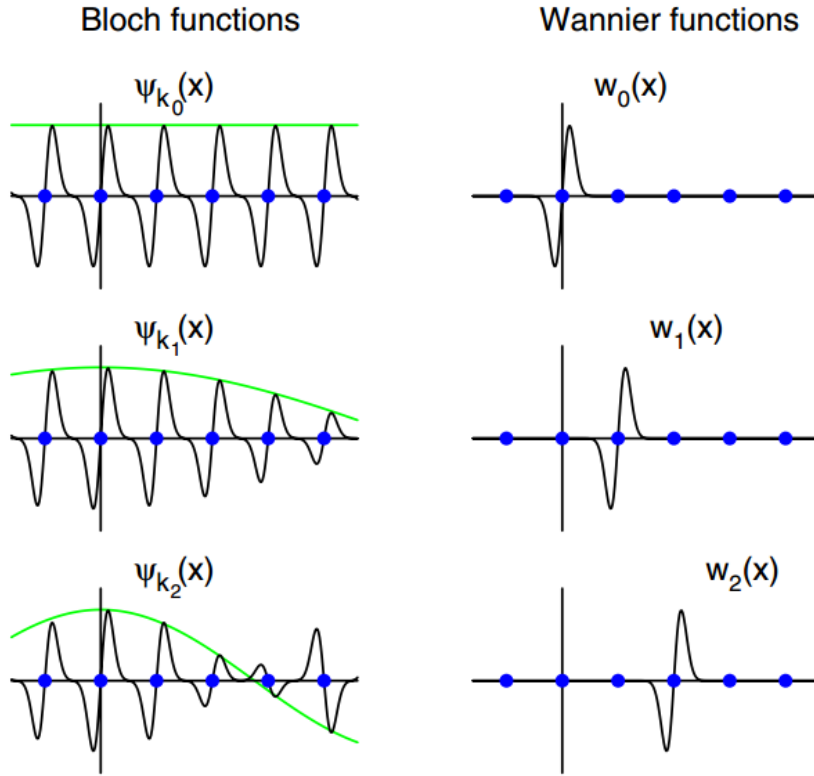
FIGURE 2.7: Transformation from Bloch functions to Wannier functions. Left: Real-space representation of three of the Bloch functions $\psi_{n,\mathbf{k}}(\mathbf{x}) = e^{i\mathbf{k}\cdot\mathbf{x}}u_{n\mathbf{k}}(\mathbf{x})$, for three different wave vector k_1, k_2 and k_3. Filled circles indicate lattice vectors, and thin lines indicate the $e^{i\mathbf{k}\cdot\mathbf{x}}$ envelopes of each Bloch function. Right: Wannier functions associated with the same band, forming periodic images of one another. The two sets of Bloch functions at every $\mathbf{k}$ in the Brillouin zone and Wannier functions at every lattice vector span the same Hilbert space. Figure from Ref. (Marzari et al., 2012).

Calculation details. For the Wannier functions plotting in Fig. 2.8, DFT part calculation was carried out by Wien2k code (Blaha et al., 2001) with the GGA correlation-exchange functional. The k-mesh was set to $15 \times 15 \times 15$. To simplify the calculations, a cubic structure of $SrRuO_3$ with lattice 3.93 Å was adopted. That is, the RuO_6 octahedra are not tilted with respect to each other.

In the Wannier representation, we can directly evaluate orbital overlaps, $t_{m,n}(\boldsymbol{R}) = \langle W_m(\boldsymbol{0})|H|W_n(\boldsymbol{R})\rangle$, that is the electron hopping energy. After obtaining the electron hopping energy, a **k**-dependent Hamiltonian matrix can be constructed as follows:

$$H_{mn}(\mathbf{k}) = \sum_{\boldsymbol{R}} t_{mn}(\boldsymbol{R})e^{i\mathbf{k}\cdot\boldsymbol{R}}. \tag{2.40}$$

Here the m and n label different orbital states, $\boldsymbol{R}$ sums over all the neighboring sites included (usually for d- or f-orbitals restriction to first- and second- neighbors is enough), **k** is the wave vector. The diagonalization of the $n \times n$ matrix at every **k**-point yields band energies $\epsilon_{n\mathbf{k}}$.
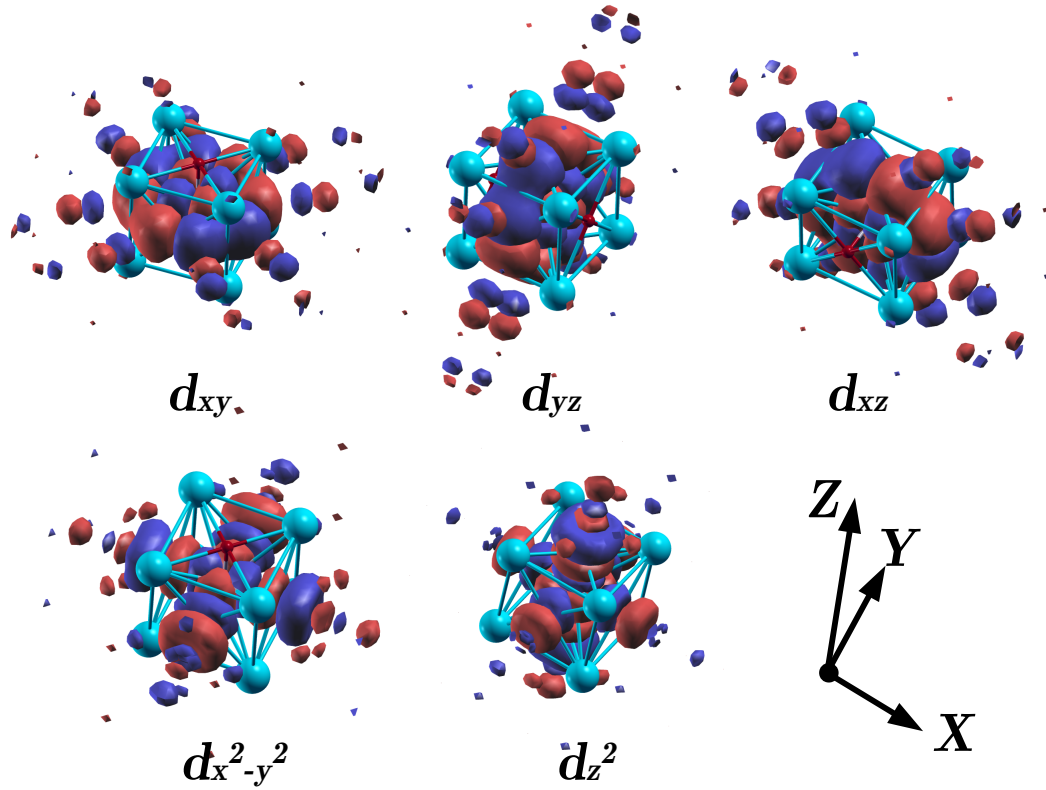
FIGURE 2.8: Localized Wannier orbitals plotting $|W_n(\mathbf{R}, \mathbf{r})|^2$ of Ru $4d$-orbitals of $SrRuO_3$.

Here we consider a simple example: the functions of the cubic phase of $SrRuO_3$. For this system, the bands around E_f are from the d-t_{2g} orbitals. Since the d_{xy}, d_{yz} and d_{xz} are orthogonal to each other, there is not off-diagonal matrix element in the Hamiltonian, all the eignstates are orbital states. From Fig. 3.2 (**Chapter 3**) one can see that the tight-binding band structure fits the DFT bands very well, this is because the $4d$-orbitals are quite localized and the orbital overlap between Ru-$4d$ t_{2g} orbitals separated by long distance is negligible. However in Fig. 3.2 the coexistence of Ru-$4d$ and O-$2p$ orbital characters around E_f can indicate the hybridization between Ru-$4d$ and O-$2p$ orbitals (i.e. the p-shape orbitals centered at O atoms, as shown in Fig. 2.8 the Wannier orbitals). In next chapter we are going to show that the large density-of-states peak of Ru-$4d$ which ranges from -2 to 1 eV not only includes Ru-$4d$-t_{2g} character but also that of O-$2p$ ($\sim$10%). Both of these conclusions strongly indicate the hybridization between $4d$ and O-$2p$ orbitals. To demonstrate the amplitude of these electronic hopping terms and compare them to a $3d$ material with more localized d-electrons, we list the major hopping terms of cubic $SrRuO_3$ and $SrVO_3$ in Table. 2.1.

As one can see from Table. 2.1, there are two main differences between the hopping terms of $SrRuO_3$ and $SrVO_3$. Firstly, the on-site hoppings $t_{\alpha\beta}(\mathbf{0})$ are -0.428 and 0.557 eV for $SrRuO_3$ and $SrVO_3$, respectively. This difference originates from the different electron filling number of $SrRuO_3$ and $SrVO_3$: in $SrRuO_3$ 4 electrons make the energy of Γ point lower than that in $SrVO_3$ with the t_{2g}^1 configuration. Secondly, all other hopping terms of $SrRuO_3$ are larger than those of $SrVO_3$, because in $3d$ $SrVO_3$ the electronic cloud is more localized than that in $4d$ $SrRuO_3$. The band width of t_{2g} in $SrRuO_3$ is $\sim$3.2 eV, which is comparable with the local Coulomb interaction

TABLE 2.1: Hopping integrals $t_{\alpha\beta}(\boldsymbol{R})$ (in eV) in the Wannier basis for fictions cubic bulk $SrRuO_3$ and $SrVO_3$. α and β are orbital indexes and $\boldsymbol{R}$ denotes the inter-atomic vector in the unit of the lattice constant a. $\boldsymbol{R}$=(0,0,0) indicates the local energy term, $\boldsymbol{R}$=(0,0,1) and $\boldsymbol{R}$=(0,0,2) are the nearest and second nearest neighbor along the z-direction, respectively. A figural illustration of definition of hopping terms is in Fig. 2.9.

$SrRuO_3$				
$t_{\alpha\beta}(\boldsymbol{R})$	$\boldsymbol{R}$=(0,0,0)	$\boldsymbol{R}$=(0,0,1)	$\boldsymbol{R}$=(0,0,2)	$\boldsymbol{R}$=(0,1,1)
$xy\ xy$	-0.428	-0.025	0.001	0.012
$yz\ yz$	-0.428	-0.337	0.007	-0.121
$xz\ xz$	-0.428	-0.337	0.007	0.012
$xy\ xz$	0.000	0.000	0.000	0.015
$SrVO_3$				
$t_{\alpha\beta}(\boldsymbol{R})$	$\boldsymbol{R}$=(0,0,0)	$\boldsymbol{R}$=(0,0,1)	$\boldsymbol{R}$=(0,0,2)	$\boldsymbol{R}$=(0,1,1)
$xy\ xy$	0.557	-0.024	0.000	0.005
$yz\ yz$	0.557	-0.247	0.006	-0.079
$xz\ xz$	0.557	-0.247	0.006	0.005
$xy\ xz$	0.000	0.000	0.000	0.009

U=3 eV that we adopt later.

In fact, constructing the Hamiltonian matrix $H_{mn}(\mathbf{k})$ from the DFT output and plotting Wannier orbital densities $|W_n(\mathbf{R}, \mathbf{r})|^2$ are not the only advantages of Wannier functions and tight-binding Hamiltonian methods. Wannier functions allow to extract a material specific microscopic Hamiltonian (the input for DMFT) from DFT band structure calculations. This Hamiltonian can be further supplemented with additional terms, such as: (1) a Zeeman magnetic field splitting between spin-up and spin-down channels can be employed to simulate ferromagnetic states; (2) the nonmagnetic Hamiltonian plus surface asymmetry term plus atomic SOC results in the Rashba effect; (3) by combining Zeeman magnetic field splitting term plus rotated SOC term, we can simulate magnetic anisotropy energy (MAE). The implementations of Wannier functions and tight-binding Hamiltonian methods will be detailedly discussed in the next section.
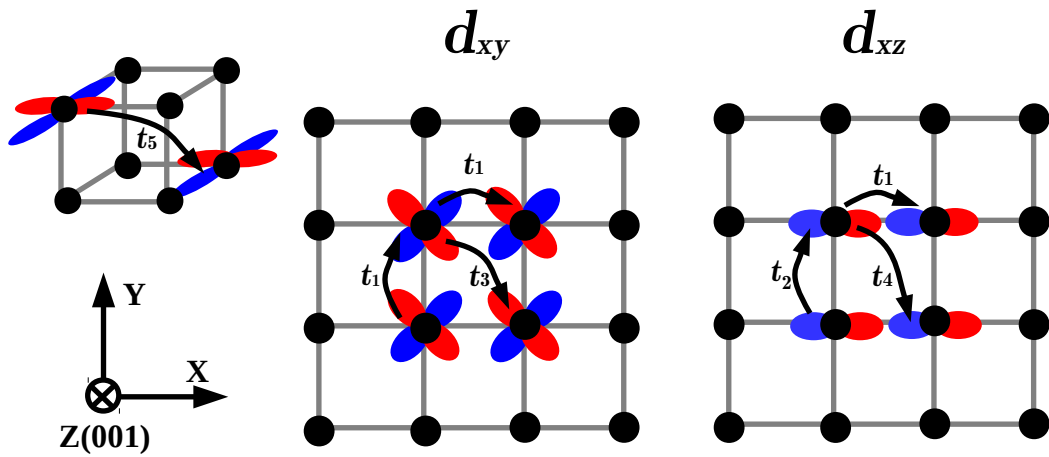
FIGURE 2.9: Definitions of hoppings for the Ru $4d$-orbitals in SrRuO$_3$. In the d_{xy} panel, a large hopping t_1 is between nearest sites along $\mathbf{R}(1,0,0)$ or $\mathbf{R}(0,1,0)$ vectors, and a smaller hopping along $\mathbf{R}(1,1,0)$ is t_3. In d_{xz} panel, along $\mathbf{R}(0,1,0)$ the hopping is t_2, and the hopping along $\mathbf{R}(1,1,0)$ is t_4. In the left up panel, the hopping along $\mathbf{R}(1,1,1)$ is t_5. Throughout this thesis we quote electronic hoppings between near sites as below: e.g. for d_{xy}-orbital, $t_1 = \mathbf{R}(1,0,0)$, $t_2 = \mathbf{R}(0,0,1)$, $t_3 = \mathbf{R}(1,1,0)$, $t_4 = \mathbf{R}(0,1,1)$ and $t_5 = \mathbf{R}(1,1,1)$.

2.6   Full Tight-Binding Hamiltonian in ABO_3 Materials

In this section we address how to derive the tight-binding t_{2g} Hamiltonians of ABO_3 perovskite materials. Such Hamiltonians depend on the momentum **k** (k_x, k_y, k_z) and are parameterized by electronic hopping terms t_1, t_2.... In essentially the same fashion we can construct the tight-binding Hamiltonian of any ABO_3 material, including SrRuO$_3$ and BaOsO$_3$ that will be studied in this thesis.

The tight-binding Hamiltonian for Bulk ABO_3 without SOC. We choose the three t_{2g} orbitals d_{yz}, d_{xz} and d_{xy} as a basis. Without SOC the non-magnetic Hamiltonian of ABO_3 reads as (all equations in this **Chapter 2.6** are in SI unit):

$$H_0(k_x, k_y, k_z) = \begin{pmatrix} h^{yz} & 0 & 0 \\ 0 & h^{xz} & 0 \\ 0 & 0 & h^{xy} \end{pmatrix}, \tag{2.41}$$

$$H_{\alpha\beta}(\vec{k}) = \sum_{\vec{R}} t_{\alpha\beta}(\vec{R}) e^{i\vec{k}\cdot\vec{R}}, \tag{2.42}$$

for t_{2g} there are (the definitions of t_1 to t_5 see Fig. 2.9):

$$h^{yz}(k_x, k_y, k_z) = t_0 + 2t_2\cos(k_xa) + 2t_1\cos(k_ya) + 2t_1\cos(k_za) + 4t_3\cos(k_ya)\cos(k_za)$$
$$h^{xz}(k_x, k_y, k_z) = t_0 + 2t_1\cos(k_xa) + 2t_2\cos(k_ya) + 2t_1\cos(k_za) + 4t_3\cos(k_xa)\cos(k_za)$$
$$h^{xy}(k_x, k_y, k_z) = t_0 + 2t_1\cos(k_xa) + 2t_1\cos(k_ya) + 2t_2\cos(k_za) + 4t_3\cos(k_xa)\cos(k_ya).$$
$$\tag{2.43}$$

In **Chapter 2.5** we already discussed the meaning of t_0, t_1, t_2 and t_3: in the case of the SrRuO$_3$: d_{yz} orbital, the hopping terms are list in Table. 2.1: $t_0 = t(0,0,0) = -0.428$ eV, $t_1 = t(0,0,1) = -0.337$ eV, $t_2 = t(1,0,0) = -0.025$ eV and $t_3 = t(0,1,1) = -0.121$ eV. With all of these major hopping terms the DFT bands of (cubic) SrRuO$_3$ can be well reproduced. Please note that for the hopping between first nearest neighbors, besides the inter-orbital hopping t_1 and t_2, there are not intra-orbital hopping and off-diagonal matrix elements because of the orthogonal of t_{2g} orbitals in cubic perovskite structures, whereas for the hopping between second and third nearest neighbors, there are intra-orbital hopping between e.g. d_{yz} and d_{xz} orbital along **R**(1,1,0) vector, and t_{2g} orbitals along **R**(1,1,1) vector. We neglect these hopping due to the fact that they are merely up to 15 meV between second nearest neighbors and 4 meV between third nearest neighbors, respectively. This setup implies that in t_{2g} orbitals the three types of carriers are not coupled. Let us note that this model is a simplified version tight-binding Hamiltonian that only contains the hoppings up to t_3. We will discuss later some properties of ABO_3 systems that are sensitive to the long-range hoppings such as t_5.

Effective mass. In solid state physics, an electron's effective mass (usually denoted m*) is the mass that it seems to have when responding to forces. One of the results from the DFT band theory is that the movement of particles in a periodic potential, over long distances larger than the lattice spacing, can be very different from their motion in a vacuum (nearly freed electrons). Usually, with the approximation of nearly free electrons we also can express the Hamiltonian with effective mass:

$$h^{yz}(k_x, k_y, k_z) = \frac{\hbar^2 k_x^2}{2m_{heavy}} + \frac{\hbar^2 k_y^2}{2m_{light}} + \frac{\hbar^2 k_z^2}{2m_{light}} \tag{2.44}$$

where $m_{heavy(light)}$ means the effective mass of heavier (lighter) electrons. Near the Γ point $(k_x, k_y, k_z = 0)$ we can estimate the DFT effective mass (heavy) for d_{yz} orbitals along the x direction:

$$- 2t_2 cos(k_x a) \sim t_2 a^2 k_x^2 = \frac{\hbar^2 k_x^2}{2m_{heavy}}, \tag{2.45}$$

$$m_{heavy} = \frac{\hbar^2}{2t_2 a^2}. \tag{2.46}$$

Similarly, the lighter mass of d_{yz} electrons along the y/z direction is:

$$-2t_1 cos(k_y a) - 4t_3 cos(k_z a) \sim (t_1 + 2t_3)a^2 k_y^2 = \frac{\hbar^2 k_y^2}{2m_{light}}, \tag{2.47}$$

$$m_{light} = \frac{\hbar^2}{2(t_1 + 2t_3)} a^2. \tag{2.48}$$

If we take $t_1 = -0.337$ eV, $t_2 = -0.025$ eV and $t_3 = -0.121$ eV from Table. 2.1,

$$m_{light}/m_{heavy} = t_2/(t_1 + 2t_3) = 0.043, \tag{2.49}$$

and thus:

$$m_{light}/m_e = \frac{\hbar^2}{2(t_1 + 2t_3)a^2 m_e} = 0.467, \tag{2.50}$$

$$m_{heavy}/m_e = 10.860. \tag{2.51}$$

Bulk ABO_3 with SOC. We choose six spinful t_{2g} orbitals $d_{yz} \uparrow$, $d_{yz} \downarrow$, $d_{xz} \uparrow$, $d_{xz} \downarrow$, $d_{xy} \uparrow$, $d_{xy} \downarrow$ as a basis. The Hamiltonian without SOC is:

$$H_0(k_x, k_y, k_z) = \begin{pmatrix} h^{yz} & 0 & 0 & 0 & 0 & 0 \\ 0 & h^{yz} & 0 & 0 & 0 & 0 \\ 0 & 0 & h^{xz} & 0 & 0 & 0 \\ 0 & 0 & 0 & h^{xz} & 0 & 0 \\ 0 & 0 & 0 & 0 & h^{xy} & 0 \\ 0 & 0 & 0 & 0 & 0 & h^{xy} \end{pmatrix}. \tag{2.52}$$

These six spinful t_{2g} orbitals are degenerate at Γ point. Generally, SOC is expressed in terms of $(\hbar/4mc^2)(\nabla V \times \mathbf{p}) \cdot \sigma$. If we focus on properties around the Γ point $(k_x, k_y, k_z = 0)$ then we can use the atomic SOC approximation $\alpha L \cdot S$ and carry out a group analyses. Taking into account the transformation properties of the spin degrees of freedom under O_h point group operations, we obtain the spinful T_{2g} electron wave functions that transform according to the irreducible representations:

$$T_{2g} \otimes \Gamma_6^+ = \Gamma_5^+ \otimes \Gamma_6^+ = \Gamma_7^+ \oplus \Gamma_8^+ \tag{2.53}$$

Γ_7^+ basis functions:

$$|\Gamma_7^+ - \tfrac{1}{2}\rangle = \frac{1}{\sqrt{3}}(-id_{yz}|\uparrow\rangle - d_{xz}|\uparrow\rangle + id_{xy}|\downarrow\rangle)$$

$$|\Gamma_7^+ \tfrac{1}{2}\rangle = \frac{1}{\sqrt{3}}(-id_{yz}|\downarrow\rangle + d_{xz}|\downarrow\rangle - id_{xy}|\uparrow\rangle) \tag{2.54}$$

Γ_8^+ basis functions:

$$|\Gamma_8^+ - \tfrac{3}{2}\rangle = \frac{1}{\sqrt{3}}(-\frac{i}{\sqrt{2}}d_{yz}|\downarrow\rangle + \frac{1}{\sqrt{2}}d_{xz}|\downarrow\rangle + i\sqrt{2}d_{xy}|\uparrow\rangle)$$

$$|\Gamma_8^+ - \tfrac{1}{2}\rangle = \frac{1}{\sqrt{2}}(id_{yz}|\uparrow\rangle - d_{xz}|\uparrow\rangle)$$

$$|\Gamma_8^+ \tfrac{1}{2}\rangle = \frac{1}{\sqrt{2}}(-id_{yz}|\downarrow\rangle - d_{xz}|\downarrow\rangle) \tag{2.55}$$

$$|\Gamma_8^+ \tfrac{3}{2}\rangle = \frac{1}{\sqrt{3}}(\frac{i}{\sqrt{2}}d_{yz}|\uparrow\rangle + \frac{1}{\sqrt{2}}d_{xz}|\uparrow\rangle + i\sqrt{2}d_{xy}|\downarrow\rangle).$$

With $\vec{J} = \vec{L} \cdot \vec{S}$, we have $\alpha L \cdot S = \frac{\alpha}{2}(J^2 - L^2 - S^2)$ so that in the $\Gamma_7^+ \oplus \Gamma_8^+$ basis:

$$H_{SOC} = \alpha L \cdot S = \begin{pmatrix} 1 & 0 & 0 & 0 & 0 & 0 \\ 0 & 1 & 0 & 0 & 0 & 0 \\ 0 & 0 & -\frac{1}{2} & 0 & 0 & 0 \\ 0 & 0 & 0 & -\frac{1}{2} & 0 & 0 \\ 0 & 0 & 0 & 0 & -\frac{1}{2} & 0 \\ 0 & 0 & 0 & 0 & 0 & -\frac{1}{2} \end{pmatrix}, \tag{2.56}$$

at the Γ point, the atomic SOC will split six degenerate spinful t_{2g} orbitals into the doublet $|\Gamma_7^+ - \tfrac{1}{2}>, |\Gamma_7^+ \tfrac{1}{2}>$, and quartet $|\Gamma_8^+ - \tfrac{3}{2}>, |\Gamma_8^+ - \tfrac{1}{2}>, |\Gamma_8^+ \tfrac{1}{2}>$ and $|\Gamma_8^+ \tfrac{3}{2}>$. We express H_{SOC} in the original t_{2g} basis, $H_{SOC} = U(\alpha L \cdot S)U^+$,

$$U = \begin{pmatrix} \frac{-i}{\sqrt{3}} & 0 & 0 & \frac{i}{\sqrt{2}} & 0 & \frac{i}{\sqrt{6}} \\ 0 & \frac{-i}{\sqrt{3}} & \frac{-i}{\sqrt{6}} & 0 & \frac{-i}{\sqrt{2}} & 0 \\ \frac{-1}{\sqrt{3}} & 0 & 0 & \frac{-i}{\sqrt{2}} & 0 & \frac{1}{\sqrt{6}} \\ 0 & \frac{1}{\sqrt{3}} & \frac{1}{\sqrt{6}} & 0 & \frac{-1}{\sqrt{2}} & 0 \\ 0 & \frac{-i}{\sqrt{3}} & i\sqrt{\frac{2}{3}} & 0 & 0 & 0 \\ \frac{i}{\sqrt{3}} & 0 & 0 & 0 & 0 & i\sqrt{\frac{2}{3}} \end{pmatrix}, \tag{2.57}$$

$$U\alpha \begin{pmatrix} 1 & 0 & 0 & 0 & 0 & 0 \\ 0 & 1 & 0 & 0 & 0 & 0 \\ 0 & 0 & -\frac{1}{2} & 0 & 0 & 0 \\ 0 & 0 & 0 & -\frac{1}{2} & 0 & 0 \\ 0 & 0 & 0 & 0 & -\frac{1}{2} & 0 \\ 0 & 0 & 0 & 0 & 0 & -\frac{1}{2} \end{pmatrix} U^+ = \frac{\alpha}{2} \begin{pmatrix} 0 & 0 & i & 0 & 0 & -1 \\ 0 & 0 & 0 & -i & 1 & 0 \\ -i & 0 & 0 & 0 & 0 & i \\ 0 & i & 0 & 0 & i & 0 \\ 0 & 1 & 0 & -i & 0 & 0 \\ -1 & 0 & -i & 0 & 0 & 0 \end{pmatrix}. \tag{2.58}$$

For the tight-binding Hamiltonian including SOC, we have $H = H_0 + H_{SOC}$. H accounts for basic SOC effects in ABO_3 bands: (i) band splitting between Γ_7^+ and Γ_8^+ at the Γ point (Zhong, Tóth, and Held, 2013), and the SOC parameter α can be obtained from this splitting, e.g. in SrRuO$_3$ (BaOsO$_3$) this splitting is about 0.210 eV (0.666 eV), thus α=0.210 (0.666)$\times \frac{2}{3}$=0.140 (0.444) eV; (ii) the effective mass will be

significantly changed. This is due to the mixture of t_{2g} bands under the effect of SOC.

H_0 **of thin films** ABO_3. Compared with the band structure of bulk ABO_3, the thin films bands have a key feature: lifting of orbital degeneracy; the d_{xy} orbital is separated from d_{yz} and d_{xz} orbitals. The splitting is a result of the dimensional reduction along z-direction by surfacing. When we describe this feature of ABO_3 films or surface/interface systems, H_0 is modified as follows: basically, H_0 of thin films has the same structure as its bulk counterpart:

$$H_0(k_x, k_y, k_z) = \begin{pmatrix} h^{yz} & 0 & 0 & 0 & 0 & 0 \\ 0 & h^{yz} & 0 & 0 & 0 & 0 \\ 0 & 0 & h^{xz} & 0 & 0 & 0 \\ 0 & 0 & 0 & h^{xz} & 0 & 0 \\ 0 & 0 & 0 & 0 & h^{xy} & 0 \\ 0 & 0 & 0 & 0 & 0 & h^{xy} \end{pmatrix}. \tag{2.59}$$

Eliminating the hoppings along k_z, h_{yz}, h_{xz} and h_{xy}:

$$h^{yz}(k_x, k_y) = t'_0 + 2t_2 cos(k_x a) + 2t_1 cos(k_y a)$$
$$h^{xz}(k_x, k_y) = t'_0 + 2t_1 cos(k_x a) + 2t_2 cos(k_y a) \tag{2.60}$$
$$h^{xy}(k_x, k_y) = t_0 + 2t_1 cos(k_x a) + 2t_1 cos(k_y a) + 4t_3 cos(k_x a) cos(k_y a).$$

The on-site terms of d_{yz} and d_{xz} will change because of the surface, e.g. for SrRuO$_3$ t'_0 is -0.122 eV, which is quite different with its bulk value -0.428 eV, the change of on-site energy of the d_{xy} orbital is however quite small because the d_{xy} orbital is mainly spread out in the xy plane. Clearly, we can see that at the Γ point the d_{xy} orbital has the eigenvalue $\triangle = t_0 + 2t_1 + 2t_1 + 4t_3 = -2.260$ eV, and for the d_{yz}/d_{xz} orbital has the eigenvalue $\triangle = t'_0 + 2t_2 + 2t_1 = -0.846$ eV.

Zeeman splitting in ABO_3. To simulate the ferromagnetic splitting we need a matrix which can split the spin-up eigenvalues with the spin-down eigenvalues by a constant B. In the basis of $|d_{yz} \uparrow\rangle$, $|d_{yz} \downarrow\rangle$, $|d_{xz} \uparrow\rangle$, $|d_{xz} \downarrow\rangle$, $|d_{xy} \uparrow\rangle$ and $|d_{xy} \downarrow\rangle$ this matrix can be:

$$H_{Zeeman} = \frac{B}{2} \begin{pmatrix} 1 & 0 & 0 & 0 & 0 & 0 \\ 0 & -1 & 0 & 0 & 0 & 0 \\ 0 & 0 & 1 & 0 & 0 & 0 \\ 0 & 0 & 0 & -1 & 0 & 0 \\ 0 & 0 & 0 & 0 & 1 & 0 \\ 0 & 0 & 0 & 0 & 0 & -1 \end{pmatrix} \tag{2.61}$$

where B is the energetic splitting between $\varepsilon(\uparrow, \mathbf{k})$ and $\varepsilon(\downarrow, \mathbf{k})$. It can be estimated from spin-polarized DFT band calculations or fixed to reproduce a given magnetism. For ferromagnetic systems $H = H_0 + H_{Zeeman}$.

Rashba spin splitting. The Rashba effect (Winkler et al., 2003) is a momentum-dependence splitting of spin bands in two-dimensional condensed matter systems (heterostructures and surfaces). The splitting is a combined effect of atomic spin-orbit coupling and asymmetry of the potential in the direction perpendicular to the two-dimensional plane. Rashba spin-splitting was observed by magneto-resistance measurement of an LaAlO$_3$/SrTiO$_3$ interface: a Rashba spin-splitting on order of meV was reported (Nitta et al., 1997; LaShell, McDougall, and Jensen, 1996). This

Rashba splitting can be tuned by an external electric field. The first theoretical explanation focuses on the free electron model and believes that the interface potential gradient ∇V, which can be tuned by external field, can explain the spin-splitting by $(\hbar/4mc^2)(\nabla V \times p) \cdot \sigma$. However, the key point is that this term $(\hbar/4mc^2)(\nabla V \times p) \cdot \sigma$ only can directly induce a splitting by order of 10^{-6} eV, which is significantly lower than the observed values.

In the TB approximation, numerical solutions of $H_0 + H_{SOC}$ always show twofold degenerate (Kramers degeneracy). This degeneracy can be broken by (i) adding a Zeeman term (breaking time-reversal symmetry) or (ii) adding a Rashba SOC term (breaking crystal inversion symmetry). The nature of Rashba splitting had been attributed to the modification of surface potential (LaShell, McDougall, and Jensen, 1996; Petersen and Hedegård, 2000). However, in our previous research we demonstrated that such a Rashba splitting is mainly from the surface orbital deformation (Zhong, Tóth, and Held, 2013). At the interface between two different ABO_3 materials or surface that faces to vacuum, the key hopping terms are:

$$\gamma = \langle d_{xy}(R_0)|H|d_{yz}(R_0 + R_x)\rangle = -\langle d_{xy}(R_0)|H|d_{yz}(R_0 - R_x)\rangle$$
$$\gamma = \langle d_{xy}(R_0)|H|d_{xz}(R_0 + R_x)\rangle = -\langle d_{xy}(R_0)|H|d_{xz}(R_0 - R_x)\rangle$$

(2.62)

where $\mathbf{R}_x$ is the nearest neighbor along x-direction, thus γ is the hopping term of d_{xy} and d_{yz} along x-direction. It is anti-symmetric and it should be *zero* at periodic bulk state because the t_{2g} orbitals are orthogonal. The Rashba hopping term (Eq. 2.62) arises from the breaking of crystal space inversion symmetry of $z \leftrightarrow -z$ at interface/surface. The physics picture of this can be understood by plotting the Wannier functions $|W_n(R, r)|^2$ of d_{xy} and d_{yz} orbitals at interface/surface (Fig. 2.10).
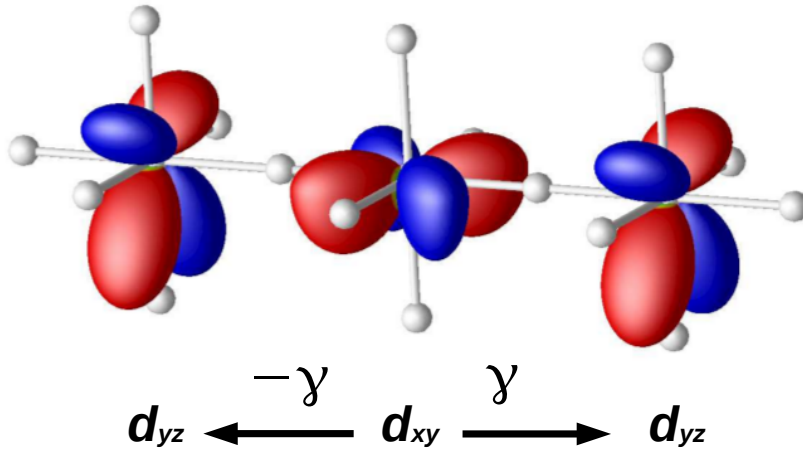

FIGURE 2.10: Schematic figure of the orbital deformation at the perovskite ABO_3 surface/interface resulting in an anti-symmetric hopping term γ.

In the previous literatures this γ term is usually treated as a parameter in a model and its value is obtained from by fitting the experiments. However we found another way to calculate γ; using Wannier projections. We can obtain the exact value of γ by projecting Wannier orbitals of $d_{xy}(0)$ and $d_{yz}(0 + R_x)$ and calculate their overlap $\langle d_{xy}(R_0)|H|d_{yz}(R_0 + R_x)\rangle$.

For the interface between $5d$ $BaOsO_3$ and $BaTiO_3$ (with $BaTiO_3$, the details of calculations will be detailed discussed in **Chapter 4.1**), our calculations indicate γ of $0.016\,eV$, and it shows anti-symmetric behavior with respect to bulk $BaOsO_3$.

Including the hopping terms γ, we express the Hamiltonian $H_0 + H_{SOC} + H_\gamma$:

$$
\begin{pmatrix}
h^{yz} & 0 & 0 & 0 & 0 & 0 \\
0 & h^{yz} & 0 & 0 & 0 & 0 \\
0 & 0 & h^{xz} & 0 & 0 & 0 \\
0 & 0 & 0 & h^{xz} & 0 & 0 \\
0 & 0 & 0 & 0 & h^{xy} & 0 \\
0 & 0 & 0 & 0 & 0 & h^{xy} \\
(Eq.23)
\end{pmatrix}
+ \frac{\alpha}{2}
\begin{pmatrix}
0 & 0 & i & 0 & 0 & -1 \\
0 & 0 & 0 & -i & 1 & 0 \\
-i & 0 & 0 & 0 & 0 & i \\
0 & i & 0 & 0 & i & 0 \\
0 & 1 & 0 & -i & 0 & 0 \\
-1 & 0 & -i & 0 & 0 & 0
\end{pmatrix}
$$

$$
+\gamma
\begin{pmatrix}
0 & 0 & 0 & 0 & 2isin(k_xa) & 0 \\
0 & 0 & 0 & 0 & 0 & 2isin(k_xa) \\
0 & 0 & 0 & 0 & 2isin(k_ya) & 0 \\
0 & 0 & 0 & 0 & 0 & 2isin(k_ya) \\
-2isin(k_xa) & 0 & -2isin(k_ya) & 0 & 0 & 0 \\
0 & -2isin(k_xa) & 0 & -2isin(k_ya) & 0 & 0
\end{pmatrix}.
$$

$$(2.63)$$

Rotation of the atomic SOC matrix: magnetic anisotropy energy. Magnetic anisotropy energy (MAE) is a very important physical quantity in ferromagnetic materials. There are two sources of MAE: (i) the interaction between magnetic dipoles, (ii) the SOC interaction. Even through its energy scale is small as μeV/atom compared to the total energy eV/atom, it is important because it governs the microscopical quantization axis, and a macroscopically ferromagnetic easy-axis or easy-plane (i.e. magnetic direction). The small scale of MAE (μeV) is beyond the ability of DFT, thus we need to use tight-binding method.

To calculate the MAE, we need at least three terms in the Hamiltonian: $H_0 + H_{Zeeman} + H_{SOC}(\theta, \varphi)$. The first term H_0 (Eq. 2.43 and Eq. 2.52) describes the non-magnetic Hamiltonian of t_{2g} orbitals, the second term H_{Zeeman} (Eq. 2.61) introduces a spin-splitting between spin-up and -down channels. The third term $H_{SOC}(\theta, \varphi)$ is different from the traditional atomic SOC matrix Eq. 2.58, where a unitary transformation is applied to the expression Eq. 2.58, thus we can rotate the direction of the quantization axis (Eq. 2.64):

$$
H_{SOC}(\theta,\varphi) =
\begin{pmatrix}
0 & 0 & i\cos(\theta) & -i\sin(\theta) & -i\sin(\theta)\sin(\varphi) & -\cos(\varphi)-i\cos(\theta)\sin(\varphi) \\
0 & 0 & -i\sin(\theta) & -i\cos(\theta) & \cos(\varphi)-i\cos(\theta)\sin(\varphi) & i\sin(\theta)\sin(\varphi) \\
-i\cos(\theta) & i\sin(\theta) & 0 & 0 & i\sin(\theta)\cos(\varphi) & -\sin(\varphi)+i\cos(\theta)\cos(\varphi) \\
i\sin(\theta) & i\cos(\theta) & 0 & 0 & \sin(\varphi)+i\cos(\theta)\cos(\varphi) & -i\sin(\theta)\cos(\varphi) \\
i\sin(\theta)\sin(\varphi) & \cos(\varphi)+i\cos(\theta)\sin(\varphi) & -i\sin(\theta)\cos(\varphi) & \sin(\varphi)-i\cos(\theta)\cos(\varphi) & 0 & 0 \\
-\cos(\varphi)+i\cos(\theta)\sin(\varphi) & -i\sin(\theta)\sin(\varphi) & -\sin(\varphi)-i\cos(\theta)\cos(\varphi) & i\sin(\theta)\cos(\varphi) & 0 & 0
\end{pmatrix}
$$

$$(2.64)$$

where θ, φ are Euler angles. For $\theta=\varphi=0$, this matrix is equal to the original atomic SOC matrix Eq. 2.58.

Summary. So far, we discussed the formalism of full TB Hamiltonian of t_{2g} orbitals of $AB\mathrm{O}_3$ perovskite materials. The formalism of atomic SOC matrix, Zeeman spin-splitting, interface/surface asymmetry (Rashba) splitting terms are reviewed. And we define a way to rotate the atomic SOC matrix, with which the total energy of a ferromagnetic system with various quantization axes can be calculated. The applications of these implementations will be shown in **Chapter 3-4**.

Chapter 3

DFT+DMFT Research of Strontium Ruthenate: SrRuO$_3$

In the previous chapter the combination of *ab-initio* DFT calculations with the many-body approach DMFT was discussed. We demonstrated that DMFT is an effective method for describing dynamic correlation effects of strongly correlated electron systems and explaining their electronic structure. In DMFT, the real and imaginary parts of self-energy $Re\Sigma(\omega)$ and $Im\Sigma(\omega)$ can be calculated and result in modifications of the k-integrated and k-resolved spectral functions $A(\omega)$ and $A(k,\omega)$. These quantities can be directly compared with experimental measured quantities, such as angle resolved photoemission spectroscopy (ARPES), X-ray absorption spectroscopy (XAS) and photoemission spectroscopy (PES). However, DMFT calculations in the presence of SOC are challenging. To solve this problem, we derived a full TB model which explicitly includes the spin-orbit coupling for t_{2g} orbitals in perovskite ABO$_3$ systems. In this way we can further calculate (i) surface/interface Rashba splitting, (ii) magnetic anisotropy energy.

In this chapter we focus on the electronic and magnetic properties of SrRuO$_3$ (SRO) in its bulk as well as in thin films. By using DFT, DFT+U and DFT+DFMT we firstly start with the discussion of bulk SRO. Secondly, we show TB results of the magnetic anisotropy energy for bulk SRO. Thirdly, we demonstrate that the electronic properties of SRO thin films are dominated by two factors: film thickness and the crystallographic orientation. Three different orientations: (001), (110) and (111) will be discussed. The DMFT spectra will be compared with the experimental observations to reveal that DMFT is the only successful method for describing the electronic structure in the presence of dynamical correlations, both DFT and DFT+U methods fail in obtaining the exact ground states of SRO thin films. Reader will see how the geometrical confinement and the crystallographic orientation give rise to new phases emerge in SRO thin films, e.g., the (001)-oriented growth turns SRO from its correlated and conductive metallic state in the bulk to an antiferromagnetic insulator, growth along the (110)-orientation entirely suppresses the critical thickness behavior regrading the metal-to-insulator transition, stabilizing the metallic state even down to a monolayer, (111)-oriented SRO thin films exhibit half-metallic ferromagnetic states with topological properties [i.e. a quantum anomalous hall (QAH) state]. Lastly, we present DFT+U results of SRO supercells with an oxygen vacancy, elucidating the relationship between the high-spin state and oxygen vacancies in SRO.

3.1 SrRuO₃ Bulk

The complex oxide perovskite $SrRuO_3$ (SRO) has fascinated researchers for over half a century because of its excellent chemical stability and electrical conductivity. Experimentally, SRO can be heterostructured with or grown on other variety perovskite materials, making it an excellent candidate for materials design. The interplay between different degrees of freedom of spin, orbital, charge, and the geometrical confinement in SRO-based systems provides a fascinating playground to explore new physics and exotic phenomenas. The crystal structure of single-crystal SRO performances as cubic, tetragonal and orthorhombic in the temperature ranges of $T>950$ K, 950 K$>T>820$ K and $T<820$ K, respectively. The cubic, tetragonal and orthorhombic phase crystal structures are shown in Fig. 3.1(a)-(f). At low-T, SRO has an orthorhombic structure with bulk lattice parameters a=5.57 Å, b=5.53 Å and c=7.84 Å (Jones et al., 1989); moreover, it can be well represented as a pseudo-cubic perovskite with a=3.93 Å. The T_C and the local magnetic moment of SRO were determined to be 160 K and 0.8-1.6 μ_B/Ru (Kiyama et al., 1996; Cao et al., 1997; Allen et al., 1996; Felner, Nomura, and Nowik, 2006). So the ground state of SRO is a ferromagnetic metal in the orthorhombic phase (space group *Pbnm*, No.62). For the d^4 configuration of the Ru^{4+} t_{2g} orbitals the maximal spin-only moment amounts to 2 μ_B/Ru. The lower experimental moment has received three explanations: (i) the electron delocalization associated with itinerancy (Longo, Raccah, and Goodenough, 1968; Klein et al., 1996), (ii) spin canting (Gibb et al., 1974), (iii) a combination of larger magnetocrystalline anisotropy and the difficulty in making single-domain crystals and films (Kanbayasi, 1978).
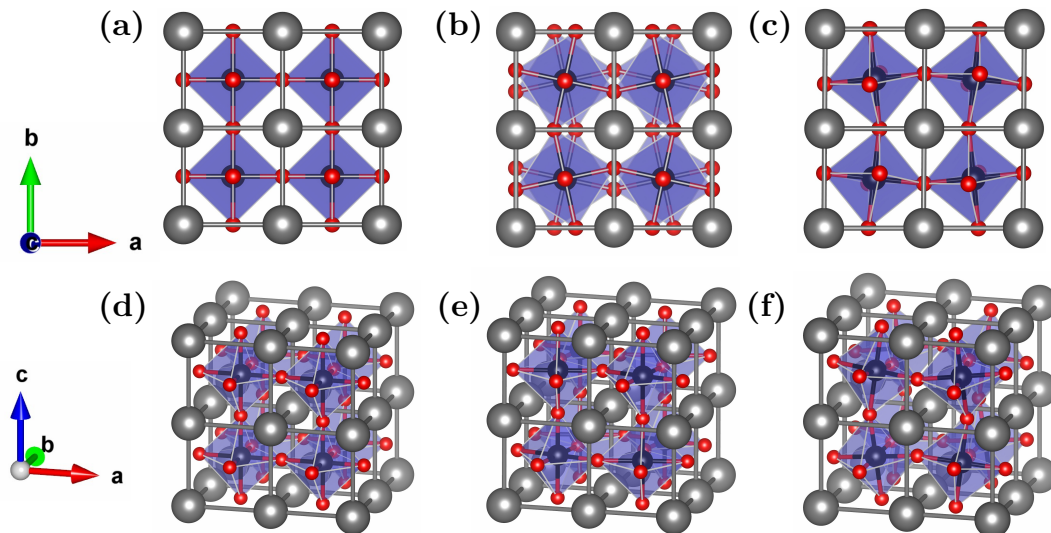

FIGURE 3.1: Cubic (a,d), tetragonal (b,e) and orthorhombic (c,f) structures of SrRuO₃.

We start with a nonmagnetic DFT calculation, for simplification and a better understanding of band characters we replace the orthorhombic phase with a fictions cubic perovskites structure. The DFT bands, the density-of-states (DOS) and Wannier projections are shown in Fig. 3.2. In the band structure (left panel), the nice

bands from $-8\,\text{eV}$ to $-2\,\text{eV}$ are from O-2p orbitals (red). The three (blue) bands, which are located around E$_f$, are from the Ru-4d t_{2g} orbitals. The two e_g bands (green) are from $1\,\text{eV}$ to $6\,\text{eV}$. At energies higher than $5\,\text{eV}$, the five (pink) bands are from Sr-3d orbitals. The bands from Wannier projections are labeled by solids black circles, and they agree with DFT bands very well, indicating the localization of Ru-4d orbitals. Along the X-Γ path, one of the three t_{2g} band has a rather flat dispersion (heavy band). This band orientates from the the yz orbital, the corresponding hopping (denoted as t_2 according to **Chapter 2**) along the x direction is much smaller than those (t_1) of xy and xz orbitals (lighter bands). However along the Γ-M path all three bands are dispersive and exhibit as light bands, and yet one of them (xy) is still lighter than others (yz, xz bands), because along the $(110)_{Cubic}$ lattice vector the hopping for xy orbital (t_3) is larger than for the yz and xz orbitals (t_4). Finally, along the Γ-R k-path, all three t_{2g} bands have larger energetic dispersions, reading the top of conduction bands at R point ($0.72\,\text{eV}$). All the three t_{2g} bands are nearly degenerate, because along $(111)_{Cubic}$ direction, all three t_{2g} orbitals have same hopping terms (t_5). The bottom of conduction (t_{2g}) bands is located at Γ point, with energy equals to $-2.48\,\text{eV}$, leading to a bandwidth of $3.20\,\text{eV}$ for cubic SRO. The bandwidth of orthorhombic SRO is reduced to $3.08\,\text{eV}$, this reduction is mainly due to the rotation and tilting of RuO$_6$ octahedron, leading to the reduction of hybridization between Ru-4d and O-2p orbitals.
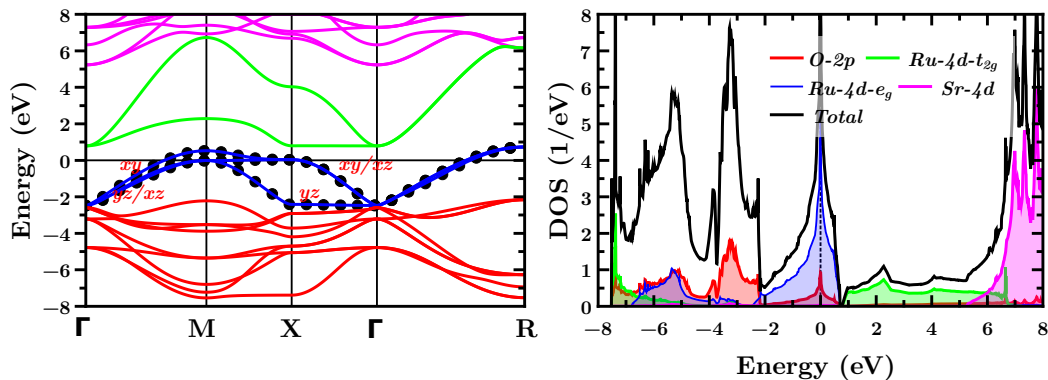

FIGURE 3.2: DFT band structure and tight-binding fitting (left panel) and the density of states (DOS, right panel) of cubic SRO.

As shown in the DOS (Fig. 3.2 right panel), the states near Fermi level (E$_f$) have predominantly Ru-4d and O-2p characters. This strong hybridization leads to a high DOS peak at E$_f$, favoring ferromagentism in accord with the Stoner criterion. Experiments confirmed that SRO is a good ferromagnetic/correlated metal at low temperature (T<160 K). Thus to realistically investigate the electronic structure of it, we have to use spin-polarized DFT and DMFT calculations. We firstly focus on the simplified cubic phase. In Fig. 3.3 we show the DFT-GGA spin-polarized DOS (a), DMFT spectral functions $A(\omega)$ at 100 K (b) and 200 K (c), respectively. Spin-polarized DFT concludes a magnetic moment of $1.76\,\mu_B/\text{Ru}$ with GGA, and $1.25\,\mu_B/\text{Ru}$ with LDA. The DFT DOS results also indicate the exchange splitting of nearly $1\,\text{eV}$ between the majority (spin-up) and minority (spin-down) bands together with a DOS reduction at E$_f$, leading to lower total electronic energy and better chemical stability.

In DFT DOS the t_{2g} bands cross E$_f$ and partly filled while there are no electrons the in e_g bands. This indicates that the e_g orbitals are unlikely to be the main source of ferromagnetism, therefore we exclude them from DMFT calculations. The magnetic moment of cubic SRO is determined as $1.20\,\mu_B/\text{Ru}$ at 100 K in DMFT, this is
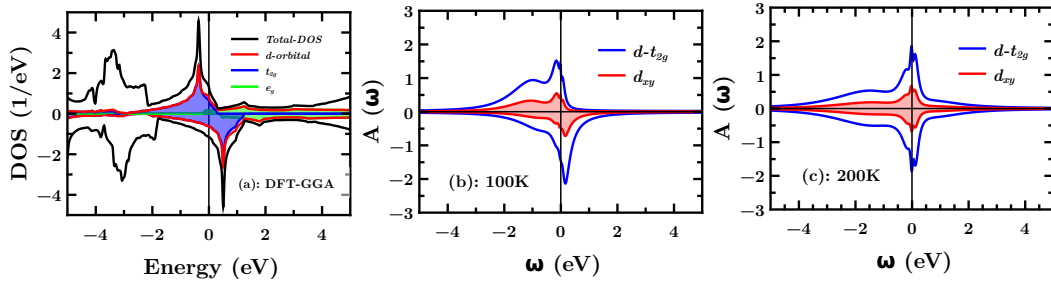
FIGURE 3.3: Spin-polarized DFT-GGA DOS (a) and DMFT spectral
functions at 100 K (b) and 200 K (c) of cubic SRO.

in reasonable agreement with the experimentally measured 0.8-1.6 μ_B/Ru. At lower temperatures, we expect the moment to increase further, but doing DMFT at lower temperatures is computationally very demanding: it leads to heavy computational tasks in CT-QMC iterations. The orbital occupations of all t_{2g} bands are 0.866 and 0.466 for spin-majority and minority channels. Because of the orbital degeneracy of O_h point group in cubic SRO, only the d_{xy} band spectral function is shown. Ferromagnetism in SRO is suppressed at 200 K [Fig. 3.3(b)]. The T_C from DMFT and CT-QMC is therefore determined to be between 100 K and 200 K. In our previous DMFT study, for orthorhombic phase SRO we obtained a T_C close to 160 K (Si et al., 2015), however a residual moment could be observed, in this thesis to show the degeneracy of spin channels in paramagnetic metallic states we choose computational-T as 100 K and 200 K.

Calculation details. For the DFT-GGA and DMFT calculations in Fig. 3.2 to Fig. 3.7, experimentally measured structural parameters are adopted thus no atomic relaxation is carried out. In DFT+DMFT calculations, nonmagnetic DFT self-consistent calculations are finished first, then we project the corresponding DFT bands structure [from Wien2k (Blaha et al., 2001)] onto Wannier functions (Marzari et al., 2012) using Wien2Wannier interface (Kuneš et al., 2010) and supplement it by a local density-density interaction with intra-orbital U=3.0 eV, inter-orbital U'=U-2J=2.4 eV and Hund's exchange J=0.3 eV. We crosscheck all results of this thesis against the choice of the interacting Hamiltonian (both density-density and also Kanamori interaction). With two different interactions, we can observe the same transition behaviors. The different choice of interaction formula only results in a tiny shift of Hund's exchange J in the overall phase diagram, this part argument is beyond the content of this thesis. The resulting tight-binding Hamiltonian of t_{2g} orbitals are then solved by DMFT at different temperatures, using continuous-time quantum Monte Carlo (CT-QMC) simulations in the hybridization expansion using the W2dynamic code (Parragh et al., 2012) and the maximum entropy method (Gubernatis et al., 1991; Sandvik, 1998) for an analytic continuation of the spectra.

The results of the orthorhombic phase of SRO are shown in Fig. 3.4. Compared with results of cubic SRO, no qualitative differences are found. The DFT magnetic moment is 1.95 μ_B/Ru and 1.53μ_B/Ru for GGA and LDA which are significantly larger than those of cubic SRO. This indicates that the RuO₆ octahedron distortion and tilting are crucial quantities for the ferromagnetism of SRO on a quantitative level. Both the GGA and LDA magnetic moments are beyond and at odds with the experimental values. This suggests that the formation of magnetic domains, which is beyond the capability of current DFT, plays a role in reducing ferromagnetism in
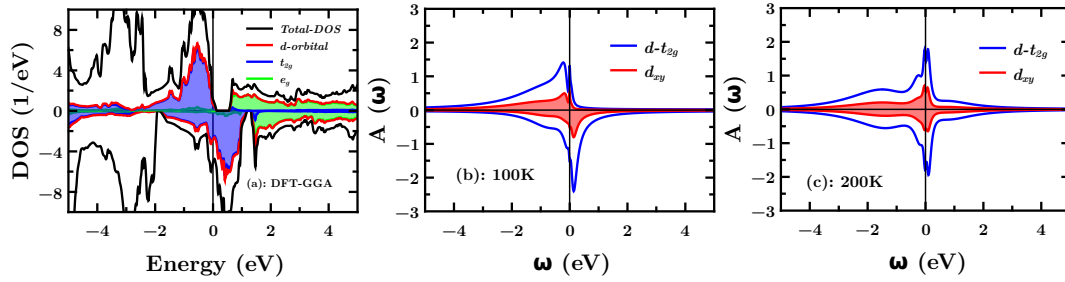
FIGURE 3.4: Spin-polarized DFT-GGA DOS (a) and DMFT spectral functions at 100 K (b) and 200 K (c) of orthorhombic SRO.

SRO. DMFT calculations yield the magnetic moments of orthorhombic SRO to be $1.31\,\mu_B/\text{Ru}$ at 100 K, we conclude orthorhombic bulk SRO to be a FM metal with orbital occupations of 0.908 (0.447), 0.866 (0.449), and 0.881 (0.449) for the majority (minority) spin of xy, yz and xz orbitals at T=100 K. Similar to the cubic case, T_C of the orthorhombic phase is below 200 K [beyond the results of Ref. (Si et al., 2015), we here also discuss the cubic phase]. Besides the excellent agreement of T_C, another advancement of DMFT is that we restore the correlated features: Hubbard bands. As shown in both cubic and orthorhombic phase, Fig. 3.3 and Fig. 3.4, respectively, distinct lower Hubbard bands can be observed in both spin-majority and spin-minority channels at $-1.5\,\text{eV}$ to $-0.5\,\text{eV}$ for the ferromagnetic case (100 K). For the paramagnetic phase at 200 K, both lower and higher bands can be observed at $-2.0\,\text{eV}$ and $1\,\text{eV}$, so are the quasi-particle peaks at E_f. Due to the fact that such Hubbard bands features are crucial and can be accessed experimentally by using e.g. X-ray absorption spectra and optic conductivity (Shai et al., 2013), while the quasi-particle peaks can be used to explain the Fermi-liquid behavior of SRO (Vollhardt, 1984). Thus our results indicate DMFT is a sensible method to describe dynamical correlation effects in SRO.

The discussed spectral functions are evaluated from Eq. 2.35, which is already after the k-vector integration. Another important physical quantities of correlated systems are the k-resolved spectral functions $A(k,\omega)$, which are both momentum k and frequency ω dependent, as demonstrated by Eq. 2.36. We calculate the k-resolved spectral functions $A(k,\omega)$ for both cubic and orthorhombic phases SRO to analyze the modifications from the viewpoint of dynamic correlations. For simplification, we also take the cubic phase of SRO as a starting case. The k-resolved spectral functions $A(k,\omega)$ of the cubic phase SRO at 100 K and 200 K are shown in Fig. 3.5. At 100 K, a clear spin splitting can be observed. For the spin-down channel the bandwidth changes from 3.2 eV to 2.5 eV (decreased by ~21%). The spin-down channel spectra mainly spreads along E_f, the flat yz band along X-Γ path is basically broadened due to the imaginary part of self-energy $Im\Sigma(\omega)$. Close to E_f the band broadening effect is tiny, this indicates a local minimum of $Im\Sigma(\omega)$ around E_f. Compared with original DFT bands [Fig. 3.5(a)], the spin-up channel spectra shrinks from the DFT bandwidth ~3.20 eV to DMFT ~2.75 eV (decreased by ~14%). To better understand the features in k-resolved spectral functions $A(k,\omega)$, we plot the real-frequency self-energy $\Sigma(\omega)$ for cubic SRO at 100 K and 200 K, as shown in Fig. 3.6.

We first focus on the 100 K results [Fig. 3.6(a)-(b)]: the spin-up channel (majority) real part self-energy $Re\Sigma(\omega)$ is always ~0.5 eV lower than the spin-down channel (minority) at any ω, this explains the spin-splitting and ferromagnetism in SRO at 100 K. For the imaginary part $Im\Sigma(\omega)$, both spin-up and spin-down channels basically show the same Fermi liquid behavior: the $Im\Sigma(\omega)$ has local minimum at E_f,
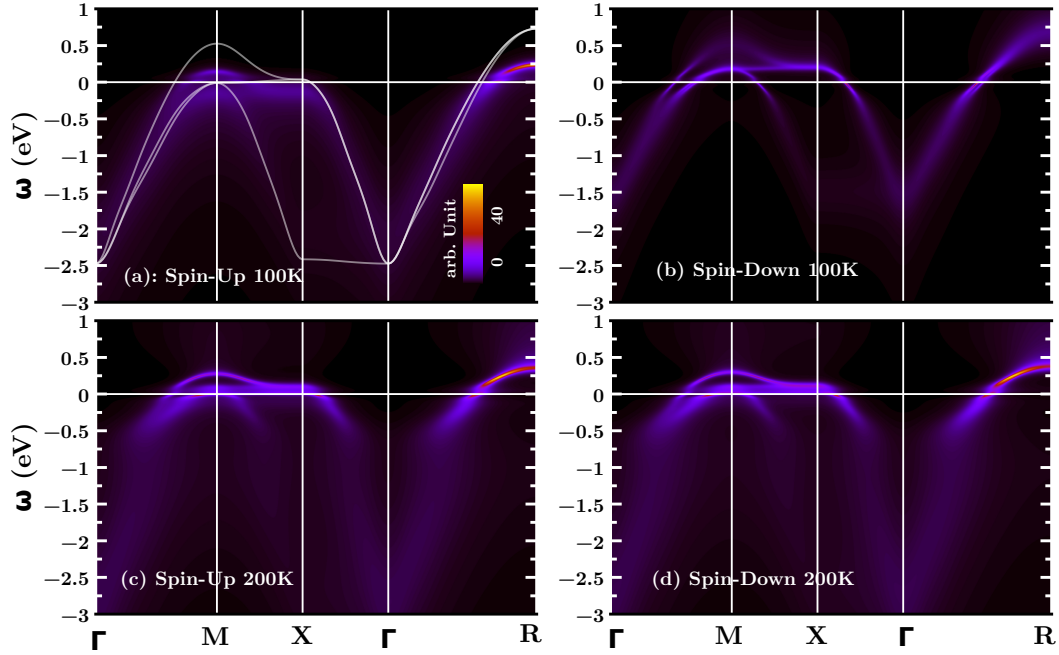
FIGURE 3.5: Spin-polarized DMFT spectral functions $A(k,\omega)$ at 100 K (a,b) and 200 K (c,d) for cubic SRO. For different $A(k,\omega)$ the maximum spectra weight corresponds to different values, for (a), (b), (c) and (d) they are 40, 80, 18 and 18.
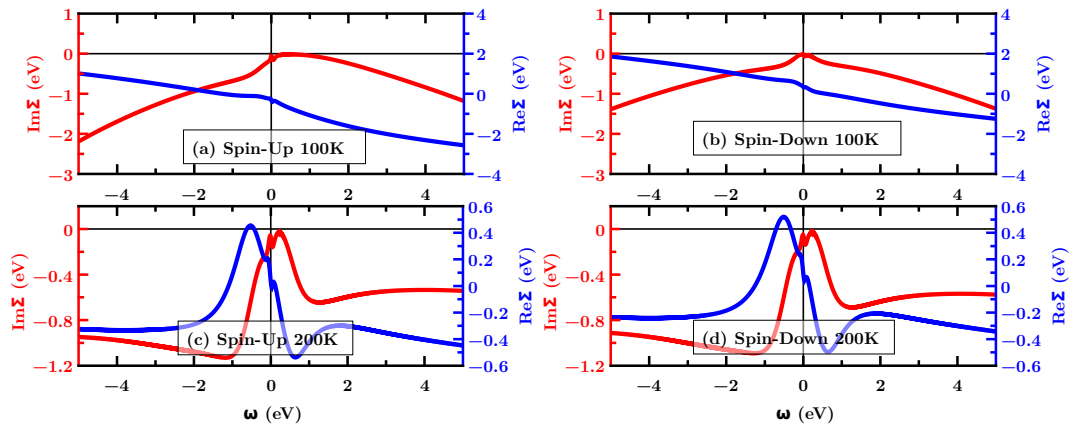

FIGURE 3.6: Spin-polarized DMFT real-frequency self-energy $\Sigma(\omega)$ at 100 K (a,b) and 200 K (c,d) for cubic SRO.

contributing to the quasi-particle peak around -0.5 eV to 0.5 eV. In Fig. 3.5 the spectra $A(k,\omega)$ around E_f only reduce the DFT bandwidth (enhance its effective mass): the broadening effect around E_f is tiny, however high-energy part (from -3 eV to -1 eV) is seriously broadened. Please note that our DMFT resulted $Re\Sigma(\omega)$ converges to a constant only beyond the interval of Fig. 3.6. For a clear observation of the Fermi liquid behavior we show a small frequency region around E_f.

Cubic SRO exhibits a paramagnetic metallic state at 200 K [Fig. 3.6(c)-(d)]. Thus we expect both the $Re\Sigma(\omega)$ and $Im\Sigma(\omega)$ to behave similarly. $Re\Sigma(\omega)$ is symmetric around E_f, it is positive when ω decreases from 0 eV and becomes negative when ω increases from 0 eV, this behavior shrinks the DFT bands near E_f and results in the quasi-particle peak. This bands shrink/reduction is shown in Fig. 3.5(c)-(d): the

$A(k,\omega)$ at 200 K from -0.5 eV to 0.5 eV shows a clear DFT band character, together with a bandwidth reduction (effective mass renormalization). From -3.0 eV to -0.5 eV, $A(k,\omega)$ is seriously broadened due to the large negative $Im\Sigma(\omega)$ from -1.0 eV and lower, it also indicates that the electronic correlation effects at higher temperature are stronger. At 200 K $Re\Sigma(\omega)$ converges faster than at 100 K, approaching -0.4 eV when $\omega > 4.0$ eV and < -4.0 eV. This demonstrates that the modifications of dynamical correlation effects at high temperature contribute to a rather smaller energetic region than those at lower temperature cases. To estimate the degree of correlation in cubic SRO, we calculate the Z factor for different spin channels at both 100 K and 200 K. The Z factor is 0.69 and 0.50 (0.51 and 0.51) from spin-up and spin-down channels at 100 K (200 K). The renormalized factor Z are obtained from such formula: $m^*/m_e = 1/Z = 1 - \frac{\partial}{\partial\omega} Re\Sigma(\omega + i0^+)|_{\omega=0}$ (m_e is DFT band effective mass and m^* is the quasi-particle effective mass). This value is in good agreement with the literature data (Grånäs et al., 2014) indicates that $m^*/m_e \approx 2$, demonstrating that electronic correlations in SRO are strong.
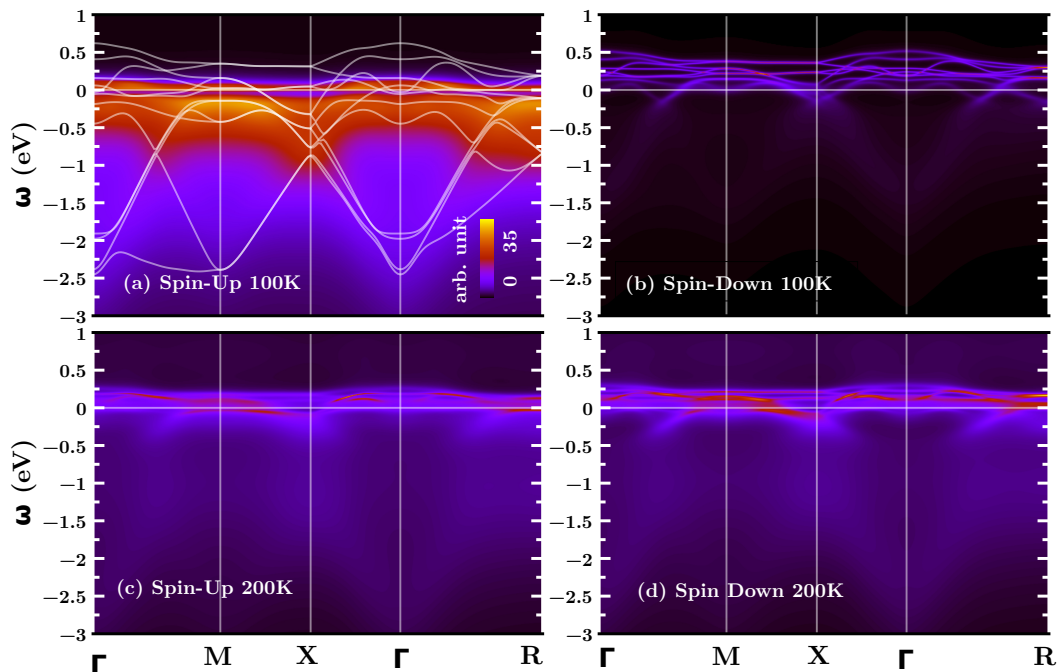

FIGURE 3.7: Spin-polarized DMFT spectral functions $A(k,\omega)$ at 100 K (a,b) and 200 K (c,d) for orthorhombic SRO. For different $A(k,\omega)$ the maximal spectra corresponds to different values, for (a), (b), (c) and (d) they are 35, 80, 25 and 25.

The $A(k,\omega)$ of the orthorhombic SRO is shown in Fig. 3.7(a)-(d). Compared with the cubic one, there are four Ru sites in the orthorhombic cell. Thus the number of bands are fourfold: altogether twelve t_{2g} bands are obtained. Rotation and tilting of RuO₆ octahedra suppress Ru-d and O-p hybridization, leading to a reduced bandwidth of the orthorhombic phase, from 3.20 eV to 3.08 eV. Because the rotation and tilting of RuO₆ octahedra reduces the Ru-O-Ru bond angle, it reduces the orbital overlap and d-p hybridization.

Calculation details. Compared with cubic phase SRO, the DFT calculations of orthorhombic SRO has to be carried out with a $\sqrt{2}\times\sqrt{2}\times2$ unit cell because of the RuO₆

rotation/tilting. This increases the number of t_{2g} bands and changes the definition of Brillouin zone. For simplification, we do not change the k-path for band plotting in Fig. 3.7. However, the reader has to note in Fig. 3.7 that the high-symmetry k points $X(0.5, 0, 0)$ and $M(0.5, 0.5, 0)$ are already different k-points compared to Fig. 3.2 and Fig. 3.5.

The general behavior of $A(k,\omega)$ of orthorhombic SRO is comparable with the cubic ones. For example, at $100\,\mathrm{K}$ the spin-up (majority) channel $A(k,\omega)$ is quite broadened in the whole energy region from $-3.0\,\mathrm{eV}$ to $0.0\,\mathrm{eV}$, and $A(k,\omega)$ as a whole is shifted downside by a Hartree-like constant $\sim 0.5\,\mathrm{eV}$. The coherent spectra around E_f induces a quasi-particle peak around $-0.3\,\mathrm{eV}$, as shown in Fig. 3.4(b). For the spin-down (minority) channel the band broadening effect is quite tiny, as related to the local minimum of $Im\Sigma(\omega)$ at $\omega=0\,\mathrm{eV}$. Because both $Re\Sigma(\omega)$ and $Im\Sigma(\omega)$ of orthorhombic SRO have basically the same behavior as in the cubic phase, we do not show them here. The different between $Re\Sigma_\sigma(\omega)$ and $Re\Sigma_{\sigma'}(\omega)$ splits spin-up and spin-down channels at $100\,\mathrm{K}$. At $200\,\mathrm{K}$, the orthorhombic SRO behaviors as a paramagnetic metal (Fig. 3.4 and Fig. 3.7).

3.2   Magnetic Anisotropy Energy in SrRuO$_3$

In **Chapter 2.6** we introduced the method to derive the full TB Hamiltonian for t_{2g} orbitals of ABO_3 perovskites. In this section we employ the TB Hamiltonian method to derive the band structures of the cubic SRO; then we calculate the magnetic anisotropy energy.

Here, to simplify our TB model, we only include electron hopping terms t_{mn} (m and n label orbitals) up to second nearest neighbors [e.g. for d_{yz} orbital it up to $\boldsymbol{R}(0,1,1)$]. The TB bands of SRO are shown in Fig. 3.8. Without ferromagnetism and SOC effect [Fig. 3.8(a)], three t_{2g} are observed: d_{yz}, d_{xz} and d_{xy} (for the detailed analysis of bands see **Chapter 3.1**). The band behavior of DFT [Fig. 3.2(a)] are successfully reproduced by only three hopping terms. One can note that the bandwidth now is ~2.8 eV, seriously smaller than in DFT: 3.2 eV. This is because most long-range hoppings are cut-off, leading to the bandwidth reduction. After turning on SOC [Fig. 3.8(b)] (SOC parameter α=140 meV), the bands split at the Γ point: one band [mostly from d_{xy} with quantization axis (001)] shifts up. However at this point no spin-splitting happens because the spin-up and spin-down channels are still energetically degenerate.

The spin-splitting is turned on by setting a nonzero Zeeman splitting which corresponds to a ferromagentic magnetism on the Hatree level (as discussed in **Chapter 2.6**). In [Fig. 3.8(c)] six t_{2g} bands are there due to the spin-splitting. The amplitude of Zeeman splitting is set as 0.6 eV. In the presence of both ferromagnetism and SOC, a further splitting happens and no orbital degeneracy is present [Fig. 3.8(d)].
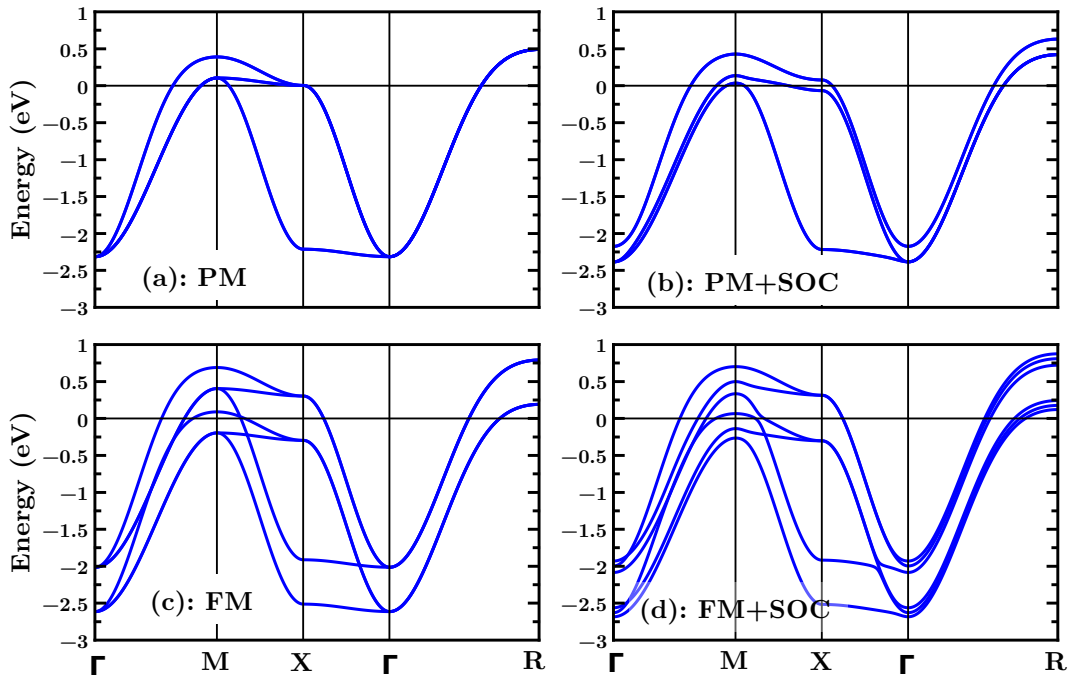

FIGURE 3.8: Tight-binding band structures of cubic SRO: (a) paramagnetic without SOC, (b) paramagnetic with SOC, (c) ferromagnetic without SOC and (d) ferromagnetic with SOC.

To calculate the magnetic anisotropy energy of SRO, we need to determine two parameters: the SOC strength α and the Zeeman splitting B. Here α is chosen as 140 meV as discussed in **Chapter 2.6**, by calculating the SOC splitting at the Γ point. However this approximation does not work for B, because it is a k-dependent quantity. At the Γ point the splitting between spin-up and spin-down channels is about 0.50 eV while at the M point it can be 0.96 eV. Here, to demonstrate that the magnetic properties of SRO are rather complicated, we change B from 0.1 eV (corresponding to weak ferromagnetism with a tiny ferromagnetic moment) to 1.0 eV (corresponding to a half-metallic ferromagnet with a moment of $2\,\mu_B/$Ru). In the process we find an intrinsic transition of the quantization axis (easy-axis) from (111) to (001), as shown in Fig. 3.9.

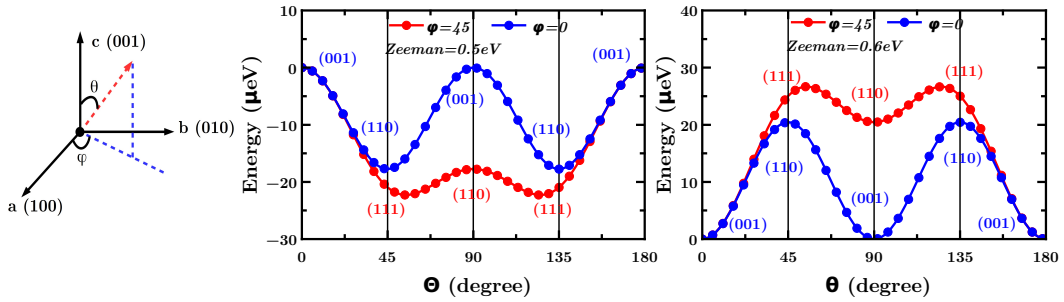FIGURE 3.9: Middle and right panels: magnetic anisotropy energy results for cubic SRO for different Zeeman splittings (B=0.5 eV and 0.6 eV). The definition of the Euler-angle ϕ and θ is shown in the left panel.

As shown in the left panel of Fig. 3.9, in our TB method, we define Euler-angle θ and ϕ as functional variables. In the middle and right panels of Fig. 3.9 we change θ from 0° to 180° and keep ϕ=0° and 45°. When the Zeeman splitting is 0.5 eV, the overall minimum of total energy is located at ϕ=45° and θ=54°, this corresponds to the (111)-quantization axis. However when the Zeenman splitting is 0.6 eV, the minimum of total energy is located at ϕ=0° and θ=0°, corresponding to the (001)-quantization axis. This conclusion is consistent with the experiments (Klein et al., 1996) in which at low temperatures the out-of-plane magnetism dominates, whereas the in-plane magnetism prevails at high temperatures.

The energy scale of the MAE of a single cell is of the order of μeV/cell. Another possible way to investigate the MAE is adopting a supercell to carry out spin-polarized DFT calculations. In the presence of SOC, however, this is very time consuming. To achieve the energy difference that safely exceeds the DFT accuracy ($\sim$1 meV), one need 1 meV/(30 μeV per cell)=333 unit cells. That is approximately corresponding to 7×7×7 supercell (1715 atoms), which is absolutely beyond the capability of DFT and current computers. The TB method we employed, is a very simplified/effective method. For systems with localized orbitals, it can be simplified by including only a few major electron hoppings, whereas long-range hoppings are not included. Only the atomic SOC effect is adopted and most importantly, no genuine correlations effects are included. Thus it is a very big approximation. The most advanced and promising method regrading the calculation of MAE in ferromagnetic systems will be DMFT+SOC. However this project is still under construction by a joint project between our group (CMS, IFP, TU Wien) and the group leaded by Prof. Masatoshi Imada at the University of Tokyo. In this project we will combine the advantages of TB and DMFT methods in the presence of atomic SOC to investigate MAE in bulk SRO.

3.3   SrRuO$_3$ (001)-oriented Thin Films

In this part we will investigate the electronic and magnetic properties of SrRuO$_3$ (001)-oriented thin films and we propose a way to realize room-T_C ferromagnetic states in SRO (001) thin films. Experimental efforts to stabilize ferromagnetism in ultrathin films of transition metal oxides have so far failed, despite expectations based on density functional theory (DFT) and DFT+U. We investigate one of the most promising materials, SRO, and include correlation effects beyond DFT by means of dynamical mean field theory. In agreement with experiment we find an intrinsic thickness limitation for metallic ferromagnetism in SRO thin films. Indeed, we demonstrate that the realization of ultrathin ferromagnetic films is out of reach of standard thin-film techniques. Proposing charge carrier doping as a new route to manipulate thin films, we predict room temperature ferromagnetism in electron-doped SRO ultra thin films.

Story so far. Thin films and heterostructures of the 4d perovskite SrRuO$_3$ (SRO) are intensively studied and used, in particular, as gate electrodes for novel oxide-based electronic devices (Junquera and Ghosez, 2003; Stengel and Spaldin, 2006). The reason for this is that SRO is a conductor with good thermal properties (Lee et al., 2004) and high chemical stability, allowing for epitaxial growth on various substrates, as well as the combining with other perovskite-based materials to form complex heterostructures (Eom et al., 1992; Koster et al., 2012). In the bulk, SRO is a ferromagnetic (FM) metal with a, for a 4d oxide, remarkably high Curie temperature, T_C =160 K, and an experimental magnetic moment in the range of 0.8 to 1.6 μ_B (Kiyama et al., 1996; Cao et al., 1997; Allen et al., 1996; Felner, Nomura, and Nowik, 2006). SRO further attracted fundamental research interests regarding, among others, magnetic monopoles (Fang et al., 2003), non-Fermi liquid (Laad and Müller-Hartmann, 2001), spin freezing (Werner et al., 2008), and the debate of itinerant (Jeong et al., 2013) versus localized magnetism (Shai et al., 2013).

However, the FM moment and Curie temperature get dramatically suppressed below a sample thickness of 4 unit cells (Toyota et al., 2005; Toyota et al., 2006; Xia et al., 2009; Chang et al., 2009), and eventually single unit cell SRO films turn antiferromagnetic (AF) and insulating (Xia et al., 2009; Chang et al., 2009). This led to the pertinent question whether there is a fundamental thickness limit for ferromagnetism (Chang et al., 2009), and concerted efforts to stabilize ferromagnetism in ultrathin SRO films by compressive and tensile strain or capping layers (Verissimo-Alves, M. et al., 2012; Gupta, Mandal, and Mahadevan, 2014). However, hitherto ferromagnetism in single unit cell thick films remains unattainable for SRO or any other oxide material, even in a heterostructured setup.

On the theoretical side, previous attempts to understand the electronic structure and the transition to an AF insulator resorted to density functional theory (DFT) and the static mean-field DFT+U approach. The former failed to reproduce the transition (Rondinelli et al., 2008), while the latter found a transition to an AF insulating state below four layers when assuming an artificial RuO$_2$ terminated surface (Mahadevan et al., 2009), while experimentally samples are found

to have a SrO termination (Koster et al., 2012). DFT+U further predicted a spin-polarized highly confined half-metallic state for an SRO mono-layer when either sandwiched with SrTiO$_3$ (STO) (Verissimo-Alves, M. et al., 2012) or grown on a strained STO substrate (Gupta, Mandal, and Mahadevan, 2014). However, such a state could not be confirmed in experiment (Bern et al., 2013). The apparent discrepancy between experiments and results from standard band-structure methods calls for a more sophisticated treatment of electronic correlation effects. Indeed already in the bulk, SRO displays signatures of electronic correlations, such as many-body satellites in photoemission or the violation of the Ioffe-Regel limit in the resistivity (Allen et al., 1996; Emery and Kivelson, 1995). Hence, SRO is to be considered an –at least– moderately correlated system. Note that a dimensional reduction/geometric constraints in thin films can be expected to further enhance electronic correlations.

For a better and unbiased treatment of these correlations effects in various SRO films and heterostructure setups, we employ realistic DFT + dynamical mean-field theory (DMFT) (Georges et al., 1996; Kotliar and Vollhardt, 2004; Held, 2007; Anisimov, Aryasetiawan, and Lichtenstein, 1997; Kotliar et al., 2006) calculations. Our main findings are: (1) Both the SRO mono-layer and bi-layer are AF insulators. (2) We demonstrate that standard thin film manipulation techniques such as strain and surface capping can neither restore ferromagnetism nor metallicity to a SRO mono-layer; interestingly, we find that surface capping pushes the AF insulator towards a paramagnetic (PM) insulator. (3) With new insight regarding the microscopic origin for the transition, we identify carrier doping as the best option to generate FM properties that are on a par with those of the bulk. We find the FM moments of doped SRO films to be stable even at room temperature, heralding a great potential for technological applications.

Calculation details We use the experimental orthorhombic crystal structure of SRO (Jones et al., 1989) for the various setups of bulk, films and heterostructures. In the films and heterostructure both the internal positions and lattice constant are relaxed; the in-plane lattice constants in films are fixed to an DFT optimized value, 3.95 Å, of STO. Fig. 3.10 exemplary shows the SRO mono-layer grown on 4 layers of STO substrate. The atomic relaxations are carried out with the VASP program package (Kresse and Hafner, 1993; Kresse and Furthmüller, 1996) using the PBE functional (Perdew, Burke, and Ernzerhof, 1996). For the optimized atomic positions, we subsequently perform WIEN2K (Blaha et al., 2001) electronic structure calculations with the mBJ exchange (Tran and Blaha, 2009) and PBE correlation functional [as detailed in the Supplemental Material (Si et al., 2015), the exchange included in mBJ does not notably affect the t_{2g} bandwidth, but it improves on the inter-orbital separation for states not included in the DMFT. It is in this sense a poor man's version of QSGW+DMFT (Tomczak, 2015)], and a Wannier function projection onto maximally localized (Marzari et al., 2012) t_{2g} Wannier orbitals (Mostofi et al., 2008) using the Wien2Wannier program package (Kuneš et al., 2010). This t_{2g} Hamiltonian is supplemented by a local Kanamori interaction and solved within DMFT using W2Dynamics (Parragh et al., 2012), employing a hybridization expansion continuous-time quantum Monte Carlo (CTQMC) algorithm (Gull et al., 2011). For the Coulomb interaction strengths, we adopt a Hund's exchange (J=0.3 eV), intra- (U=3.0 eV) and inter-orbital Coulomb repulsion (U'=2.4 eV). These values consistently yield a FM metallic state for orthorhombic bulk SRO. Performing constrained random phase approximation (cRPA) calculations (Aryasetiawan et al., 2004; Miyake and Aryasetiawan, 2008), for a free-standing cubic SRO mono-layer, we find the only sightly enhanced value U=3.5 eV, while J=0.3 eV and U'=2.9 eV, compared with SRO bulk values U=2.3 eV, while J=0.3 eV and U'=1.7 eV.

Bulk SrRuO₃. The moderately correlated electronic structure of *bulk* SRO was successfully captured in both many-body perturbation theory (Hadipour and Akhavan, 2011) and realistic DMFT calculations (Jakobi et al., 2011; Grånäs et al., 2014; Kim and Min, 2015; Dang et al., 2015; Deng, Haule, and Kotliar, 2016). Also, DFT calculations correctly predict that SRO is an itinerant ferromagnet with a moment ranging from 1.5 to 1.6 μ_B (Allen et al., 1996; Singh, 1996); similar moments have also been obtained within DFT+DMFT (Grånäs et al., 2014; Kim and Min, 2015).

Using DFT+DMFT, we indeed find orthorhombic bulk SRO to be a FM metal with orbital occupations of 0.908 (0.447), 0.866 (0.449), 0.881 (0.449) for the majority (minority) spin of xy, yz, xz orbitals at T=100K. This corresponds to a total FM magnetic moment of $1.31\mu_B$. A GdFeO₃-type distortion in which the corner-sharing octahedral tilt around the y-axis and rotate around the z-axis lifts, in principle, the t_{2g} degeneracy. The effect on the crystal field and orbital occupations of orthorhombic SRO is however minute. Our DFT+DMFT finds SRO to be a PM metal above $T_C \sim 160$ K which is in excellent agreement with the experimental Curie temperature of 160 K (cf. Fig. 3.14 below).
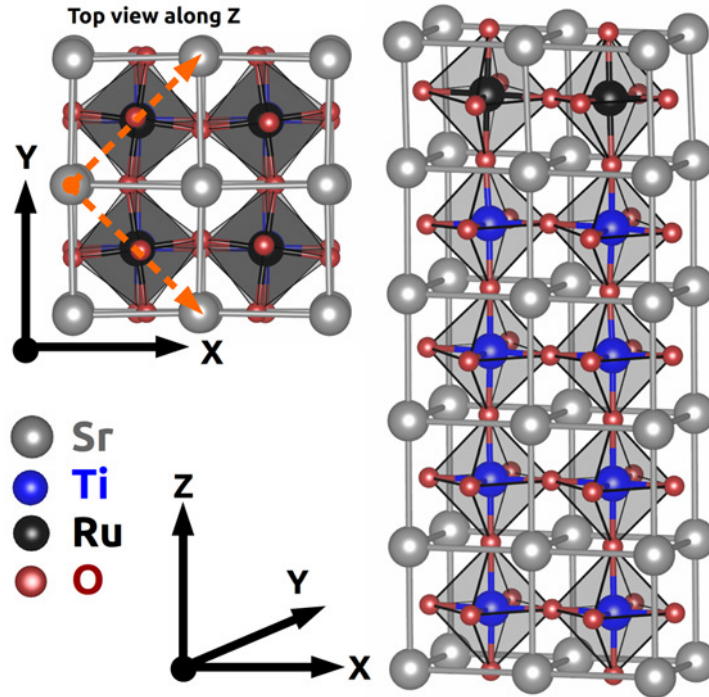
FIGURE 3.10: Right: Structure of a SRO mono-layer grown on 4-layers of STO. Upper left: Top view of the same structure. The indicated $\sqrt{2} \times \sqrt{2}$ supercell was adopted for allowing AF-ordering in each RuO₂ layer. Lower left: atomic labels and coordinate system [Figures drawn with the Vesta code (Momma and Izumi, 2011)].
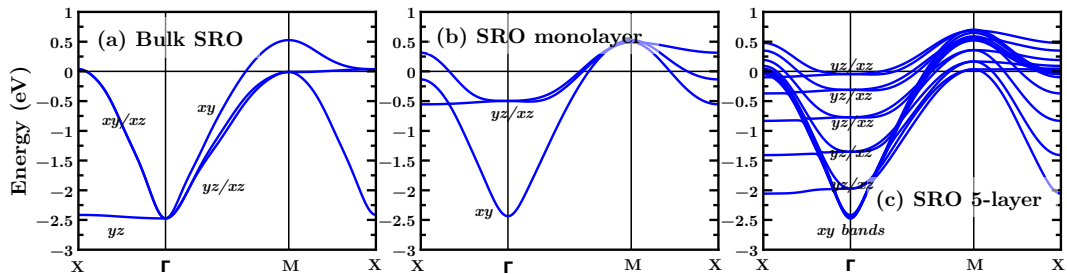

FIGURE 3.11: Tight-binding band structure of cubic bulk SRO (a), a SRO monolayer (b) and 5-layers of SRO (c).

Thin films. We now consider SRO grown on STO, and study the evolution of the electronic structure when reducing the number of SRO layers. Before starting to analyze the DFT+DMFT results, we firstly focus on a very fundamental question: how the heterostructuring/filming modifies the electronic structures of SRO thin films compared to the bulk SRO? In general one can expect that this type of heterostructuring/filming will induce similar modifications to the electronic structures of general ABO_3 bulk materials and this fundamental question will absolutely deep our understanding about SRO (001)-oriented films. To answer this question we perform nonmagnetic DFT calculations to obtain band structures of bulk SRO, monolayer and 5-layer SRO films (here for simplification we take free-standing thin films instead of films with STO substrates), then we project DFT orbitals onto Wannier orbitals and obtain tight-binding bands as shown in Fig. 3.11.

By comparing the bands of cubic bulk SRO Fig. 3.11(a) and SRO monolayer Fig. 3.11(b), we conclude that the xy band dispersion basically does not change and keep its bulk behavior. This is because surfacial cutting-off of SRO will cut off all the electronic hopping along z-axis while the xy orbital is mainly hopping along x-y plane (see Table. 2.1), thus the xy band dispersion is basically same as the bulk one. However the yz and xy bands have two main differences comparing with their bulk states: the first difference is that these two bands dramatically shrink (comparing with their bulk bandwidth 3.2 eV now their bandwidth are only 1.0 eV), the second difference is that their band center now is shifted higher in energy, e.g. the energy of Γ point is shifted from -2.5 eV to -0.5 eV. Two effects govern this behavior. Firstly, compared with their bulk values the on-site electronic hopping terms $\langle yz(0)|H|yz(0)\rangle$ and $\langle xz(0)|H|xz(0)\rangle$ increase, because the surface orbital potential is always higher than that of the bulk part. Secondly, cutting-off the hopping along z-direction also pushes the energy of Γ point to higher values.

Another question is that: what will happen if we increase the thickness of SRO thin films? How does the electronic structure gradually recover its bulk state by increasing its film thickness? To answer this question one can see the Fig. 3.11(c), which shows the tight-binding bands of 5-layers SRO films. As one can see that as increasing the thickness of SRO layers, the xy bands basically keep their bulk behaviors, the bandwidth of all five xy bands are $\sim$3.0 eV and between each xy bands there is only a constant shift (e.g. at Γ point), this is the "quantum well state" phenomena (Yoshimatsu et al., 2010; Meevasana et al., 2011; Yoshimatsu et al., 2011; Kobayashi et al., 2015) which has been experimentally observed in e.g. SrTiO₃ and SrVO₃ (001)-oriented films. For yz/xz bands, the "quantum well" states phenomenon is much more clear: 5 groups of yz/xz bands are separated with each others by a constant shift which appropriately equals to 0.5 eV. These conclusions indicate that with increasing the thickness of films, the yz/xz bands will gradually recover their bulk band dispersions and bandwidth while the change of xy bands are quite tiny.

After this qualitative understanding of the electronic structures of thin films of SRO, we start analyzing DMFT results. We find that FM is suppressed: the mono- and bi-layer SRO on STO are AF insulators, in agreement with experiments (Bern et al., 2013; Chang et al., 2009) that show a dramatic drop in the FM moment and an insulating behavior for 4-layers or lower (Toyota et al., 2005; Toyota et al., 2006; Xia et al., 2009; Bern et al., 2013; Chang et al., 2009). Recent experiments (Ishigami et al., 2015) confirm the non-ferromagnetic and insulating state in bi-layer SRO, and yield photoemission spectra in good agreement with our theoretical results [see supplementary materials of Ref. (Si et al., 2015)]. Indicative of an itinerant origin of ferromagnetism, the critical thickness of the magnetic and electronic transition coincide. Trilayer SRO films exhibit as ferromagnetic metal with weaker FM moment of 0.41 μ_B/Ru (compared with bulk 1.31 μ_B/Ru) [Fig. 3.13(a)]. Fig. 3.12(a)-(b) shows the spectral function of the mono-layer and bi-layers SRO at 150 K. Both systems are gapped by $\sim$1.0 eV and displays a large orbital polarization: the xy orbital is fully filled, and the xy and xz orbitals are half-filled and fully spin-polarized, resulting in an AF moment of $\sim$2 μ_B. This finding is supported by recent exchange bias measurements (Xia et al., 2009), for a summary see Table. 3.1.
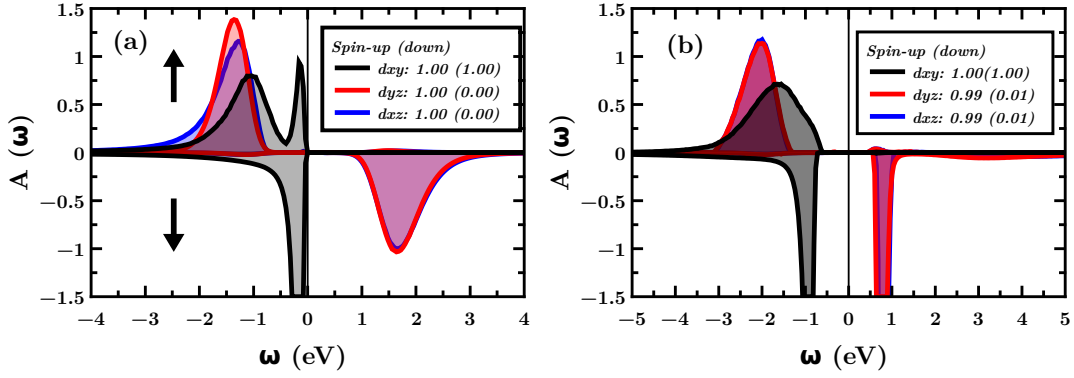
FIGURE 3.12: DFT+DMFT spectral functions of (a) the AF SRO mono-layer on a STO substrate and (b) the AFM bi-layers at 150 K. The labels give the electronic occupations of the three t_{2g} orbitals.

Note the reduction of bandwidth in Fig. 3.12(a)-(b) due to the antiferromagnetic ordering: as discussed in (Sangiovanni et al., 2006) for the one-band case, a hole moving in an antiferromagnetic background breaks antiferromagnetic bonds so that the hopping is suppressed and the so-called spin-polaron bands have a reduced bandwidth. For the almost fully filled d_{xy} band the situation is slightly more complicated and spin-dependent: if we add a hole to the majority spin band it can move freely, we even gain Hund's exchange energy if this hole moves to the next site with opposite spin polarization (since on the next site the hole removes an electron in the minority band with opposite spin to the d_{xz}/d_{yz} spin). Therefore the majority-spin d_{xy} band in Fig. 3.12 has a large bandwidth. If we have the hole in the minority band on the other hand, it instead costs the Hund's exchange energy to move it to the next site. It gets localized; the minority d_{xy} band in Fig. 3.12 has a small bandwidth.
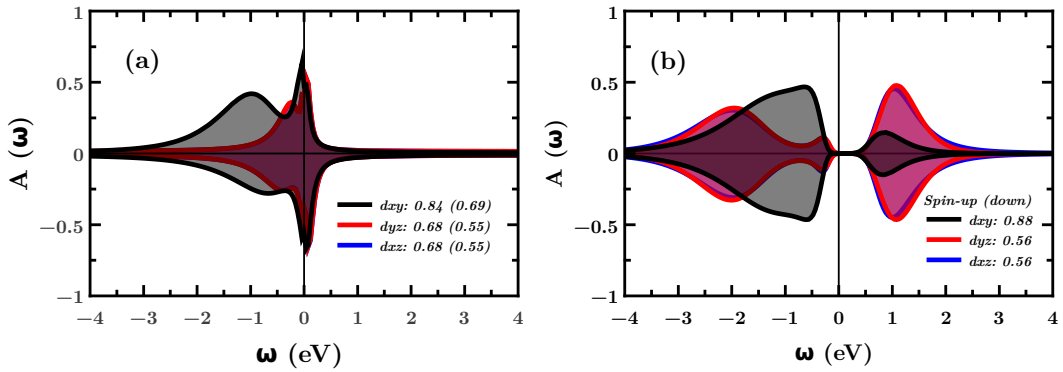

FIGURE 3.13: DFT+DMFT spectral functions of (a) the FM SRO tri-layer on a STO substrate at 150 K and (b) the AF mono-layers at 1000 K. The labels give the electronic occupations of the three t_{2g} orbitals.

We note that for the particular case of the SRO mono-layer, also LDA+U (Gupta, Mandal, and Mahadevan, 2014) can seemingly give a qualitatively correct picture, as the system is orbitally and spin-polarized. However, the underlying physics is very different: When heating the mono-layer above its Néel temperature within DMFT, the system remains insulating at non-integer filling [0.88

(0.88), 0.56 (0.56), and 0.56 (0.56) for the spin up (down) xy, yz and xz orbitals at 1000 K, Fig. 3.13(b)]. This complex Mott physics (Poteryaev et al., 2008) reveals that the AF insulating phase is beyond a simple Slater description, and thus not describable by LDA+U.

Physical origin of transition. Let us now investigate the microscopic origin of the FM-metal to AF-insulator transition. Whereas the crystal field splitting is minute for the bulk, in the SRO mono-layer the xy-orbital is energetically lower than the yz and xz orbitals, because the surface breaks the crystal symmetry in the z-direction (besides the bulk-like orthorhombic distortion in SRO layer, the surface relaxation causes surface-O to move away from the topmost RuO₂ layer, while surface-Sr move toward it). This is already the case for the DFT Wannier Hamiltonian, but correlation effects boost the crystal field splitting (Keller et al., 2004; Poteryaev et al., 2007; Poteryaev et al., 2008) of the SRO mono-layer (see Table. 3.2). Therewith, the xy-orbital become essentially fully occupied, and the two remaining electrons occupy the yz and xz orbitals: The single-layer SRO is an effective half-filled two-band system, being favorable to AF order.

Tuning the properties of the SRO mono-layer. The prime motivation for SRO-based thin films are the advantageous properties of the FM metallic *bulk*. However, the desired features, such as the magnetic moment strongly decrease for thinner films and eventually ultrathin films become non-FM, in agreement with our calculations. A natural question is whether the bulk properties can be restored, at least partially, by tuning the geometry of the films.

First we discuss the influence of straining/tensioning the mono-layer. This can be realized experimentally by choosing an appropriate substrate. Indeed, previous DFT+U calculations (Gupta, Mandal, and Mahadevan, 2014) predicted a strain-induced FM half-metallic state for the SRO mono-layer. DFT+DMFT, however, does not show any such tendency, at least for realistic U values, see Table. 3.3. Also, the effective crystal-field splitting Δ_{eff} (Table. 3.2), can only be tuned slightly through straining/tensioning.

Another way to influence the crystal-field splitting is through the deployment of capping layers. Here, we study the effect of capping the SRO mono-layer with additional layers of STO. Specifically, we consider a (STO)₅:(SRO)₁ superlattice (Verissimo-Alves, M. et al., 2012) consisting of 5 layers of STO alternating with a mono-layer of SRO. This restores, at least partially, the hopping amplitudes in the out-of-plane direction. Compared to the SRO mono-layer, the DFT crystal field splitting, shown in Table. 3.2, is now much smaller (-0.05 eV) approaching the negligible value of the bulk. As a result, the t_{2g} orbital occupations are more balanced. However, this causes only a slight reduction of the AF magnetic moment [$1.92 \mu_B$ at 150 K and $1.48 \mu_B$ at 300 K, cf. Fig. 3.14(b)] with respect to the un-capped mono-layer [for DMFT spectral functions of (STO)₅:(SRO)₁ superlattice at 150 K see Fig. 3.16(a)]. Our finding of a non-FM insulating state with a gap of $\sim$1.0 eV for the capped mono-layer is consistent with experiments (Tian et al., 2007; Bern et al., 2013), where it was concluded that SRO capped by STO leads to an insulator without a net moment. We note that previous DFT+U calculations (Verissimo-Alves, M. et al., 2012) instead predicted a FM half-metal, at variance with experiment.

Recently, C. R. Hughes *et al.* (Hughes et al., 2016) proposed that (STO)₅:(SRO)₁ superlattice is of conductivity down to 50 mK, and behaviors as a ferromagnetic state

TABLE 3.1: Magnetic and conductive states of bulk SRO, SRO mono-layer (also under 0.5% compression and 0.5% tension), SRO bi-layers, SRO tri-layer and (STO)$_5$:(SRO)$_1$ superlattice (capped mono-layer), as obtained from spin-polarized DFT and DFT+DMFT calculations in comparison with experiment. FM-M: ferromagnetic metal, AF-I: antiferromagnetic insulator; NM-I: non-ferromagnetic insulator [the magnetic nature of the experimental non-ferromagnetic state has not been fully determined yet, the exchange bias behavior hints at antiferromagnetism (Xia et al., 2009)].

System	DFT	DMFT	EXP
bulk	FM-M	FM-M	FM-M (Kiyama et al., 1996)
mono-layer 100.5%	FM-M	AF-I	—
mono-layer 100%	FM-M	AF-I	NM-I (Xia et al., 2009)
mono-layer 99.5%	FM-M	AF-I	—
bi-layer	FM-M	AF-I	NM-I (Toyota et al., 2005; Ishigami et al., 2015)
tri-layer	FM-M	FM-M	FM-M (Chang et al., 2009)
superlattice	FM-M	AF-I	NM-I (Bern et al., 2013)
hole doped superlattice	FM-M	FM-M	—
electrons doped superlattice	FM-M	FM-M	—

TABLE 3.2: Paramagnetic DFT crystal field splitting defined as the local potential difference of the Wannier orbitals (eV), $\Delta_{\text{DFT}}(i,j) = \langle j|H|j\rangle - \langle i|H|i\rangle$, and correlation enhances effective splittings, $\Delta_{eff}(i\sigma, j\sigma') = \Delta_{PM-DFT}(i,j) + [Re\Sigma_{i\sigma}(0) - Re\Sigma_{j\sigma'}(0)]$ for $i,j \in \{xy, yz, xz\}$ and $\sigma, \sigma' \in \{\uparrow, \downarrow\}$. For the AF phase $Re\Sigma(0)$ and Δ_{eff} of the second Ru atom are shown in brackets.

System	bulk	bi-layer bottom	bi-layer top	tensioned 100.5%	monolayer 100%	compressed 99.5%	capped mono-layer
DFT t_{2g} bandwidth	~3.20	~2.70		~2.30	~2.60	~2.60	~2.60
$\Delta_{\text{DFT}}(xy, yz/xz)$	~0.00	−0.06	−0.17	−0.35	−0.25	−0.22	−0.05
$Re\Sigma_{xy\uparrow}(0)$	8.06	7.32	7.31	6.62	6.63	6.64	7.19
$Re\Sigma_{xy\downarrow}(0)$	8.81	7.86	7.88	7.42	7.43	7.44	7.81
$Re\Sigma_{yz/xz\uparrow}(0)$	8.07	6.84	6.76	5.83	5.86	5.87	6.81
$Re\Sigma_{yz/xz\downarrow}(0)$	8.81	9.62	9.68	9.13	9.09	9.08	11.18
$\Delta_{eff}(xy\uparrow, xy\downarrow)$	−0.75	−0.54	−0.57	−0.80(0.80)	−0.80(0.80)	−0.80(0.80)	−0.62(0.62)
$\Delta_{eff}(xy\uparrow, yz/xz\uparrow)$	−0.01	0.42	0.38	0.44(−2.06)	0.52(−1.91)	0.55(−1.86)	0.33(−3.42)
$\Delta_{eff}(xy\uparrow, yz/xz\downarrow)$	−0.75	−2.36	−2.54	−2.86(1.24)	−2.71(1.32)	−2.66(1.35)	−4.04(0.95)

TABLE 3.3: Magnetic and conductive states of bulk SRO, SRO mono-layer (also under 0.5% compression and 0.5% tension), SRO bi-layers and (STO)$_5$:(SRO)$_1$ superlattice (capped mono-layer), as obtained from spin-polarized DFT (SP-DFT) and DFT+DMFT calculations at different U values around the expected value of $U \sim 3$ eV. The last column shows the experimental results for comparison (NM: non ferromagnetic).

System	SP-DFT	U=2.0 eV	2.5 eV	3.0 eV	4.0 eV	Exp
bulk	FM metal	FM metal	FM metal	FM metal	PM insulator	FM metal Ref.[1]
mono-layer 100.5%	FM metal	AF insulator	AF insulator	AF insulator	AF insulator	-
mono-layer 100%	FM metal	FM metal	AF insulator	AF insulator	AF insulator	AF insulator Ref.[2]
mono-layer 99.5%	FM metal	FM metal	AF insulator	AF insulator	AF insulator	-
bi-layer	FM metal	FM metal	AF insulator	AF insulator	AF insulator	NM insulator Ref.[3,4]
capped mono-layer	FM metal	FM metal	FM metal	AF insulator	AF insulator	NM insulator Ref.[5]

Ref.[1]: (Kiyama et al., 1996)
Ref.[2]: (Xia et al., 2009)
Ref.[3]: (Toyota et al., 2005)
Ref.[4]: (Ishigami et al., 2015)
Ref.[5]: (Bern et al., 2013)

with a Curie temperature of at least 30 K. However, the average ferromagnetic moment is only up to $0.1\,\mu_B$/Ru. Their conclusions are not agreement with all other experimental observations. Possible intrinsic doping (Bern et al., 2013) at the interface between STO and SRO can explain such ferromagentic metal state.

The above calculations reveal that the non-FM insulating state is a robust feature of the SRO mono-layer (with/without STO capping). Only for an unrealistically small U-to-bandwidth ratio a FM phase can be stabilized (Table. 3.3). In consequence, none of the standard manipulation strategies available to the production of thin films can tune this ratio sufficiently to induce ferromagnetism in the SRO mono-layer. This stability explains why all experimental efforts to create ultrathin ferromagnetic films have so far been unsuccessful.
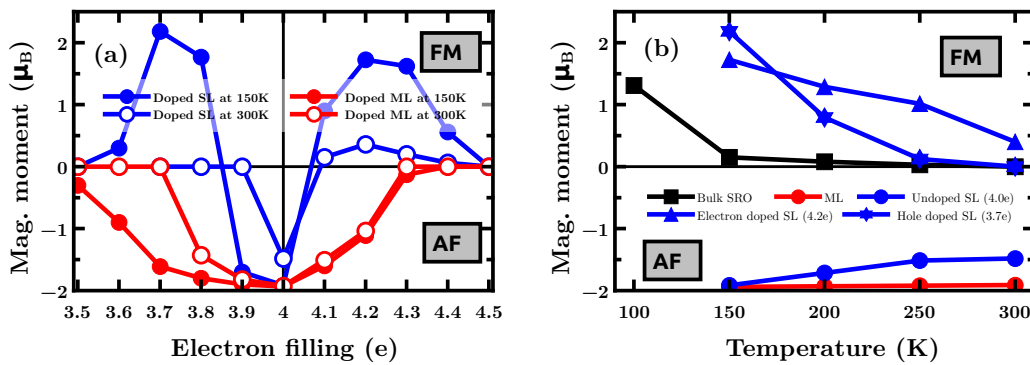

FIGURE 3.14: (a) Magnetic moment of SRO mono-layer (ML) and $(STO)_5$:$(SRO)_1$ superlattice (SL) vs. doping at 150 K and 300 K (positive [negative] moments denote FM [AF] ordering). (b) Magnetic moments vs. temperature for orthorhombic bulk SRO, mono-layer, undoped and doped $(STO)_5$:$(SRO)_1$ superlattice.

Doping. Here we propose an alternative route to achieve ultrathin FM films: doping. This strategy may seem counter-intuitive at first glance, as carrier doping causes a deterioration of the desired properties in the *bulk*. As we shall see, the situation for ultra thin films is different: Using the virtual crystal approximation to simulate carrier doping within DFT+DMFT, we obtain for the SRO mono-layer and the $(STO)_5$:$(SRO)_1$ superlattice the magnetic moments shown in Fig. 3.14. For the SRO mono-layer a significant doping corresponding to 3.5 and 4.5 electrons/site is needed to turn the AF state into a PM at both low (150 K) and high temperature (300 K) [Fig. 3.14(a)]. The AF magnetic moment is essentially symmetric around the filling with four electrons. The reason for this is the previously mentioned crystal field effect that results in an almost fully occupied xy orbital and a half-filled (particle-hole symmetric) yz/xz orbital doublet. We note that in all cases, the doping away from four electrons induces a metallic state.

Let us now turn to the more important case, the $(STO)_5$:$(SRO)_1$ superlattice: at low temperatures, e.g. at 150 K as shown in Fig. 3.15(a)-(b), both electron and hole doping can induce strong FM states. In the case of electron doping (filling $> 4\bar{e}$/Ru) the FM state is accompanied by an alternating orbital ordering of the xz/yz minority spin. The spectral function corresponding to 4.3 electrons/site is shown in Fig. 3.15(a). There, one Ru site has the orbital occupations for up (down)
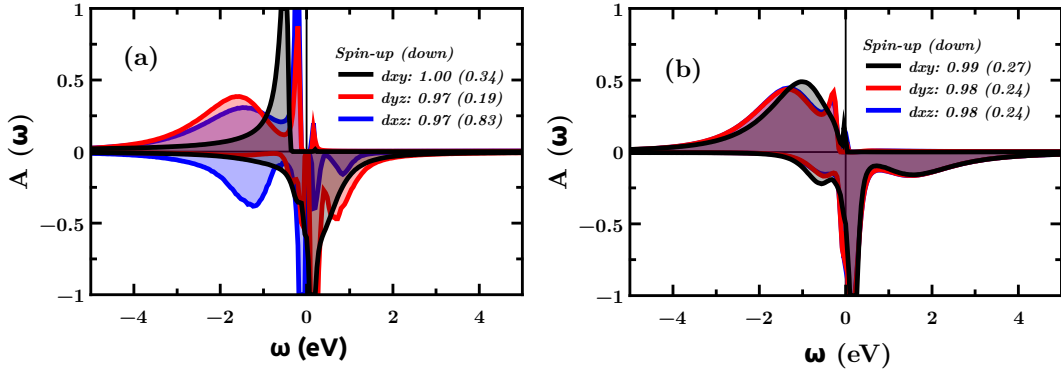
FIGURE 3.15: DFT+DMFT spectral functions of doped (SrRuO$_3$)$_1$:(SrTiO$_3$)$_5$ superlattice at 150 K, with 4.5 (a) and 3.7 (b) electrons per Ru site, respectively. The labels give the electronic occupations of the three t_{2g} orbitals.

spin: xy 1.00 (0.34), yz 0.97 (0.83), xz 0.97 (0.19); while for the second Ru site: xy 1.00 (0.34), yz 0.97 (0.19), xz 0.97 (0.83). For hole doping, e.g. at 3.7 electrons, our DMFT results indicate that the system is a FM half-metal with a moment of 2.20 μ_B/Ru at 150 K, see Fig. 3.14 for magnetic moments and Fig. 3.15 for the corresponding spectral functions. The half-metallic behavior makes this setup a prospective candidate for spintronics applications. To put this finding into perspective, we recall that bulk SRO has an FM moment of 2 μ_B/Ru or less, and an experimental (theoretical) Curie temperature of "only" 160 K ($\sim$150 K). One might thus wonder whether the ferromagnetism of the doped supercell is actually superior to the hailed properties of stoichiometric bulk SRO, which we were striving to restore. To investigate this, we perform calculations as a function of temperature [Fig. 3.14(b)]. We find that for both hole and electron doping, magnetic moments and Curie temperatures of the supercell are remarkably higher than for bulk SRO. In particular, for 4.2 electrons/Ru case, a sizable magnetic moments survives up to room temperature 300 K [Fig. 3.14(b)]. The magnetization curve has a similar shape as for the bulk (Kim and Min, 2015), despite the much higher T_c and the orbital-ordering. In Fig. 3.16(b) we also go beyond the virtual crystal approximation and show that a (STO)$_5$:(La$_{0.25}$Sr$_{0.75}$RuO$_3$)$_1$ superlattice is indeed FM. Our findings pave the road for realizing FM oxide devices that can be operated at room temperature.

Summary. Including many-body effects by means of DFT+DMFT, we show that the SRO mono-layer is an AF Mott insulator owing to a correlation enhanced crystal-field splitting at the surface/interface. While the bare (one-particle) crystal-field splitting can be tuned to almost zero by STO capping layers, electronic correlations are still strong enough to boost the orbital separation so that also the capped SRO layer remains an AF insulator. A FM metallic state is only realized for an interaction-to-bandwidth ratio that cannot be realized by experiment. This explains why no ultrathin FM films could be stabilized in experiment to date. Given the robustness of the AF state of SRO mono-layer setups to standard thin film manipulation techniques, we propose an alternative route to realize a FM state: Our study suggests that carrier doping drives ultrathin SRO films capped with STO into a strong FM state, whose ordered moment and Curie temperature even exceed the values realized in stoichiometric bulk SRO. To achieve
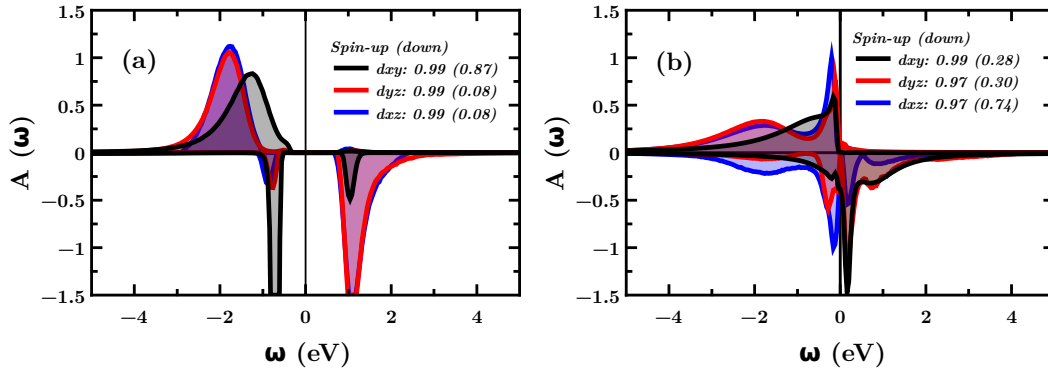
FIGURE 3.16: DFT+DMFT spectral functions of (a) an undoped (SrRuO$_3$)$_1$:(SrTiO$_3$)$_5$ superlattice and (b) a (STO)$_5$:(La$_{0.25}$Sr$_{0.75}$RuO$_3$)$_1$ superlattice (e=4.25/Ru) at 150 K. The labels give the electronic occupations of the three t_{2g} orbitals.

the long-standing quest for a FM ultrathin film in practice, we consider inducing oxygen or Sr vacancies (Kim, Chung, and Oh, 2005) or doping potassium into STO:SRO superlattices (Bern et al., 2013) as the most promising means.

Our study also opens a new, general, perspective: producing heterostructures based on materials with optimized *bulk* properties (e.g. stoichiometric SrRuO$_3$) is actually not always the optimal way for achieving those properties in a *film* geometry. Indeed the electronic structure of the thin film is so different from the bulk that it can be viewed as a completely different material. A manipulation (in our case doping) that decreases the quality of the bulk, can in fact enhance the sought-after property (FM magnetic moment) for the film setup. This suggests in turn that rather inconspicuous bulk materials might actually be good candidates for specific functionalities when deployed in a film or heterostructure. With this observation the repertoire of materials to be evaluated for oxide-electronics applications is significantly enlarged.

3.4   SrRuO$_3$ (110)-oriented Thin Films

This section is based on an article (under preparation) with a focus on (110)-oriented SrRuO$_3$ thin films.

In this section we review our research about SRO (110)-oriented mono-, bi- and tri-layers. To the best of our knowledge, quite few papers on SRO (110) thin films have been published so far, because it is generally believed that the differences between (110)- and (111)-oriented SRO films is not dramatic.
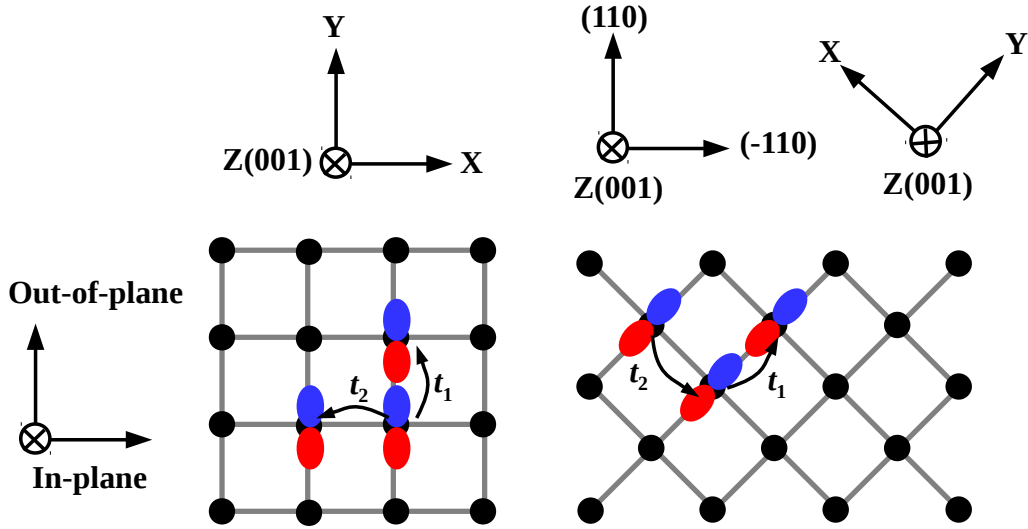

FIGURE 3.17: Differences between (001)- and SRO (110)-oriented films, in left and right panels, respectively. The d-orbital depicted is the d_{yz} orbital.

We firstly focus on the differences of structural details between (001)- and (110)-oriented SRO films. In Fig. 3.17 we show a schematic picture. As shown in Fig. 3.17(a), for (001)-oriented films we take the d_{yz} orbital as an example, along x-direction d_{yz} orbital has a smaller electronic hopping term t_2, while along y- and z-direction has a larger hopping term t_1. This is due to the fact that the d_{yz} orbital mainly spreads in the yz-plane. Note that in Fig. 3.17 for the (001)-orientation films, the y-direction corresponds to the (010) direction of pseudo-cubic SRO, i.e. out-of-plane direction, and the x/z-direction corresponds to (100)/(001) of pseudo-cubic SRO, i.e. in-plane directions. Thus when the electrons in the d_{yz} orbital hop along the in-plane x-direction they behave like heavy charge carriers, and when along the in-plane z- and the out-of-plane y-direction they behave like lighter carriers.

However when SRO films grow along (110) direction, the in-plane direction corresponds to the (-110)- and (001)-direction of pseudo-cubic SRO while the out-of-plane direction corresponds to the (110)-direction of pseudo-cubic SRO. When d_{yz} orbital electrons hop along the in-plane (001)-direction they become lighter carriers, however when they hop along in-plane (-110)- or (1-10)-direction, the electrons hop alternatively with two hopping terms: t_1 and t_2.

To understand what exotic physical phenomenas was result by such a way of electronic hopping, we derive a TB Hamiltonian by taking the t_1 and t_2 hopping terms; the N=2 (bilayer) and 3 (trilayer) cases are analyzed.

Calculation details. Initial structures of (110)-oriented thin films are pseudo-cubic, being sandwiched by band insulator STO, leading to 2:4 and 3:5 SRO:STO superlattice. Both atomic positions and out-of-plane c-direction lattice constant are relaxed while the in-plane lattice constant is set as the experimental STO value: 3.905 Å. In DFT calculations, the k-mesh is 14×10×2. In DFT+DMFT calculations we adopt the Hund's exchange (J=0.3 eV), intra-orbital (U=3.0 eV) and inter-orbital Coulomb repulsion (U'=2.4 eV), the temperature is 100 K. For the TB Hamiltonian the electronic hopping parameters are taken from Table. 2.1. For band plotting of (110) thin films, the high-symmetric BZ point $k_Z(0,0,\frac{\pi}{a})$ and $k_M(\frac{\pi}{a},\frac{\pi}{a},0)$ host same definition as in cubic SRO.

In the basis of d_{xy}, d_{yz} and d_{xz}, the Hamiltonian of SRO (110)-oriented films can be written as a $3N{\times}3N$ matrix (N is thickness), after diagonalization, analytical solutions read as below:

$$H_{xy}(k_z, k_M) = -4t_1 - 2t_2 + 2t_2 cos(k_z a) - 2(t_1 + t_1 cos(k_M\sqrt{2}a))^{\frac{1}{2}} cos(\frac{\pi n}{N+1})$$

$$H_{yz}(k_z, k_M) = -4t_1 - 2t_2 + 2t_1 cos(k_z a) - 2(t_1 + t_2 cos(k_M\sqrt{2}a))^{\frac{1}{2}} cos(\frac{\pi n}{N+1}) \quad (3.1)$$

$$H_{xz}(k_z, k_M) = -4t_1 - 2t_2 + 2t_1 cos(k_z a) - 2(t_1 + t_2 cos(k_M\sqrt{2}a))^{\frac{1}{2}} cos(\frac{\pi n}{N+1})$$

where the capital N indicates the film thickness, the n is quantum number which changes from n=0,1, ..., $N-1$, and a is the lattice constant of cubic SRO.
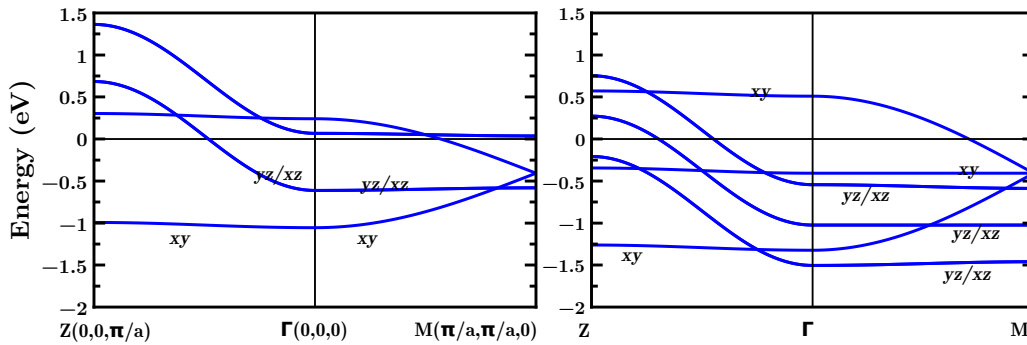

FIGURE 3.18: Simplified TB bands of SRO (110)-oriented bi- (left) and trilayer (right). Only the major hoppings t_1 and t_2 of Table. 2.1 in **Chapter 2** are included.

The resulting TB bands of SRO (110)-oriented bi- and trilayer films are shown in Fig. 3.18. The left panel shows the result of bilayers, where the d_{yz} and d_{xz} bands are degenerate because we exclude long-range hopping terms (with long-range hoppings all the degeneracies are left, see DFT bands in Fig. 3.19). Along the Z-Γ path, the d_{xy} bands flatly disperse whereas the d_{yz}/d_{xz} bands have much larger energetic dispersion of ~1.25 eV. This is due to the fact that along the Z-Γ direction the dispersion of d_{xy} bands is quantified by the smaller hopping t_2 that equals -0.025 eV while the dispersions of d_{yz}/d_{xz} bands are quantified by the larger hopping t_1 which is -0.337 eV. Along the Γ-M path, the d_{yz}/d_{xz} bands have a quite small energetic dispersion, while the d_{xy} bands have a larger energetic dispersion. This is because between Γ to M, the d_{yz}/d_{xz} bands are quantified by t_2, while the d_{xy} bands are quantified by t_1, as listed in Eq. 3.1. For the trilayer case in Fig. 3.18 right panel, no dramatic differences happen but we obtain more quantum well states, e.g., for

d_{yz}/d_{xz} bands three quantum well states can be observed, and between the three groups of d_{yz}/d_{xz} bands the bands at -1.0 eV are entirely flat. For d_{xy} bands a purely flat band appears at -0.3 eV along the Γ-M path. These purely flat bands are an intrinsic property of (110)-oriented trilayer. In Eq. 3.1 we can see that for all states along the Γ-M (k_M) path have a quantum well factor $\cos(\frac{\pi n}{N+1})$. For thickness N=3 (Fig. 3.18 right panel) the quantum number is n =0,1,2; and when n=2, this quantum well factor is zero. This indicates there must be a flat band, which is independent of vector k_M. Thus we can observe two groups of flat bands, one is from the d_{xy} orbital while the others are from d_{yz}/d_{xz} orbitals. More than these two flat bands, all the d_{yz}/d_{xz} bands are also quite flat, because they are dependent on the smaller hopping term t_2.

In fact the flat band phenomena can be extended to all odd numbers of thickness N, however one would expect that increasing thickness of SRO (110)-oriented films will eventually recover their bulk electronic and magnetic properties. Thus we suggest to observe these flat bands experimentally, e.g. in angle-resolved photoemission (ARPES) spectroscopy, measurements should be carried out with thiner samples, i.e. trilayer. These "flat bands" in bilayer and trilayer are very promising for realizing a high-temperature ferromagnet, because they can induce high DOS at a certain energy. If E$_f$ is located at such high DOS, the system may be prone to a Stoner instability, leading to spin-splitting, i.e. the ferromagnetic state. This mechanism is similar to the origin of ferromagnetism in bulk SRO, in which the ferromagnetism is also from Stoner mechanism (Chang et al., 2009).

Above TB bands are obtained without the contributions from long-range hoppings, like second neighbor t_3 and t_4 in Table. 2.1. Only the first neighbor hopping t_1 and t_2 are included. The effects of long-range hopping terms may eventually destroy these flat bands. To test this scenario we carried out nonmagnetic DFT bands and DOS calculations (Fig. 3.19).
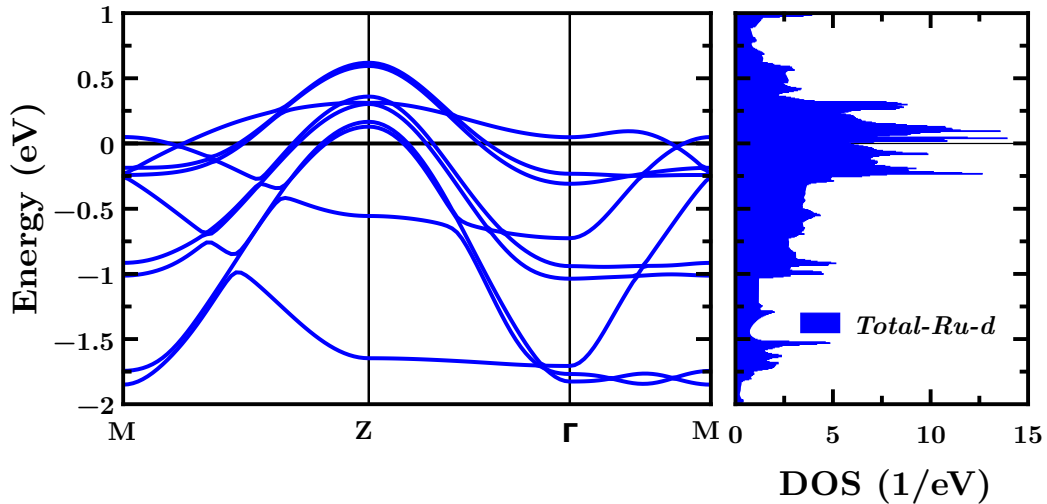
FIGURE 3.19: Nonmagnetic DFT bands of SRO (110)-oriented trilayer and its DOS.

Compared with simplified TB bands, the DFT bands are seriously distorted in the present of long-range hoppings. Three groups of flat bands are visible along the Γ-M path at -1.7 eV, -1.0 eV and -0.25 eV, respectively. Three peaks are visible in the DOS at corresponding energies (Fig. 3.19 right panel). E$_f$ is located between two DOS peaks (-0.25 eV and 0.2 eV), with a local DOS minimum. Hence any degree

of hole/electron doping can increases the DOS at E_f. This DOS behavior has been observed in some high-temperature superconductors (Dagotto, 1994), indicating the possibility of SRO (110)-oriented trilayer as candidate for superconducting states.

FIGURE 3.20: Spin-polarized DMFT spectral functions $A(k, \omega)$ of SRO (110)-oriented monolayer (a), bilayer (b) and trilayer (c) at 100 K.

In **Chapter 3.3**, with the discussion of SRO (001)-oriented monolayer, we demonstrated the standard DFT($+U$) methods fa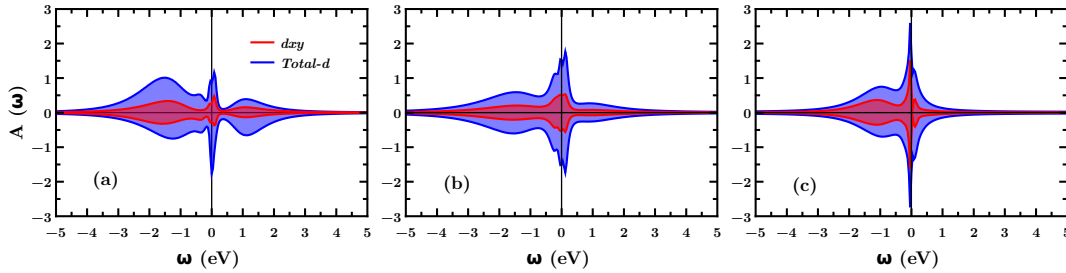il in predicting/explaining the ground states of SRO films, i.e. dynamical correlation effects paly an important role. Hence we directly carry out DFT+DMFT calculations for SRO (110) films , as shown in Fig. 3.20(a)-(b).

In Fig. 3.20(a), the (110)-oriented SRO monolayer is predicted to be a paramagnetic metal, without ferromagnetism in DMFT. This non-ferromagnetic state is consistent with the (001)-oriented monolayer, which is antiferromagnetic insulator (see **Chapter 3.3**). However, the metallic state of (110)-oriented monolayer is in contract with (001)-oriented monolayer. This indicates the metal-insulator critical thickness behavior is suppressed at (110)-oriented monolayer, and the metallic state can survive even down to monolayer. After increasing the thickness to bilayer and trilayer, the system is still a paramagnetic/correlated metal [Fig. 3.20(b)-(c)], without net magnetic moments. One can image that if we continuously increase the thickness of (110)-oriented SRO films we can finally recover the ferromagnetic metal state of bulk SRO. However since the calculation is highly expansive, the critical thickness number of this transition could not be calculated. By comparing the DMFT calculated spectral functions of (110)-oriented monolayer and trilayer we can see that for thicker films, there is clear spectra transformation from the (lower- and higher-) Hubbard peaks to the quasi-particle peak at E_f, increasing the spectral weight at E_f. This indicates that the thick film approaches ferromagentism due to the Stoner mechanism. In DMFT calculations, we found that the SRO (110)-oriented trilayer is on the verge of paramagnetism to ferromagnetism transition, if we decrease the intra-orbital U from 3.00 eV to 2.95 eV then trilayer exhibits as ferrimagnetic metal.

3.5   SrRuO$_3$ (111)-oriented Thin Films

3.5.1   Magnetic Properties

After analyzing the electronic structures of SRO (001)- and (110)-oriented thin films, we now turn to (111)-oriented thin films, that are of current experimental and theoretical interest due to both the enhanced ferromagnetism and topological properties.

Calculation details. Initial pseudo-cubic SRO units sandwiched by the band insulator STO, leading to 1:8, 2:7, 3:6 SRO:STO superlattices. The systems are constructed by alternatively growing Ru^{4+}/Ti^{4+}, SrO_3^{-4} layers along the $(111)_{pseudo-cubic}$ direction, leading to a polar system. In fact because the surface reconstruction of Ru-terminated (111) SRO thin films is dramatic (Kim and Min, 2014). Also in (111) polar layers the occurrence of atomic defects such as oxygen vacancies is inevitable. Hence we adopt STO to sandwich SRO and construct superlattices, rather than leaving SRO to face the vacuum.

Atomic relaxation are carried out using the Vasp code (Kresse and Hafner, 1993; Kresse and Furthmüller, 1996), and the electronic structures are calculated using Wien2k code (Blaha et al., 2001). Regrading the atomic relaxation, two conditions of setups are considered: (1) the in-plane lattice constant is fixed to be that of experimental lattice constant of STO: 3.905 Å, and only the out-of-plane lattice and all atomic positions are relaxed; (2) fully relaxations for all degree of freedom. Both methods yield nearly indistinguishable electronic structure. In this thesis we show the results of the first setup. In DFT calculations the k-mesh is 12×12×3. For DMFT calculation the input $H(k)$ is obtained by carrying out a Wannier projection from Bloch waves onto Wannier orbitals, then carry out Fourier-transformation from real-space Hamiltonian $H(r)$ to k-space $H(k)$. In DFT+DMFT calculations we adopt a Hund's exchange (J=0.3 eV), intra- (U=3.0 eV) and inter-orbital Coulomb repulsion (U'=U-2J=2.4 eV), the CT-QMC code **W2dynamic** (Parragh et al., 2012) is employed. For simplified tight-binding calculations the electronic hopping parameters are taken from Table. 2.1.

The crystal structure of (SRO)$_2$:(STO)$_7$ superlattice is shown in Fig. 3.21: the structure is constructed by alternative growing Ru^{4+}/Ti^{4+} and SrO_3^{4-} layers.

The DFT+DMFT calculated spectral functions of monolayer, bilayer and trilayer of (111)-oriented SRO films are shown in Fig. 3.22(a)-(c). The (111)-oriented monolayer is a paramagnetic Mott-insulator [Fig. 3.22(a)]. This naturally follows from the fact that in our nonmagnetic DFT calculations (it is the pre-requirement of carrying out Wannier projection to get the input $H(k)$ for following DMFT calculations) the bandwidth W of the (111)-oriented monolayer is merely ∼0.98 eV, 30.6% of that of bulk SRO (3.2 eV). Considering about the enhancement of U because of the surface screening effect, a larger U/W is obtained, leading to a Mott-insulating state. For the magnetic properties of the (111)-oriented monolayer, the origin of the the paramagnetic phase can be understood by considering short-range interactions between the localized moments, and accounting its nearest neighboring of Ru sites. In bulk SRO, each Ru site has 6 nearest neighbors [(±100), (0±10) and (00±1)], 12 second neighbors [(±1±10), (0±1±1) and (±10±1)] and 8 third neighbors (±1±1±1). However for the (111)-oriented monolayer, only 6 of these 24 neighbors are reserved [(-110), (1-10), (0-11), (01-1), (-101) and (10-1)]. This significantly reduces the magnetic interaction between Ru and its neighboring sites, leading to a tiny energetic difference between various magnetic orderings.
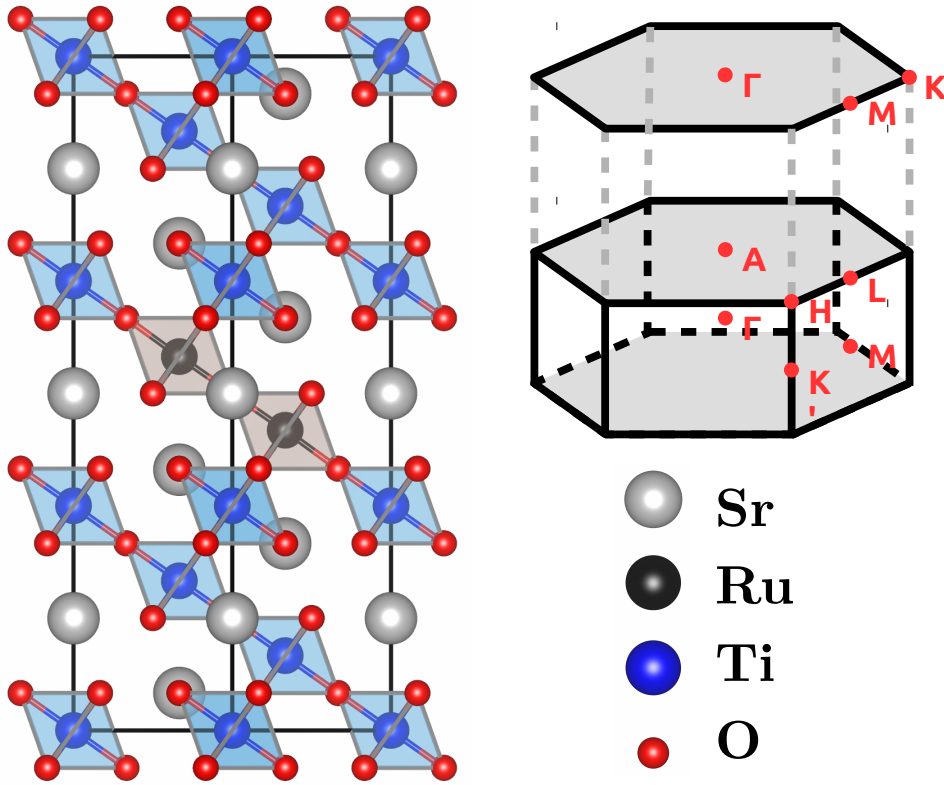
FIGURE 3.21: Example of SRO:STO 7:2 (111)-oriented superlattice (left panel), and the corresponding first Brillouin zone (right-up), and atomic label.
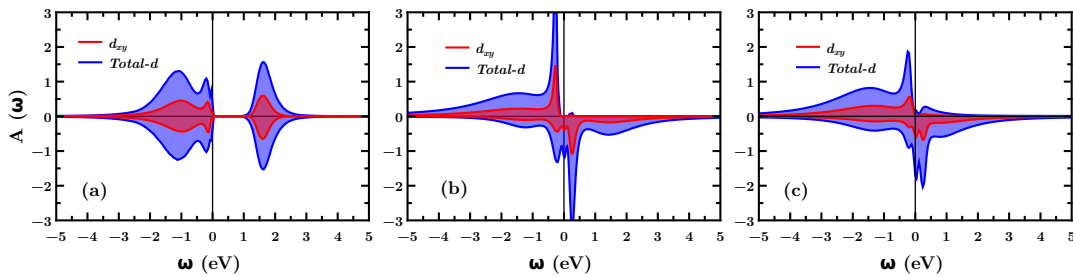
FIGURE 3.22: DMFT spectral functions of (111)-oriented SRO for monolayer (a), bilayer (b) and trilayer (c) at 200 K. To demonstrate the orbital degeneracy for the (111)-oriented SRO:STO superlattice, besides the total d-orbital spectral functions also the d_{xy} orbital functions are shown. Their contribution is about 1/3 of the total spectral weight.

Both the bilayer and trilayer exhibit ferromagnetic half-metallic states: the spin-majority (up) channels are fully occupied while the spin-minority (down) channels are partially occupied. The trilayer is a Mott-insulating state while the bilayer is more close to a band insulator. Distinct higher and lower Hubbard bands are there in both bilayer and trilayer at both spin channels, indicating strong electronic correlations. The net magnetic moments for bilayer and trilayer are $2.0\,\mu_B/\text{Ru}$ and $1.45\,\mu_B/\text{Ru}$, respectively, indicating a gradual change from half-metallic ferromagnet to paramagnetic metal that upon increasing thickness. This is understandable because our calculating temperature is set at 200 K, at which temperature bulk SRO

is already a paramagnetic metal without net moment. Increasing the thickness of (111)-oriented thin films finally recovers bulk state in SRO (111) films. It is amazing that reducing the thickness of (111)-oriented thin films dramatically enhance the ferromagnetism, leading to half-metallic ferromagnetic states at thickness N=2 or 3. This transition is different with the ferromagnetic suppression in SRO (001)-oriented monolayer and bilayer, in which the geometric confinement drives the transition from ferromagnetic metal to antiferromagnetic insulating states upon decreasing thickness of (001)-oriented thin films.

Please note that the paramagnetic Mott-insulator phase in the (111)-oriented monolayer cannot be accounted for by DFT($+U$) method, because DFT($+U$) fails at predicting Mott-Hubbard insulating phases. However for the ferromagnetic half-metal phase of (111)-oriented bilayer, we can test our conclusion by DFT+U method. For the U term chosen as 2.4 eV (same as U'=U-2J=2.4 eV in DMFT calculations). We found the ferromagnetic half-metal state which is by 400 meV/Ru energetically lower than the nonmagnetic solution, and 279 meV/Ru lower than the antiferromagnetic solution (net moment 2.0 μ_B/Ru), supporting the robust of the ferromagentic half-metallic state.
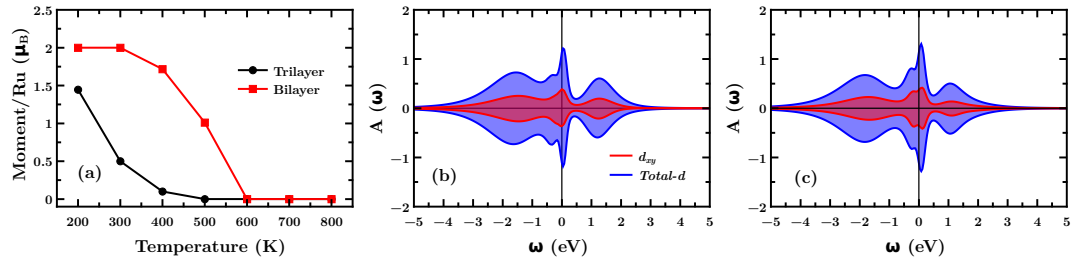

FIGURE 3.23: Average magnetic moment (μ_B) vs. temperature (K) for (111)-oriented SRO bilayer and trilayer cases (a), and the spectral functions of bilayer (b) and trilayer (c) at 600 K. At this high-temperature both systems are paramagnetic correlated metals.

To carry out a systematic investigation of magnetic properties of SRO (111)-oriented bilayer and trilayer, we calculate their magnetic moments at different temperatures (from 200 K to 800 K) [Fig. 3.23(a)]. The bilayer exhibits a half-metallic ferromagnetic state at 200 K and 300 K, with the magnetic moment of 2 μ_B/Ru. The ferromagnetism is fully suppressed at 600 K [Fig. 3.23(a)-(b)], indicating a T$_C$ which is higher than 500 K. Both magnetic moments and T$_C$ are remarkably higher than those of bulk SRO: it is an excellent ferromagnet. To the best of the author's knowledge, 500 K is one of the highest Curie temperatures in transition metal oxides. We conclude that the SRO bilayer is a strong ferromagnet and a possible candidate for spintronics devices (Zutic, Fabian, and Das Sarma, 2004). For trilayer, the T$_C$ is decreased to be between 400 K and 500 K, which is also remarkably higher than that in the bulk (160 K). The spectral functions of a trilayer at 600 K are shown in Fig. 3.23(c).

3.5.2   Topological Properties

Abstract. SrRuO$_3$ heterostructures grown in the (111) direction are a rare example of thin film ferromagnets. By means of density functional theory plus dynamical mean field theory we show that the half-metallic ferromagnetic state with an ordered magnetic moment of $2\,\mu$/Ru survives the ultimate dimensional confinement down to a bilayer, even at elevated temperatures of $500\,$K. In the minority channel, the spin-orbit coupling opens a gap at the linear band crossing corresponding to $\frac{3}{4}$ filling of the t_{2g} shell. We demonstrate that the respective state is Haldane's quantum anomalous Hall state with Chern number C=1, without an external magnetic field or magnetic impurities.

Introduction. The discovery of topological states of matter (Wen, 1990; Hasan and Kane, 2010; Qi and Zhang, 2011) has significantly broadened and advanced our understanding of solid state physics. The historically first topological phenomenon is the quantum Hall effect (Klitzing, Dorda, and Pepper, 1980) (QHE) observed in a two-dimensional electronic system exposed to a strong external magnetic field. The QHE manifests itself in the quantized transverse conductance (Hall conductance) stemming from nontrivial Berry curvatures of the filled Landau levels (Berry, 1984; Thouless et al., 1982; Xiao, Chang, and Niu, 2010) in an otherwise insulating state with a vanishing longitudinal conductance. As a result, a dissipationless edge mode appears along the boundary between the quantum Hall system and the vacuum.

In his Nobel prize winning work, Haldane (Haldane, 1988) realized that neither magnetic field nor Landau levels are actually required, but only breaking of time-reversal symmetry (TRS) and a non-trivial topology of the electronic structure. Arguably the easiest way to break TRS without magnetic field is through a spontaneous magnetization, inducing a quantized version of the conventional anomalous Hall effect, which is now known as the quantum anomalous Hall effect (QAH). Such insulating bulk systems are also called Chern insulators, as their topological edge states are characterized by the first Chern number, which is defined as an integral of the Berry curvature of the filled bands over the Brillouin zone.

Recent research on quantum spin-Hall (QSH) insulators (Kane and Mele, 2005; König et al., 2007; Hsieh et al., 2008), which can be viewed as two copies of a QAH state with equal but opposite magnetic moments, delivered an impressive number of candidate materials. In contrast, the search of QAH systems is far from being comprehensive owing to the strict conditions for realizing them, *i.e.*, realizing the spontaneous magnetization and the nontrivial Berry curvatures. One straightforward route is to magnetically dope a QSH insulator, where the presence of the magnetic impurity breaks the TRS and, thus, lifts the Kramers degeneracy of the QSH insulators to reach the QAH states (Chang et al., 2013; Checkelsky et al., 2014). However, experimentally such extrinsic impurities are difficult to control, and need to generate a sufficiently strong magnetic moment while keeping the topology of the system unaffected. Thus, it is of more fundamental interest to have a genuine magnetic system that hosts the QAH state intrinsically.

In this context, heterostructures of transition-metal oxides (TMO) are a most promising material class. These artificial materials exhibit a plethora of interesting behaviors driven by electronic correlations and the dimensional confinement (Mannhart and Schlom, 2010; Rondinelli and Spaldin, 2011; Zubko et al., 2011; Chakhalian et al., 2014). Grown perpendicular to the body diagonal of a perovskite lattice structure, i.e. along the [111] direction, bilayers of perovskite TMO form a honeycomb lattice. The d-electrons in such bilayers can show a fascinating

variety of electronic, magnetic as well as topological (Xiao et al., 2011; Okamoto et al., 2014) phases. Some heterostructures such as $LaAuO_3$-$LaCrO_3$ heterostructures were suggested as a realization of the QAH state (Liang, Wu, and Hu, 2013). However, the fabrication of such heterostructures is at best challenging, because bulk $LaAuO_3$ is not of the perovskite structure (Ralle and Jansen, 1993). Also freestanding monolayers of e.g. $NiCl_3$ and $OsCl_3$ have also been proposed (He et al., 2016; Sheng and Nikolic, 2016). Against this background, actual material realizations of Haldane's QAH state remain a great challenge.

In this letter, we investigate the electronic structure of (111)-oriented $SrRuO_3$ (SRO) bilayers sandwiched between $SrTiO_3$ (STO). This heterostructure can be routinely fabricated by advanced pulsed laser (Grutter et al., 2010) or metal-organic aerosol (Agrestini et al., 2015) deposition, and thin SRO (111) films already exist and are ferromagentic (Grutter et al., 2010; Grutter et al., 2012; Grutter et al., 2013; Ning, Wang, and Zhang, 2015). Using density functional theory (DFT) and dynamical mean field theory (DMFT) calculations, we show that SRO (111) bilayers remain ferromagnetic half-metals with a moment of $2\,\mu_B/$Ru and a Curie temperature (T_C) exceeding room temperature. The band structure of the minority channel features a linear band crossing at $\frac{3}{4}$ filling of the t_{2g} shell, which becomes gapped due to the spin-orbit coupling (SOC). By simulating the respective microscopic Hamiltonian, we find a QAH state and the Chern number $C = 1$. This result is further corroborated by a direct numerical solution of the full tight-binding Hamiltonian parameterization of the Wannier functions on a long cylinder, which shows topological edge modes in the gap.

Before presenting the results of our DFT+DMFT calculations, we briefly explain how the unit cells are constructed. In the hypothetical cubic perovskite structure of SRO [Fig. 3.24(a)], we consider layers stacked along the body diagonal [111] of the cubic lattice. By cutting out two neighboring SRO monolayers [Fig. 3.24(b)], we obtain a bilayer whose Ru atoms form a honeycomb lattice. To comply with the periodic boundary conditions and to ensure a sufficient separation of individual SRO bilayer, we interleave them with seven layers of STO. The resulting $2\,SRO:7\,STO$ superlattice with 45 atoms in the unit cell has a pseudocubic structure described within the space group $P\bar{3}m1$ (164) with an inversion center in between the SRO monolayers.
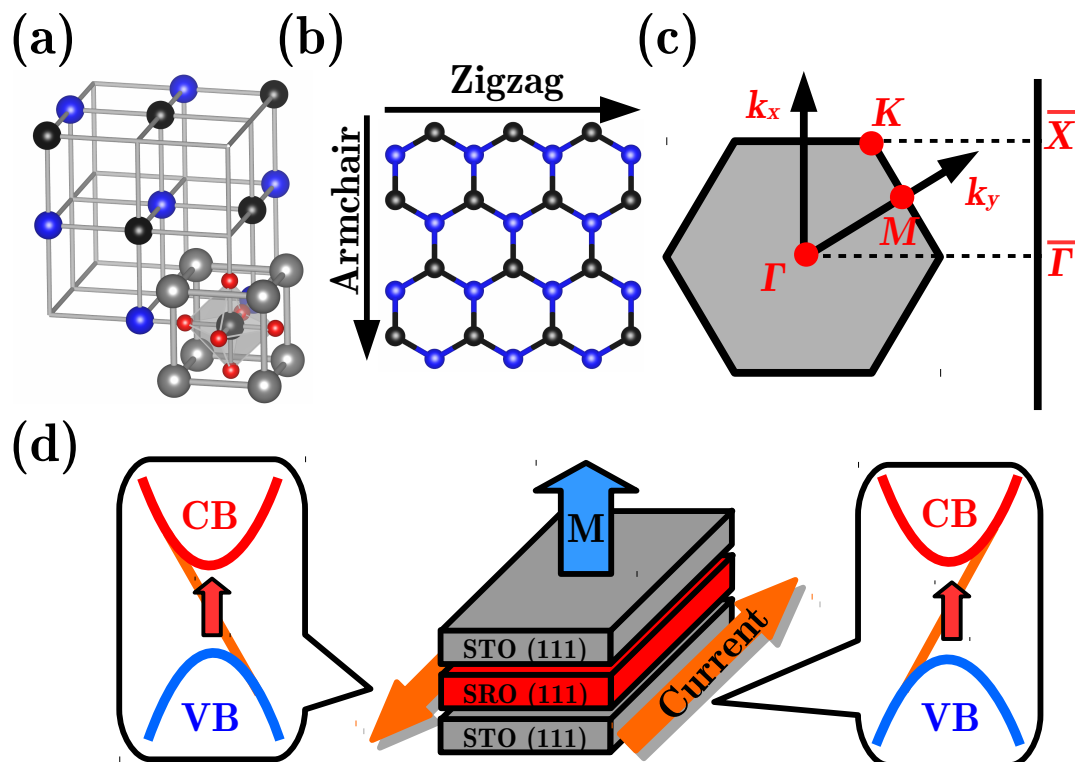
FIGURE 3.24: (Color online) Crystal and electronic structure of 2 SRO : 7 STO (111) superlattices. (a) Octahedral perovskite cage in bulk SRO. Gray and red balls denote Sr and O atoms; blue and black ones Ru atoms in two honeycomb sublattices. (b) (111) bilayers of SRO form a honeycomb lattice. (c) High-symmetry points of the first Brillouin zone of the honeycomb lattice: $\Gamma\,(0,0,0)$, $M\left(\frac{\pi}{a},0,0\right)$ and $K\left(\frac{2\pi}{3a},\frac{2\pi}{3a},0\right)$. (d) Spin-polarized minority currents develop at the edge of the bilayer, and originate from the topological states between the valence band (VB) and the conduction band (CB) illustrated on the left and right, respectively.

Calculation details. The smaller lattice constant of STO exerts a compressive strain of ∼0.45-0.63% on the SRO bilayers (Koster et al., 2012). To account for strain effects, we relax the c unit cell parameter and the internal atomic coordinates within the generalized gradient approximation (GGA) (Perdew, Burke, and Ernzerhof, 1996) as implemented in VASP code (Kresse and Hafner, 1993; Kresse and Furthmüller, 1996). All further electronic structure calculations were performed for this optimized structure using the WIEN2K (Blaha et al., 2001) code.

The nonmagnetic GGA band structure of 2 SRO : 7 STO (111) is shown in Fig. 3.25(a). The manifold crossing the Fermi level comprises six Ru t_{2g} bands. The higher-lying e_g states (not shown) are empty and can be excluded from the correlated subspace. As a necessary preparatory step for DMFT calculations, we project the Ru t_{2g} bands onto maximally localized Wannier functions (Marzari et al., 2012) using the WIEN2WANNIER code (Kuneš et al., 2010).

DMFT calculations were performed using the continuous time quantum Monte Carlo (CT-QMC) solver implemented in the code W2DYNAMICS (Parragh et al., 2012). The interaction parameters, the Coulomb repulsion $U = 3.0$ eV and the Hund's exchange $J = 0.3$ eV are adopted from Ref. (Si et al., 2015). We use the rotationally invariant form of the Hamiltonian, which implies an inter-orbital interaction $U'=U$-$2J$. For the analytical continuation of the resulting self-energy $\Sigma(i\omega_n)$ onto the real frequency axis ω, the maximum entropy method (Gubernatis et al., 1991) was used.

DMFT reveals strong similarities between 2 SRO : 7 STO (111) superlattices and bulk SRO: both are ferromagnetic and conducting in the minority channel. The ferromagnetic half-metallic behavior is in sharp contrast to (001) SRO thin films that are insulators and lack ferromagnetism (Xia et al., 2009; Si et al., 2015). This difference stems from the spatial confinement which acts differently in (001) and (111) systems: Slicing in the [001] direction lowers the onsite energy of the xy orbital compared to the xz and yz orbitals (Si et al., 2015), favoring antiferromagnetism within the half-filled xz and yz orbitals. In contrast, the degeneracy of the t_{2g} manifold is not affected by (111) slicing, and the on-site orbital energies are similar to bulk SRO. And yet, the spatial confinement is important: DMFT indicates that the ferromagnetic state of the 2 SRO : 7 STO (111) superlattice survives up to ∼500 K [inset of Fig. 3.25(b)], which is remarkably higher than the Curie temperature of bulk SRO (160 K). This result is in agreement with recent experimental reports on the enhanced T_C in SRO (111) films (Grutter et al., 2010; Grutter et al., 2012; Grutter et al., 2013; Ning, Wang, and Zhang, 2015); and opens a route to long-sought-after ultrathin layers that are ferromagnetic at room temperature [DMFT overestimates critical temperatures by 20-30% (Rohringer et al., 2011) in three dimensions. Of course strictly speaking the Mermin-Wagner theorem prevents long-range ferromagnetic order for a two-dimensional plane. However, because of the exponentially growing correlation length (Schäfer et al., 2013) even well separated bilayers would eventually order in a 2 SRO : 7 STO (111) superstructure at comparable temperatures].

Next, we evaluate the DMFT self-energy $\Sigma(\omega)$ on the real frequency axis and calculate the k-resolved spectral function $A(k,\omega)$ [Fig. 3.25(b) and 3.25(c)]. The effect of the k-independent self-energy is twofold: the real part shifts the bands
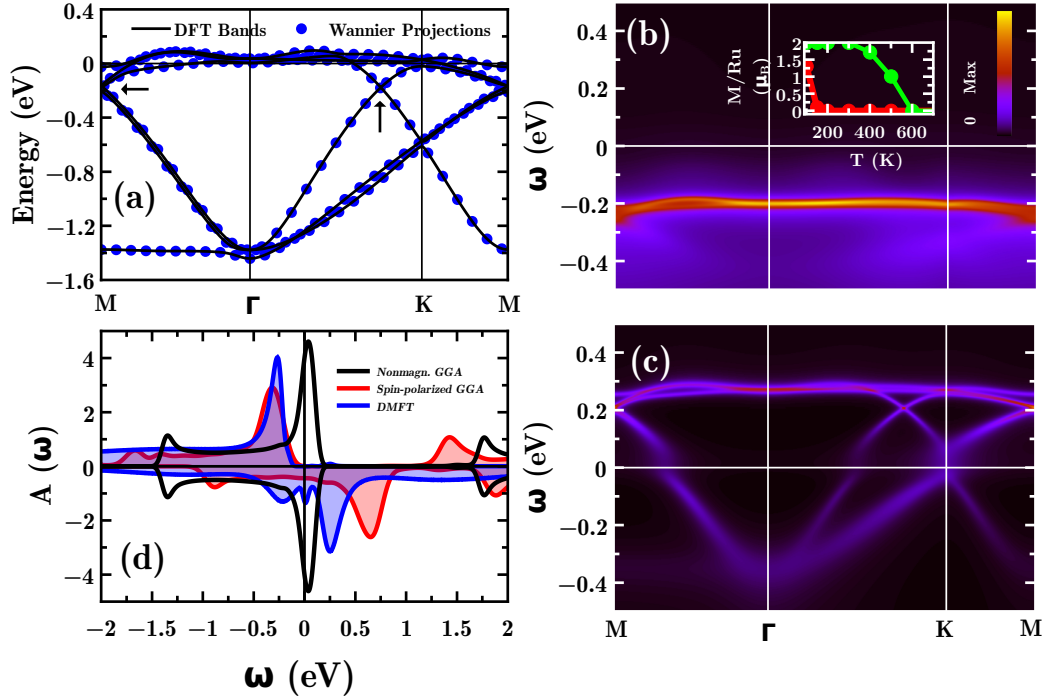
FIGURE 3.25: (Color online) (a) Nonmagnetic scalar relativistic GGA band structure of 2 SRO : 7 STO (solid lines) in comparison with the Fourier-transformed Wannier projections (circles). The arrow indicates the position of the Dirac point near M point and along the Γ–K line. (b) spin-up and (c) spin-down DMFT spectral functions at 300 K. (d) Density of states of nonmagnetic and magnetic GGA calculations in comparison with the DMFT spectral function. Inset in (b): ferromagnetic moment of bulk SRO (red) vs. the SRO (111) bilayer (green) as calculated by DFT+DMFT.

and renormalizes the band widths, while the imaginary part gives rise to broadening. The latter is particularly for the partially filled majority states: there is a broad incoherent continuum in Fig. 3.25(b) terminated by a nearly flat feature around 0.2 eV below the Fermi level. In contrast, the k-resolved spectral function for the minority channel [Fig. 3.25(c)] largely resembles the GGA band structure [Fig. 3.25(a)]. The most prominent effect of electronic correlations here is the reduction of the band width down to ∼0.8 eV, which is much smaller than that in the GGA (1.5 eV) and in the bulk SRO (3.2 eV). Altogether the DMFT self energy essentially corresponds to a bandwidth quasiparticle renormalization of $Z \sim 0.5$ and a reduction of the spin-splitting form 0.88 eV in GGA to 0.47 eV in DFT+DMFT; otherwise the electronic structure and its topology is not affected.

A remarkable property of $A(k, \omega)$ in the minority channel is the linear band crossing (at $\frac{3}{4}$ filling of the t_{2g} shell) near the M point and along the Γ–K line. This feature inherited from the band structure [Fig. 3.25(a)] is resilient to electronic correlations [Fig. 3.25(c)]. But if the SOC is taken into account a gap opens at the band crossing: the full relativistic treatment within the modified Becke-Johnson (mBJ) potential (Tran and Blaha, 2009) yields a tiny band gap of ∼1 meV. Assuming the chemical potential is placed into the gap, the system becomes insulating at low temperatures. Topological properties of this envisaged insulating state are characterized by the Chern number C of the occupied bands: zero or

nonzero for a trivial state and the QAH state, respectively.

To determine C, we employ the full tight-binding Hamiltonian parameterization of the Wannier functions. The sizable separation between SRO bilayers allows us to consider only intraplane couplings. The eigenvectors of the respective tight-binding Hamiltonian are calculated on a fine k-mesh of 120×120 points and used to calculate link variables and, in turn, Chern numbers, following the procedure described in Ref. (Fukui and Hatsugai, 2007). In this way, we find $C = 1$ for the bands below the SOC-induced gap, hence the QAH state is realized.
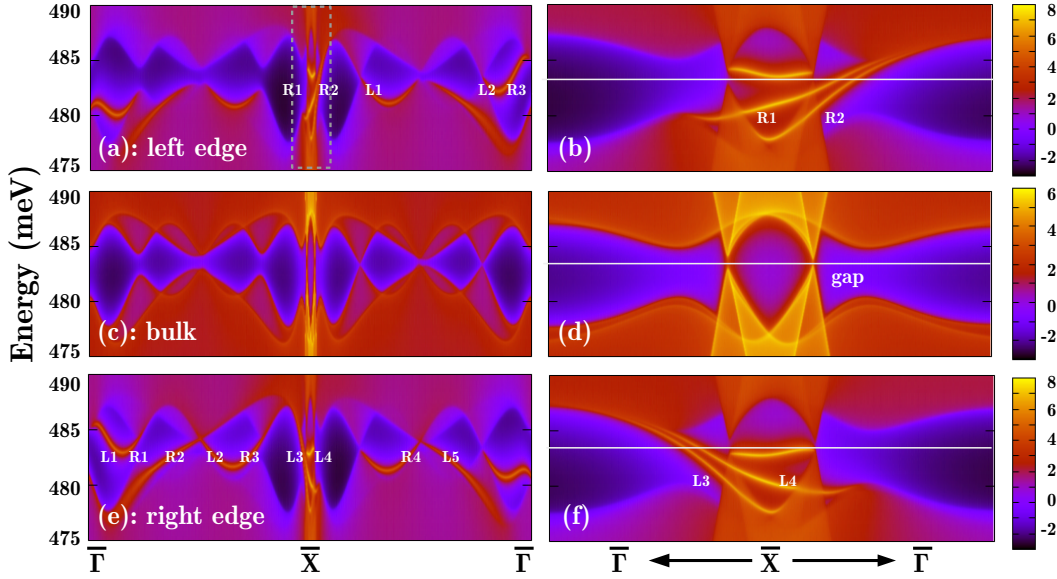
FIGURE 3.26: (Color online) Spectral functions of semi-infinite zigzag-termination slabs of SrRuO$_3$ (111) bilayer projected in the k_x direction as indicated in Fig. 3.24. The spectral functions of left edge (a, b), central bulk region (c, d) and right edge (e, f) are shown; the right panels are zoom-ins of the left panels corresponding to the white-dashed box in (a). All edge states are labeled with L_n/R_n (n=1,2,3...) indicating the nth left/right moving state. Two nearly flat edge states are identified as topological trivial and do not cross the Fermi energy at $\sim$483 meV (white solid line). The edge states agree with the Chern number $C = 1$ since e.g. on the left edge (a) there are $3 - 2 = 1$ more right than left "movers".

The Chern number $C = 1$ indicates the existence of a topological edge state, or in general, an imbalance of "right moving" and "left moving" edge states by one. To visualize this state, we recast our 2D Hamiltonian into mixed boundary conditions: periodic along one direction and open along the other. The resulting 1D model is solved by using the iterative Green's function approach (Sancho et al., 1985) to get the spectra on a semi-infinite long cylinder. The band structure (Fig. 3.26) reveals the presence of edge states of two types: Trivial edge states originate from the conduction [valence] band and rebound back to the conduction [valence] band in Fig. 3.26(b) [Fig. 3.26(f)]. In contrast, the topological edge states connect the valence band and the conduction band. The difference in "right moving" (R_n) and "left moving" (L_n) states on each edge further corroborates our Chern number analysis. Please note that the Ru honeycomb in SRO (111) is buckled; Ru atoms at the left and the right edge are at a different height,

which explains the left/right asymmetry. Let us also note that for the $C = 1$ state, the consideration of the full microscopic model is needed: restricting the model to first-neighbor or first- and second-neighbor couplings only, yields unbalanced topological states as well but with different Chern numbers.

For an experimental observation of edge states, the size of the SOC-induced band gap plays a crucial role. Unfortunately, the gap size in 2 SRO : 7 STO (111) confines the prospective QAH state to low temperatures and impedes its experimental observation. Larger gaps can be obtained by increasing the SOC and/or the trigonal crystal field (Δ_{CF}) splitting. The SOC can vary from several meV to several hundred meV, but requires the substitution of the transition metal. A more sensible approach is to tune Δ_{CF} by choosing a different substrate. But in addition to the change in the gap size, this structural alteration will affect the mutual orientation of RuO₆ octahedron and in turn alter the hopping parameters. Which of the two competing states, the QAH state or the trivial insulator, is eventually stabilized, needs to be pinpointed by a microscopic analysis. Another promising way to enlarge the gap size is electronic doping, which shifts the chemical potential to $\frac{3}{4}$ filling on t_{2g} shell. If the chemical potential is within the gap, we expect an additional enhancement of the gap as e.g. described by the scissor operator in GW, see Ref. (Held et al., 2011) and references therein.

In summary, we have shown that bilayers of SrRuO₃ on a SrTiO₃ substrate in [111] direction emerge to be a candidate of long-sought-after room-temperature ferromagnetic half-metals with an ordered moment of $\sim 2\,\mu_B$ per Ru. The spin-orbit coupling opens a gap in the unoccupied part of the spectrum, which gives rise to a quantum anomalous Hall (QAH) state with the Chern number C=1. Accordingly, a direct simulation of the tight-binding Hamiltonian indicates that the number of left and right movers differs by one. Experimentally, these QAH states can be observed by angular resolved photoemission spectroscopy after laser pumping, as e.g. demonstrated in Ref. (Cacho, 2015) for other topological surface states.

3.6   High-Spin (S=2) States in SrRuO$_3$

This section is based on an article (under preparation) focus on oxygen vacancy in bulk SrRuO$_3$.

Introduction. Point defects in transition metal oxides give rise to modifications of electronic structure and physical properties which can induce exotic physics phenomena and novel functionalities. The interplay between the degree of freedom of spin, orbital, lattice distortion and electronic correlations offers a rich playground for investigating the effects of point defects. Recently, the fast development in bulk/film growth and materials deposition enable the possibility of experiments for atomically precise epitaxial complex oxide thin films and concentration control atomic defects, e.g. oxygen vacancy (OV). The combination of atomic defects and material growth is becoming the powerful experimental technique for induce/separate the exotic microstructural effects of transition metal oxides, being away from their *stoichiometric* bulk properties.

Stoichiometric ferromagnetic metal SrRuO$_3$ (SRO) is one such oxide that has attracted much attention. SrRuO$_3$ has an orthorhombic structure with bulk lattice parameters a=5.57 Å, b=5.53 Å and c=7.84 Å; moreover, it can be well represented as a pseudo-cubic perovskite with a=3.93 Å. It is one of the most frequently used oxide electrode materials, and well/extensively studied because of its high chemical stability, good thermal properties, and pseudocubic perovskite crystal structure, which are advantageous for integration with other oxide materials into heterostructures.

Generally concluded SrRuO$_3$ is an itinerant ferromagnetic oxide with a ferromagnetic Curie temperature (T_C) of 160 K and a magnetic moment between 0.8 to 1.6 μ_B/Ru, pointing to a band rather than atomic magnetism. It is unique as the only known 4d transition metal oxide ferromagnet. In most 4d systems, the extended orbitals increase the bandwidth and decrease the density of states at the Fermi level, precluding Stoner-type ferromagnetism. The unusual ferromagnetism for 4d system is original from the strong hybridization between Ru-4d and O-2p, leading to the enhancement of density of states (DOS) in Fermi-energy (E$_f$). Consequently, bulk SRO exhibits as one of the handful ferromagnetic/correlated metal in 4d TMOs. Due to the large crystal field splitting, Ru^{4+} ions are usually expected to be in the low-spin state (S=1) with an electron configuration that corresponds to t_{2g}(3↑, 1↓) 2μ_B/Ru^{4+}, higher than what is experimentally observed. DFT-GGA calculations always overestimate its ferromagnetism by predicting the magnetic moment as 1.76 (U=0 eV) to 2.00 μ_B/Ru (U>0 eV). The low-spin state (S=1) for d^4 configuration has also never been observed experimentally. The discrepancy between theory and experiments are attributed to: (i) the electron delocalization associated with itinerancy (Longo, Raccah, and Goodenough, 1968; Klein et al., 1996), (ii) spin canting (Gibb et al., 1974), (iii) a combination of larger magnetocrystalline anisotropy and the difficulty in making single-domain crystals and films (Kanbayasi, 1978).

The high-spin (S=2) state, which corresponds to a moment large as 3.4 μ_B and higher T_C, recently was observed by several groups (Grutter et al., 2010; Grutter et al., 2012; Ning, Wang, and Zhang, 2015), in (111)-oriented SRO thin films. And these enhancement of ferromagnetism had been explained in terms of an anisotropic reduction in the crystal field resulting from anisotropically reduced orbital overlap in distorted films. One would wonder whether filming can modify its magnetism, however the most frequently grown samples, (001)$_{Cubic}$-oriented thin films, lost both of the bulk SrRuO$_3$ ferromagnetism and metallic conductivity. The ferromagnetic

moments, conductivity and T_C decrease as reducing the thickness N of SRO, resulting in a anti-ferromagnetic insulating state. Unexpected, high-spin states are experimentally obtained by (110)- and (111)-oriented films growth. As far as authors know, the first report about the spin state is from A. J. Grutter *et al.* (Grutter et al., 2010; Grutter et al., 2012), who observed the S=2 high-spin state, with magnetic moment equals to $3.4\,\mu_B$/Ru, in (111)-oriented thin films. Later on, the group of Z. D. Zhang (Ning, Wang, and Zhang, 2015) also obtained such a high-spin states by analyzing the anisotropic properties of SRO (001)-, (110)- and (111)-oriented films. In their experiments, ferromagnetic moments, $\sim 3\,\mu_B$/Ru and $\sim 4\,\mu_B$/Ru, were observed in (110)- and (111)-oriented films, respectively. However x-ray magnetic circular dichroism spectroscopy (XMCD) measurements carried out by L. H. Tjeng's group (Agrestini et al., 2015) indicate the spin state transition from S=1 to S=2 is too expensive in energy and unlikely to happen in SRO. Moreover, for (111)-oriented SRO thin films DFT(+U) also fails in predicting such high-spin state, for both Ru^{4+} and SrO$_3{}^{4-}$ terminations (Kim and Min, 2014).

Other possibilities that can modify the spin state of SRO are atomic vacancy or substitution, while later one seems unlikely to happen in the well-synthesized SRO. The Ru-vacancy was considered as the candidate that changes ferromagnetic metallic state of SRO, however numerous experiments and calculations confirmed the reduction of ferromagentism induced by Ru-vacancy (Dabrowski et al., 2004; Lv et al., 2016). Generally the reductions of T_C and ferromagnetic moments are attributed to the crystal disorder effect and stronger electronic correlation effects which are due to the existence of a Ru-vacancy that effectively reduces the bandwidth of Ru-d orbitals. Another possibility is the weakening of super-exchange between Ru^{4+}, which however, lacks evidence. The last generally believed reason is the reduction of the strong hybridization between Ru-4d and O-2p orbitals, this hybridization is also the major origin of the strong and unique ferromagnetism of SRO among numerous perovskites d-ABO$_3$ materials. DFT(+U) calculation explained the ferromagnetic reduction by obtaining the antiferromagnetic spin cluster around Ru-vacancy in SRO (Lv et al., 2016), which seems complete the puzzle of Ru-vacancy story. To authors' knowledge, little is known about Sr vacancies, probably because it is hard to create controllably, but OV in SRO is extensively researched. M. Hiratani *et al.* revealed that the conductivity of SRO samples is dramatically dependent on the oxygen pressures when samples were synthesized (Hiratani et al., 1996). All of these puzzles lead to the motivations of experiments about how to modify/enhance the ferromagnetism of SRO away from its bulk limitation?

In this part, we demonstrate that oxygen vacancy is the origin of high-spin (S=2) state in SRO, single oxygen vacancy transfers the two surrounding Ru atoms from low-spin state $t_{2g}(3\uparrow, 1\downarrow)$ to high-spin state $t_{2g}(3\uparrow)e_g(1\uparrow)$, which is impossible in stoichiometric SRO irrespective of the layer thickness and the orientation of films. We demonstrate that such high-spin state can only be created by the existence of oxygen vacancy and is independent of structural details. By comparing the total energy of paramagnetic and ferromagnetic phases we conclude that creating oxygen vacancy also can increase the T_C of SRO. By spin-polarized DFT calculations for different size of SRO supercell, we found the vacancy concentration is a key factor to decide whether the high-spin state can occur. The crucial concentration is SrRuO$_{3-x}$ ($x \leq 0.625$). The origin of such high-spin state is that the missing of single oxygen atom enlarge the overlap the Ru-d_{z^2} orbital, leading to bond and anti-bond states $\frac{1}{\sqrt{2}}$ (d_{1z^2}+d_{2z^2}), $\frac{1}{\sqrt{2}}$ (d_{1z^2}-d_{2z^2}) (index 1 and 2 labels the two Ru sites close to oxygen vacancy, respectively). The bond state $\frac{1}{\sqrt{2}}$ (d_{1z^2}+d_{2z^2}) is energetically comparable

with the unaffected t_{2g} states, contributing to the occupation in d_{z^2} states. Two free electrons, which are created by the single OV, are trapped by the two Ru atoms next to OV, leading to larger ferromagnetic moments.
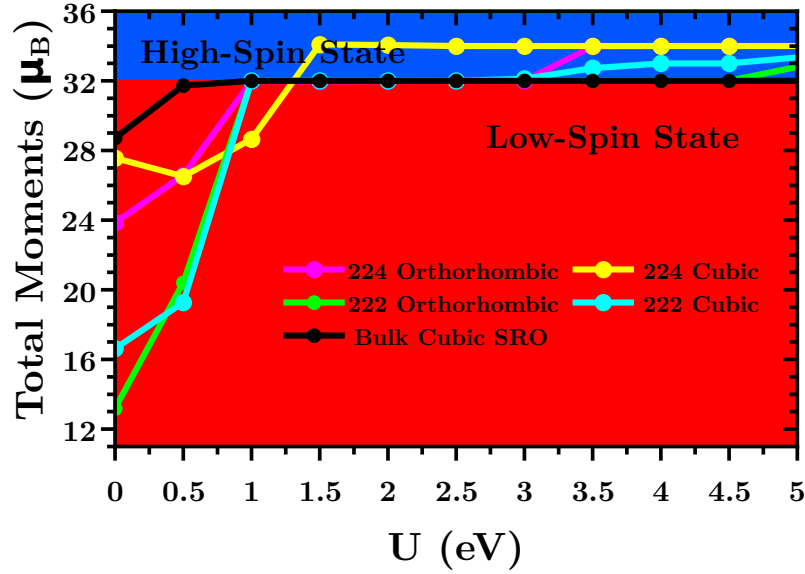

FIGURE 3.27: Total ferromagnetic moments vs. U values in DFT+U calculations.

Firstly we focus on the OV concentration, what is the critical value to switch on the high-spin state in bulk SRO. The corresponding results are shown in Fig. 3.27. For cubic bulk SRO, DFT-GGA predicts the moment to be 28.72 μ_B per cell containing 2×2×2=16 Ru atoms, corresponding to 1.79 μ_B/Ru. Then even a tiny U=0.5 eV drives the system into half-metallic state with the magnetic moment ~2.0 μ_B/Ru (total moment 32 μ_B). Larger U values fail in continuous increasing the total magnetic moments due to the large crystal splitting between t_{2g} and e_g bands. For other different settings of SRO supercell, we create one OV, thus the OV concentration in 1×1×1 (bulk cubic SRO), 1×1×2, 2×2×1, 2×2×2 and 2×2×4 supercells are 33.3%, 16.6%, 8.3% and 4.2% and 2.1%, respectively. In 1×1×1, 1×1×2 and 2×2×1 supercell, no high-spin states can be obtained even increase U to a large value (5 eV). However, when the size of supercell reaches 2×2×2 and above, high-spin states are obtained under reasonable U values. For the 2×2×2 cubic SRO supercell, the total moment exceeds ~33 μ_B when U is larger than 3.0 eV, for orthorhombic case, the critical U value shifts to 4.5 eV. For 2×2×4 cubic supercell, the total moment converges on 34 μ_B when U is larger than 1.5 eV, exceeding the low-spin limitation 32 μ_B. For orthorhombic 2×2×4 supercell, the critical U is 3.0 eV. Most importantly, we found the enhancement of magnetic moment is only from the two Ru sites next to OV: i.e. all other Ru sites stay in low-spin states with magnetic moment 1.79μ_B/Ru.

The DFT+U results lead to two conclusions: (i) to obtain high-spin states in SRO supercell with single OV, the supercell size has to be larger than 2×2×4 of pseudo-cubic cells, corresponding to a OV concentration 2.1%, the chemical formula is SrRuO$_{3-x}$ (x≤0.625); (ii) in cubic structure it is easier to obtain the high-spin state than in the orthorhombic case, because the critical U in cubic and orthorhombic cases are 1.5 eV and 3.0 eV, while the later is quite hard to reach in bulk SRO.

To compare the differences between the electronic structures of SRO with/without OV, we also show the DOS of *stoichiometric* SRO, obtained from a DFT+U calculation
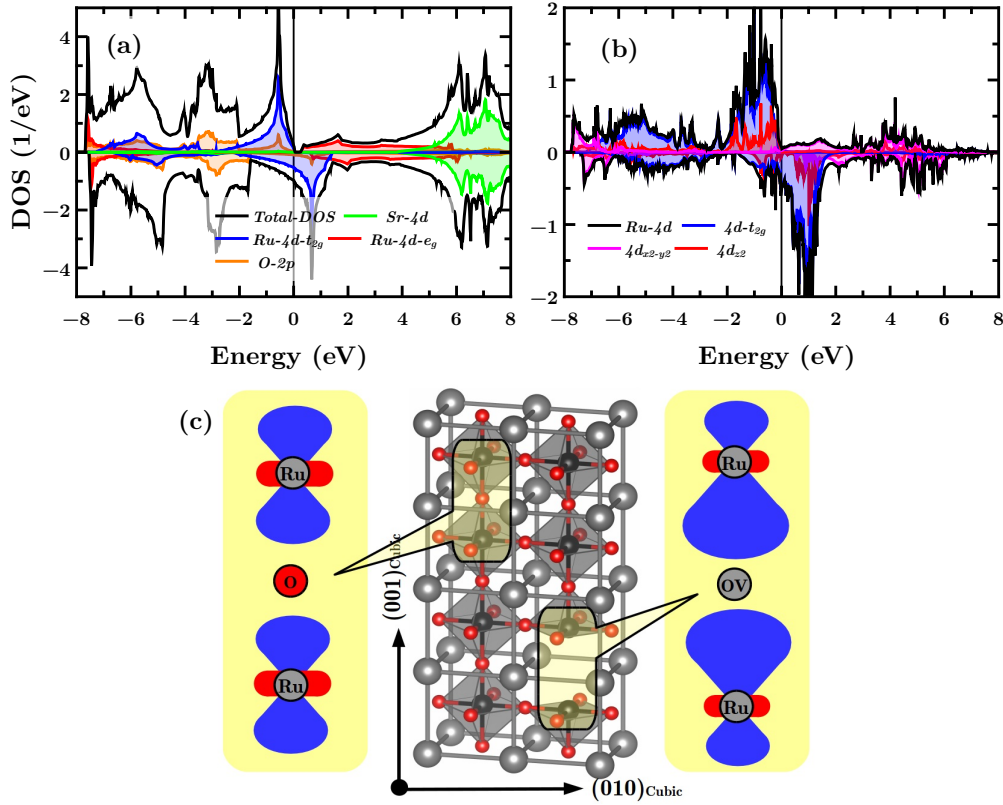
FIGURE 3.28: Orbital-resolved DOS of SRO with (a) or without (b) OV. A schematic physics picture of formation of the bonding and anti-bonding states is shown in (c).

[Fig. 3.28(a)]. Under the modification/correction of Coulomb U, the SRO is half-metallic state, Ru-4d-t_{2g} of spin-majority (up) channel is fully occupied, E$_f$ is located at spin-minority (down) channel of Ru-4d-t_{2g}, leading to the empty e_g states. The ferromagnetic moment is 2 μ_B/Ru and it is robust against increasing U, which is due to the large crystal splitting between e_g and t_{2g} bands. In Fig. 3.28(b) we show the DOS of Ru atoms that are next to the created OV. The $d_{x^2-y^2}$ state is empty, consistent with the DOS of SRO without OV [Fig. 3.28(a)]. However clear d_{z^2} occupation can be seen in spin-majority (up) channel. This leads to that the moments of Ru atoms next to OV are larger than its low-spin (S=1) limitation: 2 μ_B/Ru. The ferromagnetic moment of Ru next to OV is determined as 3.0 μ_B/Ru. The electrons that occupy d_{z^2} states are released by the created OV. We use a schematic figure to demonstrate the physics behind [Fig. 3.28(c)]. After creating an OV in SRO supercell, the d_{z^2} orbitals of Ru next to OV are more extend along z-direction [(001)$_{Cubic}$ orientation], leading to a bonding state $\frac{1}{\sqrt{2}}$ (d_{1z^2}+d_{2z^2}) and an anti-bonding state $\frac{1}{\sqrt{2}}$ (d_{1z^2}-d_{2z^2}). Compared with the original d_{z^2} states, the bonding and anti-bonding states lie energetically lower and higher, respectively.

To have a direct observation of the bonding and anti-bonding states, we plot their Wannier orbitals and also calculated the band characters of these two bands (Fig. 3.29). As shown in right panel, for the bonding state the electrons spread between two Ru atoms, leading to a lower eigenvalue while in the anti-bonding state electrons spread around two Ru sites, leading to a higher eigenvalue. The band characters plotting reveals the one-dimensional nature of bonding and anti-bonding
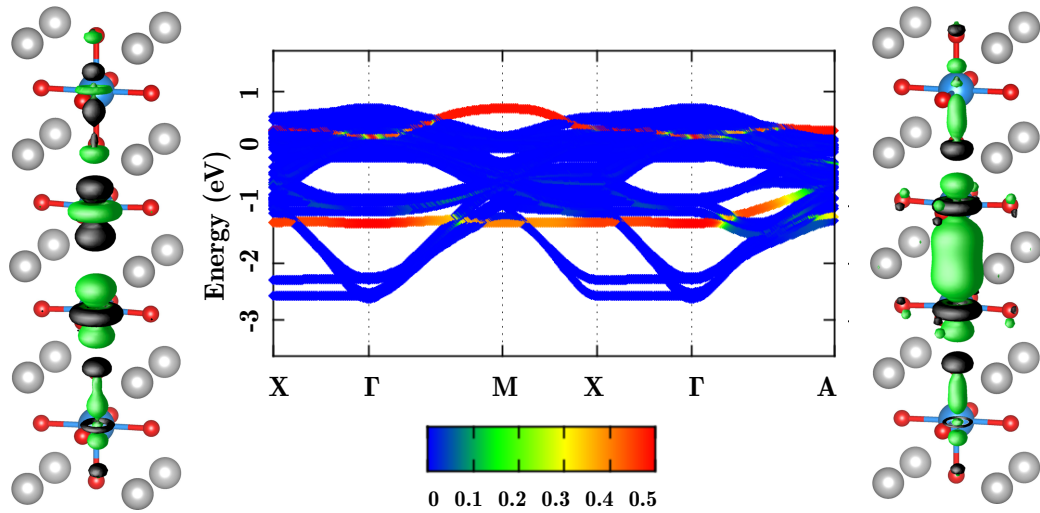
FIGURE 3.29: The wannier orbital $|W_n(R,r)|^2$ of anti-bonding $\frac{1}{2}(d_{1z^2}$-$d_{2z^2})$ (left panel) and bonding $\frac{1}{2}(d_{1z^2}+d_{2z^2})$ (right panel) state, and the corresponding band characters (middle panel), the energetically higher band is from the anti-bonding state while the energetically lower band is from the bonding state.

states: along X(0.5,0,0)-Γ(0,0,0)-M(0.5,0.5,0)-X(0.5,0,0)-Γ(0,0,0) k-path both the anti-bonding and bonding state bands are not k-dependent. Only along Γ-A(0.5,0.5,0.5) path the bonding bands disperses slightly.

Summary. In conclusion, by carrying out *first-principle* DFT+U calculations, we attribute the experimental confirmed high-spin states in SRO to the formation of oxygen vacancies. Single oxygen vacancy in bulk SRO transfers the two surrounding Ru atoms from low-spin states to high-spin ones. Two one-dimensional bonding $\frac{1}{2}(d_{1z^2}+d_{2z^2})$ and anti-bonding $\frac{1}{2}(d_{1z^2}$-$d_{2z^2})$ states are obtained, being energetically higher and lower than the original d_{z^2} states, respectively. Among these two states, the bonding state $\frac{1}{\sqrt{2}}(d_{1z^2}+d_{2z^2})$ is electronically occupied, contributing to the enhancement of magnetic moment under electronic correlation effects. The density of oxygen vacancies is a critical quantity to switch on/off such high-spin states, and the chemical formula is SRO$_{3-x}$ (x≤0.625), i.e. the concentration of oxygen vacancies can not be artificially high, otherwise the interaction between oxygen vacancies would suppress such high-spin states. For bulk SRO, the high-spin states are easier to occur in cubic phase than in orthorhombic phase, because in cubic environment a lower critical U value (1.5 eV) is needed to drive high-spin states than in orthorhombic environment (3.0 eV). All of these conclusions give hits about how to obtain high-spin states in SRO in further experiments.

But there are still more questions to answer: (1) whether orbital moments and spin-orbit interaction play a role in such high-spin states, (2) will we obtain different results from simulations of thin film cases with different orientations, e.g. (110) and (111)? (3) Whether strain can modify or stabilize, even further enhance such high-spin states? We expect to answer these questions in our further research.

Chapter 4

Tight-binding, DFT and DFT+DMFT research of Transition Metal Oxides

In **Chapter 3** we discussed our DFT($+U$) and DFT+DMFT results of SrRuO$_3$ thin films with (001)-, (110)- and (111)-orientation, and we demonstrated that how electronic correlation effects modify the DFT results. In this chapter we focus on several separated researches. These researches are devoted to the applications of DFT+U, TB and DMFT formalism for realistic materials. TB method is used to focus on the study of perovskite $A B$O$_3$ materials (e.g. BaOsO$_3$) in the present of spin-orbit coupling (SOC). DFT($+U$) is used to study the electronic structure and magnetic properties of LaSrMnO$_3$ thin films. DMFT method is employed to investigate the electronic and magnetic properties of 3d- and 4d-orbital materials, including V$_2$O$_3$ surfaces and double perovskite Sr$_2$CrMoO$_6$.

In this chapter the outline is like below: (i) with the understanding of Rashba effects in d-orbital $A B$O$_3$ materials interface/surface, we predict that giant Rashba spin splitting is indeed possible and even controllable by an external electric field by coupling ferroelectric BaTiO$_3$ and a 5d (or 4d) transition metal oxide with a large SOC, e.g. Ba(Os, Ir, Ru)O$_3$; (ii) Cooperating with experimental group, we present a theoretical study exploring surface effects on the evolution of the metal-insulator transition in the model Mott-Hubbard compound Cr-doped V$_2$O$_3$. We find a microscopic domain formation that is clearly affected by the surface crystallographic orientation. A DFT+DMFT study of different surface terminations shows that the surface reconstruction with excess vanadyl cations leads to doped, and hence more metallic, surface states, which explains the experimental observations; (iii) Using DFT+DMFT method we study the electronic structures of double perovskite compound Sr$_2$CrMoO$_6$, which is a sister compound of the much discussed material Sr$_2$FeMoO$_6$. Its ferrimagnetic half-metal nature is successfully captured after considering about both dynamic local or static correlation effects. Comparing our results with our theoretical cooperator's DFT results we reveal the robustness of its electronic structures against correlation effects; (iv) by using DFT($+U$) method, we investigate the electronic and magnetic properties of La$_{1-x}$Sr$_x$MnO3 thin films, demonstrating the relationship between structural details (film thickness, surfacing, MnO$_6$ octahedral rotation and tilting) and its ferromagnetism.

4.1   Giant Switchable Rashba Effect in Oxide Heterostructures

One of the most fundamental phenomena and a reminder of the electron's relativistic nature is the Rashba spin splitting for broken inversion symmetries in two-dimensional condensed matter systems. Typically, this splitting is a tiny relativistic correction. By coupling ferroelectric $BaTiO_3$ and a $5d$ (or $4d$) transition metal oxide with a large spin-orbit coupling, $Ba(Os, Ir, Ru)O_3$, it is shown that giant Rashba spin splittings are indeed possible and even controllable by an external electric field. Based on density functional theory and a microscopic tight-binding understanding, it is concluded that the electric field is amplified and stored as a ferroelectric Ti-O distortion which, through the network of oxygen octahedra, induces a large (Os, Ir, Ru)-O distortion. The $BaTiO_3/Ba(Os, Ru, Ir)O_3$ heterostructure is hence the ideal test station for switching and studying the Rashba effect and allows applications at room temperature.

Introduction. An electric field control of the spin degree of freedom is the key to spintronics and magnetoelectrics (Zutic, Fabian, and Das Sarma, 2004). In the prototypical spintronic device, the Datta-Das spin transistor (Datta and Das, 1990), an electric field tunes the Rashba spin splitting and with that the spin precession frequency. The precession in turn controls the spin polarized current between two ferromagnetic leads. Microscopically, the Rashba spin splitting originates from the spin orbit coupling (SOC) in a two dimensional electron gas (2DEG) with broken inversion symmetry perpendicular to the 2DEG plane (Rashba, 1960; Winkler et al., 2003). It has been observed for metal surfaces (LaShell, McDougall, and Jensen, 1996; Ast et al., 2007), semiconductor and oxide heterostructures (Nitta et al., 1997; Caviglia et al., 2010; Shalom, 2010; Nakamura, Koga, and Kimura, 2012; King et al., 2011; King et al., 2012), and even in polar bulk materials (Ishizaka et al., 2011). The Rashba effect splits parabolic bands into two subbands with opposite spin and energy-momentum dispersions $E^{\pm}(\mathbf{k}) = (\hbar^2\mathbf{k}^2/2m^*) \pm \alpha_R|\mathbf{k}|$. Here, m^* is the effective mass, $\mathbf{k}$ the wave vector in the 2DEG plane, and α_R the Rashba coefficient which depends on the strength of SOC and inversion asymmetry. An electric field modulates this inversion asymmetry and consequently the Rashba spin splittings. The electric-field induced change of α_R is however weak: up to 10^{-2} eVÅ in semiconductor (Nitta et al., 1997) or $3d$ transition metal oxide heterostructures (Caviglia et al., 2010; Shalom, 2010; Nakamura, Koga, and Kimura, 2012). A large, electric-field tunable Rashba effects are also much sought-after in the research area of topological insulators (Bahramy et al., 2012; Nakosai, Tanaka, and Nagaosa, 2012; Das and Balatsky, 2013).

Giant Rashba effects with α_R of the order of 1 eVÅ have been reported for metal surfaces (Ast et al., 2007), Bi adlayers (Mirhosseini et al., 2010) and bulk polar materials BiTeI (Ishizaka et al., 2011; Zhou, 2014). The large α_R here relies on the surface or interface structural asymmetry, which is hardly changes in an external electric field. To enhance the tunability by an electric field, Di Sante *et al.* (Di Sante, Domenico et al., 2013) hence suggested a ferroelectric semiconductor GeTe. For GeTe, an external electric field switches between paraelectric and ferroelectric phase, breaking inversion symmetry and tuning on the Rashba spin

splitting. At first glance, this perfectly realizes an electric field control of a giant Rashba effect. However, there is an intrinsic difficulty: A single material cannot be both, a conductor with large Rashba spin splitting and a ferroelectric which necessarily is insulating.

In this article, we propose to realize a giant switchable Rashba effect by heterostructures sandwiching a thin metallic film of heavy elements in-between ferroelectric insulators (Fig. 4.1). The thin film provides a 2DEG with strong SOC, while the inversion asymmetry is induced by the structural distortion of the ferroelectrics and tunable by an electric field. As a prime example, we study a heterostructure of transition metals oxides, $BaOsO_3/BaTiO_3$. $BaTiO_3$ is a well-established ferroelectric (Dawber, Rabe, and Scott, 2005). It has a simple high-temperature perovskite structure, with Ba atoms at the edges, a Ti atom at the center and the O atoms at the faces of a cube. Such a structure has an inversion symmetry center at the Ti site. At room temperature, inversion symmetry is broken since a ferroelectric structural distortion occurs with a sizable Ti-O displacement z_{Ti-O} along one of the the cubic axes. $BaOsO_3$ has been recently synthesized; it is a metallic perovskite with four Os $5d$ electrons and no sign of magnetism (Shi et al., 2013). It has a perfect lattice match with $BaTiO_3$. Both materials have the same cation, Ba, which will substantially reduce disorder during epitaxial growth. For $BaOsO_3/BaTiO_3$ we find an electric-field tunable Rashba spin splitting which is at least one magnitude larger than the current experimental record (Nitta et al., 1997; Caviglia et al., 2010; Shalom, 2010; Nakamura, Koga, and Kimura, 2012). The mechanism behind is nontrivial and summarized in Fig. 4.1. Substituting $BaOsO_3$ by $BaIrO_3$ and $BaRuO_3$ yields a similar effect; the heterostructure can also be further engineered by varying its thickness and strain.
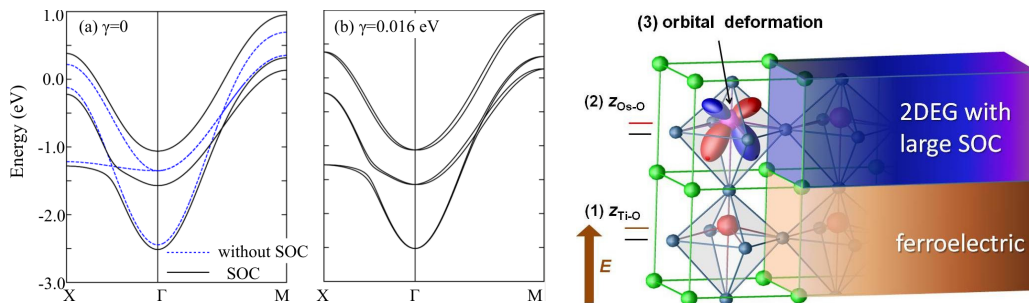
FIGURE 4.1: Left panel: tight binding bandstructure of the three Os t_{2g} orbitals for (a) the paraelectric case with and without SOC and (b) the ferroelectric case with SOC and asymmetry parameter $\gamma = 0.016\,eV$ taken from the Wannier projection. Right panel: schematics of the mechanism behind the giant switchable Rashba effect: (1) An external electric field is amplified and stored as a ferroelectric distortion, in particular Ti-O displacements. (2) These displacements entail, via the oxygen octahedron network of the perovskite heterostructure, Os-O displacements. (3) As a consequence of the Os-O displacements the Os orbitals deform, which reflects the broken inversion symmetry. This orbital deformation and the strong SOC of Os finally lead to a giant Rashba spin splittings that is controllable by an electric-field.
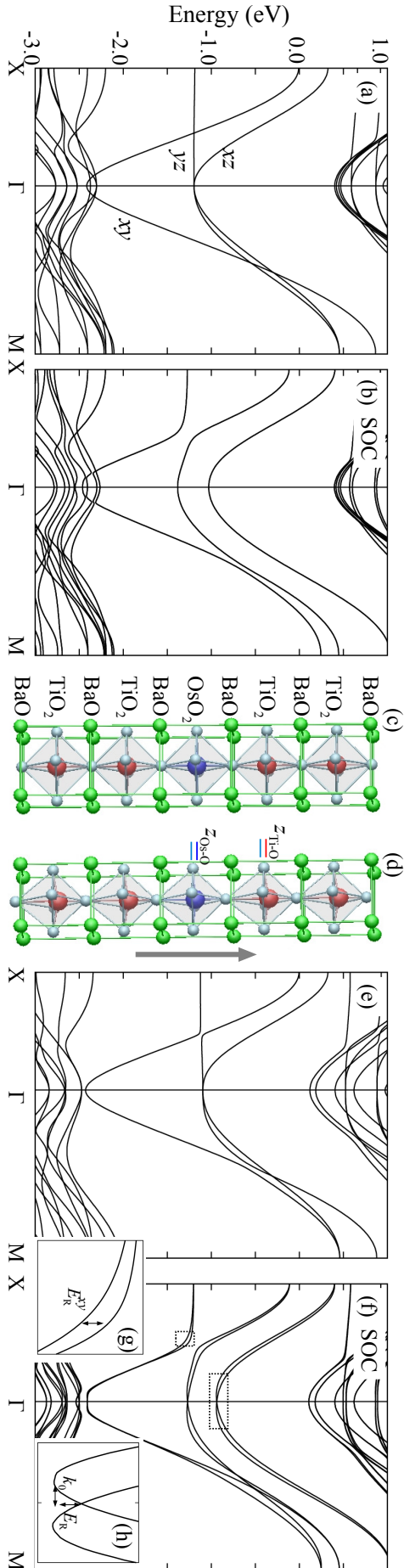
FIGURE 4.2: DFT calculated band structures of $(BaOsO_3)_1/(BaTiO_3)_4$ multilayers for the paraelectric (c) and ferroelectric structure (d). The paraelectric heterostructure breaks cubic but not inversion symmetry so that the Os xy orbital splits off from two degenerate yz/xz orbitals without SOC (a); including SOC further lifts the yz/xz degeneracy (b). The ferroelectric state further breaks inversion symmetry, which essentially does not change the bandstructure in the absence of SOC (e) but leads to substantial spin splittings in the presence of SOC (f). The spin splitting E_R^{xy} at the $xy - yz$ crossing region is magnified in (g), while the standard Rashba spin splitting E_R with momentum offset k_0 around Γ of the upper yz/xz mixed orbital is magnified in (h).

Calculation details. We mainly focus on a $BaOsO_3/BaTiO_3$ heterostructure which has two structural phases: a paraelectric perovskite phase [Fig. 4.2(a)-(c)] and a distorted ferroelectric phase [Fig. 4.2(d)-(h)], respectively. We use density-functional theory (DFT) with generalized gradient approximation (GGA) potential (Perdew, 1985) in the Vienna *Ab-initio* Simulation Package (VASP) (Kresse and Hafner, 1993; Kresse and Furthmüller, 1996) and fully relax all the atomic positions, only fixing the paraelectric or ferroelectric symmetries. At zero temperature, the ferroelectric distorted perovskite has the lower GGA energy, but -as in the bulk- the undistorted paraelectric phase will prevail at elevated temperatures. Based on the fully relaxed atomic structures, electronic band structures are calculated with modified Becke-Johnson (mBJ) (Tran and Blaha, 2009) exchange potential as implemented in the Wien2k code (Blaha et al., 2001), which improves the calculated band gap of $BaTiO_3$. The SOC is included as a perturbation using the scalar-relativistic eigenfunctions of the valence states. Employing Wien2wannier interface (Kuneš et al., 2010), we project the DFT band structure onto maximally localized (Mostofi et al., 2008) Wannier orbitals, from which the orbital deformation is analyzed and a realistic tight-binding model is derived (Zhong, Zhang, and Held, 2013). We also vary the thickness of the thin films, replace the $BaOsO_3$ by $BaRuO_3$ or $BaIrO_3$, and simulate the strain effect by fixing the in plane lattice constant to the value of a $SrTiO_3$ substrate. Correlation effects from local Coulomb interaction are studied in the Supplementary Material.

Paraelectric phase. We mainly focus on a $BaOsO_3/BaTiO_3$ heterostructure, $(BaOsO_3)_1/(BaTiO_3)_4$, which consists of one $BaOsO_3$ layer alternating with four $BaTiO_3$ layers. Bulk $BaTiO_3$ is a d^0 insulator: the empty Ti $3d$ states lie about $3\,eV$ above occupied O $2p$ states. Bulk $BaOsO_3$ is a d^4 metal: four electrons in the Os-$5d$ orbitals of t_{2g} character are $0.8\,eV$ above the filled O $2p$ states. Since $BaOsO_3$ and $BaTiO_3$ share oxygen atoms at the interface, the O $2p$ states align; and the Os $5d$ states will stay in the energy gap of $BaTiO_3$. Hence, the density functional theory (DFT) calculated band structures of $BaOsO_3/BaTiO_3$ in Fig. 4.2 shows three Os t_{2g} (xy, yz, xz) bands near the Fermi level; they are dispersionless along the z direction (not shown). That is, the low energy electronic degrees of freedom are confined by the insulating $BaTiO_3$ layers to the OsO_2 plane, forming a 2DEG. Already in the high temperature paraelectric phase, this heterostructure confinement reduces the initial cubic symmetry of the Os t_{2g} orbitals in the bulk perovskite: at Γ the xy band in Fig. 4.2(a) is $1.2\,eV$ lower in energy than the degenerate yz/xz bands. Including the SOC, the yz/xz doublet splits into two subbands with mixed yz/xz orbital character [Fig. 4.2(b)]. For the paraelectric phase [Fig. 4.2(a)-(c)], the spin degeneracy is however still preserved.

To better understand the DFT results, we construct an interface hopping Hamiltonian H_0^i (Zhong, Tóth, and Held, 2013) for the 2DEG confined Os t_{2g} electrons by a Wannier projection. The energy-momentum dispersion for the xy orbital is $\epsilon(\mathbf{k})^{xy} = -2t_1 \cos k_x - 2t_1 \cos k_y - 4t_3 \cos k_x \cos k_y$, while that of the yz is $\epsilon(\mathbf{k})^{yz} = -2t_2 \cos k_x - 2t_1 \cos k_y$ ($\epsilon(\mathbf{k})^{xz}$ is symmetrically related by $x \leftrightarrow y$). The largest hopping $t_1 = 0.392\,eV$ is along the direction(s) of the orbital lobes, $t_2 = 0.033\,eV$ and $t_3 = 0.094\,eV$ indicate a much smaller hopping perpendicular to the lobes and along $(1, 1, 0)$, respectively. The xy–yz/xz orbital splitting at Γ is $2t_1 - 2t_2 + 4t_3 = 1.1\,eV$ and arises from the anisotropy of the orbitals. Overall, the three parameter tight binding model in Fig. 4.1(a) (dashed line) is consistent with DFT in Fig. 4.2(a). Next, we include the atomic SOC Hamiltonian $H_\xi = \xi \vec{l} \cdot \vec{s}$,

expressed in the t_{2g} basis with $\xi = 0.44$ eV for Os. It lifts the yz/xz degeneracy and yields good agreement with DFT, cf. Fig. 4.1(a) (solid line) and Fig. 4.2(b).

Ferroelectric phase. In sharp contrast to the paraelectric case, ferroelectrically distorted $BaOsO_3/BaTiO_3$ exhibits evident spin splittings in the presence of SOC, see Fig. 4.2(f). Note, in the absence of SOC the DFT band structure in Fig. 4.2(e) is still very similar to the paraelectric case in Fig. 4.2(a). The spin splitting E_R^{xy} of the xy band is small around Γ, but strongly enhanced up to 50 meV around the xy/yz crossing region as shown in Fig. 4.2(g), cf. Table 4.1. The other two subbands of yz/xz character also show a strong splitting around Γ. In this respect, the upper yz/xz subband exhibits a standard Rashba behavior, see the magnification in Fig. 4.2(h), where the momentum offset k_0=0.043 Å^{-1}, the Rashba energy $E_R = 4$ meV, and hence α_R=$2E_R/k_0$=0.186 eVÅ. The behavior of the lower yz/xz subband is more complex (distorted) due to the proximity of the crossing region. A similar structure of the spin orbit splitting as well as a k-cubic splitting has been reported for other t_{2g} systems before (Zhong, Tóth, and Held, 2013; Nakamura, Koga, and Kimura, 2012).

These spin splittings arise from ferroelectric distortions which break the inversion symmetry. Bulk $BaOsO_3$ has no such ferroelectric distortions and is inversion symmetric with Os and O atom in the same plane. Also for the paraelectric heterostructure, the OsO_2 layer is still an inversion plane. The ferroelectric heterostructure breaks inversion symmetry. As listed in Table. 4.1, the averaged ferroelectric Ti-O displacement in $BaTiO_3$ layers is around 0.14 Å, which efficiently induces a sizable Os-O displacement of 0.05 Å via the oxygen octahedron network of the perovskite structure. This structural distortion modifies the crystal environment of Os t_{2g} orbitals and deforms the orbital lobes (Fig. 4.1).

In order to quantify the orbital deformation, we project the DFT results above onto maximally localized Wannier orbitals and directly extract the key parameter: a directional, spin-independent inter-orbital hopping $\gamma = \langle xy|H|yz(R)\rangle$, were R is the nearest neighbor in x direction. In **k**-space one gets as a matrix for the yz,xz,xy orbitals (independent of spin) (Zhong, Tóth, and Held, 2013):

$$H_\gamma = \gamma \begin{pmatrix} 0 & 0 & 2i\sin k_x \\ 0 & 0 & 2i\sin k_y \\ -2i\sin k_x & -2i\sin k_y & 0 \end{pmatrix}. \tag{4.1}$$

We obtain $\gamma = 0.016$ eV for the ferroelectric heterostructure, while for the paraelectric case $\gamma = 0$ due to inversion symmetry. Let us emphasize that γ is the relevant measure for the orbital deformation and inversion symmetry breaking. In combination with the strong SOC of OS $5d$ electrons, H_γ results in the present giant Rashba spin splitting.

The Hamiltonian $H_0^i + H_\xi + H_\gamma$ already well describes the spin splittings of the xy orbital in good agreement with DFT results, but underestimates the spin splittings of the yz/xz subbands near Γ. The reason for this is that the atomic SOC is not an accurate description anymore because the SOC of Os is too strong and the deviation from the inversion symmetry too large. Hence, we need to go beyond the purely atomic SOC and include an inversion asymmetry correction to the SOC matrix so that H_ξ in the t_{2g} basis ($yz|\uparrow\rangle$, $yz|\downarrow\rangle$, $xz|\uparrow\rangle$, $xz|\downarrow\rangle$, $xy|\uparrow\rangle$, $xy|\downarrow\rangle$) reads

$$
\begin{pmatrix}
0 & 2\gamma' \sin k_y & i\frac{\xi}{2} & 0 & 0 & -\frac{\xi}{2} \\
2\gamma' \sin k_y & 0 & 0 & -i\frac{\xi}{2} & \frac{\xi}{2} & 0 \\
-i\frac{\xi}{2} & 0 & 0 & -2\gamma' \sin k_x & 0 & i\frac{\xi}{2} \\
0 & i\frac{\xi}{2} & -2\gamma' \sin k_x & 0 & i\frac{\xi}{2} & 0 \\
0 & \frac{\xi}{2} & 0 & -i\frac{\xi}{2} & 0 & 0 \\
-\frac{\xi}{2} & 0 & -i\frac{\xi}{2} & 0 & 0 & 0
\end{pmatrix} . \tag{4.2}
$$

For the band structure of Fig. 4.1(b) we have taken γ'=0.022 eV from the Wannier projection, yielding good agreement with the DFT results Fig. 4.2(f).

Electric-field tunability. The Rashba spin splittings can be tuned by an electric field because of the ferroelectricity of $BaTiO_3$. It is a nature of ferroelectrics that an external electric field can tune and even reverse the polarization and structural distortion (Mathews, S. et al., 1997; Dawber, Rabe, and Scott, 2005; Duan, Jaswal, and Tsymbal, 2006; Mirhosseini et al., 2010; Tazaki, 2009), including that of the $BaOsO_3$ layer. Because of the $BaOsO_3$ layer, the ferroelectricity of the heterostructure is not as strong as in bulk $BaTiO_3$. Hence a smaller electric field change than in the bulk [E=10^3 V/cm (Tazaki, 2009)] is be needed for going through the ferroelectric hysteresis loop. Such an electric field can tune the Rashba coefficient listed in Table. 4.1, which are at least one order of magnitude more larger than in semiconductors (Nitta et al., 1997) or $3d$ oxide heterostructures (Caviglia et al., 2010; Shalom, 2010; Nakamura, Koga, and Kimura, 2012). For applications it is of particular importance that E_R now clearly exceeds 0.025 eV, the thermal energy at room temperature. Furthermore, we propose to take advantage of the ferroelectric hysteresis and the remnant ferroelectric polarization, using our heterostructure as a spintronics memory device.

By changing temperature and inducing strain one can tune the amplitude of the ferroelectric distortion and hence the Rashba splitting. At elevated temperatures, the system is close to a second order ferroelectric transition. In this situation, we have a paraelectric with huge dielectric constant so that an electric field can continuously change the amplitude of SOC splitting.

Heterostructure engineering. Besides applying an electric field, heterostructure engineering such as varying its thickness, strain, and the material combination is a powerful way to tune the Rashba spin splittings. First, we vary the thickness of $BaOsO_3$ and $BaTiO_3$. It is well known experimentally and theoretically (Junquera and Ghosez, 2003; Dawber, Rabe, and Scott, 2005) that below a few nanometer thickness of the $BaTiO_3$ film, the Ti-O displacement is reduced and eventually ferroelectricity vanishes. As shown in Table. 4.1, when decreasing the thickness of $BaTiO_3$ and increasing that of $BaOsO_3$, the Rashba spin splittings is indeed substantially reduced. Second, ferroelectricity of $BaTiO_3$ is sensitive to strain (Choi, 2004). Taking $SrTiO_3$ as a substrate provides a 2.5% in-plane compressive strain. This enhances the ferroelectric distortion as well as Rashba spin splitting, α_R=0.417 eVÅ in Table. 4.1. Given the giant Rashba splitting, photoemission and transport measurements should be able to validate this effect by comparing thin films with different thickness and substrate. Third, we replace Os by other $5d$ elements for shifting the Fermi energy; and also since some Os oxides are toxic. Indeed, similar physics can be found in $BaIrO_3/BaTiO_3$ with $\alpha_R = 0.731$ eV Å, see Table. 4.1, and in $BaRuO_3/BaTiO_3$. The latter also offers a platform to study the interplay of Rashba physics and electronic correlations; for instance, novel phenomena is expected in mixed $3d$-$5d$ transition-metal materials

TABLE 4.1: Polar distortions and Rashba spin splittings of $(BaOsO_3)_n/(BaTiO_3)_m$ multilayers, alternating n layers of $BaOsO_3$ and m layers of $BaTiO_3$. Second and third column: averaged displacement of Os-O and Ti-O along z as calculated by DFT. Forth column: strength of the interface asymmetry term γ obtained from the Wannier projection. Fifth to seventh column: DFT calculated parameters characterizing Rashba effects: momentum offset k_0, Rashba energy E_R, and Rashba coefficient α_R of the upper yz/xz subband around Γ as defined in Fig. 4.2(h). Eighth column: spin splitting E_R^{xy} around the crossing region of xy and yz orbitals as in Fig. 4.2(g). To demonstrate the effects of heterostructure engineering, we also list the results of $BaOsO_3/BaTiO_3$ strained by a $SrTiO_3$ substrate, as well as $BaRuO_3/BaTiO_3$ and $BaIrO_3/BaTiO_3$. Band structures are given in Supplementary Material of Ref. (Zhong et al, 2015).

$n:m$	Os-O (Å)	Ti-O (Å)	γ (eV)	k_0 (Å^{-1})	E_R (eV)	α_R (eVÅ)	E_R^{xy} (eV)
1:3 $BaOsO_3/BaTiO_3$	0.038	0.065	0.011	0.025	0.001	0.08	0.031
1:4	0.049	0.103	0.016	0.043	0.004	0.186	0.053
2:3	<0.010	<0.010	0.003	0	0	-	0.004
2:4	0.024	0.071	0.010	0.035	0.002	0.114	0.018
1:3 strained	0.095	0.223	0.030	0.105	0.021	0.396	0.102
1:4 strained	0.099	0.229	0.031	0.115	0.024	0.417	0.106
1:4 $BaIrO_3/BaTiO_3$	0.115	0.119	0.021	0.145	0.053	0.731	0.051
1:4 $BaRuO_3/BaTiO_3$	0.082	0.119	0.015	0.128	0.016	0.250	0.007

(Yin et al., 2013). Let us also note that a strong temperature dependence of α_R in SrIrO_3 was recently reported (Zhang et al., 2014). While in this paper we focus on t_{2g} electrons in oxide heterostructures along the (001)-orientation, a topological behaviour was reported in (111) oxide heterostructures (Xiao et al., 2011). Hence, another idea and extension of the present paper is to incorporate a ferroelectric material such as BaTiO$_3$ in a (111) heterostructure for studying the interplay of Rashba SOC and topology.

Conclusion. We propose to combine a heavy $5d$ compound such as BaOsO$_3$ and a ferroelectric such as BaTiO$_3$ in a heterostructure for realizing giant Rashba spin splittings that are switchable by an electric field. The physics behind is that ferroelectric BaTiO$_3$ amplifies the electric field through a distortion (polarization) of its TiO$_6$ octahedra. This distortion very efficiently propagates to the OsO$_6$ octahedron via the shared oxygens, breaking inversion symmetry and deforming the Os orbital lobes. Together with the strong SOC it leads to a giant tunable Rashba effect with, e.g., α_R=0.731 eVÅ for BaIrO$_3$/BaTiO$_3$. This is at least one magnitude larger than state-of-the-art. Moreover, the ferroelectric hysteresis and remnant polarization leads to a memory effect which can be exploited for spintronics memory devices.

4.2 Mott-Insulator Transition at V_2O_3 Surfaces

In this section we will introduce our DFT+DMFT applications about surface states of V_2O_3. With DMFT calculations on finite surface models with different terminations, we demonstrate that the conductivity of V_2O_3 surfaces are controlled by surface terminations.

Cr-doped V_2O_3 is the prototype Mott-Hubbard material, presenting a correlation-induced MIT without symmetry breaking. Strong electronic correlation splits the noninteracting bands into interacting upper and lower Hubbard bands. In the metallic phase a strongly renormalized quasi-particle peak remains at the Fermi level, which is reminiscent of the uncorrelated band structure. The phase diagram of V_2O_3 consists of three phases: the paramagnetic insulator (PI), paramagnetic metal (PM), and antiferromagnetic insulator (AFI) phases. The Mott transition takes place between the PI and PM phases; it can be induced by increasing pressure starting from the PI phase, as well as by decreasing temperature for doping levels with a concentration of around 1.1%Cr. The orbital degrees of freedom in V_2O_3 have to be taken into account in order to understand the MIT: the low-lying orbitals are the t_{2g} orbitals made up of singly degenerate a_{1g} and doubly degenerate e_g orbitals in the crystal field of the corundum the Hund's exchange leading to a local spin alignment throughout the transition. Although the surface of V_2O_3 has been well studied for the pure compound, and extensive experimental/theoretical investigations have been carried out on the surface termination of V_2O_3, very little is known about the effects of the surface on the Mott transition. In this part of thesis, by using DFT+DMFT we explore how the surface terminations modify the bulk states under correlation effects.

One might envisage the cleavage steps as an extra surface, and that surface effects should, thus, be enhanced. However, the usual suspects of electronic correlations at (enhanced) surfaces, i.e., an enhanced U because of the reduced screening and the removed hopping perpendicular to the surface, suggest the surface and cleavage steps to be more insulating. We find the contrary: they are more metallic. As these simple explanations fail, we need to inspect the surface more thoroughly, including the proper surface reconstruction. DFT calculations (Kresse et al., 2004) indicate, depending on the oxygen partial pressure, a VO surface termination with various excesses of vanadyl or a O_3 termination. The former has also been identified in some experiments (Feiten et al., 2015; Surnev, Ramsey, and Netzer, 2003; Kolczewski et al., 2007; Dupuis et al., 2003; Schoiswohl et al., 2004). Fig. 4.3 shows the actual supercells with VO and O_3 terminations that we consider in our calculation. One can envisage the surface as consisting of several layers of the stoichiometric (V-O_3-V) unit cell, i.e., (V-O_3-V)-(V-O_3-V)…(V-O_3-V) plus an extra V or (O_3-V) layer for the VO and O_3 termination, respectively; see Fig. 4.3 (left and right panels).
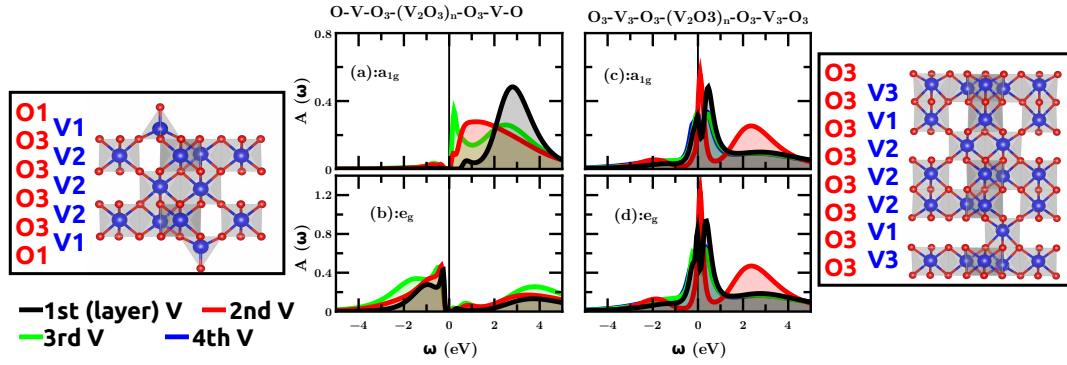
FIGURE 4.3: Top: VO termination (left) and O3 termination (right) supercell. Above the figures, we indicate how the supercell is made up from the stoichiometric (V-O$_3$-V) supercell plus the surface termination. For the O$_3$ termination, one V moves from the second to the first layer because of the surface reconstruction (Kresse et al., 2004). Bottom: Layer- and orbital-resolved spectral function $A(\omega)$ for the VO termination [(a)–(b)] and for the (O$_3$) termination [(c)–(d)]. The more excess oxygen at the surface, the more metallic are the surface layers.

Calculation details. We perform a full relaxation of the VO- and O$_3$-terminated V_2O_3 surfaces in the corundum structure, including a 12 Å-thick vacuum layer, using the Vienna ab initio simulation package (VASP) (Kresse and Hafner, 1993; Kresse and Furthmüller, 1996), with a GGA-PBE functional (Perdew, Burke, and Ernzerhof, 1996). In the case of the O$_3$ termination, the large polarity of the surface is compensated by a surface reconstruction where one subsurface V atom moves from the second layer to the first (surface) layer, so that O$_3$-V-V-O$_3$-V-V-O$_3$-V... actually becomes O$_3$-V$_3$-O$_3$-V-O$_3$-V.... The surface reconstruction for the VO termination is less dramatic. After atomic relaxation, we project the corresponding Wien2K (Blaha et al., 2001) band structure onto Wannier functions using Wien2Wannier (Kuneš et al., 2010) and supplement it by a local density-density interaction with intra-orbital U=5.5 eV, inter-orbital U'=4.1 eV and Hund's exchange J=0.7 eV. The interaction parameters are taken a bit larger than in the literature (Held et al., 2001); this is done because of the reduced screening at the surface and also to account for the more insulating nature at the experimental 1.1%Cr doping, which is too small to take into account in the supercell of our calculations. The resulting Hamiltonian is then solved by DMFT at room temperature, 300 K, using continuous-time quantum Monte Carlo simulations in the hybridization expansions Gull et al., 2011 [W2dynamic code (Parragh et al., 2012)] and the maximum entropy method (Gubernatis et al., 1991) for an analytic continuation of the spectra.

DFT+DMFT results. Fig. 4.3 (middle panels) shows the DFT+DMFT spectra for VO (left) and O$_3$ termination (right), resolved for the a_{1g} and e_g^π orbitals and the different layers. The VO-terminated surface is insulating at this interaction strength and temperature. Compared to a $3d^2$ electronic configuration for all V atoms, the vanadyl termination adds 1 extra O to each (V-O$_3$-V) unit cell in the layer, i.e., 1 hole per V in the layers. According to our DFT+DMFT results, this hole is, however, bound to the surface layer (where the single V in the surface layer is in a V^{4+} or $3d^1$ configuration) and to the second layer (where one of the two V atoms is V^{4+}). The other V atom in the second layer and all other V in the

further subsurface layers are in a V^{3+} or $3d^2$ configuration. This charge dispro-portionation explains why, despite the doping, the surface may remain insulating. Note that Fig. 4.3 shows the layer-averaged spectrum; the Supplemental Material of our publication (Lantz et al., 2015) it is resolved for the two inequivalent sites of the second layer. If we reduce the interaction strength, the VO-terminated sur-face becomes metallic. Indeed, the VO terminated surface is more metallic than bulk V_2O_3; i.e., it stays metallic up to larger values of the Coulomb interaction [see Supplemental Material of Ref. (Lantz et al., 2015)].

On the other hand, the O_3 termination (Fig. 4.3 right panel) is already metal-lic at the same Coulomb interaction and temperature. The most metallic layer is the surface/sub-surface layer, and the width of the central quasi-particle peak shrinks from layer to layer. The fourth, central layer is already close to the bulk result. The reason why the surface layer is more metallic, despite the reduced hopping, is the even larger hole doping due to the O_3 termination. In the case of the O_3 termination, the (O_3-V_2) slab adds to the stoichiometric (V-O_3-V) layers 3 holes per (V-O_3-V) unit cell in the layers (or 1.5 holes per V atom). These 1.5 holes are now, however, distributed to 3 surface layers in the DFT+DMFT charge dis-tribution: 1.2 electrons per V for the first layer, 1.5 per V for the second layer, 1.9 per V for the third layer, and 2.00 (i.e., the bulk value) for the fourth layer. That is, for the O_3 termination, vanadium is neither V^4+ nor V^3+ but in between. Con-sequently, the system is more itinerant, and the (001) surface layers of V_2O_3 are metallic. Let us emphasize that the extra oxygen stabilizes the polar (001) surface. This is not the case for the (102) layer, which is thus more stable stoichiometrically and more insulating [see Supplemental Material of (Lantz et al., 2015)].

We can, hence, conclude that excess oxygen makes the (reconstructed) surface more metallic due to hole doping. The additional surface at the steps indicates an extra surface doping such that V_2O_3 will be even more metallic at such edges. This is akin to our description of the O_3 termination versus the VO termination. As we have seen, this larger amount of doping does not have a very big effect, but it shifts the critical Coulomb interaction for the Mott-Hubbard transition some-where to the left of the phase diagram [inset of Fig. 1 of Ref. (Lantz et al., 2015)]. That means the transition temperature increases, as we found experimentally. It also explains our experiment in Fig. 3 of Ref. (Lantz et al., 2015); the cleave step is more metallic because of an accumulation of excess oxygen at the corner.

Conclusions. By using DFT+DMFT, we explained the experimentally ob-served PI-PM Mott transition in $(V_{1-x}Cr_x)_2O_3$, metallic domains appear at higher temperatures than at the bulk transition. Their evolution is determined by the surface crystallographic direction and along the cleaving steps. Our DFT+DMFT theoretical calculations show that a surface reconstruction with an excess of oxy-gen favors the formation of a metallic phase. Against common wisdom, surfaces can hence be more metallic than the bulk, and surface steps even more so. This effect observed here for $(V_{1-x}Cr_x)_2O_3$ can be of general interest for surfaces of strongly correlated oxides, oxide heterostructures, and nanostructure.

4.3 DFT+DMFT Study of Double Perovskite Sr$_2$CrMoO$_6$

Introduction. In recent years, double perovskites with general formula A$_2$BB$^{'}$O$_6$ (A: rare-earth/alkaline-earth cation, B: $3d$ transition metal, B$^{'}$: $4d/5d$ transition metal) have been in the limelight because of their half-metallic behavior, which is of importance for spintronics and related technological applications (Saitoh et al., 2002; Saitoh et al., 2005(a); Tomioka et al., 2000; Sarma et al., 2000). Some of them, such as Sr$_2$FeMoO$_6$ (SFMO), also exhibit high magnetic transition temperatures (T_C) opening up the possibility of room temperature application (Kobayashi et al., 1998; Sarma, 2001). Furthermore, these compounds, especially in powdered form, exhibit substantial tunneling magnetoresistance at low temperatures, making them valuable for the manufacture of magnetic tunnel junction devices (Garcia-Landa, B. et al., 1999; Saitoh et al., 2005(b)). The report (Kobayashi et al., 1998) of room temperature magnetoresistivity of SFMO was met with excitement and followed by a surge of activity exploring the dependence of $3d$ transition metal (TM) ion on the properties of these compounds.

In this context, Cr-based double perovskites have been synthesized and studied (Philipp et al., 2003), in particular, the sister compound of SFMO, Sr$_2$CrMoO$_6$ (SCMO) (Patterson, Moeller, and Ward, 1963). Unlike in SFMO, there can be no valence compensation between Cr and the Mo in SCMO: Cr can only be in the 3^+ state making Cr^{3+}/Mo^{5+} only possible combination, while for SFMO, both Fe^{3+}/Mo^{5+} and Fe^{2+}/Mo^{6+} combinations are possible. Thus, SCMO was expected to be an even better candidate for room temperature spintronics. However, although the measured transition temperature of SCMO is high (Arulraj et al., 2000; Patterson, Moeller, and Ward, 1963) the observed moment (Moritomo et al., 2000) and the magnitude of the tunneling magnetoresistance turned to be disappointingly low. The presence of large antisite disorder, together with oxygen vacancy was held responsible for this (Arulraj et al., 2000). The antisite disorder present in the samples was estimated to be as high as 43-50 % (Patterson, Moeller, and Ward, 1963). To appreciate the role of $3d$ TM in the properties of double perovskites, it is thus highly desirable to understand the electronic and magnetic properties of pure SCMO.

Theoretical studies on SCMO have been carried out within the framework of DFT (Wu, 2001). However no microscopic analysis has been carried out, neither has the transition temperature been calculated, except for a recent mean field analysis (Ngantso et al., 2015) based on a classical Ising model. The latter neglects the itinerant electronic character of Mo $4d$ electrons, a crucial component in understanding the behavior of these $3d$-$4d$ double perovskites.

In the present study, we aim to fill this gap by combining state-of-art DFT and DFT+DMFT calculations [for few-band model Hamiltonian and exact diagonalization of the DFT derived model Hamiltonian please see Ref. (Sanyal et al., 2016)]. Our microscopic study shows a considerable suppression of the Cr t_{2g} - Mo t_{2g} hybridization in SCMO compared to that in SFMO, driven by the change in charge transfer energy between B and B$^{'}$ sites in two compounds. The suppressed hybridization in SCMO makes the Mo t_{2g} electrons more localized compared to SFMO. This, in turn, opens up an additional, super-exchange contribution to

magnetism. The calculated magnetic transition temperature T_C without super-exchange contribution, gives about 79% of the measured T_C. The consideration of additional super-exchange contribution makes the calculated T_C comparable to the measured one. Our work highlights the importance of the super-exchange in SCMO, in addition to the hybridization-driven mechanism operative in SFMO (Kobayashi et al., 1998). We further study the effect of correlation on the half-metallic property of SCMO by including local correlations on top of DFT within the framework of DMFT. The DMFT results confirm the half-metallic ground state below the magnetic transition temperature, implying that the qualitative description remains unaffected by correlation effects.

Calculation details. The first-principles DFT calculations have been carried out using the plane-wave pseudopotential method implemented within the VASP (Kresse and Hafner, 1993; Kresse and Furthmüller, 1996) and Wien2K codes (Blaha et al., 2001). The exchange-correlation functional was considered within GGA-PBE (Perdew, Burke, and Ernzerhof, 1996). The projector-augmented wave (PAW) potentials (Kresse and Hafner, 1993; Kresse and Furthmüller, 1996) were used and the wave functions were expanded in the plane-wave basis with a kinetic-energy cutoff of 500 eV. Reciprocal-space integrations were carried out with a k-space mesh of 8×8×8.

In order to extract a few-band tight-binding (TB) Hamiltonian out of the full DFT calculation which can be used as input to following DMFT calculations. Our wannier projections calculations were carried out using Wien2wannier (Kuneš et al., 2010). This generates maximally localized Wannier functions (Marzari et al., 2012; Mostofi et al., 2008) from Wien2K which employs a full potential linear augmented plane wave (FLAPW) basis. For self-consistent DFT calculation in the FLAPW basis the number of k-points in the irreducible Brillouin zone was chosen to be 64. The commonly used criterion relating the plane wave and angular momentum cutoff, l_{max}=$R_{MT} \times K_{max}$ was chosen to be 7.0, where R$_{MT}$ is the smallest MT sphere radius and K_{max} is the plane wave cutoff for the basis. The chosen atomic radii for Sr, Cr, Mo and O were 1.43 Å, 1.01 Å, 1.01 Å, and 0.87 Å, respectively.

The DFT+DMFT calculations have been carried out using the Wien2wannier (Kuneš et al., 2010)-derived maximally localized Wannier functions of Wien2K as a starting point. We restricted the DMFT to the low energy degrees of freedom, i.e., to the t_{2g} orbitals of Mo and the t_{2g} and e_g orbitals of Cr (these low energy orbitals are actually a mixture between predominately transition metal t_{2g} (e_g) character with some admixture of oxygen p character). We supplemented the DFT low-energy Hamiltonian in the Wannier basis by a local Coulomb interaction in Kanamori parametrization [for details see Ref. (Parragh et al., 2012)]. For the interaction values we chose the typical values for $3d$ and $4d$ transition metal oxides. The choices were: inter-orbital Coulomb repulsion of U'=4 eV (2.4 eV) and a Hund's coupling J_H=0.7 eV (0.3 eV) for Cr (Mo) as estimated for neighboring vanadium (Taranto et al., 2013) [ruthenium (Si et al., 2015)] perovskites. The intra-orbital (Hubbard) repulsion follows from orbital symmetry as U=U'+2J_H; and the pair hopping term is of equal strength as J_H. As a DMFT impurity solver, continuous-time quantum Monte-Carlo simulations (Gull et al., 2011) in the W2dynamics (Parragh et al., 2012) implementation was used hich includes the full $SU(2)$ symmetry. The effect of electronic correlations beyond GGA, within the framework of static theory was also checked by performing GGA+U calculations with choice of same U parameters, as in DMFT calculation.

DFT Electronic Structure. We first revisit the basic DFT electronic structure of SCMO, which has been calculated before using variety of basis sets, including plane wave (Li, Zhu, and Chen, 2008), LAPW (Bonilla et al., 2007) and LMTO (Wu, 2001). SCMO crystallizes in the cubic No.225 *Fm3m* space group, with lattice parameter of 7.84 Å (Arulraj et al., 2000). The crystal structure, non-magnetic DFT-GGA band structure (Wannier projection) and DOS of SCMO is shown in Fig. 4.4(a). Combining of the band structure [Fig. 4.4(b)] and DOS results [Fig. 4.4(c)] demonstrates that Cr d-orbitals and Mo t_{2g}-orbitals contribute to the active bands around E$_f$. The Mo e_g-orbitals are far away from E$_f$ due to

the large crystal-field splitting of $4d$ transition-metal oxides, thus we exclude Mo e_g-orbitals in following DMFT calculations.

The left panel of Fig. 4.5(a) shows the spin-polarized DOS calculated in a plane wave basis. The basic features of the DOS, which agree very well with previous studies (Li, Zhu, and Chen, 2008; Bonilla et al., 2007; Wu, 2001) are the following: the states close to Fermi level, E_f (set as zero in the figures), are dominated by Cr and Mo d states hybridized with O p states (O-$2p$ is not shown here). The states of dominant O p character are positioned further down in energy, separated by a small gap from Cr and Mo d states in spin-up (majority) channel. Empty Sr states, not shown in the energy scale of the figure, remain far above E_f. Due to the large octahedral crystal field at Mo sites, the empty Mo e_g states lie far above E_f. The Cr t_{2g} states are occupied in the majority spin channel and empty in the minority spin channel. The Cr e_g states are empty in both spin channels, in agreement with the nominal Cr^{3+} (d^3) valence. The empty and highly peaked Mo t_{2g} states in the majority spin channel appear in between the crystal field split Cr t_{2g} and Cr e_g states for the same spin. In contrast for the minority spin channel, the Mo t_{2g} states hybridize more strongly with Cr t_{2g} states, which explains their much larger bandwidth.

The above described basic features for B and B$'$ states, are rather similar for SCMO and SFMO (Sanyal, Das, and Saha-Dasgupta, 2009), and in that respect also for Sr_2CrWO_6 (SCWO) (Das et al., 2011) which is another double perovskite from the Cr family but with $5d$ W instead of $4d$ Mo. Nevertheless, the spin-polarized DOS of SCMO differs from both SFMO and SCWO in important details. The hybridization between B t_{2g} and B$'$ t_{2g} in the minority spin channel, is found to be significantly lower compared to that of SFMO or SCWO (Sanyal, Das, and Saha-Dasgupta, 2009; Das et al., 2011). A measure of this is the Cr contribution in the minority spin bands crossing E_f of predominant Mo character. We estimate this contribution or admixture to be 35% for SCMO, while the corresponding estimates for SCWO and SFMO are much larger, 66% and 72%, respectively.
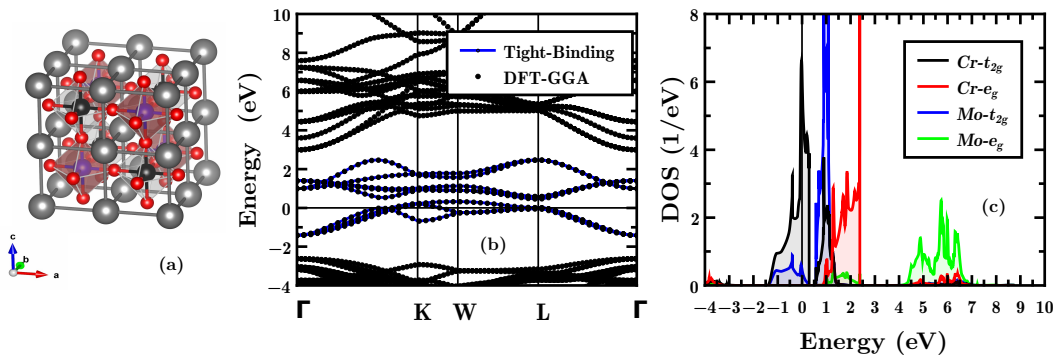
FIGURE 4.4: (a): Crystal structure of Sr_2CrMoO_6, Sr, Cr, Mo and O atoms are labeled by gray, blue, black and red balls, respectively. (b): GGA-PBE non-ferromagnetic band structures (blakck dots) and wannierop projections (bulk lines) onto Cr t_{2g}, Cr e_g and Mo t_{2g} states. (c): GGA-PBE non-ferromagnetic density of states (DOS) of Cr $3d$ and Mo $4d$ orbitals.

The top row in Table. 4.2, shows the calculated magnetic moments at Cr and Mo sites, as well as the total moment in DFT-GGA calculations. The total magnetic moment is found to be $2.0\,\mu_B$, with finite moments residing at O sites, in
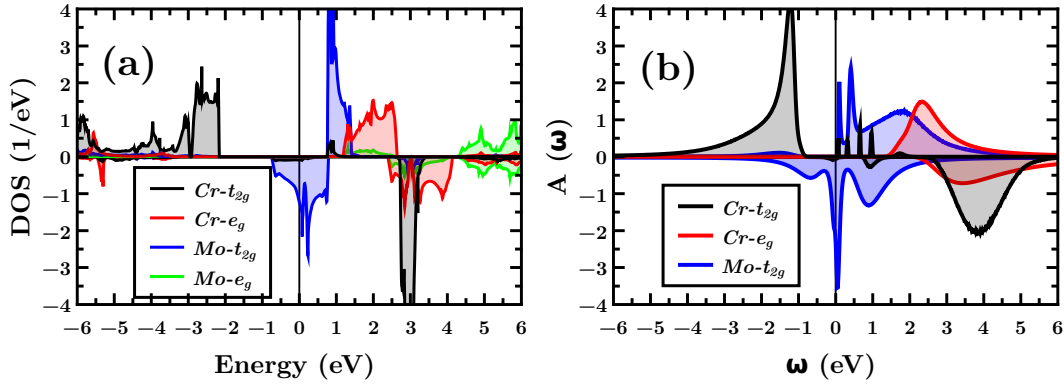
FIGURE 4.5: (a): Spin-polarized DFT+U density of states (DOS) and (b): DMFT spectral functions at 200 K of Sr$_2$CrMoO$_6$.

TABLE 4.2: Calculated magnetic moments (in μ_B) within GGA, GGA+U and DMFT. Note that within GGA there is also a moment on the oxygen sites which is accounted for in the Cr and Mo moment in DMFT as the predominately metal d Wannier functions also have some oxygen admixture.

	Sr	Cr	Mo	total
GGA	0.00	−2.29	0.43	−2.00
GGA+U	0.00	−2.54	0.58	−2.00
DMFT	0.00	−2.84	0.84	−2.00

accordance with the half-metallic behavior of SCMO. Our calculated magnetic moments at Cr and Mo sites are in good agreement with that reported by Li *et al* (Li, Zhu, and Chen, 2008). The calculated moment reported by Wu (Wu, 2001) is however much smaller than that of our results as well as that from Li *et al* (Li, Zhu, and Chen, 2008). This is presumably due to different choices of the muffin-tin radii as well as the exchange-correlation functional. The latter was chosen to be LDA in Ref. (Li, Zhu, and Chen, 2008), rather than GGA.

The measured magnetic moments are significantly smaller than the theoretical values. Experimentally, the total moment is only 0.5 μ_B (Moritomo et al., 2000) and the moment on the Cr sites is 0.8 μ_B (Blasco et al., 2002). This discrepancy was hitherto argued to be due to the large disorder present in the samples (Arulraj et al., 2000). It is interesting to note that the value of the calculated magnetic moment at the Mo sites (0.43 μ_B) is larger than the calculated B$'$ site moment for SFMO (0.23 μ_B) and SCWO (0.30 μ_B). This indicates a weaker itinerancy of the Mo electrons in SCMO, compared to SFMO or to that of W in SCWO. This in turn suggests that a small, but finite intrinsic moment develops at the Mo site as a consequence of the weaker hybridization between Cr and Mo. The suppression of the hybridization and the reduced itinerancy of the Mo t_{2g} electrons in SCMO has been also pointed out in the study by Wu (Wu, 2001), though no detailed understanding of the mechanism of magnetism was provided.

For the following DMFT calculations, all TB parameters of the model Hamiltonian, i.e., Δ, t_{Cr-Mo}, t_{Mo-Mo}, t_{Cr-Cr}, are extracted from a non-spin-polarized DFT calculations through two independent means as listed in Table. 4.3: (i) through the NMTO downfolding technique, and (ii) through the construction of

TABLE 4.3: Tight-binding parameters (in eV) of the few orbital Hamiltonian in Wannier function basis, extracted out of DFT calculations.

	Δ	t_{Cr-Mo}	t_{Mo-Mo}	t_{Cr-Cr}
NMTO	-0.35	0.33	0.14	0.08
Wannier90	-0.42	0.30	0.12	0.06

maximally localized Wannier functions in the basis of the effective Cr and Mo t_{2g} degrees of freedom. The latter scheme has been also employed in the DMFT study and calculations details were presented before. In both cases we integrate out all other degrees of freedom except for the Cr and Mo t_{2g} states. The comparison of the full DFT non-spin-polarized band structure and the few orbital TB bands in maximally localized Wannier function basis is shown in Fig. 4.4(b). The agreement between DFT-GGA and tight-binding bands are found to be as good as possible, proving the effectiveness of the Wannier function projection.

While the estimated hopping parameters of SCMO are rather similar to that reported for SCWO (Das et al., 2011), we find the charge transfer energy Δ ($\sim$0.4 eV) to be quite different from that estimated for SFMO ($\sim$1.0 eV) (Sanyal, Das, and Saha-Dasgupta, 2009) and for SCWO (-0.7 eV) (Das et al., 2011) (the charge transfer energy is defined as the on-site energy difference between Cr t_{2g} and Mo t_{2g} levels is $\Delta = \epsilon_{Cr}$-ϵ_{Mo}). This change in the bare, non-spin-polarized charge transfer energy (Δ), in turn, modifies the renormalized charge transfer energy Δ_R between Cr and Mo in the minority spin channel in the spin-polarized phase. It is much larger in SCMO (0.81 eV) compared to that in SCWO (0.51 eV) (Das et al., 2011), due to the moving down the column of the periodic table from the 4d element Mo in SCMO to the 5d element W in SCWO. As a consequence of the larger charge transfer splitting Δ_R the effect of the hybridization which is governed by t_{Cr-Mo}^2/Δ_R is significantly suppressed in SCMO, by about 63% compared to the corresponding value for SCWO.

DMFT spectral functions. In order to study the effect of electronic correlations, specially the dynamical correlation which may be important for SCMO due to the metallic nature of the ground state, we further carry out DMFT calculations in the Wannier function basis. The right panel in Fig. 4.5(b), shows the DMFT spectral density calculated at 200 K. The spectrum shows qualitatively similar behavior to that obtained from DFT+U calculations, though the minority spin spectrum shows the correlation physics with a feature resembling lower and upper Hubbard bands and a well defined quasi-particle peak at Fermi energy. This demonstrates the dual nature of the Mo minority spin with localized electrons (Hubbard bands) and itinerant electrons (quasi-particle band) at the same time. The fully spin-polarized conducting electrons are Fermi-liquid-like with a linear frequency-dependence of the self energy (not shown). Hence the quasi-particle peak will lead to a Drude peak in the optical conductivity.

The DMFT magnetic moments are shown in the last row of Table. 4.2. We note the DMFT calculated magnetic moments are in the basis of Cr and Mo t_{2g} Wannier functions, which includes the effect of oxygen sites. This makes a direct comparison between DMFT and GGA values somewhat more difficult. However since the difference between GGA and DMFT magnetic moments is larger than the GGA

oxygen contribution, we can conclude that electronic correlations somewhat enhance the magnetic moments on both, Mo and Cr, sites. This is further supported by the magnetic moments calculated within the static theory of GGA+U, shown in the second row of Table. 4.2, which shows an enhancement of the moment both at Cr and Mo sites, compared to that of GGA.

Summary. Starting from a DFT description we provide a microscopic analysis of the magnetic behavior of SCMO, a sister compound of SFMO. DFT calculations on pure, defect-free SCMO show that, like SFMO and SCWO, it is a half-metallic magnet. The calculated DMFT results confirm the robustness of the half-metallicity of SCMO upon inclusion of dynamical correlation effects. The DMFT results show a splitting of the Mo minority spin band into Hubbard bands and quasi-particle peak. This indicates the dual nature of the Mo electrons having both, a local spin moment and itinerant behavior.

The origin of magnetism in SCMO turns out to be somewhat different than in SFMO. The charge transfer energy between Cr and Mo in the minority spin channel of SCMO is found to be larger than that between Fe and Mo in SFMO. This suppresses the effect of hybridization between B and B$'$ sites in SCMO compared to SFMO and has two consequences: (i) the hybridization-driven mechanism for magnetism is reduced and (ii) a small but finite intrinsic moment develops at the Mo sites. The latter gives rise to a partial localized character of the Mo electrons, which was absent in SFMO. This in turn opens up a super-exchange contribution to magnetism in SCMO, which was absent for SFMO. We compare our results on SCMO to another Cr based double perovskite, SCWO. The magnetism in the latter, like SFMO, is well described by a hybridization-only picture. In the publication [Ref. (Sanyal et al., 2016)] the computed T_C obtained through exact diagonalization of the *ab-initio* derived model Hamiltonian show the T_C of SCMO to be similarly high as in SCWO, only upon inclusion of both, super-exchange and hybridization-driven contribution in case of SCMO. Thus while magnetism in both, SCWO and SFMO, is governed by hybridization, the story in SCMO appears with a twist. It needs to be described by a combination of hybridization and superexchange mechanism.

We conclude that, in general, the magnetism in the double perovskite family has to be understood as an interplay between the hybridization and super-exchange between B and B$'$ sites. The relative contribution of one mechanism vs. the other one is dictated by the charge transfer between the $3d$ transition metal at the B site and the $4d$ or $5d$ transition metal at the B$'$ site.

4.4 d-p **Hybridization in La$_{(1-x)}$Sr$_x$MnO$_3$ Thin Films**

Introduction. Electronic phase transition driven by the spatial confinement are quite common for different types of functional perovskite heterostructures. Whether is it solely a spatial confinement effect, or other mechanisms (such as e.g. structural changes in thin films) are at work remains an open issue. Here, we present a direct evidence for the change in hybridization of oxygen $2p$ and Mn $3d$ orbitals (p-d) driven by rotations and tilting of MnO$_6$ octahedra at the interface. The atomically resolved lattice, electronic and magnetic structures together with thickness dependent X-ray absorption spectroscopy (XAS) demonstrate a central role of thickness dependent p-d hybridization in widely observed dimensionality effects happening in these correlated oxide heterostructures [for experimental results see Ref. (Liao et al., 2017)].

A diverse range of phenomena spanning from colossal magnetoresistance, metal-to-insulator transition (MIT) to superconductivity has been attracting tremendous interest in transition metal oxides (TMOs) for both fundamental research as well as technological applications (Dagotto, 2005). Of particular interest are the phase transitions in TMOs, which can be manipulated by tuning either bandwidth or band-filling (Zaanen, Sawatzky, and Allen, 1985; Imada, Fujimori, and Tokura, 1998). Various phase transitions (MIT, ferroelectricity to paraelectricity, ferromagnetic to antiferromagnetic) can already be achieved in different types of TMOs heterostructures by just varying the thickness (Boris et al., 2011; King et al., 2014; Yoshimatsu et al., 2010; Wang et al., 2015; Koster et al., 2012; Junquera and Ghosez, 2003; Huijben et al., 2008). In recent literature several physical models are used as a design principle in order to control the reconfigurable properties by changing the thickness. For example, very well-known are the reduced dimensionality tipping the delicate competition between collective quantum phases which are proposed to contribute to the MIT in ultrathin LaNiO$_3$ and SrVO$_3$ thin films (Boris et al., 2011; King et al., 2014; Yoshimatsu et al., 2010), while a polar catastrophe is proposed to generate a magnetic phase transition in polar LaMnO$_3$ ultrathin films (Wang et al., 2015).

However, the more obvious structural coupling at interfaces induced by the modulation of the oxygen coordination across interfaces is mostly ignored, whereas recently the role of interfacial structural coupling has been directly visualized at the atomic scale (Kan et al., 2016; Liao et al., 2016). High resolution transmission electron microscopy using the latest scanning and imaging techniques for both SrRuO$_3$ (Kan et al., 2016) and La$_{2/3}$Sr$_{1/3}$MnO$_3$ (LSMO) (Liao et al., 2016) clearly show a thickness dependent oxygen coordination. Given the close similarity of the structures in the previously mentioned examples with the latter systems, the question arises why in the earlier examples a structural effect is not present. What is lacking is an exact physical relationship between the observed modified structure and the changes of the underlying physical phenomena for these thickness-driven phase transitions. Here, we provide *ab-initio* calculations and experimental evidence (in the main paper) for the structure-property

relationship in an epitaxial model system, LSMO on NdGaO$_3$ (NGO), where orbital hybridization can be identified as the main driving mechanism for thickness-dependent property changes. It is very plausible that similar effects play a role in other heterostructures and can be used as a leading design principle for a further development of these functional heterostructures into miniaturized oxide electronic devices.

The half metallic ferromagnet LSMO is of great importance due to 100% spin polarization nature (Tokura and Tomioka, 1999; Park et al., 1998) and is a promising material for oxide spintronic applications. For LSMO thin films previous studies have already shown that the ferromagnetic behavior severely depends on the film thickness (Huijben et al., 2008; Tebano et al., 2008; Lepetit, 2012; Pesquera et al., 2012; Boschker et al., 2012; Dulli et al., 2000; Sandiumenge et al., 2013; Lee et al., 2010). Tremendous efforts have been taken to unravel this thickness dependency, but its origin is still debated (Huijben et al., 2008; Tebano et al., 2008; Lepetit, 2012; Pesquera et al., 2012; Boschker et al., 2012; Dulli et al., 2000; Sandiumenge et al., 2013; Lee et al., 2010; Vailionis et al., 2014; Kourkoutis et al., 2010). The two main proposed mechanisms responsible for this deterioration of ferromagnetism are orbital reconstruction and the variation of Mn^{3+}/Mn^{4+} ratio (Huijben et al., 2008; Tebano et al., 2008; Lepetit, 2012; Pesquera et al., 2012; Boschker et al., 2012; Dulli et al., 2000; Sandiumenge et al., 2013; Lee et al., 2010). The preference for 3$d_{z^2-r^2}$ occupation is suggested to favor the antiferromagnetic insulating ground state (Tebano et al., 2008; Lepetit, 2012; Fang, Solovyev, and Terakura, 2000; Konishi et al., 1999), while the enrichment of Mn^{3+} would also enhance Jahn-Teller distortions (Sandiumenge et al., 2013; Lee et al., 2010). However, an interfacial charge transfer limited to ∼2 unit cells (uc) cannot explain the long range thickness dependency in thicker films (Fang, Solovyev, and Terakura, 2000; Bhattacharya et al., 2008). Also the observed ferromagnetic behavior (with T_C>250 K) over a wide range of 0.15<x<0.5 (Tokura and Tomioka, 1999) indicates the limited impact of any possible charge transfer. Also here, possible changes in the overlap of the orbitals due to structural changes were disregarded in previous thin film studies, although a strong correlation with magnetic behavior had been demonstrated in bulk manganites (Imada, Fujimori, and Tokura, 1998; Radaelli et al., 1997; Garcia-Munoz, J. L. et al., 1996). Recently it has been shown that the oxygen octahedral rotation (OOR) pattern in LSMO thin films can be tuned by direct coupling to the OOR pattern of the underlying substrate (Liao et al., 2016). NGO substrates provide a certain octahedral tilt angle, and the corresponding orbital overlap, which can be reduced by increasing the thickness of the LSMO layer as well as by incorporation of SrTiO$_3$ (STO) buffer layers. In our study we will unravel the correlation between the orbital overlap and the thickness dependency by systematically investigating the relation between magnetic behavior, crystal structure, orbital reconstruction and bandwidth in LSMO films of various thicknesses. Our results demonstrate the dominant role of the local O-2p and Mn-3d (p-d) orbital hybridization for the ferromagnetic ordering at the atomic scale in LSMO films. We show, in particular, that spatial variation in p-d orbital hybridization, due to octahedral relaxation within LSMO, is responsible for the observed thickness dependency in material properties.

d-p hybridization **vs. MnO$_6$ octahedra rotation and tilting.** The impact of octahedral rotations and tilting on the electronic structure of LSMO is investigated using first principles density functional theory calculations. The atomic relaxations are carried out with the VASP code (Kresse and Hafner, 1993; Kresse and Furthmüller, 1996) by using the projector augmented-wave (PAW) method Blöchl,

1994. Subsequent electronic structure calculations were performed using the Wien2K code (Blaha et al., 2001) within the full-potential linearized augmented plane-wave method (Slater, 1937; Singh and Nordstrom, 2006). In both codes the generalized gradient approximation (GGA) of Perdew, Burke, and Ernzerhof (PBE) (Perdew, Burke, and Ernzerhof, 1996) was adopted to treat the exchange-correlation effects. The Sr doping in $LaMnO_3$ bulk ($La_{0.67}Sr_{0.33}MnO_3$) system is realized by using the virtual crystal approximation.

TABLE 4.4: Summary of structural parameters [lattice constants, Mn-O-Mn angles (θ_{xy}, θ_z and average value $\langle\theta\rangle$) and Mn-O bond length]. We consider three crystal structures (cubic, GFO- and NGO-type) and either keep the Mn-O distance constant (Group-I) or the Mn-Mn distance constant (Group-II).

Group-I: Mn-O constant								
Structure	a(Å)	b(Å)	c(Å)	Mn-O-Mn θ (degree)			Mn-O bond (Å)	
				θ_{xy}	θ_z	$\langle\theta\rangle$	x/y	z
Cubic	3.848	$=a$	$=a$	180	180	180	1.924	1.924
GFO-type	3.834	3.793	3.810	162.8	162.8	162.8	1.924	1.924
NGO-type	3.829	3.633	3.771	151.6	151.2	151.2	1.924	1.924
Group-II: Mn-Mn constant								
Structure	a(Å)	b(Å)	c(Å)	Mn-O-Mn θ (degree)			Mn-O bond (Å)	
				θ_{xy}	θ_z	$\langle\theta\rangle$	x/y	z
Cubic	3.848	$=a$	$=a$	180	180	180	1.924	1.924
GFO-type	3.848	3.848	3.848	159.4	160.5	159.9	1.952	1.953
NGO-type	3.848	3.848	3.848	151.6	151.2	151.5	1.984	1.987

To study the effect of MnO_6 octahedral rotation/tilting, three different structures are considered in our study: cubic, $GdFeO_3$(GFO)-type and $NdGaO_3$(NGO)-type. For the cubic structure, there is no octahedral tilting, the Mn-O-Mn bond angle is 180°. The GFO- and NGO-type structures are those of LSMO but adopted to the GFO and NGO orthorhombic distortion, with the NGO-type having larger octahedral tilting. In order to summarize the effects of the change of the Mn-O-Mn bond angle and the Mn-O bond length on the LSMO electronic structure, two groups of calculations have been carried out: In the first group (Group-I) we keep the Mn-O distance constant. In this way any effect from Mn-O bond length is excluded, only the bond angle is changed (and subsequently the lattice parameters). In the second group (Group-II) we keep the Mn-Mn distance constant but otherwise relax the structure, rotating the MnO_6 octahedron in the xy plane and tilting them along the z-direction. This yields the GFO-type as an energy minimum; for the NGO-type we enhance the Mn-O-Mn angle according to the experimental NGO structure. Thus in the process of rotation and tilting the Mn-O bond length is also increased for Group-II calculations. By this confinement we can investigate the effect from both Mn-O-Mn bond angle and Mn-O bond length separately. All the structural parameters are summarized in Table. 4.4.

The half-metal ferromagnetic state of LSMO system is already obtained even without considering electronic correlations, e.g. by DFT+U or DFT+DMFT methods. We also test the robustness of our results using a reasonably large Coulomb
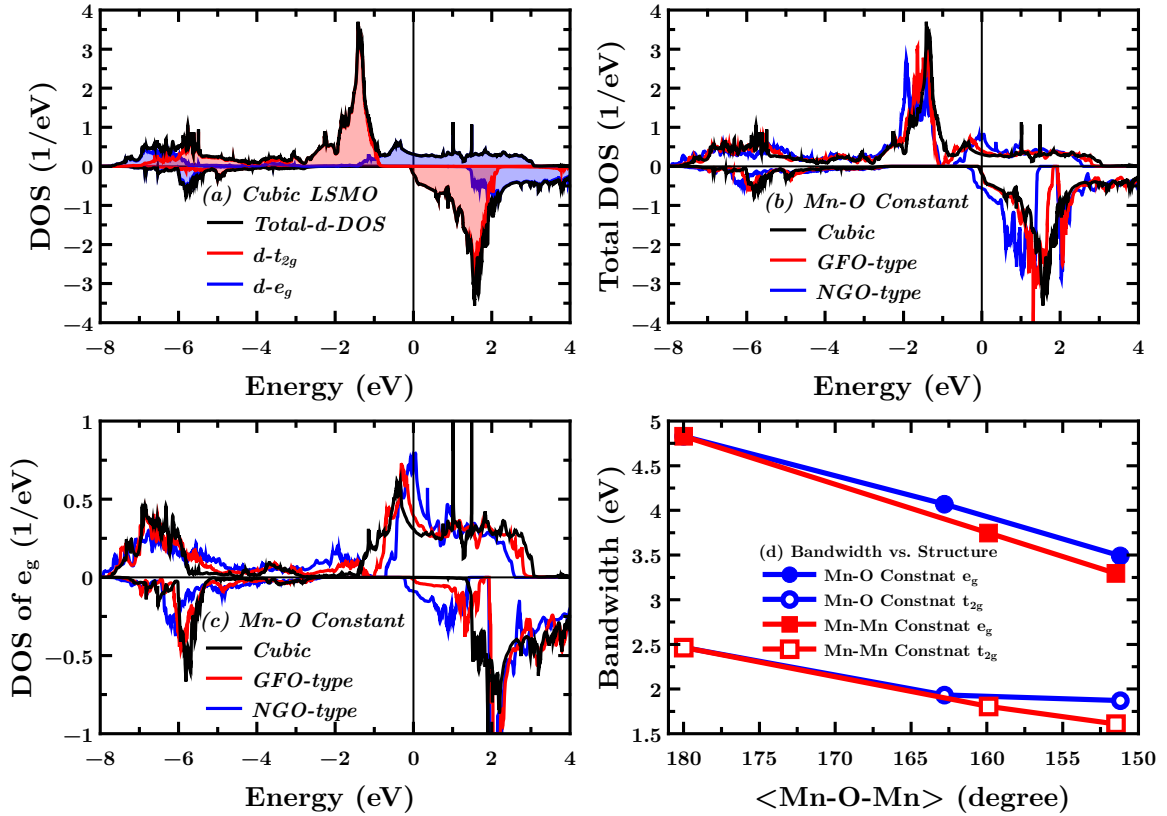
FIGURE 4.6: Octahedral tilt effect on bandwidth. (a) Calculated orbital- and spin-resolved DOS for both e_g and t_{2g} orbitals for cubic LSMO. (b) Spin-resolved total-d DOS and (c) majority e_g DOS orbital of LSMO comparing cubic to GFO- and NGO-type of distortion with constant Mn-O bond length (Group-I). (d) Bandwidth as a function of the tilting angle for both, constant Mn-O bond length (Group-I) and constant Mn-Mn distance (Group-II).

interaction U in DFT+U calculations: no remarkable change occurs. To include the effect of octahedral rotation and tilting, a $\sqrt{2} \times \sqrt{2} \times 2$ supercell (20 atoms) was used in our electron structure calculations of the density of states (DOS) and the bandwidth. Fig. 4.6(a) shows an example of the orbital-resolved density of states (DOS) for cubic LSMO ($\theta = 180°$) from which we can extract the bandwidth of the $3d$ majority e_g and t_{2g} orbitals, which is 4.8 eV and 3.3 eV, respectively. States lying between -7.5 eV and -4.0 eV arise from the hybridization between O $2p$ and Mn $3d$-orbitals and are excluded from the bandwidth. By decreasing the bond-angle without changing the Mn-O bond length from 180° (cubic-type), 162.8° (GFO-type) to 151.5° (NGO-type) the effect of bond-angle on the electronic structure of LSMO (Group-I) is shown in Fig. 4.6(b)-(c). There is a valley around -1.0 eV for the total DOS as shown in Fig. 4.6(b), above and below which the DOS mainly comes from e_g and t_{2g}, respectively. In cubic LSMO, the bandwidth of both t_{2g} and e_g are so big that the t_{2g} and e_g bands overlap, but their overlap is getting smaller with increasing the octahedral tilting (i.e. reducing bond-angle) as shown in Fig. 4.6(b). In NGO-type LSMO, the bandwidths of both t_{2g} and e_g become narrower. As a result a gap opens between t_{2g} and e_g orbital [zero DOS at the valley Fig. 4.6(b)]. Fig. 4.6(c) shows the partial DOS of majority e_g orbital, clearly demonstrating the narrowing of the e_g band with decreasing the bond-angle.

The bandwidth versus the bond-angle is plotted in Fig. 4.6(d). The bandwidths of both t_{2g} and e_g decrease with decreasing the bond angle, e.g., in cubic LSMO the e_g bandwidth is 4.8 eV, while it is 3.5 eV for NGO-type LSMO. Therefore, reducing the bond angle from 180° to 151.5° results in a 28% reduction of bandwidth. Since the oxygen $2p$ orbital points towards the e_g orbital lobes not to those of the t_{2g} orbitals, the e_g orbitals have larger bandwidth as well as a larger bandwidth reduction in Fig. 4.6(d).

Fig. 4.6(d) also shows the calculated bandwidth of three different LSMO structures from Group-II, where we keep the Mn-Mn distance constant but vary the bond angle. The bandwidth is again reduced with decreasing bond angle, similar to our finding in Group-I LSMO. However, differently from Group-I, the bandwidth of Group-II LSMO gets to a large extent as the bond angle is reduced [Fig. 4.6(d)]. The bandwidth of e_g is reduced by 32% when the bond angle changes from 180° to 154° for a constant Mn-Mn distance. That is, both the elongated Mn-O bond and the increased octahedral tilt reduce the bandwidth cooperatively. Therefore, the effect of octahedral tilt on bandwidth reduction will be enhanced somewhat if the Mn-Mn distance instead of the Mn-O bond length is locked. Taken together, both calculations show that the main driving force behind the reduced bandwidth is the tilting of the Mn-O-Mn angle in the distorted structure.

Magnetism* vs. *MnO$_6$ octahedra rotation and tilting. Above we investigated the relationship between d-p hybridization and rotation/tilting of MnO$_6$ octahedra. We have shown that rotating/tilting the MnO$_6$ octahedra shrinks the bandwidth of Mn-3d orbital, reducing the hybridization between Mn-3d and O-2p. Magnetic properties also depend on the rotation/tilting. The DFT-GGA resulted magnetic moments are shown in Table. 4.5. In Group-I, the total magnetic moments M_{total} of cubic, GFO- and NGO-type are 3.61, 3.59 and 3.28μ_B/us, respectively. Excluding the contribution from O-p, the averaged substantial moments M_{Mn} in the Mn sphere, which approximates the 3d contribution, is 3.12, 3,09, 2.81μ_B/Mn (M_{Mn}/M_{total} is 86.4%, 86.0% and 85.6%, respectively), all of other contributions are from O-2p. The first noticeable conclusion is that the ratios M_{Mn}/M_{total} decreases from ∼86.4% to ∼85.6%, this indicates the Mn-O-Mn angle θ is a key governing the degree of d-p hybridization. The second notable effect is the suppression of moment from 3.62μ_B to 3.28μ_B as the structure changes from cubic to NGO-type. This remarkable reduction of the moment is mainly due to the lattice compression, at a fixed Mn-O distance.

In Group-II, as increasing the MnO$_6$ octahedra rotation/tilting the magnetic moments do not deviate from ∼3.61-3.67 μ_B/uc. One thing we have to notice is that in this group of calculations the Mn-Mn distance is fixed, thus the only variable is the d-p hybridization (which is quantitatively measured by Mn-O-Mn angle θ). Thus we conclude that mere enhancing the Mn-O bond length cannot effectively reduce d-p hybridization. Lattice compression or Mn-Mn bond compression are the key factors to reduce the ferromagnetism in LSMO, if no other variables are tuned, e.g. thickness. In our main paper we already demonstrate thiner samples have weaker ferromagnetism, combined with DFT-GGA magnetic calculations we can infer that there are only two possible reasons which can explain the suppression of ferromagnetism in thiner samples are: surface/interface lattice compression (which also can be considered as shorter Mn-Mn distance), or the critical thickness behavior. The surface/interface lattice compression gives rise to the "magnetic dead layer" results which we already discussed in main paper [for the "magnetic dead layer" phenomenon see e.g. Ref. (Curiale et al., 2009)].

In Group-II, even the total magnetic moments per cell site M$_{total}$ of cubic, GFO- and NGO-type are unchanged, however the M$_{Mn}$/M$_{total}$ is increased as increasing the rotation/tilting of MnO$_6$, changing from 86.4% to 87.7%. This conclusions means the d-p hybridization gets weaker as the rotation/tilting of MnO$_6$ increases.

Thickness effect **vs.** d-p ***hybridization and magnetism.*** Surfacing of LSMO should affects the magnetic properties. To answer this question we firstly compare the ferromagnetism of bulk and limitation of thiner films: monolayer LSMO. For similarity we eliminate the MnO$_6$ octahedra rotation/tilting, i.e. cubic cell is adopted in this analysis.

For bulk cubic case a total magnetic moment (M$_{total}$) of 3.61 μ_B/Mn is obtained, the contribution from Mn (M$_{Mn}$) is determined to be 3.12 μ_B/Mn, and M$_{Mn}$/M$_{total}$ is 86.4%. For LSMO monolayer, M_{total} and M_{Mn} is 3.48 μ_B/Mn and 2.95 μ_B/Mn, M$_{Mn}$/M$_{total}$ is 84.7%. The M$_{total}$ decreased by (0.14 μ_B) 3.8% because of filming. This reduction is due to: (1) in LSMO the ferromagnetism mainly originates from the double exchange mechanism under hole doping (0.33 hole/Mn), however filming excludes the electron hopping along z-direction, this will suppress ferromagnetism to some degree. (2) The exchange effect between Mn sites are also cut-off because of filming. The ratio M$_{Mn}$/Mn$_{total}$ is somehow decreased (86.5% in bulk cubic and 84.7% in monolayer), the tiny reduction is due to that filming suppresses the hybridization between Mn t_{2g} orbitals and O-$p_{x/y}$ along x/y-direction, while it enhances the hybridization along z-direction, for this view of point we will discuss later.

The above DFT results are obtained without surfacial atomic relaxation. To investigate the effects of surface reconstruction, we carried out atomic relaxation for LSMO 1 unit-cell film. We found the total magnetic moment M$_{total}$ and Mn moment M$_{Mn}$ continuously decreased to 3.32 μ_B and 2.87 μ_B. These moments are only 91.7% and 91.6% of the bulk M$_{total}$ and M$_{Mn}$, indicating the surfacial reconstruction is the second major origin of the "magnetic dead layer" in LSMO surface systems, besides filming. As in non-relaxed LSMO film the moments M$_{total}$ and M$_{Mn}$ are 3.48 μ_B and 2.95 μ_B, i.e. significantly larger than in the relaxed LSMO film, we can conclude that recovering the surface structure can also recover the ferromagnetism of the surface. This explains why STO capping/buffing layers can boost the ferromagnetism of interface LSMO layers. However 100% recovering seems impossible because STO capping/buffing anyhow fails in constructing the electronic hopping along Mn-O-Mn bond (i.e. double exchange mechanism), which effect is the major origin for the ferromagnetism in LSMO systems.

Even with a simple cubic (unrelaxed) model the magnetic suppression (surface/interface "magnetic dead layer" phenomena) can still be obtained, the surface relaxation only boosts it. That hints at a more *intrinsic* physical difference between relaxed and non-relaxed film systems, that can continuously suppress the top surface layer ferromagnetism. A detailed analysis shows that the most noticeable difference are lattice constants. By fixing the in-plane lattice constants of LSMO and relaxing out-of-plane lattice and all atomic positions, the out-of-plane lattice constant c_{film}^{relax} is 3.420 Å, only 88.9% of the original $c_{film}^{non-relax}$ (3.848 Å). This dramatic lattice compression is due to the fact that the (La$_{0.66}$Sr$_{0.33}$O)$^{+0.33}$/(MnO$_2$)$^{-0.67}$/(La$_{0.66}$Sr$_{0.33}$O)$^{+0.33}$ systems are polar, the intrinsic charge attractive force brings the layers closer together. Thus the interface/surface magnetic suppression is due to the compression of c_{film}. This

TABLE 4.5: Magnetic moment (μ_B) of M_{total} and M_{Mn}, and the ratio between M_{Mn} and M_{total}.

Group-I: Mn-O-Mn constant								
Cubic (M_{total})	M_{Mn}	M_{Mn}/M_{total}	GFO (M_{total})	M_{Mn}	M_{Mn}/M_{total}	NGO (M_{total})	M_{Mn}	M_{Mn}/M_{total}
3.61	3.12	86.4%	3.59	3.09	86.0%	3.28	2.81	85.6%
Group-II: Mn-Mn constant								
Cubic (M_{total})	M_{Mn}	M_{Mn}/M_{total}	GFO (M_{total})	M_{Mn}	M_{Mn}/M_{total}	NGO (M_{total})	M_{Mn}	M_{Mn}/M_{total}
3.61	3.12	86.4%	3.67	3.19	86.9%	3.67	3.22	87.7%

conclusion agrees with our observation in Group-I (Table. 4.5): the lattice compression will suppress ferromagnetism in LSMO systems. Besides of the Sr-Sr compression, the second result is the distance between M and the O in surface LaSrO layer is 2.07 Å, which is larger than the original 1.92 Å, this extension will remarkably reduce the hybridization between O-p_x/p_y and Mn-d, however for O-p_z orbital its space distribution is largely along z-direction, thus the influence of Mn-O extension is tiny (which will be further discussed in the DOS analysis below).
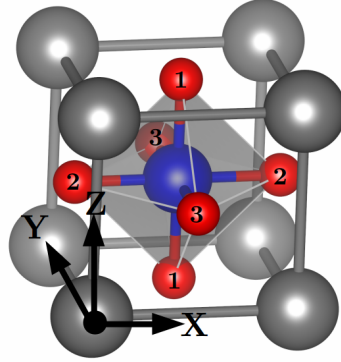
FIGURE 4.7: Crystal structure of LaMnO$_3$.

To investigate the microscopic roots of the alteration of the electronic structure and ferromagnetism of LSMO, we calculated the spin-polarized DOS of bulk cubic and 1 unit-cell film of LSMO. The lattice constant is adopted as the cubic one (3.848 Å), for film case we both obtain the DOS results by with/without atomic relaxations, however no dramatic difference occurs, the results without relaxation are shown [Fig. 4.8(a-h)]. The DFT-GGA DOS of cubic LSMO is shown in Fig. 4.8(a-d). In cubic bulk LSMO, all three Mn-t_{2g}/e_g orbitals are degenerate and equivalent, so are all the O sites and O-p orbitals. Here to compare the results with that of film case, we remove the *Pm3m* space group symmetry and artificially consider all three O sites are inequivalent. In Fig. 4.8(a), the states between -1.0 to -3.0 eV in spin majority channel are contributed by Mn-t_{2g} orbitals, in spin-minority channel, these states are located at around 1.5 eV because of the spin-splitting (~3.0 eV), the e_g states are from -1.0 to 3.0 eV (1.0 to 4.0 eV) in spin-majority (minority) channel. The Mn-d orbitals also contribute to the DOS from -8.0 to -4.0 eV, which are due to the d-p hybridization. Fig. 4.8(b) shows the DOS of O1 in bulk LSMO (the definition of O1, O2 and O3 is shown in Fig. 4.7), the p_z orbital is largely hybridized with Mn-e_g orbital from -8.0 to -5.7 eV (-6.0 to -5.0 eV) in spin-majority (minority) channel, and p_x/p_y orbitals are hybridized with t_{2g} orbitals from -6 to -4 eV in both spin-majority/minority channels. For the DOS of O2 and O3 Fig. 4.8(c,d), because the crystal symmetry the results can be analyzed by exchanged p_x, p_y and p_z orbitals with each others.

For film case the DOS results are shown in Fig. 4.8(e-h). In the DOS of Mn-d [Fig. 4.8(e)], for both spin-up (majority) and down (minority) channels, the d_{xy} keeps its single peak DOS, same as its bulk state, while for d_{yz} and d_{xz} the DOS acquires two-peak structures, unlike their DOS of bulk, this is due to the 2-dimensional geometrical confinement. The second conclusion is that the bandwidth reduction of d_{yz} and d_{xz} orbitals, due to the cutting-off of electronic hopping terms $t_{yz/xz}(0,0,1)$ along out-of-plane z-direction. The d_{xy} bandwidth is

FIGURE 4.8: Density of states (DOS) of Mn-3d orbital (a), O-2p orbital (b-d) in cubic bulk LSMO, Mn-3d orbital (e) and O-2p (f-h) orbital in 1 unit-cell film LSMO. For film case, the results of two nonequivalent O sites are shown. The surface O is positioned at LaO layer while the center O is positioned at MnO$_2$ layer.

basically unchanged, because the electronic hopping $t_{xy}(001)$ along z-direction is however small. This bandwidth reduction of d_{yz} and d_{xz} orbitals demonstrates that at least the hybridization between d_{yz}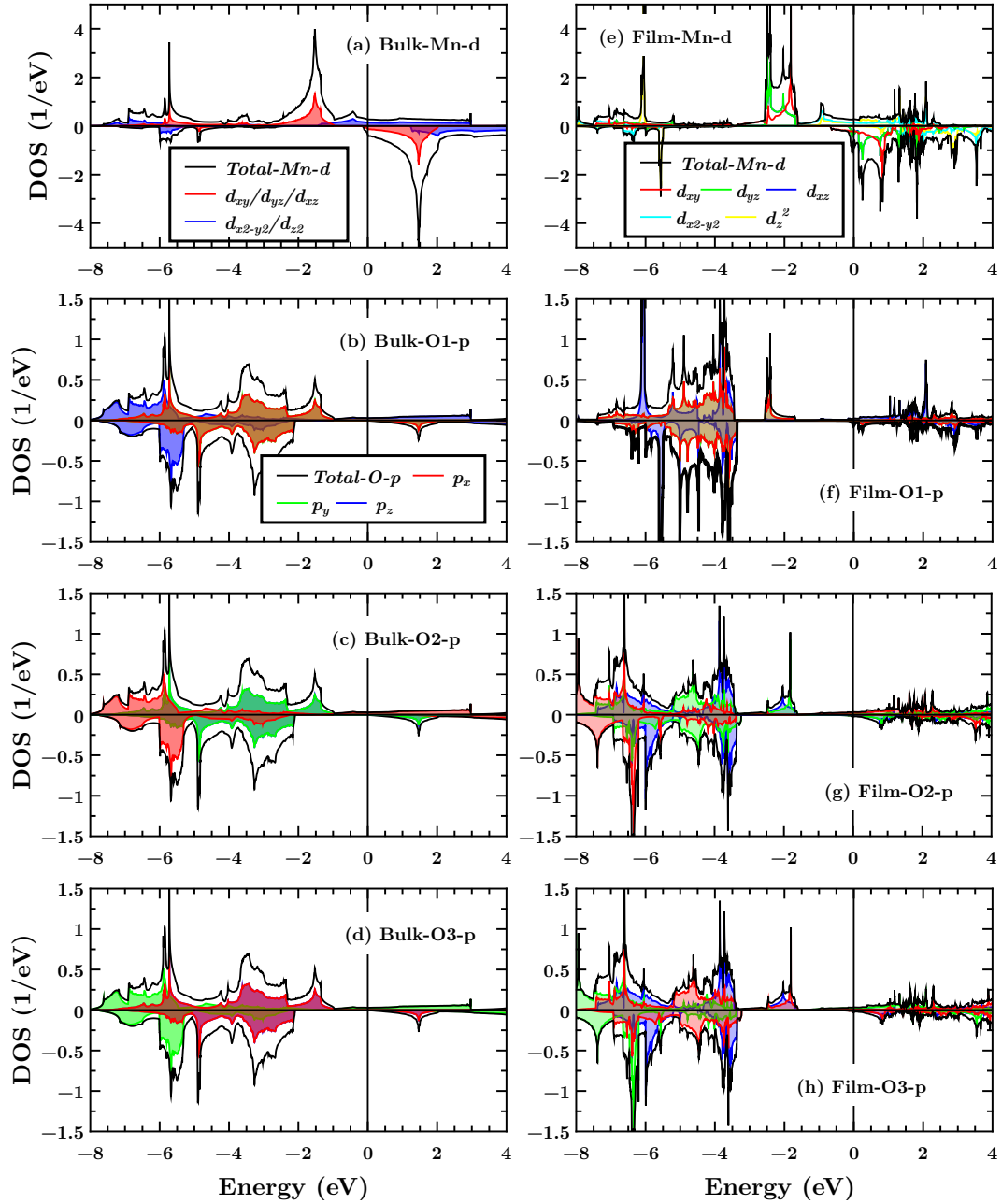 and d_{xz} orbitals and O-p orbitals should be reduced. In Fig. 4.8(f) the DOS of O1-p is shown. Altogether, three hybridization peaks can be found: the first one is at spin-majority channel around $-2\,\text{eV}$, which is composed of p_x and p_y orbitals, in Fig. 4.8(e) there is a corresponding DOS peak which is composed of d_{yz} and d_{xz} orbitals. This result indicates the hybridization between p_x/p_y and d_{xz}/d_{yz} is reserved, however the hybridization between Mn-d_{xy} and O1-p is totally destroyed. This is a surface/filming effect, because no surface Mn-O bond extension is considered here. The second and third hybridization peaks are around $-6\,\text{eV}$ at both spin-up and down channels and are from the hybridization between Mn-d_{z^2} and O1-p_z orbitals [Fig. 4.8(e-f)]. Comparing with p_x and p_y orbitals, p_z orbital lost its hybridization with Mn-$d_{x^2-y^2}$ orbital but the hybridization with d_{z^2} is boosted because the both d_{z^2} and p_z orbitals are spread along z-direction.

For the DOS of O2 and O3 Fig. 4.8(g)-(h), the largest hybridization peak is around $-2\,\text{eV}$, for O2 is mainly from p_y and p_z and for O3 is from p_x and p_z orbitals. However if one observes the DOS carefully, not only the O2-p_x and O3-p_y hybridization with d_{xy} becomes apparent, but also it is not difficult to infer that O2-p_z only hybridize with Mn-d_{xz} and O3-p_z hybridize with Mn-d_{yz}.

In summary, for cubic bulk LSMO in O1/O2/O3, p_x & p_y/p_y & p_z/p_x & p_z are hybridized to Mn-d_{t2g}, $p_z/p_x/p_y$ are hybridized to Mn-e_g. For film LSMO in O1, p_z, p_x and p_y are hybridized to d_{z^2}, d_{xy} and d_{yz}, respectively. In O2, p_y and p_z are hybridized to d_{xy} and d_{xz}, respectively. For O3, p_x and p_z are hybridized to d_{xy} and d_{yz}, respectively. All other d-p hybridization in film LSMO are eliminated by materials' surfacing/filming. Besides of MnO$_6$ octahedra rotation/tilting, surfacial bandwidth reduction and surfacical Mn-O bond extension, now we found the fourth mechanism drives the reduction of d-p hybridization: surface effects.

Finally, we focus on the interplay between thickness and magnetic moments. To explore their relationship, we perform spin-polarized DFT-GGA calculations for bulk LSMO free-standing thin films (thickness N=1-3 unit-cell). For thicknesses N=1,2,3, the M$_{total}$ (M$_{Mn}$) are 3.48 (2.95), 3.51 (2.98), 3.59 (3.06) μ_B, respectively. The averaged moments, no matter from the whole cell or only from Mn sites, both are enhanced as increasing the thickness N. The M$_{total}$ and M$_{Mn}$ for N=3, 3.59 and 3.06 μ_B are already close to the bulk values: 3.61 and 3.12 μ_B. This conclusion demonstrates that the "magnetic dead layer" phenomena in LSMO probably only happens at the top- and sub-surface layers: i.e. it is a surface/interface phenomenon.

Chapter 5

Summary & Outlook

This thesis has been aiming at reviewing the *ab-initio* DFT method and many body DMFT method as well as their applications of correlated materials. Let us in the following summarize the three **Chapters 2-4** following a pedagogical introduction.

In **Chapter 2** we reviewed the development of DFT: from the Hartree, to the Hartree-Fock approximations to the Hohenberg-Kohn theorem and the Kohn-Sham equation. We encountered two successful approximations regrading to the correlation-exchange energy: LDA and GGA. To improve on Coulomb interaction effects in strongly electronic correlated materials, we discussed DFT+U and DFT+DMFT methods. To solve the shortcoming of DMFT regrading SOC, we derived a full TB formalism to carry out *ab-initio* calculations for ABO_3 perovskite materials in the presence of SOC.

In **Chapter 3** we encountered one of the most well studied correlated materials, strontium ruthenate $SrRuO_3$. We systematically investigated $SrRuO_3$ by using DFT($+U$) and DFT+DMFT methods to understand the differences between different methods. DFT+DMFT method is functional to explain the Hubbard bands of $SrRuO_3$. For (001)-oriented thin films we performed DFT+DMFT calculations. In this way we were able to explain the experimentally confirmed nonmagnetic insulating states. In (110)-oriented thin films we found robust paramagnetic metallic states, whose property is different with the critical thickness behaviors in normal ABO_3 thin films. For (111)-orientation we predicted a strong ferromagnetic half-metallic state with T_C of 600 K and moment of $2\,\mu_B$/Ru. By DFT+U+SOC we found this strong ferromagnet indeed to host a QAH state, with the possibility of its experimental observation. Previous experiments were not able to reduce the thickness of $SrRuO_3$ (111) thin films to bilayer, so that our results fill an important piece in the ground state puzzle of $SrRuO_3$ films. Furthermore, by using DFT+U method we successfully simulated the high-spin states in $SrRuO_3$ by the help of single oxygen vacancy.

Chapter 4 was devoted to applying TB, DFT($+U$) and DFT+DMFT to various correlated transition metal oxides. In order to simulate surface/interface Rashba spin-splitting, we applied the DFT and TB methods to a $BaOsO_3$:$BaTiO_3$ superlattice. As a result we predicted such heterostructures can be candidates for observing a giant Rashba effect. Bulk (Cr-doped) V_2O_3 is intensively researched because of its Mott-Hubbard metal-insulator transitions. By using DFT+DMFT we found the surface termination can enhance the metallicity by self-doping. In double perovskite Sr_2CrMoO_6, we found that both the DFT+U and DFT+DMFT methods can explain the ferrimagnetic half-metallic state. Our study reveals that the magnetic transition temperature of Sr_2CrMoO_6 remains high since an additional superexchange contribution to magnetism arises with a finite intrinsic moment developed at the Mo sites. Lastly we studied $La_{1-x}Sr_xMnO_3$ films by DFT($+U$) method, we found the interplay between MnO_6 octahedral rotation and tilting, surfacing, lattice compression:

all contribute to the magnetic properties of $La_{1-x}Sr_xMnO_3$ films.

In this thesis we employed TB, DFT($+U$) and DFT+DMFT methods and studied transition metal oxides at bulk, heterostructure, thin films, surface and interface states. The DFT+DMFT method is functional for dynamical correlations, however several shortcomings limit its applications: (i) as a DFT/TB self-consistent calculations is necessary to generate the input Hamiltonian, for large-scale systems both the DFT and DMFT circles can be very time consuming; (ii) for $4d$- and $5d$-orbitals oxides, electronic structure can be seriously modified by SOC effect, thus a DFT+DMFT calculation without SOC is a approximation. When we consider dynamical correlation effects and how to perform it in the present of SOC is the next step; (iii) most importantly, dynamical correlation effects are included in DMFT only at local level, i.e. the self-energy only depends on frequency ω but not on momentum k. How to include non-local correlation effects, which are important in some transition metal oxides, is still challenging; (iv) additionally, in this thesis we used "one-shot" DFT+DMFT: the DMFT resulted quantities do not return back to DFT, i.e. we did not performed charge self-consistent DFT+DMFT calculations. We believe that these improvements will not qualitatively change our conclusions, however in the future systematic double checks are essential to be done.

Acknowledgements

I can not image that whether I could finish this thesis without the help from the people whose names will appear below. Maybe at the beginning of doing something new one always feels that everything will be achieved nicely if the two conditions are satisfied: a smart mind and hard working. However, the truth is always that *life is never easy, when/if you feel that is easy, that means someone is carrying the difficulty parts for you*. Fortunately, there are always some nice persons who are willing to support me. In this part, I want to thank all the people who contributes to my Ph.D study (and apologize to the ones I may have forgotten).

First of all, I want to thank **Prof. Dr. Karsten Held**, who gives me this great honor to study in his group as a Ph.D candidate. His supervision, generous and patience change the further of mine, and my family. He opens a door for me, and there is something called *infinite* behind it. Every night when I close my eyes, I can still remember that period of time, February of 2013 when I came to Vienna for the Ph.D candidate interview. I was excited and nervous, because to go for that interview I gave up all other chances at hand, I had nothing to lose. It did not take long then I found that I made one of the best decisions in my life: I was studying in the best group in the world, and the one who supervises me is the best scientist/supervisor ever. Karsten has the best physical intuition and motivations in our field: I do learn so much from him. I also appreciate his great leading skills, he successfully manage a large group and guide different research topics, keep a friendly, cooperative and productive environment at the same time, this could be very hard for others, but he makes it and everyone in his group enjoys this very much. Some day in the further I will also be a professor, teaching and supervising somewhere. I really want to be a scientist like him.

I have to thank **Dr. Zhicheng Zhong**, who I work with between 2013 to 2014. In fact all the stories began at the moment when I saw the announcement of opening Ph.D position, which was from him. He is the one who knows that how bad my physics background was, but he still choses to trust me. Basically, he rebuilds my knowledge frame of physics and my attitude to science. He not only supervises my Ph.D study but also teaches me how to live in foreign countries. I had no friends at the moment I came here, and it was him who introduced his friends to me and often invited me to have dinner with his family. Some of his friends also became my friends after that. He also encourages me when I face difficulties by telling me his own past experiences. I am honestly indebted to him.

I want to thank **Angelika Bosak**, the secretary of Institute of Solid State Physics. As a foreigner in Austria, from daily life to visa application, there are always something that I totally have no ideas how to process them. She is always patient to help me. I also want to thank **Dr. Andre Vogel**, the coordinator of Doctoral School Solids4Fun (Building Solids for Function), thank you for your help and generous.

I want to thank three persons who I collaborated with: **Dr. Jan M. Tomczak**, **Dr. Oleg Janson** and **Dr. Gang Li**. Any research is a truly complex project that is not possible to achieve on one's own. Dr. Oleg Janson not only supervises my thesis but also teaches me the *art of scientific writing*, he is really talent at writing. I learn *topological physics* from Dr. Gang Li, he is an expert in this field. I usually ask Dr. Jan Tomczak about physics problems, every time he is very patient, I do learn quite a lot from the discussions with him. All my research can not be finished smoothly without their help.

During my Ph.D study in Vienna, I am so lucky that there are so many interesting, kind and inspiring people who I know. Thank **Prof. Dr. Ulrike Diebold** from

IAP, TU Wien. She is my second-supervisor from Doctoral School Solids4Fun, she gave lots of useful comments to my research, she also wrote recommendation letters for me when I was searching for my first post-doctoral job. Thank **Prof. Dr. Alessandro Toschi** for teaching me the language of *Green's functions*. Thank **Prof. Dr. Tanusri Saha-dasgupta** and **Prof. Dr. Prabuddha Sanyal** from India for the collaborations about double pervoskite. Thank **Dr. Elias Assmann** for teaching me how to use *Wien2k* and *Wien2wannier*. Thank **Dr. Thomas Schäfer** for carrying on organizing group lunch, he successfully makes me fall in love with *sushi*. Thank **Dr. Markus Wallerberger** and **Anna Galler**, we shared a really big office in the first year of my Ph.D study, that period of time is really good memory to me, both of them are very nice persons. Later on we moved into a bigger office, **Patrik Gunacker**, **Tin Ribic**, **Michael Wais** and **Josef Kaufmann** joined us, our "team" is larger and has more fan than before. Thank **Dr. Philipp Hansmann** (he really looks like the Hollywood star Matt Damon!) and **Dr. Patrik Thunström** for helpful discussions, I really learn quite a lot from that. Thank **Dr. Georg Rohringer** for organizing the very successful workshop. Thank **Dr. Marco Battiato** for sharing his interesting experiences and sad animals stories to us. Thank **Dr. Sumanta Bhandary** for letting us know what is the real Indian food. At the beginning year of my Ph.D study I did attend lots of sporty activities, this is due to the successful organization of **Dr. Ciro Taranto** and **Dr. Angelo Valli**. Thank **Dr. Daniel Springer** (shooting expert!), **Dr. Anna Kauch** (welcome!) and **Petra Pudleiner** (good lucky in Shanghai), the lunch time talks around our big lunch table are always funny and interesting.

Lastly, I truthfully want to thank my wife, **Xiang Fiona Li**, for all the things she does for our family. To came to Vienna living with me, she had to give up everything she had obtained in Beijing, I really appreciate that. During the time when I was preparing this thesis, she gave birth to our first child at the same time. To give me a relax environment to carry on writing, she took most parts of the house work and take care of our child. Thank you for everything! My daughter, **Nian Charlotte Si**, is a lovely angel. I really hope she can have a wonder life, being happy and healthy.

Thanks for everyone passing by in my life...

Bibliography

Agrestini, S. et al. (2015). "Electronic and spin states of $SrRuO_3$ thin films: An x-ray magnetic circular dichroism study". In: *Phys. Rev. B* 91 (7), p. 075127.

Allen, P. B. et al. (1996). "Transport properties, thermodynamic properties, and electronic structure of $SrRuO_3$". In: *Phys. Rev. B* 53 (8), pp. 4393–4398.

Alperin, H. A. (1962). "NiO magnetic moments". In: *J. Phys. Soc. Jpn. Suppl. B (3)* 17, p. 12.

Andersen, O. K. et al. (1980). "Electronic structure of transition metal compounds; ground-state properties of the $3d$-monoxides in the atomic sphere approximation". In: *Pure and Applied Chemistry* 52.1, pp. 93–118.

Anderson, P. W. (1961). "Localized Magnetic States in Metals". In: *Phys. Rev.* 124 (1), pp. 41–53.

Anisimov, V. I., M. A. Korotin, and E. Z. Kurmaev (1990). "Band-structure description of mott insulators (NiO, MnO, FeO, CoO)". In: *Journal of Physics: Condensed Matter* 2.17, p. 3973.

Anisimov, Vladimir I, F Aryasetiawan, and AI Lichtenstein (1997). "First-principles calculations of the electronic structure and spectra of strongly correlated systems: the LDA+U method". In: *J. Phys.: Condens. Matter.* 9.4, p. 767.

Anisimov, Vladimir I., Jan Zaanen, and Ole K. Andersen (1991). "Band theory and Mott insulators: Hubbard U instead of Stoner I". In: *Phys. Rev. B* 44 (3), pp. 943–954.

Arulraj, Anthony et al. (2000). "Magnetoresistance in the double perovskite Sr_2CrMoO_6". In: *Journal of Solid State Chemistry* 155.1, pp. 233–237.

Aryasetiawan, F. et al. (2004). "Frequency-dependent local interactions and low-energy effective models from electronic structure calculations". In: *Phys. Rev. B* 70 (19), p. 195104.

Ast, Christian R. et al. (2007). "Giant Spin Splitting through Surface Alloying". In: *Phys. Rev. Lett.* 98 (18), p. 186807.

Bahramy, MS et al. (2012). "Emergence of non-centrosymmetric topological insulating phase in BiTeI under pressure". In: *Nature communications* 3, p. 679.

Baym, Gordon and Christopher Pethick (2008). *Landau Fermi-liquid theory: concepts and applications*. John Wiley & Sons.

Bern, F et al. (2013). "Structural, magnetic and electrical properties of $SrRuO_3$ films and $SrRuO_3$/$SrTiO_3$ superlattices". In: *J. Phys.: Condens. Matter.* 25.49, p. 496003.

Berry, Michael V (1984). "Quantal phase factors accompanying adiabatic changes". In: *Proceedings of the Royal Society of London A: Mathematical, Physical and Engineering Sciences*. Vol. 392. 1802. The Royal Society, pp. 45–57.

Bhattacharya, A. et al. (2008). "Metal-Insulator Transition and Its Relation to Magnetic Structure in $(LaMnO_3)_{2n}$/$(SrMnO_3)_n$ Superlattices". In: *Phys. Rev. Lett.* 100 (25), p. 257203.

Bickers, N. E., D. J. Scalapino, and S. R. White (1989). "Conserving Approximations for Strongly Correlated Electron Systems: Bethe-Salpeter Equation and Dynamics for the Two-Dimensional Hubbard Model". In: *Phys. Rev. Lett.* 62 (8), pp. 961–964.

Biermann, S. et al. (2005). "Dynamical Singlets and Correlation-Assisted Peierls Transition in VO_2". In: *Phys. Rev. Lett.* 94 (2), p. 026404.

Blaha, Peter et al. (2001). "Wien2k". In: *An augmented plane wave+ local orbitals program for calculating crystal properties*.

Blankenbecler, R. et al. (1987). "Ground-state properties of the periodic Anderson model". In: *Phys. Rev. Lett.* 58 (4), pp. 411–414.

Blasco, J et al. (2002). "Structural, magnetic and transport properties of $Sr_2Fe_{1-x}Cr_xMoO_{6-y}$". In: *Solid state sciences* 4.5, pp. 651–660.

Blöchl, P. E. (1994). "Projector augmented-wave method". In: *Phys. Rev. B* 50 (24), pp. 17953–17979.

Bonilla, CM et al. (2007). "Half-metallic behavior and electronic structure of Sr_2CrMoO_6 magnetic system". In: *Physica B: Condensed Matter* 398.2, pp. 208–211.

Boris, AV et al. (2011). "Dimensionality control of electronic phase transitions in nickel-oxide superlattices". In: *Science* 332.6032, pp. 937–940.

Born, Max and Robert Oppenheimer (1927). "Zur quantentheorie der molekeln". In: *Annalen der Physik* 389.20, pp. 457–484.

Boschker, Hans et al. (2012). "Preventing the reconstruction of the polar discontinuity at oxide heterointerfaces". In: *Advanced functional materials* 22.11, pp. 2235–2240.

Cacho, C. et al. (2015). "Momentum resolved spin dynamics of bulk and surface excited states in the topological insulator Bi_2Se_3". In: *Phys. Rev. Lett.* 114, p. 097401.

Caffarel, Michel and Werner Krauth (1994). "Exact diagonalization approach to correlated fermions in infinite dimensions: Mott transition and superconductivity". In: *Phys. Rev. Lett.* 72 (10), pp. 1545–1548.

Cao, G. et al. (1997). "Thermal, magnetic, and transport properties of single-crystal $Sr_{1-x}Ca_xRuO_3$ ($0<\sim x<\sim1$)". In: *Phys. Rev. B* 56 (1), pp. 321–329.

Caviglia, A. D. et al. (2010). "Tunable Rashba Spin-Orbit Interaction at Oxide Interfaces". In: *Phys. Rev. Lett.* 104.12, p. 126803.

Ceperley, D. M. and B. J. Alder (1980). "Ground State of the Electron Gas by a Stochastic Method". In: *Phys. Rev. Lett.* 45 (7), pp. 566–569.

Chakhalian, Jak et al. (2014). "*Colloquium*: Emergent properties in plane view: Strong correlations at oxide interfaces". In: *Rev. Mod. Phys.* 86 (4), pp. 1189–1202.

Chang, Cui-Zu et al. (2013). "Experimental observation of the quantum anomalous Hall effect in a magnetic topological insulator". In: *Science* 340.6129, pp. 167–170.

Chang, Young Jun et al. (2009). "Fundamental Thickness Limit of Itinerant Ferromagnetic $SrRuO_3$ Thin Films". In: *Phys. Rev. Lett.* 103 (5), p. 057201.

Checkelsky, JG et al. (2014). "Trajectory of the anomalous Hall effect towards the quantized state in a ferromagnetic topological insulator". In: *Nature Physics* 10.10, pp. 731–736.

Cheetham, A. K. and D. A. O. Hope (1983). "Magnetic ordering and exchange effects in the antiferromagnetic solid solutions $Mn_xNi_{1-x}O$". In: *Phys. Rev. B* 27 (11), pp. 6964–6967.

Choi, K. J. et al. (2004). "Enhancement of Ferroelectricity in Strained $BaTiO_3$ Thin films". In: *Science* 306, p. 1005.

Curiale, J et al. (2009). "Magnetic dead layer in ferromagnetic manganite nanoparticles". In: *Applied Physics Letters* 95.4, p. 043106.

Dabrowski, B. et al. (2004). "Reduced ferromagnetic transition temperatures in $SrRu_{1-v}O_3$ perovskites from Ru-site vacancies". In: *Phys. Rev. B* 70 (1), p. 014423.

Dagotto, Elbio (1994). "Correlated electrons in high-temperature superconductors". In: *Rev. Mod. Phys.* 66 (3), pp. 763–840.

— (2005). "Complexity in strongly correlated electronic systems". In: *Science* 309.5732, pp. 257–262.

Dang, Hung T. et al. (2015). "Electronic correlations, magnetism, and Hund's rule coupling in the ruthenium perovskites SrRuO$_3$ and CaRuO$_3$". In: *Phys. Rev. B* 91 (19), p. 195149.

Das, Hena et al. (2011). "Origin of magnetism and trend in T_c in Cr-based double perovskites: Interplay of two driving mechanisms". In: *Phys. Rev. B* 83 (10), p. 104418.

Das, Tanmoy and Alexander V Balatsky (2013). "Engineering three-dimensional topological insulators in Rashba-type spin-orbit coupled heterostructures". In: *Nature communications* 4.

Datta, Supriyo and Biswajit Das (1990). "Electronic analog of the electro-optic modulator". In: *Applied Physics Letters* 56.7, pp. 665–667.

Dawber, M., K. M. Rabe, and J. F. Scott (2005). "Physics of thin-film ferroelectric oxides". In: *Rev. Mod. Phys.* 77 (4), pp. 1083–1130.

Deng, Xiaoyu, Kristjan Haule, and Gabriel Kotliar (2016). "Transport Properties of Metallic Ruthenates: A DFT + DMFT Investigation". In: *Phys. Rev. Lett.* 116 (25), p. 256401.

Di Sante, Domenico et al. (2013). "Electric Control of the Giant Rashba Effect in Bulk GeTe". In: *Advanced Materials* 25.4, pp. 509–513. ISSN: 1521-4095.

Duan, Chun-Gang, S. S. Jaswal, and E. Y. Tsymbal (2006). "Predicted Magnetoelectric Effect in Fe/BaTiO$_3$ Multilayers: Ferroelectric Control of Magnetism". In: *Phys. Rev. Lett.* 97 (4), p. 047201.

Dulli, Hani et al. (2000). "Surface segregation and restructuring of colossal-magnetoresistant manganese perovskites La$_{0.65}$Sr$_{0.35}$MnO$_3$". In: *Phys. Rev. B* 62 (22), R14629–R14632.

Dupuis, A-C et al. (2003). "V$_2$O$_3$ (0001) on Au (111) and W (110): growth, termination and electronic structure". In: *Surface science* 539.1, pp. 99–112.

Eastman, D. E. and J. L. Freeouf (1975). "Photoemission Partial State Densities of Overlapping p and d States for NiO, CoO, FeO, MnO, and Cr$_2$O$_3$". In: *Phys. Rev. Lett.* 34 (7), pp. 395–398.

Emery, V. J. and S. A. Kivelson (1995). "Superconductivity in bad metals". In: *Phys. Rev. Lett.* 74.16, p. 3253.

Eom, CB et al. (1992). "Single-crystal epitaxial thin films of the isotropic metallic oxides Sr$_{1-x}$Ca$_x$RuO$_3$ (O$\leq x \leq 1$)". In: *Science* 258.5089, pp. 1766–1769.

Falicov, L. M. and J. C. Kimball (1969). "Simple Model for Semiconductor-Metal Transitions: SmB$_6$ and Transition-Metal Oxides". In: *Phys. Rev. Lett.* 22 (19), pp. 997–999.

Fang, Z., I. V. Solovyev, and K. Terakura (2000). "Phase Diagram of Tetragonal Manganites". In: *Phys. Rev. Lett.* 84 (14), pp. 3169–3172.

Fang, Zhong et al. (2003). "The anomalous Hall effect and magnetic monopoles in momentum space". In: *Science* 302.5642, pp. 92–95.

Feiten, Felix E. et al. (2015). "Surface Structure of V$_2$O$_3$(0001) Revisited". In: *Phys. Rev. Lett.* 114 (21), p. 216101.

Felner, Israel, Kiyoshi Nomura, and Israel Nowik (2006). "Mössbauer and magnetic studies of bulk and fine-powder SrRuO$_3$ and Sr-Cu-RuO$_3$ systems". In: *Phys. Rev. B* 73.6, p. 064401.

Fermi, Enrico (1928). "Eine statistische Methode zur Bestimmung einiger Eigenschaften des Atoms und ihre Anwendung auf die Theorie des periodischen Systems der Elemente". In: *Zeitschrift für Physik* 48.1-2, pp. 73–79.

Fetter, Alexander L and John Dirk Walecka (2003). *Quantum theory of many-particle systems*. Courier Corporation.

Filippi, Claudia, C. J. Umrigar, and M. Taut (1994). "Comparison of exact and approximate density functionals for an exactly soluble model". In: *The Journal of chemical physics* 100.2, pp. 1290–1296.

Fock, V (1930). "Näherungsmethode zur Lösung des quantenmechanischen Mehrkörperproblems". In: *Zeitschrift für Physik* 61.1-2, pp. 126–148.

Franchini, C. et al. (2012). "Maximally localized Wannier functions in $LaMnO_3$ within PBE+U, hybrid functionals and partially self-consistent GW: an efficient route to construct *ab initio* tight-binding parameters for eg perovskites". In: *Journal of Physics: Condensed Matter* 24.23, p. 235602.

Fukui, Takahiro and Yasuhiro Hatsugai (2007). "Quantum spin Hall effect in three dimensional materials: Lattice computation of Z2 topological invariants and its application to Bi and Sb". In: *Journal of the Physical Society of Japan* 76.5, p. 053702.

Galler, Anna et al. (2016). "*Ab initio* dynamical vertex approximation". In: *arXiv preprint arXiv:1610.02998*.

Garcia-Landa, B. et al. (1999). "Magnetic and magnetotransport properties of the ordered perovskite Sr_2FeMoO_6". In: *Solid state communications* 110, pp. 435–438.

Garcia-Munoz, J. L. et al. (1996). "Bandwidth narrowing in bulk magnetoresistive oxides". In: 8.50, p. L787.

Georges, Antoine and Gabriel Kotliar (1992). "Hubbard model in infinite dimensions". In: *Phys. Rev. B* 45 (12), pp. 6479–6483.

Georges, Antoine and Werner Krauth (1992). "Numerical solution of the $d=\infty$ Hubbard model: Evidence for a Mott transition". In: *Phys. Rev. Lett.* 69 (8), pp. 1240–1243.

Georges, Antoine, Luca de' Medici, and Jernej Mravlje (2012). "Strong electronic correlations from Hund's coupling". In: *arXiv preprint arXiv:1207.3033*.

Georges, Antoine et al. (1996). "Dynamical mean-field theory of strongly correlated fermion systems and the limit of infinite dimensions". In: *Rev. Mod. Phys.* 68.1, p. 13.

Gibb, Terence C et al. (1974). "A study of the magnetic superexchange interactions in the solid-solution series $Ca_xSr_{1-x}RuO_3$ by ruthenium-99 Mössbauer spectroscopy". In: *Journal of Solid State Chemistry* 11.1, pp. 17–25.

Grånäs, Oscar et al. (2014). "Electronic structure, cohesive properties, and magnetism of $SrRuO_3$". In: *Phys. Rev. B* 90.16, p. 165130.

Grutter, A. J. et al. (2010). "Enhanced magnetism in epitaxial $SrRuO_3$ thin films". In: *Applied Physics Letters* 96.8, p. 082509.

Grutter, A. J. et al. (2012). "Evidence of high-spin Ru and universal magnetic anisotropy in $SrRuO_3$ thin films". In: *Phys. Rev. B* 85 (13), p. 134429.

Grutter, A. J. et al. (2013). "Stabilization of spin-zero Ru^{4+} through epitaxial strain in $SrRuO_3$ thin films". In: *Phys. Rev. B* 88 (21), p. 214410.

Gubernatis, J. E. et al. (1991). "Quantum Monte Carlo simulations and maximum entropy: Dynamics from imaginary-time data". In: *Phys. Rev. B* 44.12, p. 6011.

Gukelberger, Jan, Li Huang, and Philipp Werner (2015). "On the dangers of partial diagrammatic summations: Benchmarks for the two-dimensional Hubbard model in the weak-coupling regime". In: *Phys. Rev. B* 91 (23), p. 235114.

Gull, Emanuel et al. (2011). "Continuous-time Monte Carlo methods for quantum impurity models". In: *Rev. Mod. Phys.* 83 (2), pp. 349–404.

Gupta, Kapil, Basudeb Mandal, and Priya Mahadevan (2014). "Strain-induced metal-insulator transition in ultrathin films of $SrRuO_3$". In: *Phys. Rev. B* 90.12, p. 125109.

Hadipour, H and M Akhavan (2011). "Electron correlation in $Sr(Ca)RuO_3$ by GWA and LSDA+U". In: *Eur. Phys. J. B* 84.2, pp. 203–217.

Haldane, F. D. M. (1988). "Model for a Quantum Hall Effect without Landau Levels: Condensed-Matter Realization of the "Parity Anomaly"". In: *Phys. Rev. Lett.* 61 (18), pp. 2015–2018.

Hartree, Douglas R (1928). "The wave mechanics of an atom with a non-Coulomb central field. Part I. Theory and methods". In: *Mathematical Proceedings of the Cambridge Philosophical Society*. Vol. 24. 01. Cambridge Univ Press, pp. 89–110.

Hasan, M. Z. and C. L. Kane (2010). "*Colloquium*: Topological insulators". In: *Rev. Mod. Phys.* 82 (4), pp. 3045–3067.

He, Junjie et al. (2016). "$NiCl_3$ Monolayer: Dirac Spin-Gapless Semiconductor and Chern Insulator". In: *arXiv preprint arXiv:1610.00407*.

Hedin, Lars (1965). "New Method for Calculating the One-Particle Green's Function with Application to the Electron-Gas Problem". In: *Phys. Rev.* 139 (3A), A796–A823.

Held, K (2007). "Electronic structure calculations using dynamical mean field theory". In: *Adv. Phys.* 56.6, pp. 829–926.

Held, K. (2014). "Dynamical Vertex Approximation". In: *arXiv preprint arXiv:1411.5191*.

Held, K. et al. (2001). "Mott-Hubbard Metal-Insulator Transition in Paramagnetic V_2O_3: An $LDA + DMFT$(QMC) Study". In: *Phys. Rev. Lett.* 86 (23), pp. 5345–5348.

Held, Karsten et al. (2008). "Bandstructure meets many-body theory: the LDA+ DMFT method". In: *J. Phys.: Condens. Matter.* 20.6, p. 064202.

Held, Karsten et al. (2011). "Hedin equations, GW, GW+ DMFT, and all that". In: *arXiv preprint arXiv:1109.3972*.

Hettler, M. H. et al. (1998). "Nonlocal dynamical correlations of strongly interacting electron systems". In: *Phys. Rev. B* 58 (12), R7475–R7479.

Hewson, Alexander Cyril (1997). *The Kondo problem to heavy fermions*. Vol. 2. Cambridge university press.

Heyd, Jochen, Gustavo E Scuseria, and Matthias Ernzerhof (2003). "Hybrid functionals based on a screened Coulomb potential". In: *The Journal of Chemical Physics* 118.18, pp. 8207–8215.

Heyen, E. T., J Kircher, and M Cardona (1992). "Resonant Raman scattering in insulating $YBa_2Cu_3O_6$ as a probe of its electronic structure". In: *Physical Review B* 45.6, p. 3037.

Hiratani, Masahiko et al. (1996). "$SrRuO_3$ thin films grown under reduced oxygen pressure". In: *Japanese journal of applied physics* 35.12R, p. 6212.

Hirsch, J. E. and R. M. Fye (1986). "Monte Carlo Method for Magnetic Impurities in Metals". In: *Phys. Rev. Lett.* 56 (23), pp. 2521–2524.

Hohenberg, P. and W. Kohn (1964). "Inhomogeneous Electron Gas". In: *Phys. Rev.* 136 (3B), B864–B871.

Hsieh, David et al. (2008). "A topological Dirac insulator in a quantum spin Hall phase". In: *Nature* 452.7190, pp. 970–974.

Hubbard, John (1963). "Electron correlations in narrow energy bands". In: *Proceedings of the Royal Society of London. Series A. Mathematical and Physical Sciences* 276.1365, pp. 238–257.

— (1964[a]). "Electron correlations in narrow energy bands. II. The degenerate band case". In: *Proceedings of the Royal Society of London. Series A. Mathematical and Physical Sciences* 277.1369, pp. 237–259.

— (1964[b]). "Electron correlations in narrow energy bands. III. An improved solution". In: *Proceedings of the Royal Society of London. Series A. Mathematical and Physical Sciences* 281.1386, pp. 401–419.

Hüfner, S et al. (1984). "Photoemission and inverse photoemission spectroscopy of NiO". In: *Solid state communications* 52.9, pp. 793–796.

Hughes, C. R. et al. (2016). "Ferromagnetism and conductivity in atomically thin $SrRuO_3$". In: *arXiv preprint arXiv:1609.08901*.

Huijben, M. et al. (2008). "Critical thickness and orbital ordering in ultrathin $La_{0.7}Sr_{0.3}MnO_3$ films". In: *Phys. Rev. B* 78 (9), p. 094413.

Imada, Masatoshi, Atsushi Fujimori, and Yoshinori Tokura (1998). "Metal-insulator transitions". In: *Rev. Mod. Phys.* 70 (4), pp. 1039–1263.

Ishida, Hiroshi and Ansgar Liebsch (2010). "Fermi-liquid, non-Fermi-liquid, and Mott phases in iron pnictides and cuprates". In: *Phys. Rev. B* 81 (5), p. 054513.

Ishigami, K. et al. (2015). "Thickness-dependent magnetic properties and strain-induced orbital magnetic moment in $SrRuO_3$ thin films". In: *Phys. Rev. B* 92 (6), p. 064402.

Ishizaka, K. et al. (2011). "Giant Rashba-type spin splitting in bulk BiTeI". In: *Nat. Mat.* 10.7, p. 521.

Jakobi, E et al. (2011). "LDA+DMFT study of Ru-based perovskite $SrRuO_3$ and $CaRuO_3$". In: *Phys. Rev. B* 83.4, p. 041103.

Jarrell, M. (1992). "Hubbard model in infinite dimensions: A quantum Monte Carlo study". In: *Phys. Rev. Lett.* 69 (1), pp. 168–171.

— (1995). "Symmetric periodic Anderson model in infinite dimensions". In: *Phys. Rev. B* 51 (12), pp. 7429–7440.

Jarrell, M., Hossein Akhlaghpour, and Th. Pruschke (1993). "Periodic Anderson model in infinite dimensions". In: *Phys. Rev. Lett.* 70 (11), pp. 1670–1673.

Jarrell, M. and Th. Pruschke (1994). "Anomalous properties of the Hubbard model in infinite dimensions". In: *Phys. Rev. B* 49 (2), pp. 1458–1461.

Jeong, D. W. et al. (2013). "Temperature Evolution of Itinerant Ferromagnetism in $SrRuO_3$ Probed by Optical Spectroscopy". In: *Phys. Rev. Lett.* 110.24, p. 247202.

Jones, C. W. et al. (1989). "The structure of $SrRuO_3$ by time-of-flight neutron powder diffraction". In: *Acta Cryst.* C45.3, pp. 365–367.

Junquera, Javier and Philippe Ghosez (2003). "Critical thickness for ferroelectricity in perovskite ultrathin films". In: *Nature* 422.6931, pp. 506–509.

Kan, Daisuke et al. (2016). "Tuning magnetic anisotropy by interfacially engineering the oxygen coordination environment in a transition metal oxide". In: *Nature materials* 15.4, pp. 432–437.

Kanbayasi, Akio (1978). "Magnetic Properties of $SrRuO_3$ Single Crystal. II". In: *Journal of the Physical Society of Japan* 44.1, pp. 89–95.

Kane, C. L. and E. J. Mele (2005). "Z_2 Topological Order and the Quantum Spin Hall Effect". In: *Phys. Rev. Lett.* 95 (14), p. 146802.

Keller, G. et al. (2004). "Electronic structure of paramagnetic V_2O_3: Strongly correlated metallic and Mott insulating phase". In: *Phys. Rev. B* 70 (20), p. 205116.

Kennedy, Tom and Elliott H Lieb (1986). "An itinerant electron model with crystalline or magnetic long range order". In: *Physica A: Statistical Mechanics and its Applications* 138.1-2, pp. 320–358.

Kim, Bongjae and B. I. Min (2014). "Termination-dependent electronic and magnetic properties of ultrathin $SrRuO_3$ (111) films on $SrTiO_3$". In: *Phys. Rev. B* 89 (19), p. 195411.

Kim, Jungho, Jaegwan Chung, and S-J Oh (2005). "In situ photoemission study on $SrRuO_3/SrTiO_3$ films grown by pulsed laser deposition". In: *Phys. Rev. B* 71.12, p. 121406.

Kim, Minjae and B. I. Min (2015). "Nature of itinerant ferromagnetism of $SrRuO_3$: A DFT+DMFT study". In: *Phys. Rev. B* 91 (20), p. 205116.

King, P. D. C. et al. (2011). "Large Tunable Rashba Spin Splitting of a Two-Dimensional Electron Gas in Bi_2Se_3". In: *Phys. Rev. Lett.* 107 (9), p. 096802.

King, P. D. C. et al. (2012). "Subband Structure of a Two-Dimensional Electron Gas Formed at the Polar Surface of the Strong Spin-Orbit Perovskite $KTaO_3$". In: *Phys. Rev. Lett.* 108 (11), p. 117602.

King, P.D.C. et al. (2014). "Atomic-scale control of competing electronic phases in ultrathin $LaNiO_3$". In: *Nature Nanotechnology* 9.6, pp. 443–447.

Kiyama, T. et al. (1996). "Invar effect of $SrRuO_3$: Itinerant electron magnetism of Ru $4d$ electrons". In: *Phys. Rev. B* 54 (2), R756–R759.

Klein, L et al. (1996). "Transport and magnetization in the badly metallic itinerant ferromagnet". In: *Journal of Physics: Condensed Matter* 8.48, p. 10111.

Klitzing, K. v., G. Dorda, and M. Pepper (1980). "New Method for High-Accuracy Determination of the Fine-Structure Constant Based on Quantized Hall Resistance". In: *Phys. Rev. Lett.* 45 (6), pp. 494–497.

Kobayashi, K-I et al. (1998). "Room-temperature magnetoresistance in an oxide material with an ordered double-perovskite structure". In: *Nature* 395.6703, pp. 677–680.

Kobayashi, Masaki et al. (2015). "Origin of the Anomalous Mass Renormalization in Metallic Quantum Well States of Strongly Correlated Oxide $SrVO_3$". In: *Phys. Rev. Lett.* 115 (7), p. 076801.

Kohn, W. and L. J. Sham (1965). "Self-Consistent Equations Including Exchange and Correlation Effects". In: *Phys. Rev.* 140 (4A), A1133–A1138.

Kolczewski, Christine et al. (2007). "Identification of the vanadyl terminated V_2O_3 (0001) surface by NEXAFS spectroscopy: A combined theoretical and experimental study". In: *Surface Science* 601.23, pp. 5394–5402.

König, Markus et al. (2007). "Quantum spin Hall insulator state in HgTe quantum wells". In: *Science* 318.5851, pp. 766–770.

Konishi, Yoshinori et al. (1999). "Orbital-state-mediated phase-control of manganites". In: *Journal of the Physical Society of Japan* 68.12, pp. 3790–3793.

Koster, Gertjan et al. (2012). "Structure, physical properties, and applications of $SrRuO_3$ thin films". In: *Rev. Mod. Phys.* 84 (1), pp. 253–298.

Kotliar, Gabriel and Dieter Vollhardt (2004). "Strongly correlated materials: Insights from dynamical mean-field theory". In: *Phys. Today* 57.3, pp. 53–60.

Kotliar, Gabriel et al. (2006). "Electronic structure calculations with dynamical mean-field theory". In: *Rev. Mod. Phys.* 78.3, p. 865.

Kourkoutis, L Fitting et al. (2010). "Microscopic origins for stabilizing room-temperature ferromagnetism in ultrathin manganite layers". In: *Proceedings of the National Academy of Sciences* 107.26, pp. 11682–11685.

Kresse, G. and J. Hafner (1993). "*Ab initio* molecular dynamics for open-shell transition metals". In: *Phys. Rev. B* 48 (17), pp. 13115–13118.

Kresse, G et al. (2004). "V_2O_3 (0001) surface terminations: a density functional study". In: *Surface science* 555.1, pp. 118–134.

Kresse, Georg and Jürgen Furthmüller (1996). "Efficiency of ab-initio total energy calculations for metals and semiconductors using a plane-wave basis set". In: *Computational Materials Science* 6.1, pp. 15–50.

Kuneš, Jan et al. (2010). "Wien2wannier: From linearized augmented plane waves to maximally localized Wannier functions". In: *Comp. Phys. Comm.* 181.11, pp. 1888–1895.

Laad, M. S. and E. Müller-Hartmann (2001). "Origin of the Non-Fermi Liquid Behavior of $SrRuO_3$". In: *Phys. Rev. Lett.* 87 (24), p. 246402.

Lang, N. D., S Lundqvist, and N. H. March (1983). "Theory of the Inhomogeneous Electron Gas". In: *S. Lundqvist and NH March, eds*, p. 309.

Lantz, G. et al. (2015). "Surface Effects on the Mott-Hubbard Transition in Archetypal V_2O_3". In: *Phys. Rev. Lett.* 115 (23), p. 236802.

LaShell, S., B. A. McDougall, and E. Jensen (1996). "Spin Splitting of an Au(111) Surface State Band Observed with Angle Resolved Photoelectron Spectroscopy". In: *Phys. Rev. Lett.* 77 (16), pp. 3419–3422.

Lee, Ho Nyung et al. (2004). "Thermal stability of epitaxial $SrRuO_3$ films as a function of oxygen pressure". In: *Appl. Phys. Lett.* 84.20, pp. 4107–4109.

Lee, J.-S. et al. (2010). "Hidden Magnetic Configuration in Epitaxial $La_{1-x}Sr_xMnO_3$ Films". In: *Phys. Rev. Lett.* 105 (25), p. 257204.

Lepetit, Marie-Bernadette et al. (2012). "Interface Effects in Perovskite Thin Films". In: *Phys. Rev. Lett.* 108 (8), p. 087202.

Li, Q. F., X. F. Zhu, and L. F. Chen (2008). "First-principles investigations of disorder effects on electronic structure and magnetic properties in Sr_2CrMoO_6". In: *Journal of Physics: Condensed Matter* 20.25, p. 255230.

Liang, Qi-Feng, Long-Hua Wu, and Xiao Hu (2013). "Electrically tunable topological state in [111] perovskite materials with an antiferromagnetic exchange field". In: *New Journal of Physics* 15.6, p. 063031.

Liao, Z et al. (2016). "Controlled lateral anisotropy in correlated manganite heterostructures by interface-engineered oxygen octahedral coupling". In: *Nature materials* 15.4, pp. 425–431.

Liao, Zhaoliang et al. (2017). "Thickness dependent properties in oxide heterostructures driven by structurally induced metal-oxygen hybridization variations". In: *arXiv preprint arXiv:1701.07930*.

Lichtenstein, A. I. and M. I. Katsnelson (2000). "Antiferromagnetism and d-wave superconductivity in cuprates: A cluster dynamical mean-field theory". In: *Phys. Rev. B* 62 (14), R9283–R9286.

Lieb, Elliott H (2004). "A model for crystallization: A variation on the Hubbard model". In: *Condensed Matter Physics and Exactly Soluble Models*. Springer, pp. 107–117.

Lieb, Elliott H and FY Wu (2003). "The one-dimensional Hubbard model: a reminiscence". In: *Physica A: Statistical Mechanics and its Applications* 321.1, pp. 1–27.

Liechtenstein, AI, VI Anisimov, and J Zaanen (1995). "Density-functional theory and strong interactions: Orbital ordering in Mott-Hubbard insulators". In: *Phys. Rev. B* 52.8, R5467.

Longo, J. M., P. M. Raccah, and J. B. Goodenough (1968). "Magnetic properties of $SrRuO_3$ and $CaRuO_3$". In: *Journal of Applied Physics* 39.2, pp. 1327–1328.

Lv, Kai et al. (2016). "Electronic and magnetic properties of $SrRuO_3$ with Ru-vacancy: First-principle calculations". In: *EPL (Europhysics Letters)* 113.2, p. 27001.

Maezono, Ryo, Sumio Ishihara, and Naoto Nagaosa (1998). "Phase diagram of manganese oxides". In: *Phys. Rev. B* 58 (17), pp. 11583–11596.

Mahadevan, Priya et al. (2009). "Evolution of the electronic structure of a ferromagnetic metal: Case of $SrRuO_3$". In: *Phys. Rev. B* 80.3, p. 035106.

Maier, Th. et al. (2000). "d-Wave Superconductivity in the Hubbard Model". In: *Phys. Rev. Lett.* 85 (7), pp. 1524–1527.

Maier, Th. A., Th. Pruschke, and M. Jarrell (2002). "Angle-resolved photoemission spectra of the Hubbard model". In: *Phys. Rev. B* 66 (7), p. 075102.

Mannhart, Jochen and DG Schlom (2010). "Oxide interfaces—an opportunity for electronics". In: *Science* 327.5973, pp. 1607–1611.

Marzari, Nicola et al. (2012). "Maximally localized Wannier functions: Theory and applications". In: *Rev. Mod. Phys.* 84.4, p. 1419.

Mathews, S. et al. (1997). "Ferroelectric Field effect Transistor based on Epitaxial Perovskite Heterostructures". In: *Science* 276, p. 238.

Meevasana, W et al. (2011). "Creation and control of a two-dimensional electron liquid at the bare $SrTiO_3$ surface". In: *Nature materials* 10.2, pp. 114–118.

Metzner, Walter and Dieter Vollhardt (1989). "Correlated Lattice Fermions in $d = \infty$ Dimensions". In: *Phys. Rev. Lett.* 62 (3), pp. 324–327.

Mirhosseini, H. et al. (2010). "Toward a ferroelectric control of Rashba spin-orbit coupling: Bi on $BaTiO_3$ from first principles". In: *Phys. Rev. B* 81 (7), p. 073406.

Mitchell, J. F. et al. (1996). "Structural phase diagram of $La_{1-x}Sr_xMnO_{3+\delta}$: Relationship to magnetic and transport properties". In: *Phys. Rev. B* 54 (9), pp. 6172–6183.

Miyake, Takashi and F. Aryasetiawan (2008). "Screened Coulomb interaction in the maximally localized Wannier basis". In: *Phys. Rev. B* 77 (8), p. 085122.

Moeller, Goetz et al. (1995). "Critical Behavior near the Mott Transition in the Hubbard Model". In: *Phys. Rev. Lett.* 74 (11), pp. 2082–2085.

Momma, Koichi and Fujio Izumi (2011). "VESTA 3 for three-dimensional visualization of crystal, volumetric and morphology data". In: *J. Appl. Cryst.* 44.6, pp. 1272–1276.

Moritomo, Y. et al. (2000). "Electronic structure of double-perovskite transition-metal oxides". In: *Phys. Rev. B* 61 (12), R7827–R7830.

Mostofi, Arash A et al. (2008). "wannier90: A tool for obtaining maximally-localised Wannier functions". In: *Comp. Phys. Comm.* 178.9, pp. 685–699.

Mott, Nevill Francis and L Friedman (1974). "Metal-insulator transitions in VO_2, Ti_2O_3 and $Ti_{2-x}V_xO_3$". In: *Philosophical Magazine* 30.2, pp. 389–402.

Nakamura, H., T. Koga, and T. Kimura (2012). "Experimental Evidence of Cubic Rashba Effect in an Inversion-Symmetric Oxide". In: *Phys. Rev. Lett.* 108 (20), p. 206601.

Nakosai, Sho, Yukio Tanaka, and Naoto Nagaosa (2012). "Topological Superconductivity in Bilayer Rashba System". In: *Phys. Rev. Lett.* 108 (14), p. 147003.

Nekrasov, I. A. et al. (2006). "Momentum-resolved spectral functions of $SrVO_3$ calculated by $LDA + DMFT$". In: *Phys. Rev. B* 73 (15), p. 155112.

Ngantso, G Dimitri et al. (2015). "Study of the Magnetic Properties and Phase Transitions of Sr_2CrMoO_6 by Mean-Field Approximation". In: *Journal of Superconductivity and Novel Magnetism* 28.8, pp. 2589–2596.

Ning, X. K., Z. J. Wang, and Z. D. Zhang (2015). "Anisotropy of electrical and magnetic transport properties of epitaxial $SrRuO_3$ thin films". In: *Journal of Applied Physics* 117.9, p. 093907.

Nitta, Junsaku et al. (1997). "Gate Control of Spin-Orbit Interaction in an Inverted $In_{0.53}Ga_{0.47}As/In_{0.52}Al_{0.48}As$ Heterostructure". In: *Phys. Rev. Lett.* 78 (7), pp. 1335–1338.

Okamoto, Satoshi et al. (2014). "Correlation effects in (111) bilayers of perovskite transition-metal oxides". In: *Phys. Rev. B* 89 (19), p. 195121.

Park, J-H et al. (1998). "Direct evidence for a half-metallic ferromagnet". In: *Nature* 392.6678, pp. 794–796.

Parragh, Nicolaus et al. (2012). "Conserved quantities of SU(2)-invariant interactions for correlated fermions and the advantages for quantum Monte Carlo simulations". In: *Phys. Rev. B* 86.15, p. 155158.

Patterson, Frank K, Carl W Moeller, and Roland Ward (1963). "Magnetic oxides of molybdenum (V) and tungsten (V) with the ordered perovskite structure". In: *Inorganic Chemistry* 2.1, pp. 196–198.

Patterson, J. D. (1972). "Exact Eigenvalues of the Constant-Coupled One-Band Model with a Finite Number of Sites". In: *Phys. Rev. B* 6 (3), pp. 1041–1047.

Perdew, J. P. and Alex Zunger (1981). "Self-interaction correction to density-functional approximations for many-electron systems". In: *Phys. Rev. B* 23 (10), pp. 5048–5079.

Perdew, John P. (1985). "Accurate Density Functional for the Energy: Real-Space Cutoff of the Gradient Expansion for the Exchange Hole". In: *Phys. Rev. Lett.* 55 (16), pp. 1665–1668.

Perdew, John P., Kieron Burke, and Matthias Ernzerhof (1996). "Generalized Gradient Approximation Made Simple". In: *Phys. Rev. Lett.* 77 (18), pp. 3865–3868.

Pesquera, D et al. (2012). "Surface symmetry-breaking and strain effects on orbital occupancy in transition metal perovskite epitaxial films". In: *Nature communications* 3, p. 1189.

Petersen, Lars and Per Hedegård (2000). "A simple tight-binding model of spin–orbit splitting of sp-derived surface states". In: *Surface science* 459.1, pp. 49–56.

Philipp, J. B. et al. (2003). "Structural and doping effects in the half-metallic double perovskite A_2CrWO_6 (A =Sr, Ba, and Ca)". In: *Phys. Rev. B* 68 (14), p. 144431.

Pickett, Warren E. (1989). "Electronic structure of the high-temperature oxide superconductors". In: *Rev. Mod. Phys.* 61 (2), pp. 433–512.

Poteryaev, A. I., A. I. Lichtenstein, and G. Kotliar (2004). "Nonlocal Coulomb Interactions and Metal-Insulator Transition in Ti_2O_3: A Cluster LDA + DMFT Approach". In: *Phys. Rev. Lett.* 93 (8), p. 086401.

Poteryaev, Alexander I. et al. (2007). "Enhanced crystal-field splitting and orbital-selective coherence induced by strong correlations in V_2O_3". In: *Phys. Rev. B* 76 (8), p. 085127.

Poteryaev, Alexander I. et al. (2008). "Effect of crystal-field splitting and interband hybridization on the metal-insulator transitions of strongly correlated systems". In: *Phys. Rev. B* 78 (4), p. 045115.

Pruschke, Th., D. L. Cox, and M. Jarrell (1993). "Hubbard model at infinite dimensions: Thermodynamic and transport properties". In: *Phys. Rev. B* 47 (7), pp. 3553–3565.

Qi, Xiao-Liang and Shou-Cheng Zhang (2011). "Topological insulators and superconductors". In: *Rev. Mod. Phys.* 83 (4), pp. 1057–1110.

Qiu, Xiangyun et al. (2005). "Orbital Correlations in the Pseudocubic O and Rhombohedral R Phases of $LaMnO_3$". In: *Phys. Rev. Lett.* 94 (17), p. 177203.

Radaelli, P. G. et al. (1997). "Structural effects on the magnetic and transport properties of perovskite $A_{1-x}A'_xMnO_3$ (x=0.25, 0.30)". In: *Phys. Rev. B* 56 (13), pp. 8265–8276.

Ralle, Martina and Martin Jansen (1993). "Synthesis and crystal structure determination of LaAuO₃". In: *Journal of Solid State Chemistry* 105.2, pp. 378–384.

Rashba, EI (1960). "Properties of semiconductors with an extremum loop. 1. Cyclotron and combinational resonance in a magnetic field perpendicular to the plane of the loop". In: *Sov. Phys. Solid State* 2, pp. 1109–1122.

Rice, T. M. and K. Ueda (1985). "Gutzwiller Variational Approximation to the Heavy-Fermion Ground State of the Periodic Anderson Model". In: *Phys. Rev. Lett.* 55 (9), pp. 995–998.

Robaszkiewicz, S., R. Micnas, and J. Ranninger (1987). "Superconductivity in the generalized periodic Anderson model with strong local attraction". In: *Phys. Rev. B* 36 (1), pp. 180–201.

Rohringer, G. et al. (2011). "Critical Properties of the Half-Filled Hubbard Model in Three Dimensions". In: *Phys. Rev. Lett.* 107 (25), p. 256402.

Rondinelli, James M and Nicola A Spaldin (2011). "Structure and properties of functional oxide thin films: insights from electronic-structure calculations". In: *Advanced Materials* 23.30, pp. 3363–3381.

Rondinelli, James M et al. (2008). "Electronic properties of bulk and thin film $SrRuO_3$: search for the metal-insulator transition". In: *Phys. Rev. B* 78.15, p. 155107.

Roth, W. L. (1958). "Magnetic Structures of MnO, FeO, CoO, and NiO". In: *Phys. Rev.* 110 (6), pp. 1333–1341.

Rozenberg, M. J., X. Y. Zhang, and G. Kotliar (1992). "Mott-Hubbard transition in infinite dimensions". In: *Phys. Rev. Lett.* 69 (8), pp. 1236–1239.

Rubtsov, A. N., V. V. Savkin, and A. I. Lichtenstein (2005). "Continuous-time quantum Monte Carlo method for fermions". In: *Phys. Rev. B* 72 (3), p. 035122.

Saitoh, T. et al. (2002). "Half-metallic density of states in Sr_2FeMoO_6 due to Hund's rule coupling". In: *Phys. Rev. B* 66 (3), p. 035112.

Saitoh, T et al. (2005[a]). "Electronic structure of $Sr_{2-x}La_xFeMoO_6$". In: *Journal of electron spectroscopy and related phenomena* 144, pp. 601–603.

Saitoh, T. et al. (2005[b]). "Unusual electron-doping effects in $Sr_{2-x}La_xFeMoO_6$ observed by photoemission spectroscopy". In: *Phys. Rev. B* 72 (4), p. 045107.

Sánchez, M. C. et al. (2003). "Cooperative Jahn-Teller Phase Transition in $LaMnO_3$ Studied by X-Ray Absorption Spectroscopy". In: *Phys. Rev. Lett.* 90 (4), p. 045503.

Sancho, MP Lopez et al. (1985). "Highly convergent schemes for the calculation of bulk and surface Green functions". In: *Journal of Physics F: Metal Physics* 15.4, p. 851.

Sandiumenge, Felip et al. (2013). "Competing Misfit Relaxation Mechanisms in Epitaxial Correlated Oxides". In: *Phys. Rev. Lett.* 110 (10), p. 107206.

Sandvik, Anders W. (1998). "Stochastic method for analytic continuation of quantum Monte Carlo data". In: *Phys. Rev. B* 57 (17), pp. 10287–10290.

Sangiovanni, G. et al. (2006). "Static versus dynamical mean-field theory of Mott antiferromagnets". In: *Phys. Rev. B* 73 (20), p. 205121.

Sanyal, Prabuddha, Hena Das, and T. Saha-Dasgupta (2009). "Evidence of kinetic-energy-driven antiferromagnetism in double perovskites: A first-principles study of La-doped Sr_2FeMoO_6". In: *Phys. Rev. B* 80 (22), p. 224412.

Sanyal, Prabuddha et al. (2016). "Magnetism in Sr_2CrMoO_6: A combined *ab initio* and model study". In: *Phys. Rev. B* 94 (3), p. 035132.

Sarma, D. D. (2001). "A new class of magnetic materials: Sr_2FeMoO_6 and related compounds". In: *Current Opinion in Solid State and Materials Science* 5.4, pp. 261–268.

Sarma, D. D. et al. (2000). "Electronic Structure of Sr_2FeMoO_6". In: *Phys. Rev. Lett.* 85 (12), pp. 2549–2552.

Sawada, H. et al. (1997). "Jahn-Teller distortion and magnetic structures in $LaMnO_3$". In: *Phys. Rev. B* 56 (19), pp. 12154–12160.

Sawatzky, G. A. and J. W. Allen (1984). "Magnitude and Origin of the Band Gap in NiO". In: *Phys. Rev. Lett.* 53 (24), pp. 2339–2342.

Schäfer, T. et al. (2013). "Divergent Precursors of the Mott-Hubbard Transition at the Two-Particle Level". In: *Phys. Rev. Lett.* 110 (24), p. 246405.

Schoiswohl, J et al. (2004). "V_2O_3 (0001) surface terminations: from oxygen-to vanadium-rich". In: *Surface science* 555.1, pp. 101–117.

Schollwöck, U. (2005). "The density-matrix renormalization group". In: *Rev. Mod. Phys.* 77 (1), pp. 259–315.

Shai, D. E. et al. (2013). "Quasiparticle Mass Enhancement and Temperature Dependence of the Electronic Structure of Ferromagnetic $SrRuO_3$ Thin Films". In: *Phys. Rev. Lett.* 110 (8), p. 087004.

Shalom, M. B. et al. (2010). "Tuning Spin-Orbit Coupling and Superconductivity at the $SrTiO_3/LaAlO_3$ Interface: A Magnetotransport Study". In: *Phys. Rev. Lett.* 104.12, p. 126802.

Sheng, Xian-Lei and Branislav K Nikolic (2016). "Correlation-driven topological phase transition from in-plane magnetized quantum anomalous Hall to Mott insulating phase in monolayer transition metal trichlorides". In: *arXiv preprint arXiv:1610.02719*.

Shi, Youguo et al. (2013). "High-Pressure Synthesis of $5d$ Cubic Perovskite $BaOsO_3$ at 17 GPa: Ferromagnetic Evolution over $3d$ to $5d$ Series". In: *Journal of the American Chemical Society* 135.44, pp. 16507–16516.

Si, Liang et al. (2015). "Route to room-temperature ferromagnetic ultrathin $SrRuO_3$ films". In: *Phys. Rev. B* 92 (4), p. 041108.

Silins, E and Vladislav Capek (1994). *Organic molecular crystals: interaction, localization, and transport phenomena*. American Institute of Physics.

Singh, David J (1996). "Electronic and magnetic properties of the $4d$ itinerant ferromagnet SrRuO$_3$". In: *J. Appl. Phys.* 79.8, pp. 4818–4820.

Singh, David J and Lars Nordstrom (2006). *Planewaves, Pseudopotentials, and the LAPW method*. Springer Science & Business Media.

Slater, John C (1930). "Note on Hartree's method". In: *Physical Review* 35.2, p. 210.

— (1937). "Wave functions in a periodic potential". In: *Physical Review* 51.10, p. 846.

Stengel, Massimiliano and Nicola A Spaldin (2006). "Origin of the dielectric dead layer in nanoscale capacitors". In: *Nature* 443.7112, pp. 679–682.

Surnev, S, MG Ramsey, and FP Netzer (2003). "Vanadium oxide surface studies". In: *Progress in surface science* 73.4, pp. 117–165.

Taranto, C. et al. (2013). "Comparing quasiparticle GW+DMFT and LDA+DMFT for the test bed material SrVO$_3$". In: *Phys. Rev. B* 88 (16), p. 165119.

Taranto, C. et al. (2014). "From Infinite to Two Dimensions through the Functional Renormalization Group". In: *Phys. Rev. Lett.* 112 (19), p. 196402.

Tahvildar-Zadeh, A. N. and Jarrell, M. and Freericks, J. K. (1997). "Protracted screening in the periodic Anderson model". In: *Phys. Rev. B* 55 (6), R3332–R3335.

— (1998). "Low-Temperature Coherence in the Periodic Anderson Model: Predictions for Photoemission of Heavy Fermions". In: *Phys. Rev. Lett.* 80 (23), pp. 5168–5171.

Tazaki, Ryoko et al. (2009). "Lattice distortion under an electric field in BaTiO$_3$ piezoelectric single crystal". In: *J. Phys.: Condens. Matter.* 21, p. 215903.

Tebano, A. et al. (2008). "Evidence of Orbital Reconstruction at Interfaces in Ultrathin $La_{0.67}Sr_{0.33}MnO_3$ Films". In: *Phys. Rev. Lett.* 100 (13), p. 137401.

Thio, Tineke et al. (1990). "Determination of the energy gap for charged excitations in insulating La_2CuO_4". In: *Physical Review B* 42.16, p. 10800.

Thomas, Llewellyn H (1927). "The calculation of atomic fields". In: *Mathematical Proceedings of the Cambridge Philosophical Society*. Vol. 23. 05. Cambridge Univ Press, pp. 542–548.

Thouless, D. J. et al. (1982). "Quantized Hall Conductance in a Two-Dimensional Periodic Potential". In: *Phys. Rev. Lett.* 49 (6), pp. 405–408.

Tian, W et al. (2007). "Epitaxial growth and magnetic properties of the first five members of the layered $Sr_{n+1}Ru_nO_{3n+1}$ oxide series". In: *Appl. Phys. Lett.* 90.2, p. 022507.

Tokura, Y and Y Tomioka (1999). "Colossal magnetoresistive manganites". In: *Journal of magnetism and magnetic materials* 200.1, pp. 1–23.

Tomczak, Jan M (2015). "QSGW+ DMFT: an electronic structure scheme for the iron pnictides and beyond". In: *Journal of Physics: Conference Series*. Vol. 592. 1. IOP Publishing, p. 012055.

Tomioka, Y. et al. (2000). "Magnetic and electronic properties of a single crystal of ordered double perovskite Sr_2FeMoO_6". In: *Phys. Rev. B* 61 (1), pp. 422–427.

Toschi, A., A. A. Katanin, and K. Held (2007). "Dynamical vertex approximation: A step beyond dynamical mean-field theory". In: *Phys. Rev. B* 75 (4), p. 045118.

Toyota, D et al. (2005). "Thickness-dependent electronic structure of ultrathin $SrRuO_3$ films studied by in situ photoemission spectroscopy". In: *Appl. Phys. Lett.* 87.16, pp. 162508–162508.

Toyota, D et al. (2006). "Ferromagnetism stabilization of ultrathin $SrRuO_3$ films: Thickness-dependent physical properties". In: *J. Appl. Phys.* 99.8, 08N505.

Tran, Fabien and Peter Blaha (2009). "Accurate band gaps of semiconductors and insulators with a semilocal exchange-correlation potential". In: *Phys. Rev. Lett.* 102.22, p. 226401.

Tranquada, J. M. (1988). "Antiferromagnetism in $YBa_2Cu_3O_{6+x}$". In: *Journal of Applied Physics* 64.10, pp. 6071–6074.

Tranquada, J. M. et al. (1988). "Neutron-Diffraction Determination of Antiferromagnetic Structure of Cu Ions in $YBa_2Cu_3O_{6+x}$ with x=0.0 and 0.15". In: *Phys. Rev. Lett.* 60 (2), pp. 156–159.

Trimarchi, G. and N. Binggeli (2005). "Structural and electronic properties of $LaMnO_3$ under pressure: An *ab initio* LDA+U study". In: *Phys. Rev. B* 71 (3), p. 035101.

Ueda, Kazuo, Hirokazu Tsunetsugu, and Manfred Sigrist (1992). "Singlet ground state of the periodic Anderson model at half filling: A rigorous result". In: *Phys. Rev. Lett.* 68 (7), pp. 1030–1033.

Vailionis, A et al. (2014). "Symmetry and lattice mismatch induced strain accommodation near and away from correlated perovskite interfaces". In: *Applied physics letters* 105.13, p. 131906.

van Dongen, P. G. J. and Vollhardt, D. (1989). "Exact solution and thermodynamics of the Hubbard model with infinite-range hopping". In: *Phys. Rev. B* 40 (10), pp. 7252–7255.

— (1990). "Exact mean-field Hamiltonian for fermionic lattice models in high dimensions". In: *Phys. Rev. Lett.* 65 (13), pp. 1663–1666.

Verissimo-Alves, M. et al. (2012). "Highly confined spin-polarized two-dimensional electron gas in $SrTiO_3/SrRuO_3$ superlattices". In: *Phys. Rev. Lett.* 108 (10), p. 107003.

Vollhardt, Dieter (1984). "Normal ^3He: an almost localized Fermi liquid". In: *Rev. Mod. Phys.* 56 (1), pp. 99–120.

Wang, X Renshaw et al. (2015). "Imaging and control of ferromagnetism in $LaMnO_3/SrTiO_3$ heterostructures". In: *Science* 349.6249, pp. 716–719.

Wannier, Gregory H. (1937). "The Structure of Electronic Excitation Levels in Insulating Crystals". In: *Phys. Rev.* 52 (3), pp. 191–197.

Wei, Pan and Zheng Qing Qi (1994). "Electronic structure of La_2CuO_4 and $YBa_2Cu_3O_6$: A local-spin-density approximation with on-site Coulomb- U correlation calculations". In: *Phys. Rev. B* 49 (17), pp. 12159–12164.

Wen, Xiao-Gang (1990). "Topological orders in rigid states". In: *International Journal of Modern Physics B* 4.02, pp. 239–271.

Werner, Philipp et al. (2008). "Spin freezing transition and non-Fermi-liquid self-energy in a three-orbital model". In: *Phys. Rev. Lett.* 101.16, p. 166405.

Wilson, Kenneth G. (1975). "The renormalization group: Critical phenomena and the Kondo problem". In: *Rev. Mod. Phys.* 47 (4), pp. 773–840.

Winkler, R et al. (2003). *Spin-Orbit Coupling in Two-Dimensional Electron and Hole Systems*. Vol. 41. Springer.

Wu, Hua (2001). "Electronic structure study of double perovskites A_2FeReO$_6$($A =$ Ba, Sr, Ca) and Sr$_2$$MMoO_6$ ($M =$ Cr, Mn, Fe, Co) by LSDA and LSDA + U". In: *Phys. Rev. B* 64 (12), p. 125126.

Xia, Jing et al. (2009). "Critical thickness for itinerant ferromagnetism in ultrathin films of SrRuO$_3$". In: *Phys. Rev. B* 79 (14), p. 140407.

Xiao, Di, Ming-Che Chang, and Qian Niu (2010). "Berry phase effects on electronic properties". In: *Rev. Mod. Phys.* 82 (3), pp. 1959–2007.

Xiao, Di et al. (2011). "Interface engineering of quantum Hall effects in digital transition metal oxide heterostructures". In: *Nature communications* 2, p. 596.

Yamasaki, A. et al. (2006). "Pressure-Induced Metal-Insulator Transition in LaMnO$_3$ Is Not of Mott-Hubbard Type". In: *Phys. Rev. Lett.* 96 (16), p. 166401.

Yang, Y.-F. and K. Held (2007). "Localization of strongly correlated electrons as Jahn-Teller polarons in manganites". In: *Phys. Rev. B* 76 (21), p. 212401.

Yin, Wei-Guo et al. (2013). "Ferromagnetic Exchange Anisotropy from Antiferromagnetic Superexchange in the Mixed $3d$-$5d$ Transition-Metal Compound Sr$_3$CuIrO$_6$". In: *Phys. Rev. Lett.* 111 (5), p. 057202.

Yoshimatsu, K. et al. (2010). "Dimensional-Crossover-Driven Metal-Insulator Transition in SrVO$_3$ Ultrathin Films". In: *Phys. Rev. Lett.* 104 (14), p. 147601.

Yoshimatsu, K et al. (2011). "Metallic quantum well states in artificial structures of strongly correlated oxide". In: *Science* 333.6040, pp. 319–322.

Zaanen, J., G. A. Sawatzky, and J. W. Allen (1985). "Band gaps and electronic structure of transition-metal compounds". In: *Phys. Rev. Lett.* 55 (4), pp. 418–421.

Zhang, Lunyong et al. (2014). "Sensitively Temperature-Dependent Spin–Orbit Coupling in SrIrO$_3$ Thin Films". In: *Journal of the Physical Society of Japan* 83.5, p. 054707.

Zhong, Zhicheng, Anna Tóth, and Karsten Held (2013). "Theory of spin-orbit coupling at LaAlO$_3$/SrTiO$_3$ interfaces and SrTiO$_3$ surfaces". In: *Phys. Rev. B* 87 (16), p. 161102.

Zhong, Zhicheng, Qinfang Zhang, and Karsten Held (2013). "Quantum confinement in perovskite oxide heterostructures: Tight binding instead of a nearly free electron picture". In: *Phys. Rev. B* 88 (12), p. 125401.

Zhong, Zhicheng et al. (2015). "Giant switchable Rashba effect in oxide heterostructures". In: *Advanced Materials Interfaces* 2.5.

Zhou, Jin-Jian et al. (2014). "Engineering Topological Surface States and Giant Rashba Spin Splitting in BiTeI/Bi$_2$Te$_3$ Heterostructures". In: *Scientific Reports* 4, p. 3841.

Zubko, Pavlo et al. (2011). "Interface physics in complex oxide heterostructures". In: *Annu. Rev. Condens. Matter Phys.* 2.1, pp. 141–165.

Zutic, Igor, Jaroslav Fabian, and S. Das Sarma (2004). "Spintronics: Fundamentals and applications". In: *Rev. Mod. Phys.* 76 (2), pp. 323–410.

Appendix A

Curriculum Vitae

Liang SI

Curriculum Vitae

Information

Gender	Male
Born	October 1986, FuShun City, LiaoNing Province, P. R. China
Family Status	Married, one daughter
Nationality	P. R. China
Email	liang.si@ifp.tuwien.ac.at siliangnwu@gmail.com
Telephone	+43-1-58801-138920 (Office) +43-0-660-4592843 (Handy)
Address	Institute of Solid State Physics, Vienna University of Technology, Wiedner Hauptstraβe 8-10/E138, 1040 Vienna, Austria

Education

2013.07– present   **Doctoral Program in Technical Physics**, *Institute of Solid State Physics, Vienna University of Technology, Vienna, Austria.*
- Research Supervisor: Prof. Dr. Karsten Held.
- Research Topics: Electronic structures of transition metal oxides at heterostructures, interfaces, surfaces and thin films [1-6].

2010.09– 2013.07   **Master Degree in Theoretical Physics**, *Institution of Modern Physics, Northwest University, China.*
- Research Topics: First-principles study of structural phase transformation in shape memory alloys, e.g. TiNi and TiRh [7-11].

2006.09– 2010.07   **Bachelor Degree in Applied Physics**, *Department of Physics, Northwest University, China.*
- Research Topics: Electronic property of hydrogen storage materials, e.g. $LiBH_4$ [12].
- Minor in Law.

Research Interests

1. Transition-Metal Oxide Heterostructures, Interfaces, Surfaces and Thin Films
2. Spin-Orbit Interaction

3. Strongly Electronic Correlated Systems
4. Topological Insulating States
5. High-Temperature Superconductors

Research Skills and Tools

Methods: Density-Functional-Theory (DFT) Calculations, Dynamical mean field Theory (DMFT)

Wannier Functions, Tight-binding Method, Green's Functions

Codes: Wien2k, VASP, Wien2Wannier, Wannier90 and W2Dynamic (CT-QMC)

Programing Languages: Fortran, C, C++

Academic Services

Referee for American Physical Society (APS) journal: Physical Review Letters (PRL), Physical Review B (PRB).

Publications

1. **Quantum anomalous Hall state in ferromagnetic SrRuO$_3$ (111) bilayers**.
   - Liang Si, Oleg Janson, Gang Li, Zhicheng Zhong, Zhaoliang Liao, Gertjan Koster and Karsten Held.
   - Phys. Rev. Lett. under review, arXiv:1610.01948 (2016)

2. **Thickness dependent properties in oxide heterostructures driven by structurally induced metal-oxygen hybridization variations**.
   - Z. L. Liao, N. Gauquelin, R. J. Green, S. Macke, J. Gonnissen, S. Thomas, Z. Zhong, L. Li, L. Si, S. van Aert, P. Hansmaan, K. Held, J. Xia, J. Verbeeck, G. Van Tendeloo, B. Keimer, G. A. Sawatzky, G. Koster, M. Huijben, G. Rijnders.
   - Advanced Functional Materials accpeted, arXiv:1701.07930 (2017)

3. **Magnetism in Sr$_2$CrMoO$_6$: A combined *ab initio* and model study**.
   - Prabuddha Sanyal, Anita Halder, Liang Si, Markus Wallerberger, Karsten Held, and Tanusri Saha-Dasgupta.
   - Phys. Rev. B 94, 035132 (2016)

4. **Surface Effects on the Mott-Hubbard Transition in Archetypal V$_2$O$_3$**.
   - G. Lantz, M. Hajlaoui, E. Papalazarou, V. L. R. Jacques, A. Mazzotti, M. Marsi, S. Lupi, M. Amati, L. Gregoratti, L. Si, Z. Zhong, and K. Held.
   - Phys. Rev. Lett. 115, 236802 (2015)

5. **Route to room-temperature ferromagnetic ultrathin SrRuO$_3$ films**.
   - Liang Si, Zhicheng Zhong, Jan M. Tomczak, and Karsten Held.
   - Phys. Rev. B 92, 041108(R) (2015)

6. **Giant switchable Rashba effect in oxide heterostructures**.
   - Zhicheng Zhong, Liang Si, Qinfang Zhang, Wei-Guo Yin, Seiji Yunoki, and Karsten Held.
   - Advanced Materials Interfaces 2, 1400445 (2015)

7. **Structural, elastic, phonon, and electronic properties of MnPd alloy**.
   - Jun-Fei Wang, Wen-Zhou Chen, Zhen-Yi Jiang, Xiao-Dong Zhang and Liang Si.
   - Chinese Physics B, 7, 077102 (2012)

8. **First-principles study of martensitic phase transformation of TiRh alloy**.
   - Liang Si, Zhen-Yi Jiang, Bo Zhou, Wen-Zhou Chen.
   - Physica B: Condensed Matter, 407, 347 (2012)

9. **Electronic band structure, stability, structural, and elastic properties of IrTi alloys**.
   - Wen-Zhou Chen, Qian Li, Zhen-Yi Jiang, Xiao-dong Zhang, Liang Si, Li-Sha Li, Rui Wu.
   - Physica B: Condensed Matter, 407, 2744 (2012)

10. **First-principles study of structural stability, elastic, vibrational, and electronic properties of TaRu alloys**.
    - Qian Li, Zhen-Yi Jiang, Ming Li, Yu-Qing Hou, Liang Si, Xiao-Dong Zhang and Bo Zhou.
    - Europhysics Letters. 95, 18002 (2011)

11. **First-principles study of martensitic transformation of IrTi alloy**.
    - Wen-Zhou Chen, Zhen-Yi Jiang, Liang Si, Li-Sha Li, Bo Zhou.
    - Solid State Communications, 151, 1433 (2011)

12. ***Ab initio* calculations of higher-pressure phase electronic structure of LiBH$_4$**.
    - Li-Sha Li, Wen-Zhou Chen, Liang Si, Qi Song, Jun-Qing Wen, Zhen-Yi Jiang.
    - Journal of Northwest University, 41, 235 (2011)

Contributions to Conferences

1. **Electronic correlation effects in SrRuO$_3$ ultra-thin films**.
   - Contributed talk. APS March Meeting 2016. March 14-18, 2016; Baltimore, Maryland.

2. **Route to room temperature ferromagnetic ultrathin SrRuO$_3$ films**.
   - Poster presentation. The 22_{nd} International Workshop on Oxide Electronics, 7-9 October 2015, College de France, Paris, France.

3. **(001), (110) and (111)-oriented ABO$_3$ thin films**.
   - Contributed talk. Solids4Fun Summer School 2015, 29 June - 3 July 2015, Hernstein, Austria.

4. **Electronic correlations: origin of the fancy transition in SrRuO$_3$**.
   - Poster presentation. Solids4Fun Summer School 2014, 14-18 July 2014, Hernstein, Austria.

5. ***Ab initio* study of electronic correlation in SrRuO$_3$**.
   - Poster presentation. DPG Spring Meeting, 30 March-4 April 2014, Dresden, Germany.

6. **First-principles study of martensitic phase transformation of Ti-based alloy**.
   - Contributed talk. The 10th International Conference on Condensed Matter Theory and Computational Materials Science, 2011, Jinhua, China.

7. **Origin of martensitic phase transformation of Ti-based alloys**.
   - Contributed talk. International Conference on Theoretical and High Performance Computational Chemistry, 2011, Xi'an, China.

Research Summary

Transition-metal oxides (TMOs) in the bulk form exhibit diverse physical behaviors. Artificial structures of TMOs, e.g. heterostructures, interfaces, surfaces and thin films, open new avenues for manipulating and tuning the physical properties to realize novel states and functionalities. In my doctoral studies, I applied state-of-the-art computational methods to search for novel physical properties in such TMO-based materials. An *ab-initio* description of the electronic structures of real

materials are facilitated by the density functional theory (DFT) and the local-density approximation (LDA). But LDA and its generalizations, such as the general gradient approximation (GGA), fail for systems with strong electronic correlations, such as TMOs and TMO-based materials.

To account for correlation effects, I employ a mixture of the tight-binding analysis, DFT($+U$) and DFT+DMFT. The general scheme of my computational approach contains four steps: (i) band structure calculations, including accurate structural optimizations for a given material; (ii) a projection of the DFT bands onto maximally localized Wannier orbitals to construct a realistic tight-binding (TB) model; (iii) supplementing the TB model with the missing terms, such as spin-orbit coupling and on-site correlations, and solving it using dynamical mean field theory (DMFT); and as final step, (iv) the analysis of electronic, magnetic or topological properties of the resulting model to understand the microscopic roots of the experimentally observed behavior or to predict the emergence of novel states and in this way motivate experimental activity.

This scheme is a viable way to describe strongly correlated systems, as evidenced by good agreement with experiments [1, 4, 5]. My DFT+DMFT prediction [5] of a ferromagnetic state in doped, ultrathin (001) $SrRuO_3$ films is recently experimentally confirmed [Phys. Rev. B 92, 115153]. Our prediction of the room-temperature half-metallic ferromagnetic state and quantum anomalous Hall (QAH) effect in $SrRuO_3$ (111)-oriented bilayers [1] will underpin the experimental attempts to realize these exotic ferromagnetic and topological states in $SrRuO_3$ heterostructures. By introducing a $BaOsO_3$ monolayer into a $BaTiO_3$ heterostructure, we predict a giant switchable Rashba effect in oxide heterostructures [6]. By using DFT+DMFT and model calculations, we investigate the magnetic and electronic structures of double-perovskite materials Sr_2CrMoO_6 [3]. Ref. [2, 4] are cooperation articles with experimental groups, in which we used DFT/DMFT to explain the experimental observed electronic structures of TMOs surfaces or thin films systems.

Awards

2007-2009	Student Union Leader in Northwest University
2007.6	The First Prize of Undergraduate Academic Science and Technology Works of Northwest University
2007.6	The Second Prize of 'Challenge Cup' Undergraduate Academic Science and Technology Works of Shaanxi Province
2007.12	The First Prize Scholarship of Northwest University (top 5%)
2007.12	The Third Prize of Simulation Recruitment Contest of Northwest University
2008.5	Outstanding student leader title of Northwest University
2008.5	Outstanding Communist Youth League member of Northwest University
2008.6	The Scholarship of Prof. Jie-Heng Yue (only one in department)
2009.1	Outstanding student leader Scholarship of Northwest University
2009.1	Outstanding Communist Youth League member of Shaanxi Province (only one winner in every university)
2009.5	Excellent cadre of Communist Youth League of Northwest University
2009.12	Individual Scholarship of Northwest University
2010.12	The Second Prize Scholarship of Northwest University

2011.12   The First Prize Scholarship of Northwest University (top 5%)
2011.11   The Third Prize of Simulated International Conference Report of Physics Department
2011.12   Prize for excellent paper of Northwest University

Languages

Chinese   **Mothertongue**
English   **Good**   *International English Language Testing System (IELTS): 6.0/9.0 (2013)*
German   **Basic**   *A1 Courses*

References

1. **Prof. Dr. Karsten Held**.
   - Chairman of Computational Materials Science group, Vienna University of Technology, Austria.
   - Phone: +43-1-58801-13710
   - E-mail: held@ifp.tuwien.ac.at

2. **Prof. Dr. Ulrike Diebold**.
   - Deputy Department Head, Chairman of Surface Physics group, Vienna University of Technology, Austria.
   - Phone: +43-1-58801-13425
   - E-mail: diebold@iap.tuwien.ac.at

3. **Prof. Dr. Wen-Li Yang**.
   - Director of Institution of Modern Physics, Northwest University, China.
   - Phone: +86-029-88303490
   - E-mail: wlyang@nwu.edu.cn

4. **Prof. Dr. Zhicheng Zhong**.
   - Magnetoresistive Materials/Structures and Devices, Ningbo Institute of Materials Technology and Engineering, Chinese Academy of Sciences, Ningbo, Zhejiang 315201, P. R. China.
   - E-mail: zhong@nimte.ac.cn